Forschungszentrum Karlsruhe
in der Helmholtz-Gemeinschaftt

Wissenschaftliche Berichte
FZKA 6591

Low Pressure Corium Dispersion Experiments in the DISCO Test Facility with Cold Simulant Fluids

L. Meyer, M. Gargallo, M. Kirstahler, M. Schwall, E. Wachter, G. Wörner

Institut für Kern- und Energietechnik
Programm Nukleare Sicherheitsforschung

August 2006

Forschungszentrum Karlsruhe

in der Helmholtz-Gemeinschaft

Wissenschaftliche Berichte

FZKA 6591

Low Pressure Corium Dispersion Experiments in the DISCO Test Facility with Cold Simulant Fluids

L. Meyer, M. Gargallo,

M. Kirstahler, M. Schwall, E. Wachter, G. Wörner

Institut für Kern- und Energietechnik

Programm Nukleare Sicherheitsforschung

Forschungszentrum Karlsruhe GmbH, Karlsruhe

2006

Forschungszentrum Karlsruhe GmbH
Postfach 3640, 76021 Karlsruhe

Mitglied der Hermann von Helmholtz-Gemeinschaft
Deutscher Forschungszentren (HGF)

ISSN 0947-8620

urn:nbn:de:0005-065918

ZUSAMMENFASSUNG

Experimente zur Dispersion der Kernschmelze bei niedrigem Druck in der DISCO Anlage mit kalten Modellfluiden

Das Versagen des RDB unter vollem Systemdruck wird durch systemtechnische Maßnahmen verhindert. Ein Versagen bei einem zu unterstellenden Druck von 1 bis 2 MPa kann u.U. noch zu starker Dispersion und Umverteilung der Schmelze in die Reaktorräume und den Dom und damit zur direkten Aufheizung der Containmentatmosphäre führen. Das Zusammenwirken der hierbei auftretenden Materialtransportprozesse sowie der thermischen und chemischen (Wasserstofferzeugung und -verbrennung) Wechselwirkungen ist komplex und kann derzeit mit Computercodes noch nicht oder nur bedingt berechnet werden. Notwendig sind daher Einsichten und Daten aus experimentellen Untersuchungen, insbesondere auch integrale Experimente, deren Ergebnisse mit Modellen und Coderechnungen auf die Reaktorgeometrie übertragen werden können. Das Hauptziel der Untersuchungen ist die Bestimmung eines maximal zulässigen Druckes zum Zeitpunkt des RDB-Versagens, bei dem keine relevante Dispersion der Schmelze auftritt, im Zusammenspiel mit einer für dieses Ziel optimierten Grubengeometrie.

Im Versuchsstand DISCO-C (DIspersion of Simulant COrium – Cold), der die Reaktorgrube und die anschließenden Räume eines großen europäischen Reaktors im Maßstab 1:18 modelliert, wurde der erste Teil des Versuchsprogrammes mit kalten Modellfluiden durchgeführt, um die fluiddynamischen Prozesse zu studieren. Als Modellflüssigkeit für die Schmelze diente Wasser und eine Blei-Wismuthlegierung, und anstelle von Dampf wurde Stickstoff und Helium verwendet. Als Versagensart wurden runde Löcher verschiedener Größe am Boden und an der Seite der RDB-Kalotte, und seitliche Risse bis zum totalen Abriss der ganzen Kalotte untersucht.

Zum Studium der Ähnlichkeitsbeziehungen wurden an DISCO-C 22 Experimente mit einer Basisgeometrie unter Variation der Fluide, des Versagensdruckes und der Lochgröße durchgeführt. Die Basisgeometrie ist definiert durch zentrale Löcher in der RDB-Kalotte und einen einzigen Strömungspfad aus der Grube entlang den Hauptkühlmittelleitungen in die Pumpen- und Dampferzeugerräume. Die ausgetragenen Flüssigkeitsmassen betragen zwischen 0% bei kleinen Löchern (0.3 m Durchmesser skaliert) und niedrigen Versagensdrücken (0.3 MPa) und 78% bei großen Löchern (0.9 m) und höheren Drücken (1 MPa). Eine bestimmte Flüssigkeitsmenge lagert sich in dem Ringraum am RDB-Auflager ab, was bei dem verwendeten Gesamtvolumen von 0.0034 m³ (entspricht 20 m³ skaliert) ca. 25 % entspricht. Bei kleineren Flüssigkeitsvolumen steigt der im Ringraum abgelagerte Anteil entsprechend. Aus den gemessenen Druckverläufen im RDB und der Grube kann eine mittlere Gasgeschwindigkeit im Grubenringspalt berechnet werden. Mit dem maximalen Wert dieser Geschwindigkeit, den Dichten des Gases und der Flüssigkeit und der Oberflächenspannung kann eine Kutadeladse-Zahl, $Ku = \rho_G u_G^2/(\rho_L\ g\ \sigma)^{1/2}$, gebildet werden. Die Austragsraten für alle Stoffkombinationen, Lochgrößen und Versagensdrücke lassen sich gut mit dieser Ähnlichkeitszahl korrelieren. Allerdings gilt das nur für gleiche Grubengeometrien und gleiche Schmelzemassen.

In einer zweite Versuchsserie wurde der Einfluss der Position und der Form des RDB-Versagens untersucht. Außerdem wurden spezielle Grubengeometrien untersucht, u.a. auch eine Vorrichtung, die den Schmelzeaustrag reduziert. Das seitliche Versagen wurde mit vier verschiedenen Öffnungen simuliert; zwei Löcher mit 25 mm und 50 mm Durchmesser unter einem Winkel von 45°, ein horizontaler Schlitz mit der Fläche eines 25 mm Loches, und ein Abkippen der Kalotte. Für zentrale Löcher am Boden waren die beiden wichtigsten Parameter für den Dispersionsprozess die Lochgröße und der Versagensdruck. Bei seitlichem Versagen gibt es einen zusätzlichen Parameter; das ist die Höhe des Flüssigkeitsspiegels in der Kalotte in Bezug auf die obere und die untere Kante der Versagensöffnung. In den meisten Fällen wird nur ein Teil der Flüssigkeit aus dem RDB ausgetragen. Wenn der Flüssigkeitsspiegel anfangs über der Oberkante liegt, beginnt der Austrag mit einer einphasigen Flüssigkeitsströmung, getrieben von der Druckdifferenz zwischen RDB und Grube, wie bei zentralen Löchern. Allerdings findet der Gasdurchbruch bzw. der Übergang auf zweiphasiges Ausströmen früher statt. In der folgenden Phase wird die Flüssigkeit durch Entrainment aus dem RDB ausgetragen. Neben der Gasgeschwindigkeit bestimmen das Dichteverhältnis zwischen Gas und Flüssigkeit, die Oberfläche des Flüssigkeitspools und die Dauer des Gasaustritts den Entrainmentprozess. So kann der Flüssigkeitsanteil, der durch Entrainment ausgetragen wird, bei einem kleinen Loch größer sein als bei einem großen Loch, da die Ausblaszeit länger, aber die maximalen Gasgeschwindigkeiten ähnlich sind.

Wird die Versagensöffnung von der zentralen Position an die Seite verlegt, so reduziert sich der Flüssigkeitsaustrag aus der Reaktorgrube, auch wenn man den ausgetragenen Anteil nur auf die Flüssigkeitsmasse bezieht, die aus dem RDB ausgetreten ist. Die Hauptursache ist wahrscheinlich die vorhandene Umfangskomponente der Geschwindigkeit in der Grube. Bei seitlichem Versagen führt eine größere Öffnung nicht notwendigerweise zu einem größeren Schmelzeaustrag aus der Grube. Für Versagensdrücke bis zu 1.6 MPa wurden maximale Dispersionsanteile von 48% mit Wasser und 1% mit Flüssigmetall gemessen.

ABSTRACT

In a severe accident special pressure relief valves in the primary circuit of German Pressurized Water Reactors (PWR) will transfer a high pressure accident into a low pressure scenario. However, there may be a time window during late in-vessel reflooding scenarios where the pressure is in the order of 1 or 2 MPa at the moment of the reactor vessel rupture. A failure in the bottom head of the reactor pressure vessel, followed by melt expulsion and blowdown of the reactor cooling system, might disperse molten core debris out of the reactor pit, even at such low pressures. The mechanisms of efficient debris-to-gas heat transfer, exothermic metal/oxygen reactions, and hydrogen combustion may cause a rapid increase in pressure and temperature in the reactor containment. Integral experiments are necessary to furnish data for modeling these processes in computer codes, that will be used to apply these result to the reactor case. The acquired knowledge can lead to realize additional safety margins for existing or future plants.

The test facility DISCO-C (DIspersion of Simulant COrium – Cold) models the annular reactor cavity and the subcompartments of a large European reactor in a scale 1:18. The fluid dynamics of the dispersion process was studied using model fluids, water or bismuth alloy instead of corium, and nitrogen or helium instead of steam. The effects of different breach sizes and locations, and different failure pressures on the dispersion were studied, specifically by testing central holes, lateral holes, horizontal rips, and complete ripping of the bottom head.

22 experiments were performed in a basic cavity geometry with holes at the bottom of the lower head to study the similarity relations. Variables were the hole diameter, the initial pressure in the RPV and the fluids used. The only flow path out of the reactor pit was the annular gap between the inner wall of the reactor pit and the RPV, and then along the main coolant lines into the subcompartments. Dispersal rates between 0% with small holes (0.3 m scaled) and low pressure (0.3 MPa) and 78% with large holes (0.9 m) and higher pressures ($\geq$ 1 MPa) were observed. A certain amount of liquid (approximately 25% of 0.0034 m³) is trapped in the space near the RPV support structure, independent of the initial conditions. The dispersed fractions are lower with metal than with water, but still high. The results concerning the dispersed fractions could be correlated by the Kutateladze number $Ku = \rho_G u_{G2} / (\rho_L\ g\ \sigma)^{1/2}$, with u_G, the maximum gas velocity in the annular space around the RPV, for all hole sizes, both driving gases, nitrogen and helium, and both liquids, water and Bi-alloy, with $f_d = 0.4 \log10(Ku) \leq 0.76$. The Kutateladze number represents the conditions to levitate droplets against gravity. No sharp threshold velocity or pressure could be found, below which no dispersion occurred. From the similarity correlations we can deduce that the results from the liquid metal tests represent the lower bound for the dispersed melt fractions in the reactor case.

In a second test series the effect of the position and the shape of the breach in the lower head was investigated. Four different opening were studied: two different hole sizes at an angle of 45 degrees, one horizontal slot, and the unzipping and tilting of the lower head. With lateral breaches the liquid height in the lower head relative to the upper and lower edge of the breach is an additional parameter for the dispersion process. In most cases not all the liquid is discharged out of the RPV. If the initial liquid level is above the upper edge, the

blowdown starts with the single-phase liquid discharge, driven by the pressure difference between vessel and cavity, as for central holes. However, the gas blowthrough occurs earlier than with central holes. In the subsequent stage the liquid is carried out of the lower head by entrainment. The gas velocity, the density ratio of gas and liquid, the surface area of the liquid pool, and the duration of the blowdown govern this entrainment process. Therefore, the entrained liquid fraction can be higher with a small breach than with a large one, because the blowdown time is longer while the maximum velocity may be the same.

Shifting the break from the central position towards the side of the lower head leads to a smaller dispersion of liquid, even if the dispersed fraction is related only to the liquid mass that has been ejected out of the RPV. The main effect is probably the circumferential component of the velocity in the cavity. With lateral failures maximum dispersed fractions of 48% were found with water as melt simulant and less than 1% with liquid metal.

As for the central breaches, we can make the cautious statement, that taking the known similarity correlations, the results from the liquid metal tests represent the lower bound for the dispersed melt fractions, however, they are probably closer to the expected values than the results from the water tests, that represent the upper bound. So, significantly less dispersion of melt can be expected for lateral breaches at pressures below 2 MPa, probably less than 10%. If higher dispersion occurs, due to higher pressure at failure, simple devices to mitigate the dispersion out of the cavity may be feasible. For the investigation of thermal and chemical effects, experiments with alumina-iron melt and steam will be performed in a similar geometry.

CONTENTS

List of Figures

List of Tables

NOMENCLATURE

A_h	flow area of hole, m^2
c_d	discharge coefficient at hole
D	inner diameter of RPV-vessel, m
d	diameter of hole in lower head, m
f	fraction of liquid
Fr	Froude number
g	gravitational constant, m/s^2
h_b	critical liquid level in lower head at the onset of blowthrough, m
Ku	Kutadeladze number
m	mass, kg
p	pressure, MPa
R	gas constant, J/(kg K)
T	temperature, K, °C
t_b	time duration until onset of blowthrough, s
t_s	time duration until onset of blowthrough, s
u	velocity, m/s
V	volume, m^3
ε	contraction factor
η	dynamic viscosity, Pa s
κ	ratio of specific heats c_p/c_v
ρ	density, kg/m^3
σ	surface tension, N/m

Subscripts

C	cavity
G	gas
L	liquid
V	vessel

1 INTRODUCTION

In a severe accident special pressure relief valves in the primary circuit of German Pressurized Water Reactors (PWR) and future European PWRs will transfer a high pressure accident into a low pressure scenario. However, there may be a time window during late in-vessel reflooding scenarios where the pressure is in the order of 1 or 2 MPa at the moment of the reactor vessel rupture. A failure in the bottom head of the reactor pressure vessel, followed by melt expulsion and blowdown of the reactor cooling system, might disperse molten core debris out of the reactor pit, even at such low pressures. The mechanisms of efficient debris-to-gas heat transfer, exothermic metal/oxygen reactions, and hydrogen combustion may cause a rapid increase in pressure and temperature in the reactor containment, and are collectively referred to as direct containment heating (DCH). Investigating the DCH-issue a number of problems have to be addressed: (i) final location of corium debris, (ii) loads on the containment in respect to pressure and temperature, (iii) amount of hydrogen produced, (iv) loads on reactor pit and support structures, (v) impact on safety components. Knowledge of these points can lead to realize additional safety margins for existing plants and is needed for the development of the next generation of nuclear power plants. Specifically, the final location of the corium debris determines the efficacy of the melt collecting and cooling concepts that are planned for future reactors.

A large amount of work has been done to investigate the melt dispersal/DCH-phenomena for cavity designs with large instrument tunnels leading into subcompartments (Nucl. Eng. Des. 1996). Only a few experiments have been done with an annular cavity design (Blanchat, et al.,1997; Bertodano, et al.1996). The German PWRs and the planned European Pressurized Reactor (EPR) have an annular cavity design where the only large pathway out of the cavity is the narrow annular gap between the RPV and the cavity wall. The past experiments focused on relatively small holes at the center of the lower head and high failure pressures. Our investigations have been extended to low failure pressures and larger breach sizes with a cavity design similar to the planned EPR cavity (Fig.1.1), that is similar to the cavity of the German Konvoi reactors (Fig.1.2). Also, the effect of lateral breaches has been investigated for the first time.

The following failure modes of the lower head were studied:

1. Central breaches
2. Lateral holes
3. Lateral slots
4. Unzipping and tilting of the lower head

Recently two experiments were performed at the Sandia National Laboratories (SNL) in cooperation with Forschungszentrum Karlsruhe (FZK), Institut de Protection et de Surete Nucleaire (IPSN) and the U.S. Nuclear Regulatory Commission (NRC) (Blanchat, et al., 1999). These tests were performed with thermite melt, steam and a prototypic atmosphere in the containment in a scale 1:10. For the first time, a test with a large break at low pressure was conducted. The initial pressure in the RPV-model was 1.1 and 1.5 MPa, and the breach was a hole at the center of the lower head with a scaled diameter of 100 cm and 40 cm, respectively. The main results were: 78% of melt mass were ejected out of the cavity with the large hole

and 21% with the small hole; the maximum pressures in the model containment were 0.6 MPa and 0.4 MPa, respectively.

At FZK the test facility DISCO-C has been built for performing dispersion experiments with cold simulant materials in an annular cavity geometry in a scale 1:18. The fluids employed are water or a bismuth alloy (MCP-58®, Bi-Pb-Sn-In-alloy, ρ = 9230 kg m^{-3}, T_{melt} = 60°C, similar to Wood's metal) instead of corium, and nitrogen or helium instead of steam. Subsequently, selected experiments in a DISCO-H facility in the same scale will be performed with thermite melt, steam and a prototypic atmosphere in the containment. A detailed scaling analysis was performed [2], that demonstrated the quality of the model fluids used in this investigation.

Several different scaling analysises for severe accident modeling have been performed by different authors [5, 18,19]. Based on the method of Tutu and Ginsberg [5], that starts with the differential equations describing the processes, a scaling analysis was performed for the isothermal DISCO experiments [2]. Common to all analysises is the necessity to neglect some processes. Thus, the mode of melt discharge was not considered, but it was assumed that after the discharge of the melt from the vessel, the melt spreads along the floor and the walls of the cavity as a liquid film. Thereafter, during gas blow-down, melt droplets are entrained from the film into the gas flow, neglecting droplet deposition, trapping and re-entrainment. A set of eleven dimensionless scaling groups were found and were evaluated for 54 DISCO cases in comparison with a reactor benchmark case. The DISCO cases included three different melt simulants, water, gallium alloy and Wood's metal, two driving gases, nitrogen and helium, and various different initial pressures and holes sizes. As expected, large mismatches of the groups between model and prototype could be observed. The cases with water as melt simulant showed the largest deviations, and certainly give to high values for the carry-over of dispersed melt from the cavity. Certain cases with Wood's metal seemed to give a lower bound for the dispersed melt fraction.

The main conclusion from all scaling considerations is that an exact geometrical scaling is essential. If the volumes of gas and liquid are scaled accordingly (length scale to the power of 3), the initial pressure can be scaled 1:1. Then the gas velocity and the droplet size are mainly functions of the properties of the model fluids used. The duration of the blow down is scaled as the length scale. Central for similarity is the ratio of characteristic times, e.g. the ratio of the dispersal time to the time constant of the blowdown, defined as the coherence ratio [7,20]. Again, if the geometry including the failure mode is modeled accurately, this parameter depends mainly on the properties of the model fluids used.

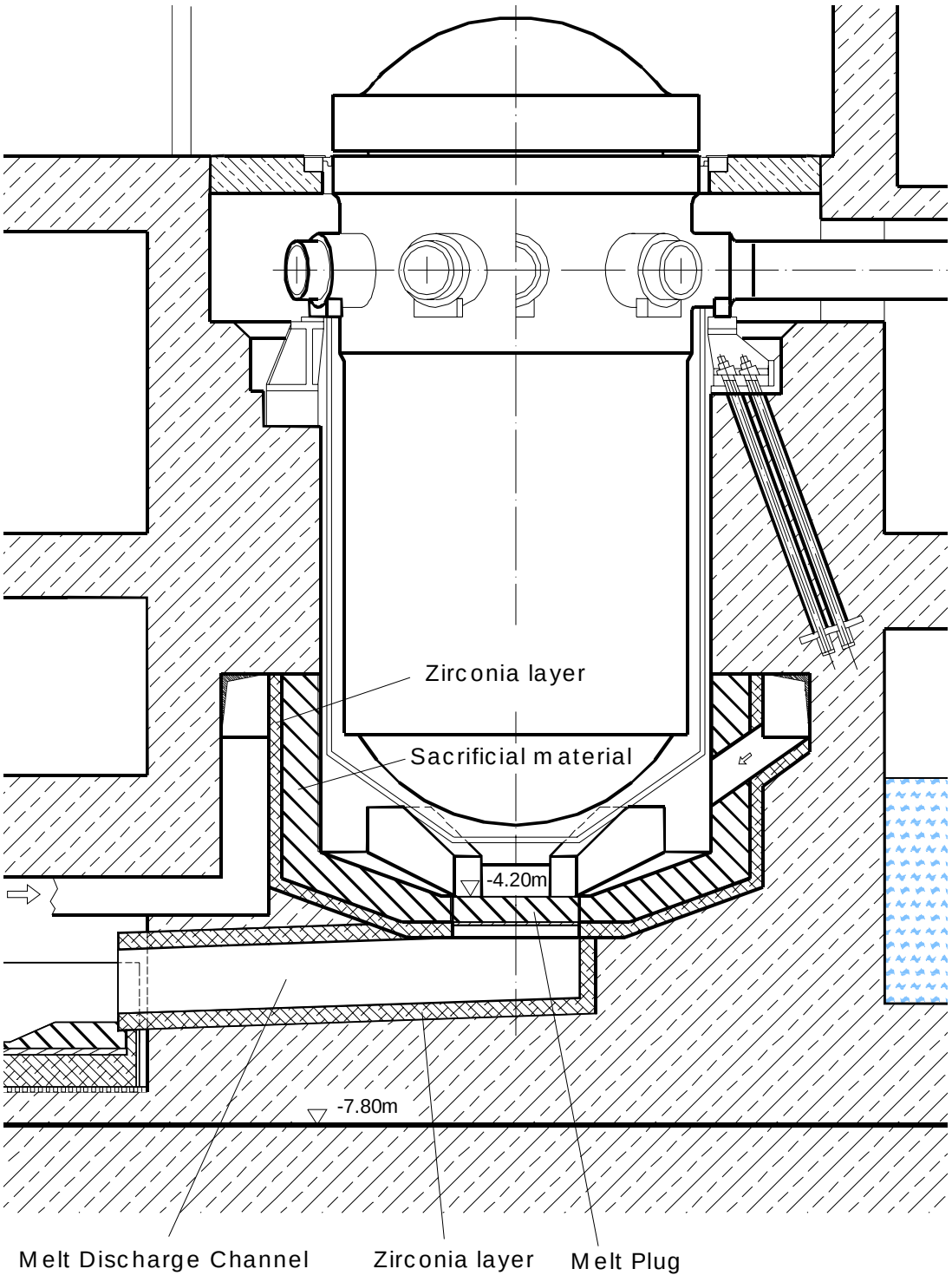

Fig. 1.1 The reactor pressure vessel and cavity of the planned EPR

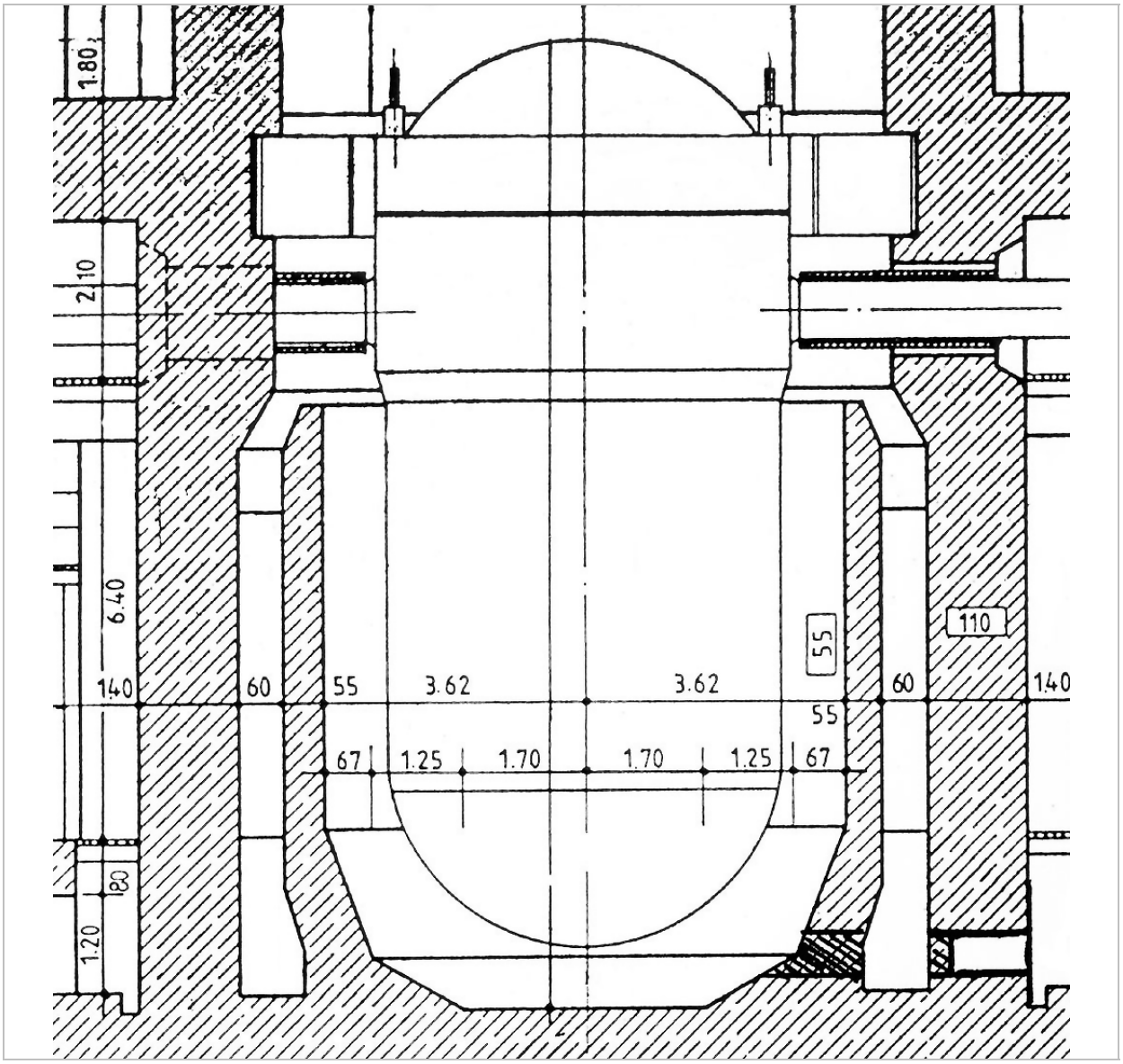

Fig. 1.2 The Reactor pressure vessel and cavity of the KONVOI reactor

2 THE TEST FACILITY DISCO-C

2.1 General layout of the test facility

A schematic diagram of the test facility DISCO-C is shown in figure 2.1, which consists of three major parts, i.e., the pressure vessel, the cavity and the subcompartments.

The pressure vessel is a steel pipe with a model of the reactor pressure vessel at its lower end (Fig.2.2). It models the volumes of both, the reactor pressure vessel (RPV) and part of the reactor cooling system (RCS). A disk holding 8 pipes (44 mm I.D., 250 mm length) separates the two partial volumes in ratio 60:40 (RCS:RPV). This arrangement models the main cooling lines with respect to the flow constriction between RCS and RPV. The lower head of the RPV can hold 3.4×10^{-3} m³ of liquid, which corresponds to 20 m³ or 160 t of corium. The various diameters inside of the vessel originate from an intended method of the blowdown mechanism. That employed two rupture disks inside the lower part of the vessel. It turned out to lead to unprototypical blowdown characteristics and was therefore replaced by a single rupture disk at the lower head [Jahresbericht 1998]. This change lead to a too large volume of the model RPV (see Table2.2).

The cavity, a Plexiglas cylinder with an inner diameter of 342 mm, is attached to the vessel support structure (Fig.2.4).The main flow path out of the cavity is the annular gap existing between the cavity itself and the RPV. This annular gap, with a width of 21.75 mm and a *total flow cross section of 0.022 m²*, leads to the main coolant lines and subsequently to the compartments.

The constriction of the flow path at the pressure vessel support in the upper part of the cavity is modeled by a conical ring, that reduces the annular gap width from 21.75 mm to 10.75 mm. An additional flow cross section is given by 16 holes (26 mm diameter) in the conical ring. The *total flow cross section through the vessel support reduces thereby to 0.019 m²*. In the annular space behind the conical ring liquid is collected in the experiments up to the height of the lower edge of the holes (0.6×10^{-3} m³). This space was filled with silicon rubber in some of the later experiments (s. Fig.2.2, left side).

The eight main coolant lines are modeled each one by a rod, that is attached to the RPV-model. The rod extends into the subcompartments through a cutout in the upper cavity wall. Thereby a flow path is created similar to an annular nozzle. *These nozzles have a total flow cross section of 0.031 m²*.

The compartments, eight boxes which model in volume the steam generator and pump rooms (0.3 m³ and 0.131 m³ each respectively), are connected to the nozzles and are placed on the vessel support structure around the RPV. They contain some baffles to block the direct path to openings at the top. These openings are covered by filters for the extraction of fog and drops. Two boxes have one Plexiglas wall to permit optical access for flow visualization (Fig.2.4 and 2.5).

There are two potential flow paths out of the test cavity. A path straight up into the refueling canal was not realized and tested in the present test series. The main flow path is the free flow area around the 8 main coolant lines into the pump and steam generator rooms. The other way out of the reactor pit can be through four ventilation openings in the lower part of the cavity leading to the spreading compartment via an annular channel around the pit, and a connecting channel. This second path was closed in all experiments except one. The pump and steam generator rooms are open to the dome in the prototype and open to the atmosphere in the experiment.

The exact dimensions of the cavity and pressure vessel are shown in Fig. 2.2 and in Table 2.1. Table 2.2 shows a comparison of the most important geometrical data of the EPR with the scaled DISCO data. DISCO models the RPV and RCS without insulation, because it is assumed that the insulation will be eliminated by the first contact with corium.

The fluids employed are water or a bismuth alloy (similar to Wood's metal: MCP-58®,Bi-Pb-Sn-In-alloy, ρ = 9230 kg m^{-3}, T_{melt} = 60°C) instead of corium, and nitrogen or helium instead of steam. The pressure vessel is filled with gas to a pressure slightly lower than the failure pressure of the rupture disk. A small auxiliary pressure vessel (30 liter), filled to a somewhat higher pressure is connected to the main pressure vessel (Fig.2.3). By opening a valve electropneumatically in the line between the two vessels the pressure in the main vessel increases up to the failing pressure of the rupture disk and the blowdown starts. A break wire at the hole gives the signal for closing the valve again and for the time mark t = 0. The valve is closed at t = 70 ms.

2.2 Basic geometry with central holes

The failure modes investigated in the first series were central holes in the lower head. These holes were closed by a rupture disk, that had an opening diameter larger than the hole diameter. Figure 2.6 shows an example of a 50 mm diameter hole. The rupture disk is scored, which causes the disk to shear along the score lines, providing a full relief opening. The tips of the four blades might hinder a horizontal spreading of the jet. However, a horizontal spreading is not to be expected. The RPV lower head can hold 3.4×10^{-3} m^3 of liquid (liquid height in the hemisphere is 96 mm). This corresponds to 20 m^3 or approximately 160 t of corium. When lateral breaches were investigated, smaller amounts of liquid were used, because the focusing effect of the metal layer above the corium pool in the lower head was to be modeled. So the liquid level was just above the upper edge of the breach.

To investigate the effect of different initial liquid pool depths a standpipe was mounted inside the pressure vessel (Fig. 2.7). The standpipe can hold the same amount of liquid as the lower head, but in the outflow we get two distinct stages, first the liquid jet and than the gas jet, without a stage of a two-phase flow in between. That geometry was used by Bertodano et al. [3], Kim et al. [15] and others. Because of the required length of the standpipe the disk separating the RCS from the RPV volume had to be moved up. Therefore two different dimensions are given in figure 2.2 defining the position of the separation plate. This plate has little effect on the blowdown except for the largest breaches.

2.3 Geometry of lateral breaches

Three types of lateral breaches were investigated. The first type are round holes of 25 and 50 mm diameter on the side of the lower head (Fig. 2.8 and 2.9). The inclination of the axis of the holes is 45 degrees. Their center measured at the inside lies 50 mm above the bottom of the calotte. So, the lower edges of the holes at the inside are 41.15 and 32.4 mm above the bottom of the calotte, respectively.

The second type is a horizontal slot, that models a partial rip in the lower head, as it might occur with a side-peaked heat flux distribution. The flow cross section is equivalent to a 25 mm hole (Fig. 2.10). The slot is 12.5 mm wide (high, inclined 45 degrees), and 42.5 mm long with a 6.25 mm radius. The lower edge of the slot is 56.1 mm above the bottom of the calotte. These two types of openings were closed by round rupture disks as with the central holes.

The third type models the horizontal rip propagating around the circumference of the lower head leaving only a small section attached (Fig.2.11), as it was observed in the lower head failure (LHF) experiments performed at SNL [14]. Here the calotte was a separate part that was held in position by a steel rod from below at its center. The rod penetrated the bottom of the pit through an airtight lead-in hole. At the start of the experiment the rod was released by breaking the bolts that held the rod in place by detonators. The lower head moved down and was stopped by crushing material on the four pedestals. Two different heights of pedestal were used to obtain different flow cross sections (Fig.2.12).

2.4 Geometry of the cavity

The diameter of the cavity was increased from 342 mm to 386 mm, to make room for an extra cylinder, that should trap the liquid mass and prevent the dispersion into the reactor rooms (Fig.2.13).

The other change in the cavity geometry deals with the venting openings of the reactor pit. There are four holes in the lower part of the pit that are connected by a circumferential channel and a tube to an extra compartment modeling the spreading compartment (Fig.2.14).

Table 2.1 Dimensions of the experiment

	Name	diameter [m]	length [m]	area [m²]	volume [m³]
1	**Upper pressure vessel (RCS)**	0.227	1.240	0.04047	**0.050184**
2	**Lower pressure vessel (RPV)**				
	space below separator disk	0.227	0.144	0.04047	0.005828
	cone	0.217	0.034	0.03698	0.001257
	cylinder	0.207	0.300	0.03365	0.010096
	annular gap	0.276 - 0.267	0.246	0.00384	0.000944
		0.276	0.275	0.05983	0.016453
	lower head (hemisphere)	0.276	0.091		0.003117
	RPV volume				**0.037695**
	RCS+RPV volume				**0.087879**
3	Lower cavity	0.342	0.137		0.008399
4	annular space between RPV and cavity	0.342 - 0.2985	0.327	0.021883	0.007155
5	space at RPV support and main cooling lines				0.021134
	Cavity total				0.036688
6	Pumproom (each)	0.186	0.940		0.13113
7	steam generator room (each)	0.240	1.615		0.29850
	Melt spreading room	0.320	0.300	0.096	0.11712
	Venting channel, entry hole (1)	0.0038		0.001134	
	Total flow cross section of entry holes			0.004536	

Table 2.2 Comparison of reactor and DISCO dimensions

Geometric Parameters	**EPR**	**EPR**	**DISCO**
Scale	**Plant**	**1:18**	**1:18**
Reactor Coolant System and Pressure Vessel			
RCS Volume (m^3)	292.6	0.05017	0.05018
RPV Volume (m^3)	147.6	0.02531	0.03770
Total Volume (m^3)	440.2	0.07548	0.08788
Reactor Pressure Vessel			
RPV Shell Mid-Vessel OD (m)	5.385	0.299	0.2985
RPV Lower Head ID (m) (curvature diam.)	5.400	0.300	0.300
RPV Lower Head Volume (m^3)	17.28	0.002963	0.00359
Length from Melt Plug to Cavity Floor (m)	1.12	0.0622	0.0620
Length from Melt Plug to Nozzle Centerline (m)	8.72	0.484	0.485
Annular Gap/Cavity			
Effective Annular Gap below Nozzles (m)	0.383	0.02128	0.02175
Flow Area below Nozzles (m^2)	7.0	0.02161	0.02188
Flow Area at Support Girder (m^2)	6.0	0.01852	0.01890
Cavity Diameter below Nozzles (m)	6.145	0.3417	0.3420
Cavity Height (m)	11.84	0.6578	0.6120
Loop Piping and Cavity Cutouts (without insulation)			
Hot and cold Leg OD (m)	0.886	0.04889	0.0500
Hot and cold Leg Cutout Diameter (m)	1.550	0.08611	0.0860
Hot and cold Leg Area (m^2)	0.616	0.00190	0.00196
Hot and cold Leg Cutout Area (m^2)	1.887	0.00582	0.00581
Total Leg Area (m^2)	4.93	0.01522	0.01570
Total Cutout Area (m^2)	15.08	0.04654	0.04647
Total Bypass Flow Area (Cutout - Leg) (m^2)	10.20	0.03148	0.03077

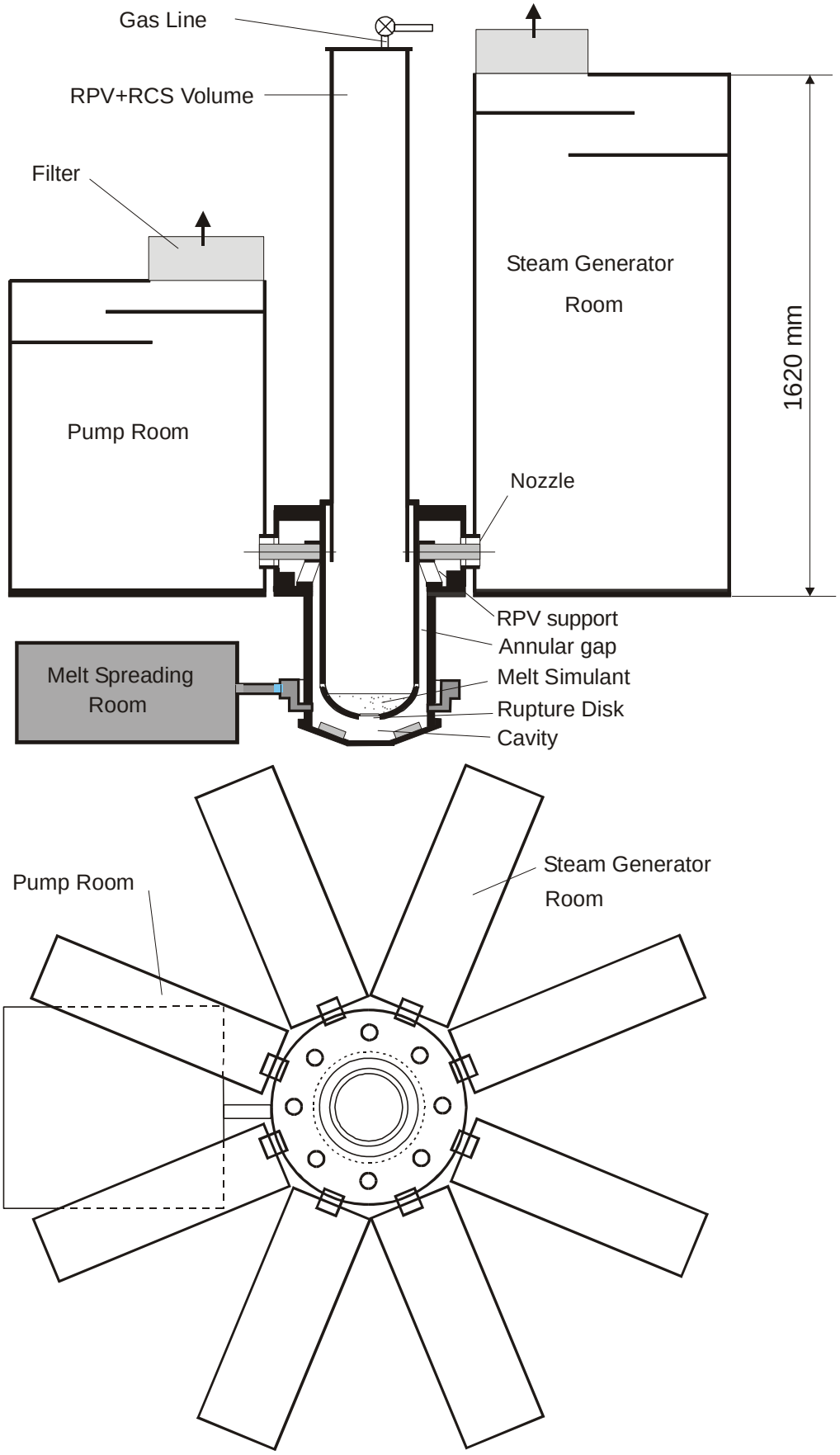

Fig. 2.1 Scheme of the DISCO-C-test facility

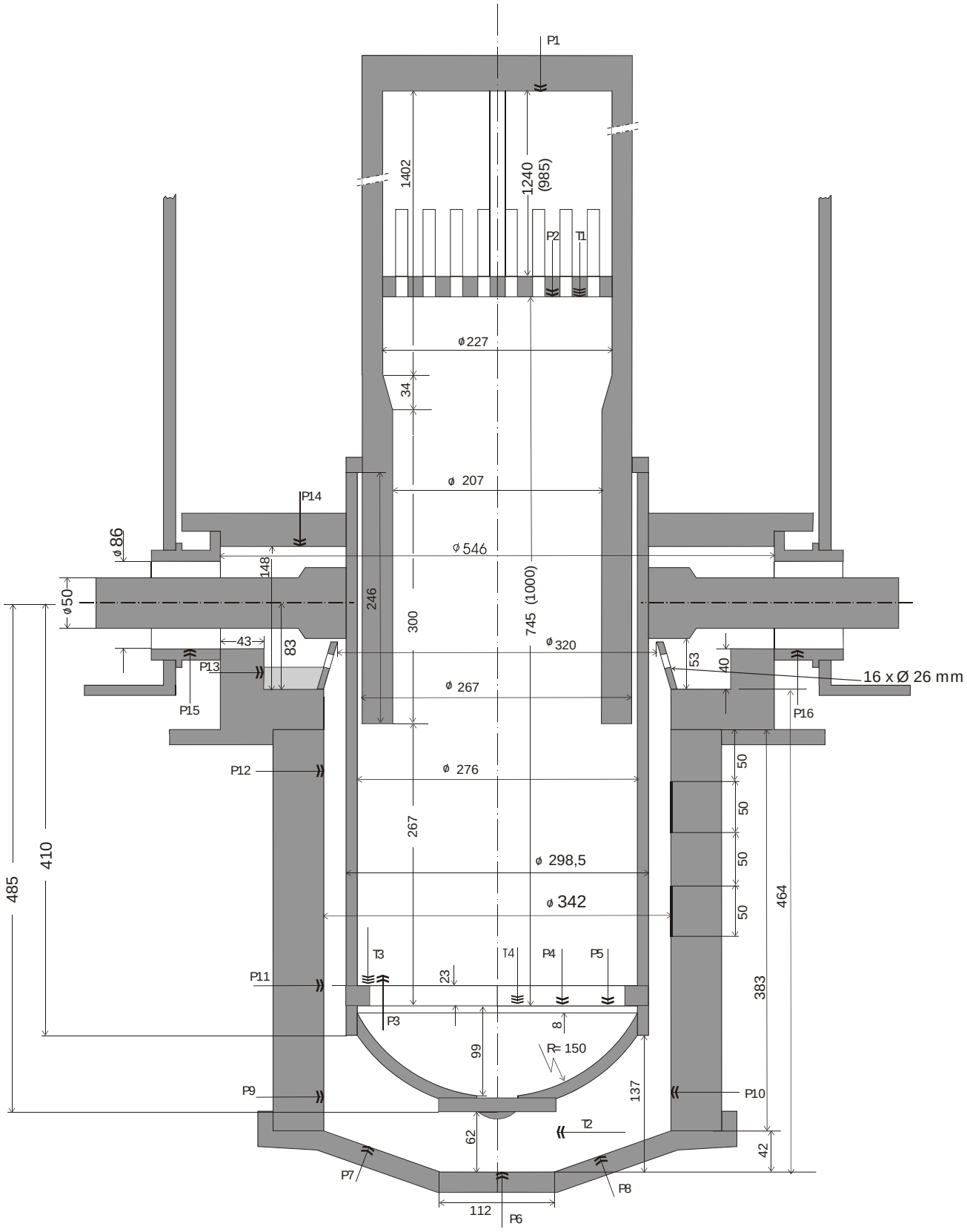

Fig. 2.2 The configuration of the pressure vessel with a rupture disk at the lower head (dimension in mm).

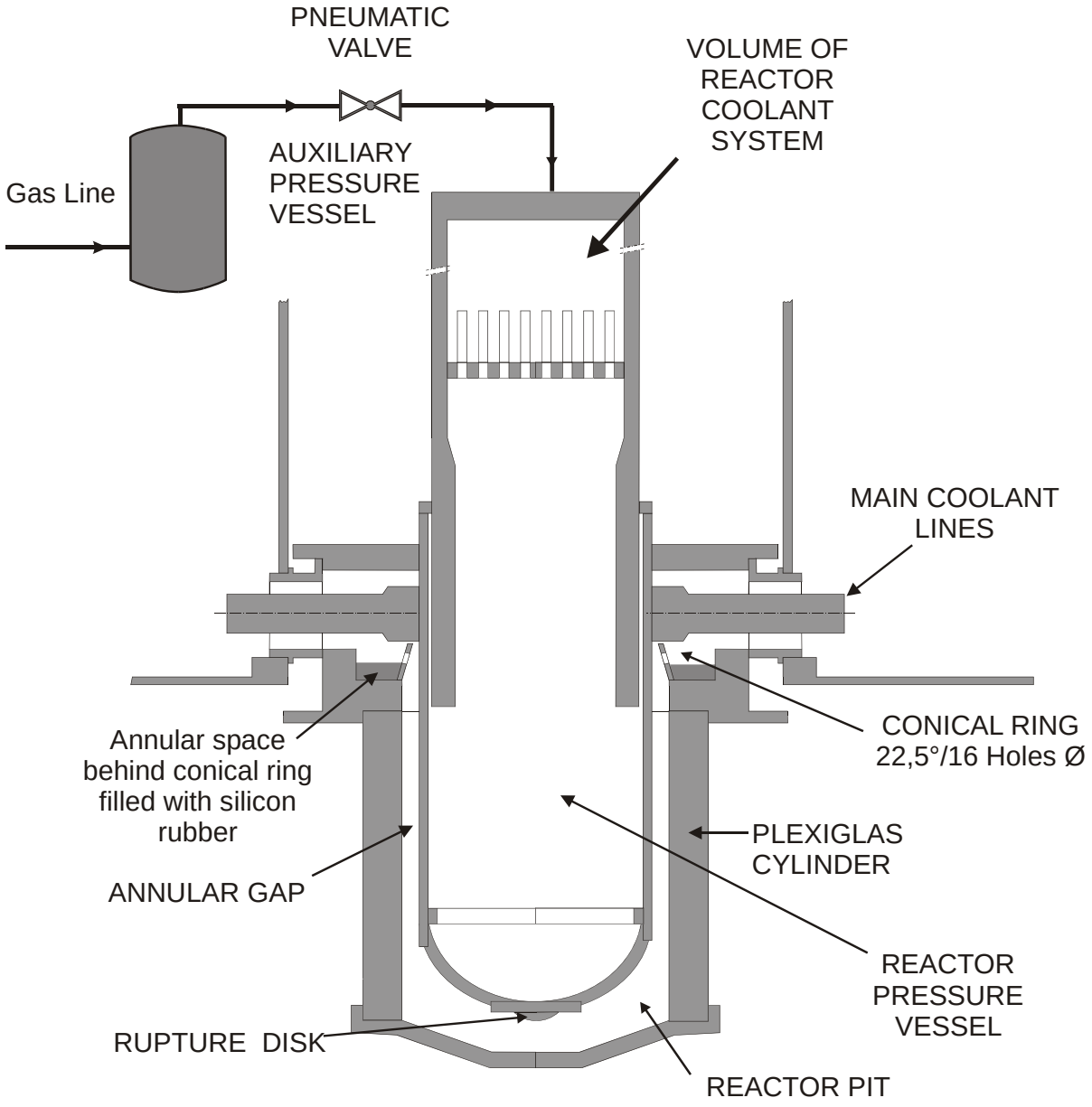

Fig. 2.3 Terminology of the facility

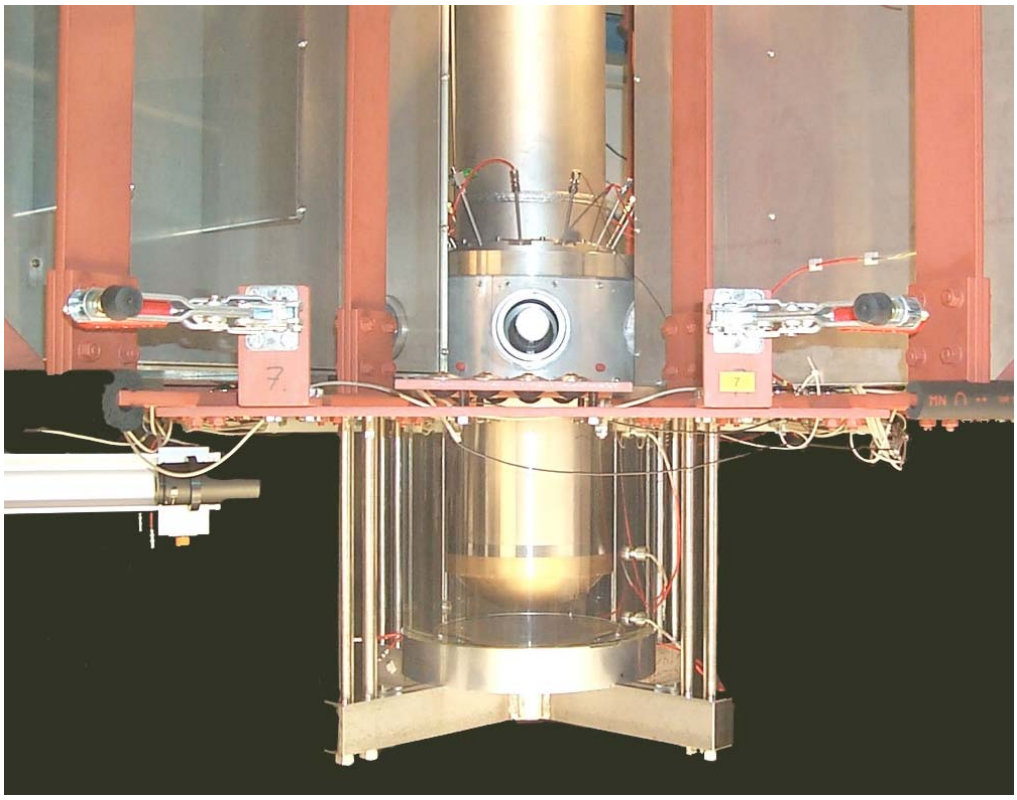

Fig. 2.4 The transparent cavity and the RPV-model;
one nozzle can be seen, because one subcompartment has been taken off.

Fig. 2.5 Top view of the test facility;
four large subcompartments can be seen, and the RCS-RPV pressure vessel at the center.

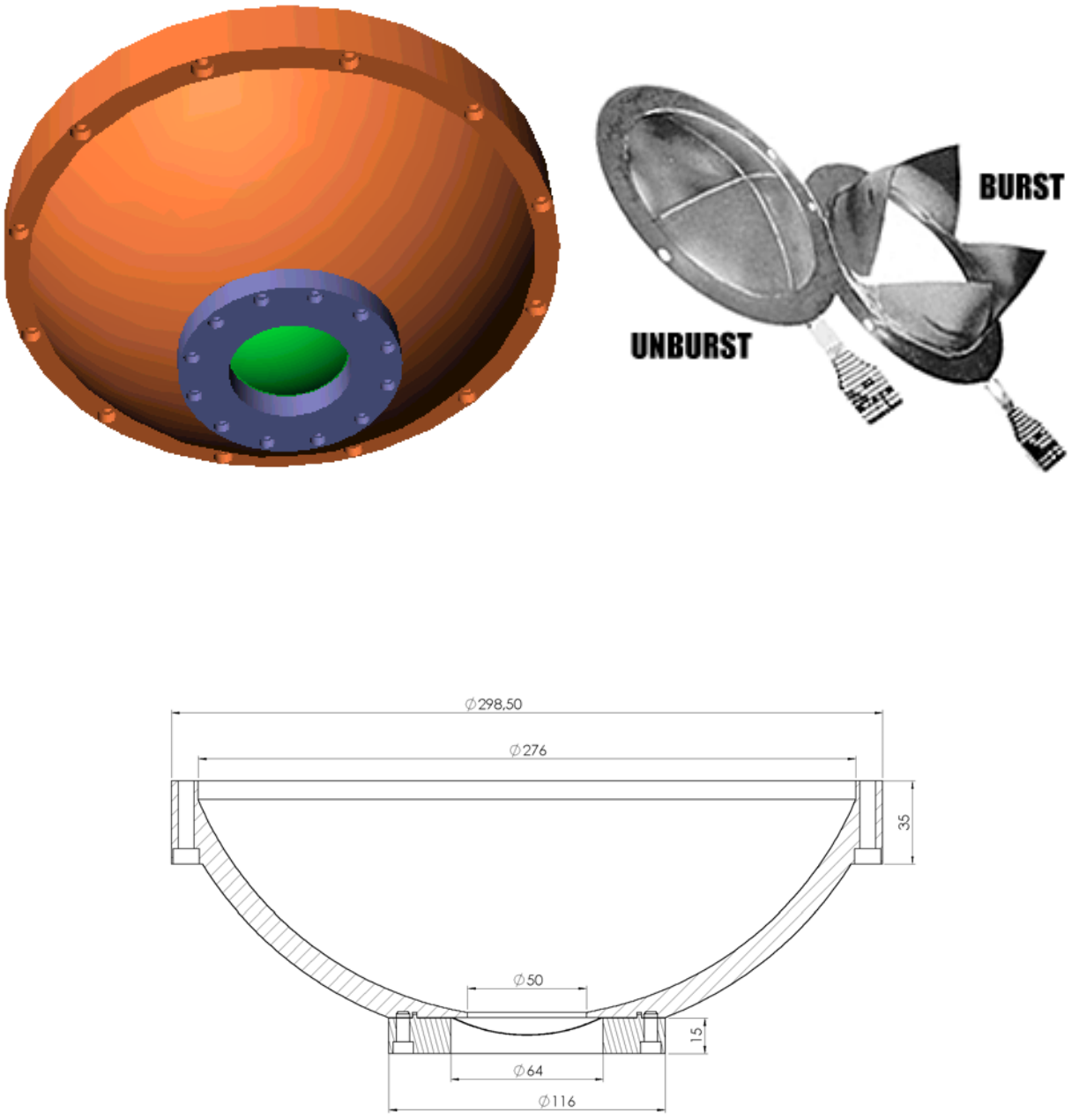

Fig. 2.6 Lower head with central hole and rupture disk

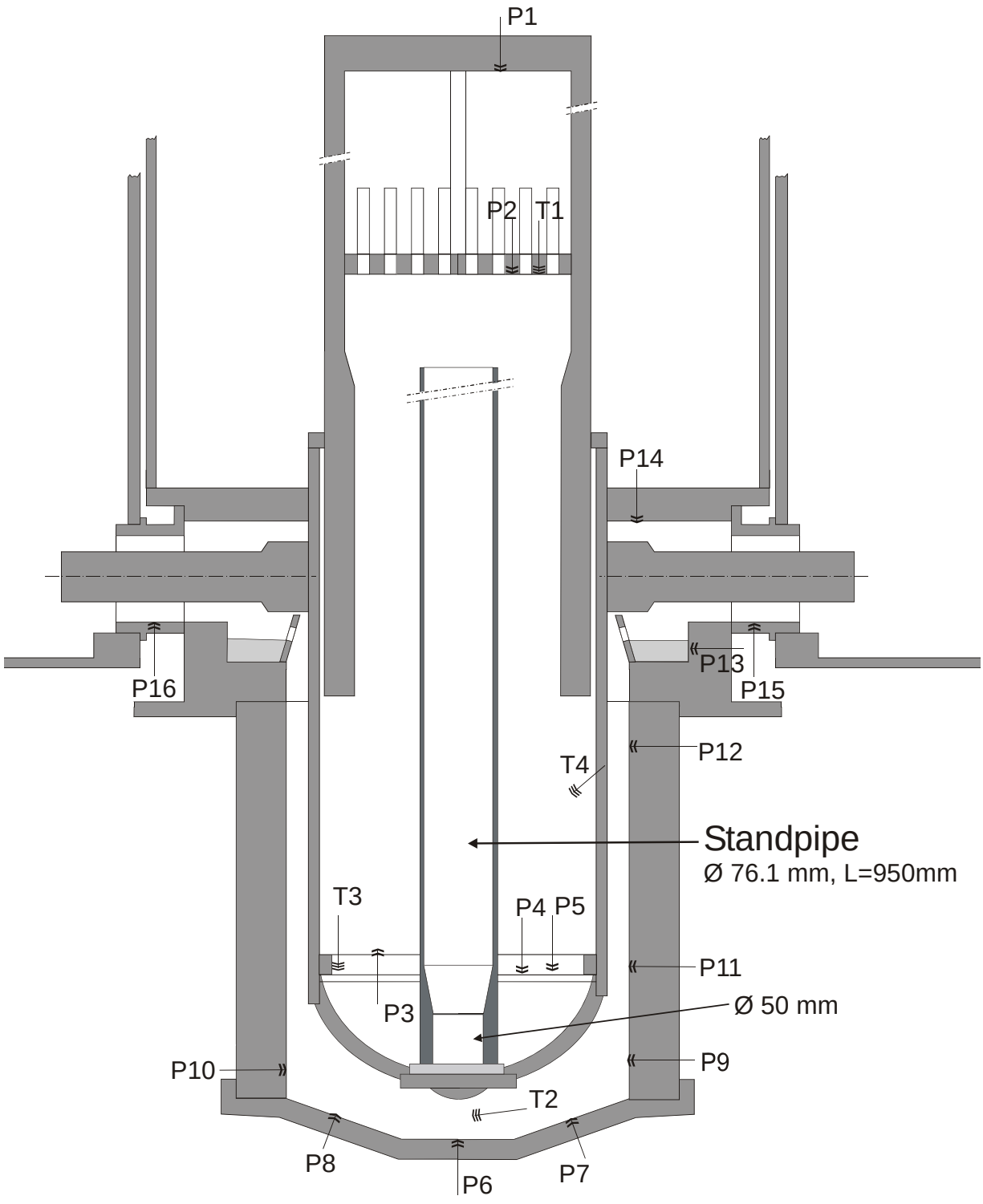

Fig. 2.7 Lower head with standpipe to prevent gas blow through

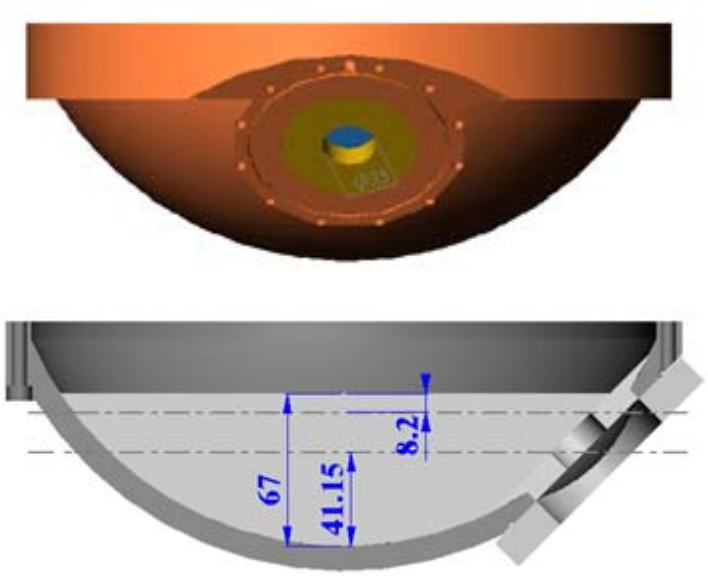

Fig. 2.8 Lower head with lateral hole with 25 mm diameter

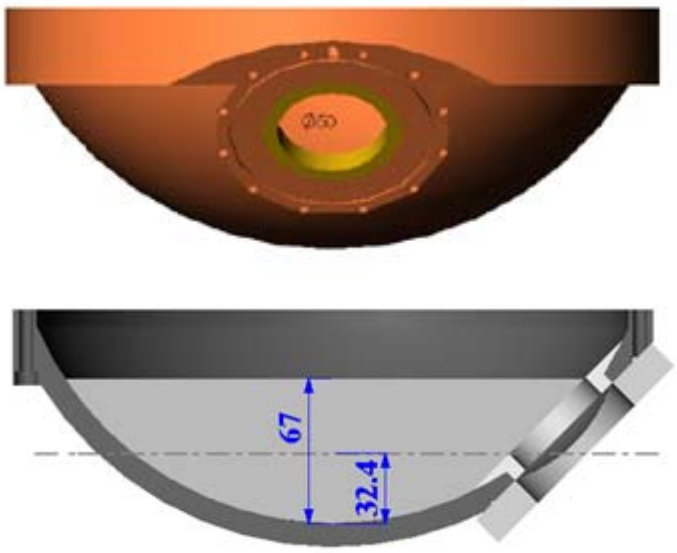

Fig. 2.9 Lower head with lateral hole with 50 mm diameter

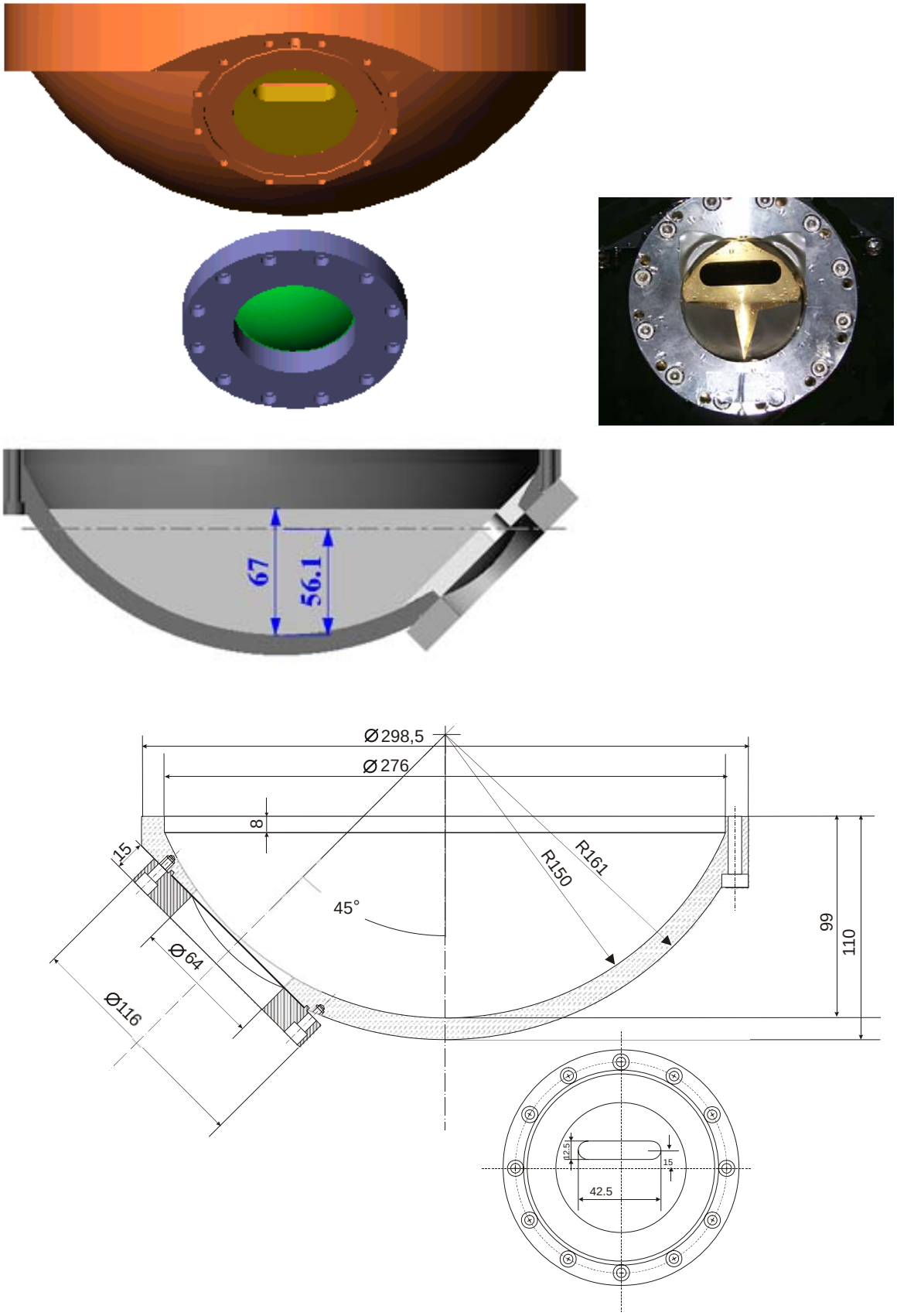

Fig. 2.10 Lower head with lateral slot with a cross section equivalent to a 25 mm diameter hole

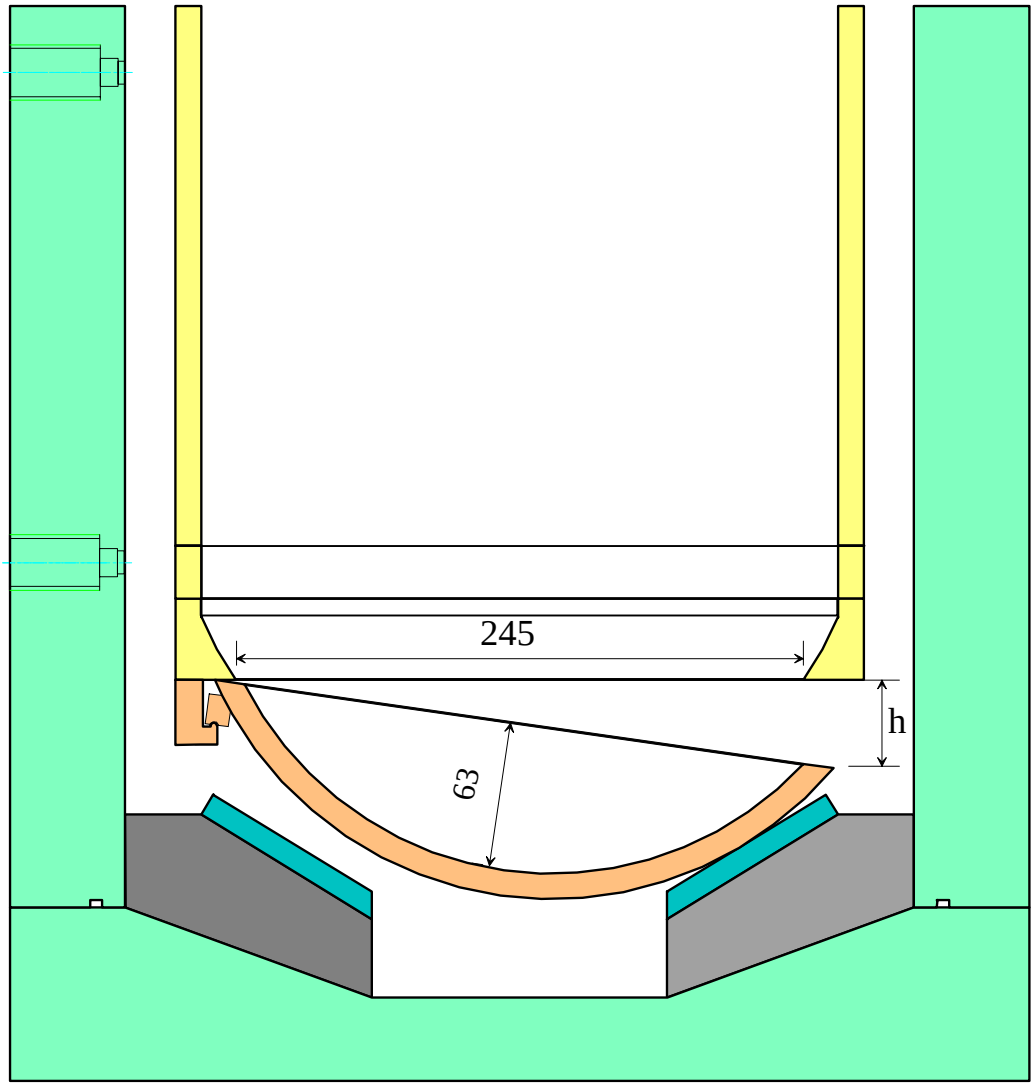

Fig. 2.11 Unzipping and tilting of the lower head

Fig. 2.12 Pedestals to stop the lower head

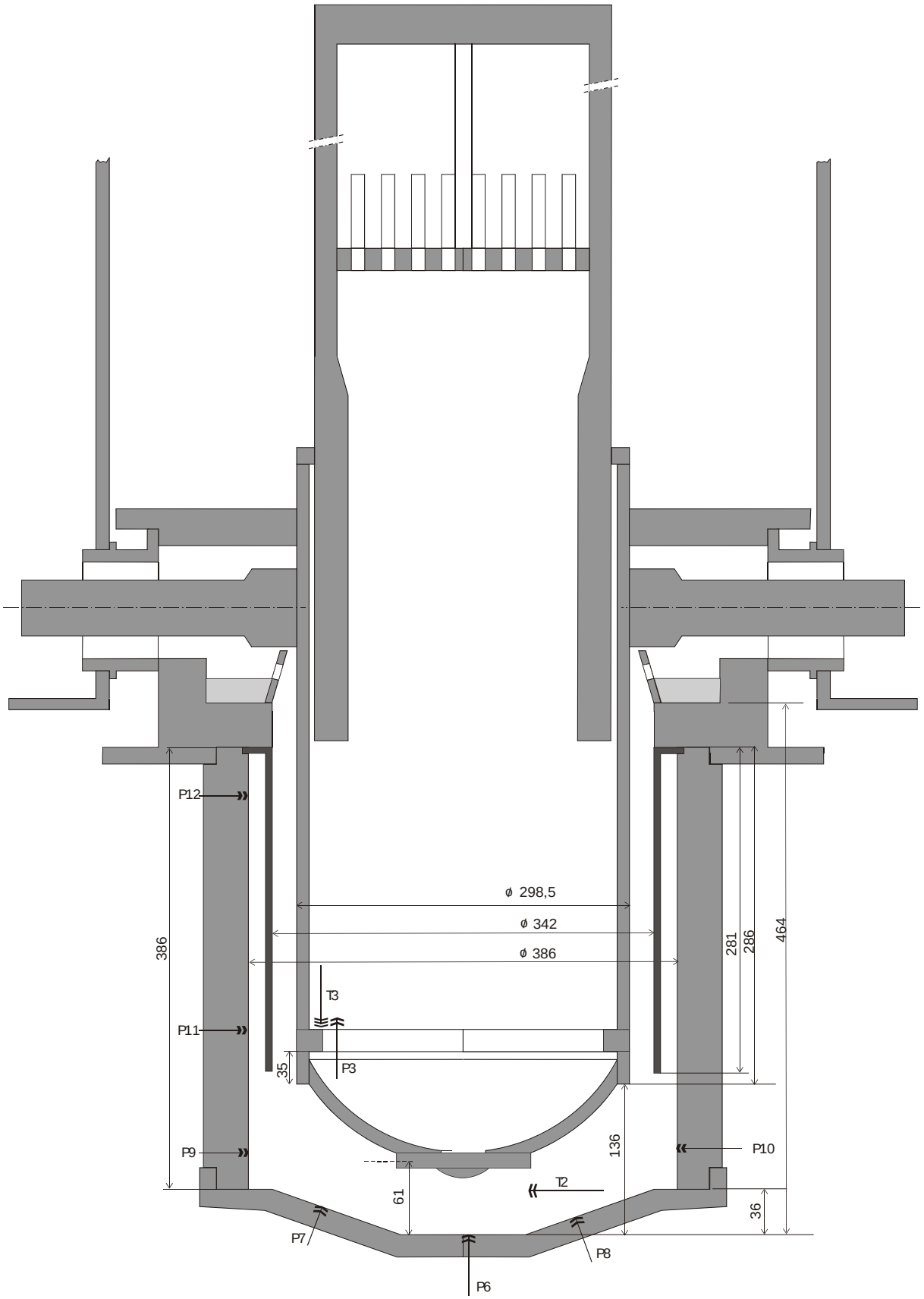

Fig. 2.13 Configuration of the wider cavity with a melt trapping device

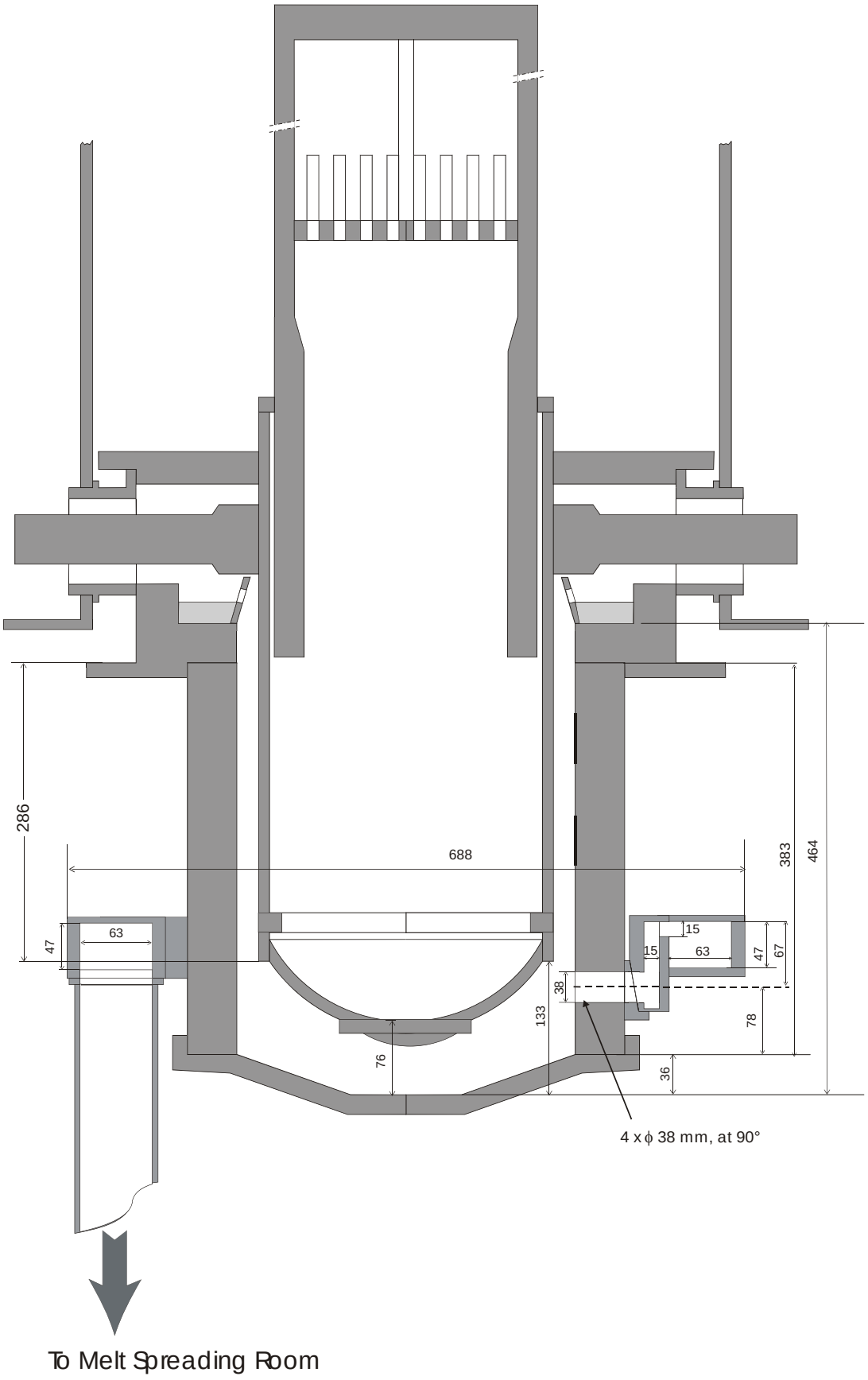

Fig. 2.14 Cavity with venting holes and channel

3 INSTRUMENTATION AND MEASUREMENT

3.1 Pressure Measurement

Transient pressures were measured at the positions indicated in Fig.2.2 and 2.7 by the labels P1 through P16, and in the subcompartments. Piezo-resistive transducers are used, type Kistler, OEM RES12A, with ranges 2, 5,10 and 20 bar absolute pressure. The sensors are compensated in the temperature range –20 ...+ 120 °C. The sensors have a diameter of 12 mm and are mounted in the wall with the steel diaphragm almost flush with the wall. They have a high natural frequency, good linearity and low hysteresis (±0.3% FSO) and good reproducibility (<0.2%).

3.2 Temperature Measurement

Although the DISCO-C experiments are not intended to investigate thermal effects, temperatures must be measured because the gas temperature changes during the blowdown and the liquid metal must be heated above the melting temperature of 58°C. Three thermocouples in the pressure vessel and one in the lower cavity measure the gas and liquid temperature (for positions see Fig.2.2 and 2.7, labels T1 through T6). The K-type thermocouples have a diameter of 0.36 mm. The time constant for gas temperature measurement is between 0.5 s and several seconds, depending on the heat transfer coefficient, with an estimate for our conditions of 0.6 s < τ < 1.2 s. Therefore all temperature signals for gas will be attenuated.

3.3 Gas Velocity Measurement

The velocity of the gas in the annular flow cross section was measured by the Particle Imaging Velocimetry method (PIV) for some selected tests. Tracer particles consisting of oil droplets (with a diameter of approximately 10 μm) were added to the gas in the pressure vessel by a Laskin nozzles seeding generator immediately before the blow down. A region about 30 mm high near the top end of the annular cross section was illuminated by a pulsed Nd-YAG laser light sheet through a special window at intervals of 35 μs with a frequency of 15 Hz. The pulse energy was approximately 20 mJ and its duration 5 ns. Perpendicular to the illumination (tangential to the RPV-vessel) a second window was installed in the plexiglass cylinder, through which a camera had a view of the flow cross section (Fig.3.1). The dimensions of the interrogation area (21.75 x 23 mm) are shown in Fig. 3.2. The wall of the RPV can be recognized as a dark region placed at the right of the 21.75 mm wide annular gap. A special CCD-video camera (640x480 pixels) recorded 15 double frames per second, shifted in time by 10 to 20 microseconds. With the PIV-software the velocity field of the gas between the two cylinders can be determined.

The bulk gas velocity in the gap can also be determined with the information of pressure and temperature histories in the RPV and in the cavity, together with the flow cross section of the gap. This gas velocity is a mean velocity over the cross section and it is a lower bound, because the partial blocking of the flow cross section by the liquid was not taken into account. The true bulk value will be higher whenever liquid is present.

3.4 Drop and Liquid Jet Velocities

Measurements of drops and water jet velocities at one of the nozzles were carried out for some experiments. Two subcompartment boxes were removed for a better view and lighting. Again, the measurements were based on a PIV technique. The two phase flow was illuminated with a laser sheet and recorded with a CCD-Camera. However, no tracer particles were used since the flow conditions would not have permitted their visualization. On one hand, the particles present in the water jet would not have been illuminated due to the fact, that the laser light is strongly reflected by the moving jet surface. On the other hand, tracer particles contained in droplets are useless because the droplets itself can be used as seeding. With the PIV-software the velocity of the liquid and the gas can be determined

3.5 Liquid Mass Flow Measurement

For the determination of the liquid mass flow rate through the annular flow cross section a capacitive measurement system was applied. The capacitor consists of a thin metal foil (50 μm thickness, 50 mm vertical, 300 mm horizontal) fixed to the inside wall of the plexiglass cylinder (cavity) and the pressure vessel as the second electrode. The capacitance without liquid between the two electrodes is approximately 27 pF. It depends on how much material lies between the outer probe and the vessel wall. This capacitance is measured by feeding a high frequency voltage at a constant frequency (5,3 V, 33 kHz) to the electrodes. The higher the capacitance of the capacitor, (and therefore the larger the liquid mass) the greater is the high frequency current flowing through the capacitor. An electronic converts the high frequency current into a frequency proportional to the liquid mass. The electronic unit was originally built for a liquid level meter, that works on the same principle (Endress + Hauser, EC 37Z). Two such probes were used in some experiments in a vertical distance of 50 mm (Positions see Fig.2.2).

3.6 Dispersed Liquid Mass Fraction Measurement

The mass fraction of the water or liquid metal in the compartments was determined by weighing the boxes before and after the test with a precision scale with an uncertainty of ±0.1 gram. The water in the cavity was absorbed in dry cloth, that was weighed. The metal was solid after the test and could be weighed directly.

3.7 Flow Visualization

Two high speed movie film cameras (LOCAM II, 500 frames/second) are used to record the flow phenomena in the cavity; they are arranged in a view angle of 90 degree to each other. Additionally two CCD-video cameras are taking pictures from the cavity for a quick view. The liquid flow along the cooling pipes into the subcompartments is filmed by a CCD-video camera with high shutter speeds (50 frames/second).

3.8 Data Acquisition and Experiment Control

The pressure and temperature data are acquired by a Data Translation Board DT2839 at a sampling rate of 2.5 kHz. 30 channels for pressure and 4 channels for temperature are

currently used. Additionally the signals are recorded from the electro-pneumatic valve (open/closed) and the break wire as a time-zero and sync-signal. A second computer acquires the data from the liquid mass flow measurement with a sampling rate of 35 kHz and the sync-signal. A third computer controls and acquires the PIV-data and images.

The test sequence is as follows: Three video cameras are started manually, the data acquisition systems and the high speed cameras are started by a starter key, two seconds later the signal for opening the valve is given and the rupture disk breaks within 200 ms. The break wire signal closes the valve that is fully closed 70 ms later. The break wire signal also starts a LED-clock and several single light emitting diodes, which can be seen by various cameras.

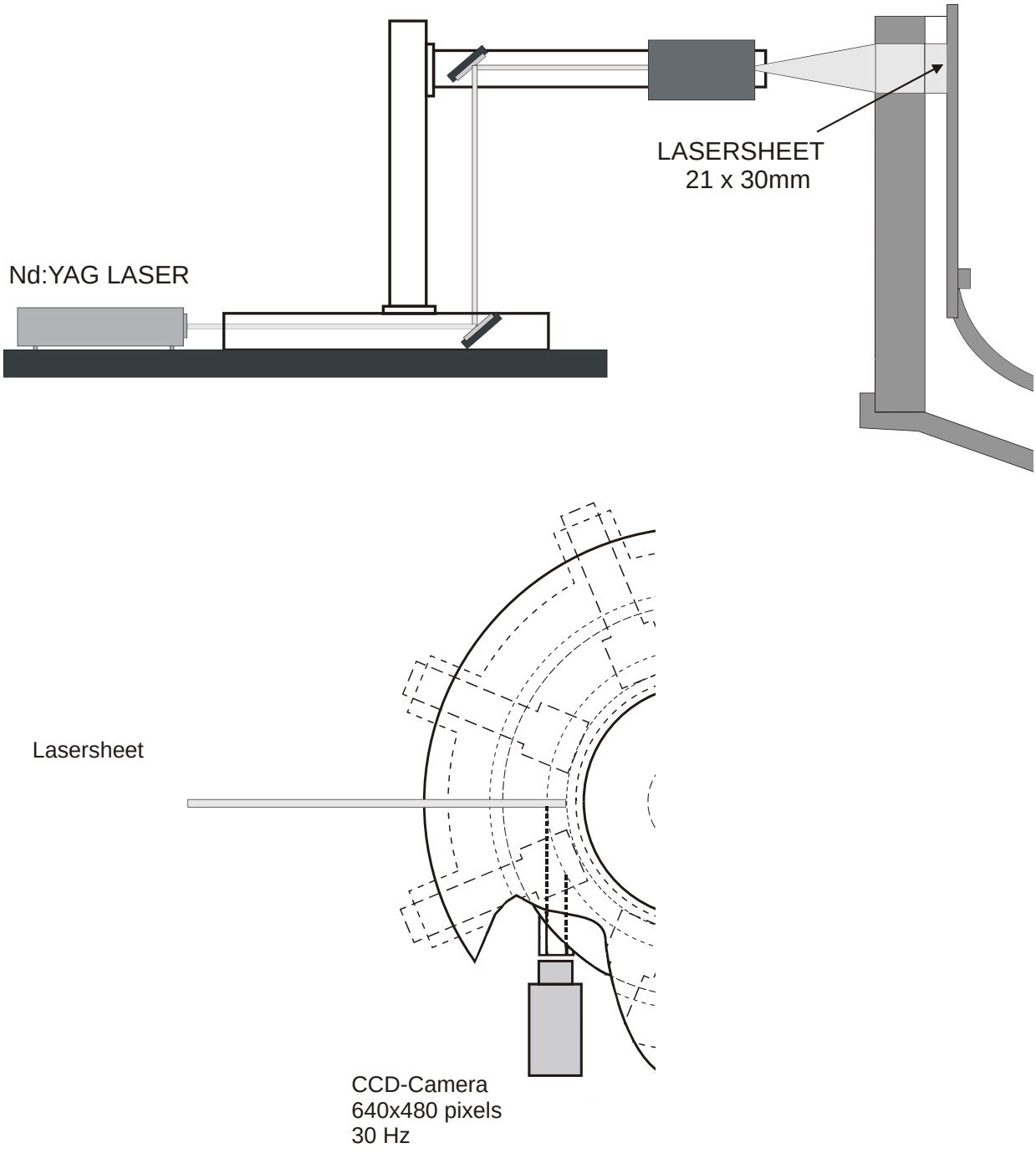

Fig. 3.1 Configuration of the PIV measurement system

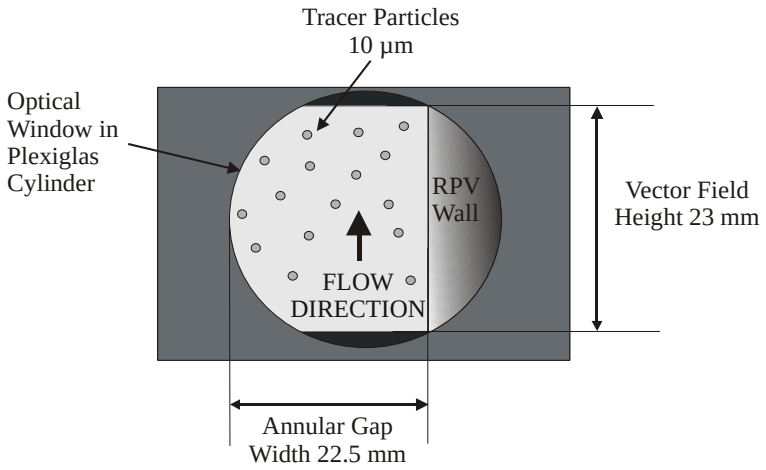

Fig. 3.2 Vector field dimensions in annular gap

4 EXPERIMENTAL RESULTS OVERVIEW

In this chapter an overview of the experimental results will be given and processes will be described, which pertain to all or many experiments. The special features and effects of different initial conditions and test parameters will be described and presented in chapter 5. Experiments with different gas-liquid combinations were conducted. The first choice was nitrogen-water, with which most tests were run. Special tests were run with helium - water and with nitrogen - liquid metal. From the scaling analysis [2] the cautious conclusion could be drawn, that the combination nitrogen-water will rather overpredict the dispersed melt fraction and the combination nitrogen-metal probably underpredicts the amount of melt that will be ejected out of the cavity. Table 4.1 shows the test matrix indicating the test numbers for easy reference. The properties of the model fluids are listed in Table 4.2. The precise initial conditions for all tests are listed in Table 4.3 together with the liquid fractions found in the different compartments after the test.

4.1 Pressures

An experiment was performed without liquid in the lower head to check measured pressure and temperature data against theoretical data for a pure gas blowdown. The hole diameter was 50 mm and the initial pressure of nitrogen was 1.12 MPa. The data are shown in Fig. 4.1. For the theoretical data different methods were compared.

The mass flow m for an inviscid isentropic flow of an ideal gas through a nozzle is given by [12]

$$m = c_d A_H \psi p_V \sqrt{\frac{2}{R T_V}} \tag{4.1}$$

$$\text{with } \psi = \sqrt{\frac{\kappa}{\kappa - 1}} \sqrt{\left(\frac{p_C}{p_V}\right)^{\frac{2}{\kappa}} - \left(\frac{p_C}{p_V}\right)^{\frac{\kappa+1}{\kappa}}} \tag{4.2}$$

As long as the ratio of p_C/p_V is smaller than the critical value (0.53 for nitrogen with $\kappa = 1.4$), the value of Ψ is $\Psi = \Psi max = 0.484$. The flow in the nozzle can be treated as quasi-steady. That is, the steady-state equations (4.1) and (4.2) may be written for each instant of time and can be applied to calculate the mass flow out of the vessel within short time steps. From the remaining mass in the vessel and the law for the ideal gas the pressure in the vessel is calculated for the next time step. The effect of the temperature change (s. next chapter) on the pressure was taken into account by applying equation (4.7). The agreement with the measured pressure is very good (Fig. 4.1) if a constant discharge coefficient of $c_d = 0.9$ is used. The coefficient of contraction of a jet through a sharp-edged hole is actually not a constant but decreases with decreasing velocity or decreasing pressure ratio p_V/p_C, respectively.

Other formulas based on an isentropic process can be used (e.g. [13]) but then the temperature decrease is to large, and a discharge coefficient of 0.8 or lower has to be used in order to obtain agreement with the measured pressure.

The duration of the blow down process is inversely proportional to the flow area of the hole (Fig.4.2). According to scaling laws it is also proportional to the length scale; however, different gases lead to different blowdown times. The steam blow down would fall between the cases for nitrogen and helium but closer to nitrogen. Scaling laws predict a blow down time dependency on the initial pressure as $t \sim \ln(p_0/p)$ [8]. The experiments show that the pressure effect is smaller than that. The reason is the presence of the liquid. A pure gas blow down has an entirely different trend with a steeper gradient in the beginning (Fig. 4.3).

A distinctive pressure measurement is that on the cavity floor below the hole (P6). This gauge measures the impact of the jet and should give the total pressure in an ideal case. Because of the nature of the outflow the pressure signal deviates from the total pressure, and this deviation can be used to distinguish and qualify the different stages of the jet flow. The static pressure in the RPV and the total pressure on the cavity floor below the hole are shown for one typical test in Fig. 4.4. From the total pressure signal we can infer that there are four distinct stages of the outflow:

1. the single-phase liquid flow,
2. the blowthrough with two-phase flow,
3. single-phase choked flow, and
4. subsonic single-phase gas flow.

The duration of the individual stages depends on the hole size, the height of the liquid in the lower head, the pressure and the liquid density.

The pressure in the pressure vessel still increases after the opening of the rupture disk, because the valve between the auxiliary vessel and the main vessel is fully closed only after approximately 70 ms, while the outflow of the gas through the break is still blocked by the liquid. The maximum pressure is taken as initial pressure and is listed in table 4.2.

4.2 Temperature

During the blowdown the gas temperature drops due to the expansion. The temperature signals are attenuated because of the large time constant of the thermocouples. (s. chapter 3.2). Usually the minimum temperature is not yet reached at the end of the blowdown.

The relation between pressure and temperature for an isentropic process of a perfect gas is

$$\frac{T_2}{T_1} = \left(\frac{p_2}{p_1}\right)^{\frac{\kappa-1}{k}} \qquad (4.3)$$

with index 1 and 2 denoting the state before and after the blowdown, respectively. However, the resulting temperature drop of 150 K is much higher than the measured one in our example. Therefore a different approach was chosen.

The energy equation of an expansion of an ideal gas from volume V_1 into volume V_2 and the volume displacement work, with u, the inner energy of the gas and with equalization of temperature is

$$u_1 - u_2 = p_2 (v_2 - v_1) \tag{4.4}$$

and it is

$$u_1 - u_2 = c_v (T_1 - T_2) , \tag{4.5}$$

so

$$c_v (T_1 - T_2) = p_2 (v_2 - v_1) \tag{4.6}$$

With $pv = RT$ and $c_v = R/(\kappa-1)$ this can be transformed to

$$\frac{T_2}{T_1} = \frac{\frac{p_2}{p_1} + \frac{1}{\kappa - 1}}{1 + \frac{1}{\kappa - 1}} \tag{4.7}$$

The temperature drop during the gas blowdown (hole diameter 50 mm, no liquid present) is shown in Fig. 4.1. The measured temperature drop of 77 K agrees well with equation (4.7). The difference in time shows the effect of the time constant of the thermocouple (diameter of thermocouple is 0.36 mm).

For our test series, nitrogen (κ = 1,4) at room temperature cools down by 61 to 78 K, depending on the pressure ratio, and helium (κ = 1,667) by 86 to 109 K. This causes the formation of a thick fog that obscures the view into the cavity and some ice formation at the walls. In order to avoid a too low temperature drop the gas was heated to approximately 70°C before the test.

4.3 Velocities

4.3.1 Gas velocity

With the information of pressure and temperature in the pressure vessel and in the cavity, and the flow cross section of the annular space around the RPV, a mean gas velocity in the annulus, u_G, can be determined. The gas mass m_{Gi} in the pressure vessel at any time t_i is determined from

$$m_{Gi} R T_{Vi} = p_{Vi} V \tag{4.8}$$

with p_{Vi} and T_{Vi}, the measured pressure and temperature in the vessel, and V, the vessel volume. The mass flow is calculated by

$$\Delta m_{Gi} = (m_{Gi} - m_{Gi-1})/(t_i - t_{i-1}), \tag{4.9}$$

and the velocity in the annular space is then

$$u_{Gci} = \Delta m_{Gi} / (\rho_{Gci} A_c), \qquad (4.10)$$

with $\rho_{ci} = p_{ci} /(R T_{ci})$ and A_c , the flow cross section of the annular space (index c = cavity). This gas velocity is a mean velocity over the cross section and it is a lower bound, because the partial blocking of the flow cross section by the liquid was not taken into account. The true mean value will be higher whenever liquid is present, and the maximum value is higher because of the velocity profile across the annular gap. The figures 5.159 through 5.169 show these gas velocities. Depending on hole size and pressure the peak gas velocities in each test lie between 5 and 90 m/s.

Two special experiments were performed to compare the calculated velocities with measurements by PIV. The tests L04 and L05 were conducted without liquid, because of the interference of the liquid with the field of view. The pressures and temperatures measured in the vessel and the cavity are shown in figures 4.5, 4.6, 4.9 and 4.10. The velocity profiles across the annular gap are shown in figures 4.7 and 4.11. With some exceptions they are relatively flat. The higher velocities can be found near to the RPV wall, contrary to our expectations. The reason might be the vertical measurement position close to the RPV support and cavity exit. The mean values of the velocity are compared with the calculated data in figures 4.8 and 4.12. They show quite good agreement.

4.3.2 Liquid velocity

The theoretical velocity of the liquid at the hole can be calculated by

$$u_L = (2 (p_V - p_{atm}) / \rho_L)^{1/2} . \qquad (4.11)$$

For water the exit velocities lie between 22 and 46 m/s, and for liquid metal they are 10 and 14 m/s (s. Table 4.4).

The velocity of the liquid film at the cavity wall can be estimated from the high speed film visualization.

4.4 Visualization

All high speed film frames and video pictures were digitized and stored on CD-ROMs. For a detailed analysis they can be viewed on the PC-monitor as video-files (AVI-format). In this report only special frames are presented, that show distinct stages of the flow (s. Figs. 5.170 through 5.213). The transparent cavity was filmed by high speed cameras and therefore the timing is exact to 2 ms. The flow in the subcompartments was filmed by video and therefore the timing is accurate to only 20 ms. Up to test D-07, no time zero signal was recorded by the video camera, that increases the uncertainty to an estimation of how long it takes the water to appear at the nozzles. The description of the flow is given in chapter 5, were the experiments are presented in detail.

4.5 Dispersed Liquid Fractions

The data of the liquid fractions found in the cavity and the compartments are given in table 4.3. In figures 4.13 through 4.16 the data are plotted over the burst pressure. Liquid fractions larger than 0.76 were not found in the compartments, but this is a specific feature of the geometry. The liquid mass in the cavity is the sum of the mass found at the cavity bottom and the mass found in the annular space behind the RPV support (the geometry of the support structure is described in chapter 2 and is shown in Fig. 2.2). When the first experiment with liquid metal was done, it was very difficult to remove the frozen metal from that space. Therefore this space behind the conical ring was filled with silicon rubber (0.6×10^{-3} m^3) and all subsequent experiments were conducted with this geometry. In the early tests without the filling compound a mass fraction of 23 to 28% was trapped at the RPV support. In comparable tests (same total mass) with the filling the mass fraction was lower with 15 to 18% trapped there. However, the total mass in the cavity was not different with and without filling. Two comparable experiments were conducted with the filling. D18 and D19 can be compared with D06 and D07, respectively, and the difference in the total mass fraction remaining in the cavity is only about 1%.

With helium as driving gas the dispersed fractions are smaller than with nitrogen. Because of the higher velocity of sound the blowdown time is much shorter and the velocities in the cavity are higher. However, the higher velocities cannot compensate for the lower density of the gas and the shorter time available for entrainment of the liquid. With liquid metal the entrainment of liquid droplets is smaller due to the higher density and the higher surface tension of liquid metal. The droplets of metal were larger than those of water at corresponding tests. The dispersed fractions are lower with metal than with water, but still high. From the similarity correlations we can deduce that the results from the liquid metal tests represent the lower bound for the dispersed melt fractions in the reactor case. Thus, if the ejected melt fraction has to be less than 10%, the pressure at failure must not be higher than approximately 0.5 MPa and the hole size not bigger than 0.5 m, unless the cavity is specially designed for trapping the melt. This statement pertains to large melt masses and failures in the lower part of the bottom head.

The results concerning the dispersed fractions into the compartments, f_d, could be correlated by the Kutateladze number

$$Ku = \rho_G u_G^2 / (\rho_L g \sigma)^{1/2} \qquad (4.12)$$

with u_G, the maximum gas velocity in the annular space around the RPV, for all hole sizes, both driving gases, nitrogen and helium, and both liquids, water and Bi-alloy (Fig. 4.17), with

$$f_d = 0.4 \log_{10}(Ku) \leq 0.76 \qquad (4.13)$$

The Kutateladze number represents the conditions to levitate droplets against gravity; some authors use Ku^2 for the same expression. If the threshold for droplet levitation up the annulus was applied according to the Kutateladze criterion Ku > 14, the velocity limit for the nitrogen/water combination would be 18 m/s, and for both, helium/water and nitrogen/Wood's metal systems it would be 47 m/s. The results, however, show no sharp threshold and dispersal occurs also at lower velocities. The above correlation should not be overrated and applies only for the tested geometry. It does not reflect the complexity of the blowdown and dispersion processes.

4.6 Gas blowthrough

For the analysis of the processes governing the melt dispersal and the heating of the containment atmosphere (DCH) [7,13] it is important to know the duration of the three stages of the blowdown, the single-phase liquid flow, the two-phase flow and the single-phase gas flow. The single-phase liquid discharge progresses until, at some critical level, a funnel-like depression forms over the outlet hole. This is termed gas blowthrough. Pilch and Griffith [6] have done a detailed literature survey with regard to the application to the DCH-problem. A short abstract of their work will be given here, and we will compare our data with the correlations from the literature.

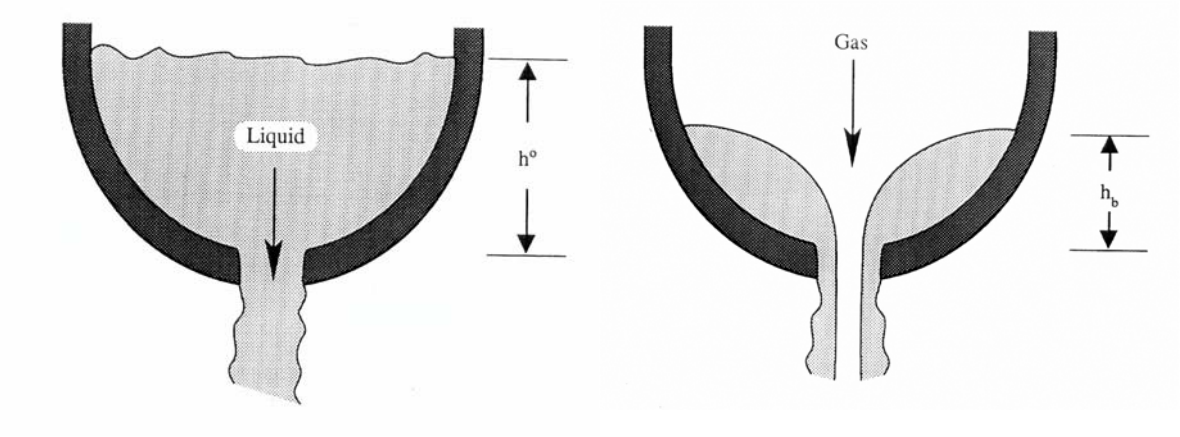

Single-phase discharge Blowthrough and two-phase discharge

Gas Blowthrough Phenomena (from Pilch and Griffith [6])

For a scaling analysis the variables are listed, that have an effect on the critical liquid level at the onset of blowthrough in a cylindrical vessel:

$$h_b = f(u_L, u_t, g, \rho_G, \rho_L, \mu_L, \sigma, d, D)$$

where

h_b	=	critical liquid level at the onset of blowthrough,
u_L	=	velocity of liquid out the hole,
u_t	=	tangential velocity characterizing swirl near the hole,
g	=	acceleration due to gravity,
ρ_G	=	gas density,
ρ_L	=	liquid density,
μ_L	=	liquid viscosity,
σ	=	liquid surface tension,
d	=	diameter of the hole through which the liquid flows,
D	=	characteristic diameter of the tank.

The implied assumption in formulating this list is that the onset of gas blowthrough is dominated by hydrodynamic phenomena that are not significantly influenced by the presence of solid particles, heat transfer, and chemical reactions. A number of non-dimensional scaling groups can be found, such as the Froude number, the Reynolds number, the Bond number, a circulation number, and the density ratio and diameter ratio. The results of the investigations found in the literature suggest that most of the scaling groups do not have a significant effect, and Pilch and Griffith recommend to use the Gluck correlation [16]:

$$\frac{h_b}{d} = 0.43 \frac{D}{d} \tanh\left(Fr^{1/2} \frac{d}{D} \right) \qquad (4.14)$$

where

$$Fr = u_L/(gd)^{1/2}. \qquad (4.15)$$

This correlation was found to be valid for 3.2 < D/d < 20 and 0.32 < Fr < 320. The correlation was developed for upright cylinders with both flat and hemispherical bottoms. For large D/d ratios, it limits to

$$\frac{h_b}{d} = 0.43 \cdot Fr^{0.5} \qquad (4.16)$$

The blowthrough times t_b, determined from the pressure signal P6 are listed in Table 5.1, together with the time t_s it would take to blow out all liquid in a single-phase flow,

$$t_s = V_L / (\varepsilon A_h u_L), \qquad (4.17)$$

with the liquid velocity

$$u_L = (\Delta p\ 2 / \rho_L)^{1/2}, \qquad (4.18)$$

and the measured pressure difference, Δp, between the RPV and the lower cavity. A contraction factor $\varepsilon = 0.6$ was applied for the determination of the time t_s. This is typical for sharp edged openings at high Reynolds numbers, however it could be a function of the pressure and the shape of the opening. A_h is the cross section of the hole and V_L is the liquid volume. The height h_b, at which the blowthrough starts can be calculated with the above data in the following way. The liquid volume blown out during the time up to the time t_b is

$$V_{Lb} = \varepsilon A_h u_L t_b . \qquad (4.19)$$

The liquid volume remaining in the lower head up to the time t_b is then

$$V_{Lr} = V_L - V_{Lb} , \qquad (4.20)$$

and the liquid height h_b can be determined from

$$V_{Lr} = 1/3\ \pi\ h_b^2\ (3\ R - h_b) , \qquad (4.21)$$

with the inner radius R of the lower head.

Fig.4.18 shows the water height h_b in the lower head at blowthrough reduced by the hole diameter d as function of the Froude number. There is no difference between nitrogen and helium driven liquid flows, however. The general trend and the absolute values compare well with the Gluck correlation, Equation 4.14. A different or variable contraction factor ε would, of course, change the data. The prediction by the correlation, that the h_b/d-ratio is less dependent on the Froude number for small D/d-ratios is true for our data as well.

Table 4.1 Test matrix of the experiments with central holes

	Nitrogen /Water			**Helium / Water**			**Nitrogen / Metal**		
	Pressure Δp [bar]			***Pressure Δp [bar]***			***Pressure Δp [bar]***		
Hole ∅ [mm]	***2,5***	***5***	***10***	***2,5***	***5***	***10***	***2,5***	***5***	***10***
15	D12	11	10		H05				
25	15	07,19	04	H02	H01	H03		M02	M01
50	13	06,18	05		H04			M03	M04
100	14	08	09		H06				

Table 4.2 Properties of the model fluids

Property		Helium	Nitrogen	Water	Bismut-alloy Bi 49.5, Pb 17.6 Sn 11.6, In 21.3
Molecular weight	kg/kmol	4.003	28.013	18.015	165
Gas constant	J/kg K	2077.22	296.8	-	-
Melting point	°C			0	58
Density at 10^5 Pa 20 °C , 5 10^5 Pa 20 °C , 10 10^5 Pa	kg/m^3	0.164 0.82 1.63	1.145	1000	9104
Isentropic exponent κ	-	1.667	1.4	-	-
Prandtl-Num. $\eta\ c_p / \lambda$	-	0.665	0.7	7	*≈0.032*
Dyn.Viscosity , 293 K	10^{-3} Pa s	0.0196	0.0178	1.002	*1.6* [1]
Surface tension	10^{-3} N/m	-	-	72	*485* [2]
Sound velocity	m/s	1020	353		
Specific heat c_p	kJ/kg K	5.193	1.038	4.182	0.201[3]
Therm. conductivity	W/mK	0.150	0.026	0.600	10 [3]
Electr. resistivity	μOhm cm	-	-	ca. 50 kΩ	78.8 [3]

[1] estimated

[2] estimated by taking the properties of the components from Liquid-Metals Handbook, NAVEXOS P-733, Atomic Energy Commision, Washington, D.C. 1952

[3] given by the manufacturer, MCP, HEK GmbH, Lübeck

Table 4.3 Parameters and dispersed liquid fractions in DISCO-C experiments

						Liquid fraction found in				
Test	Gas	Liquid **w**ater/ **m**etal 10^{-3} m^3	Hole Dia. (mm)	Burst Press. abs. (MPa)	Blow-through t_b (s)	Compartments f_d	Cavity Bottom f_b	RPV Support f_s	Cavity total $f_c=f_b+f_s$	RPV
D-12	N_2	3.4 w	18	0.270	-	0.000	0.950	0.050	1.000	0
D-11	N_2	3.4 w	15	0.643	0.688	0.161	0.583	0.256	0.839	0
D-10	N_2	3.4 w	15	1.141	0.419	0.382	0.387	0.231	0.618	0
D-15	N_2	3.4 w	25	0.348	0.359	0.193	0.537	0.270	0.807	0
D-07	N_2	3.4 w	25	0.620	0.106	0.518	0.224	0.258	0.482	0
D-04	N_2	3.4 w	25	1.190	0.047	0.698	0.056	0.245	0.302	0
D-13	N_2	3.4 w	50	0.353	0.032	0.551	0.212	0.237	0.449	0
D-06	N_2	3.4 w	50	0.619	0.024	0.669	0.061	0.270	0.331	0
D-05	N_2	3.4 w	50	1.200	0.018	0.759	0.012	0.229	0.241	0
D-14	N_2	3.4 w	100	0.351	0.012	0.580	0.136	0.284	0.420	0
D-08	N_2	3.4 w	100	0.613	0.013	0.717	0.052	0.231	0.283	0
D-09	N_2	3.4 w	100	1.137	-	0.741	0.021	0.239	0.259	0
H-02	He	3.4 w	25	0.388	0.335	0.123	0.621	0.256	0.877	0
H-01	He	3.4 w	25	0.641	0.104	0.350	0.399	0.252	0.651	0
H-03	He	3.4 w	25	1.156	0.065	0.616	0.123	0.261	0.384	0
H-04	He	3.4 w	50	0.621	0.025	0.469	0.378	0.153*	0.531	0
H-05	He	3.4 w	15	0.637	0.076	0.087	0.781	0.132*	0.913	0
H-06	He	3.4 w	100	0.620	0.	0.525	0.298	0.177*	0.475	0
M-02	N_2	3.25 m	25	0.595	0.790	0.060	0.862	0.077*	0.940	0.001
M-01	N_2	3.41 m	25	1.045	0.515	0.358	0.428	0.215	0.643	0
M-03	N_2	3.28 m	50	0.582	0.090	0.379	0.495	0.125*	0.620	0.001
M-04	N_2	3.24 m	50	1.000	0.053	0.730	0.159	0.109*	0.268	0.001
D-19	N_2	3.4 w	25	0.615	0.105	0.511	0.344	0.145*	0.489	0
T-02	N_2	3.4 w	25	0.604	0.245	0.553	0.293	0.154*	0.447	0
D-18	N_2	3.4 w	50	0.604	0.025	0.681	0.139	0.180*	0.319	0
T-01	N_2	3.4 w	50	0.610	0.066	0.760	0.072	0.168*	0.240	0

Table 4.3 Continued

						Liquid fraction found in				
Test	Gas	Liquid **w**ater/ **m**etal 10^{-3} m^3	Hole Dia. (mm)	Burst Press. abs. (MPa)	Blow-through t_b (s)	Compartments f_d	Cavity Bottom f_b	RPV Support f_s	Cavity total $f_c=f_b+f_s$	RPV
D-17	N_2	1.8 w	25	0.612	0.033	0.407	0.123	0.470	0.593	0
D-20	N_2	1.8 w	25	1.140	0.033	0.553	0.024	0.423	0.447	0
D-21§	N_2	1.8 w	25	0.630	0.032	0.385	0.144	0.471	0.615	0
D-22	N_2	1.8 w	25	0.63		0.360	0.414	0.226	0.640	0
D-23	N_2	1.8 w	25	1.1		0.652	0.146	0.201	0.348	0
R-01	N_2	1.8 w	25[#]	0.611	-	0.029	0.423	0.185	0.608	0.363
R-02	N_2	1.8 w	25[#]	1.102	-	0.250	0.244	0.244[*]	0.488	0.262
R-03	N_2	1.8 w	25	1.100	-	0.358	0.294	0.238[*]	0.531	0.111
R-04	N_2	1.8 w	50	1.100	-	0.477	0.266	0.209[*]	0.475	0.048
R-06	N_2	1.8 w	25	1.610	-	0.469	0.204	0.242[*]	0.446	0.085
R-05	N_2	1.8 m	25	1.050	-	0.0005	0.657	0.006[*]	0.663	0.336
R-07	N_2	1.8 m	25	1.650	-	0.0034	0.652	0.042[*]	0.656	0.296
K-01	N_2	2.1 w	h=57	0.500	-	0.011	0.851	0.043[*]	0.894	0.095
K-04	N_2	2.1 w	h=57	0.800	-	0.091	0.632	0.210[*]	0.842	0.067
K-02	N_2	2.1 w	h=16	0.800	-	0.225	0.320	0.270[*]	0.588	0.187
K-03	N_2	2.0 m	h=16	1.100	-	0.007	0.455	0.124[*]	0.579	0.413
F-03	N_2	3.4 w	25	1.076	0.070	0.632	0.233	0.135[*]	0.367	0
F-04	N_2	3.4 w	25	1.100	0.070	0.280	0.590	0.130[*]	0.720	0
F-05	N_2	3.4 w	50	1.110	0.018	0.266	0.574	0.159[*]	0.734	0
F-06	N_2	1.8 w	(R)25	1.110	-	0.097	0.578	0.206[*]	0.784	0.119
S-01	N_2	3.4 w	25	1.102	0.070	0.713	0.146	0.128[*]	0.274	0

§ Holes closed at the support

[*] Space behind conical ring at the support girder was filled with 0.6×10^{-3} m^3 silicon rubber up to the lower edge of the holes, so all liquid could flow back into the lower cavity, except a thin film and the frozen material at the walls.

[#] horizontal slot, 40 × 12.5 mm

Table 4.4 Blowthrough parameters

No.	d (m)	Δp (MPa)	u_{Liquid} (m/s)	t_b (s)	t_s (s)	t_s/t_b -	Fr -	h_b (m)	h_b/d -	D/d -
D11	0.015	0.540	32.9	0.688	0.976	1.41	85.7	0.049	3.27	18.40
D10	0.015	1.040	45.6	0.419	0.703	1.67	118.9	0.058	3.87	18.40
D15	0.025	0.250	22.4	0.359	0.516	1.43	45.2	0.050	2.00	11.04
D07	0.025	0.520	32.2	0.106	0.358	3.31	65.1	0.078	3.12	11.04
D04	0.025	1.060	46.0	0.047	0.251	5.22	93.0	0.085	3.40	11.04
D13	0.050	0.260	22.8	0.032	0.127	3.62	32.6	0.081	1.62	5.52
D06	0.050	0.520	32.2	0.024	0.089	3.50	46.0	0.080	1.60	5.52
D05	0.050	1.060	46.0	0.018	0.063	3.30	65.7	0.079	1.58	5.52
D14	0.100	0.250	22.4	0.012	0.032	2.15	22.6	0.073	0.73	2.76
D08	0.100	0.510	31.9	0.013	0.023	1.51	32.2	0.059	0.59	2.76
H05	0.015	0.537	32.8	0.758	0.979	1.29	85.4	0.042	2.82	18.40
H02	0.025	0.288	24.0	0.335	0.481	1.42	48.5	0.050	2.00	11.04
H01	0.025	0.641	35.8	0.104	0.351	3.31	66.4	0.078	3.14	11.04
H03	0.025	1.056	46.0	0.065	0.251	3.77	92.8	0.081	3.24	11.04
H04	0.050	0.521	32.3	0.023	0.089	3.58	46.1	0.081	1.62	5.52
D17	0.025	0.505	31.8	0.031	0.191	5.79	64.6	0.061	2.44	11.04
M01	0.025	0.945	14.4	0.511	0.707	1.37	29.1	0.044	1.77	11.04
M02	0.025	0.495	10.4	0.784	0.977	1.24	21.1	0.037	1.48	11.04
M03	0.050	0.482	10.3	0.084	0.248	2.75	14.7	0.071	1.41	5.52
M04	0.050	0.900	14.1	0.049	0.181	3.42	20.1	0.075	1.49	5.52

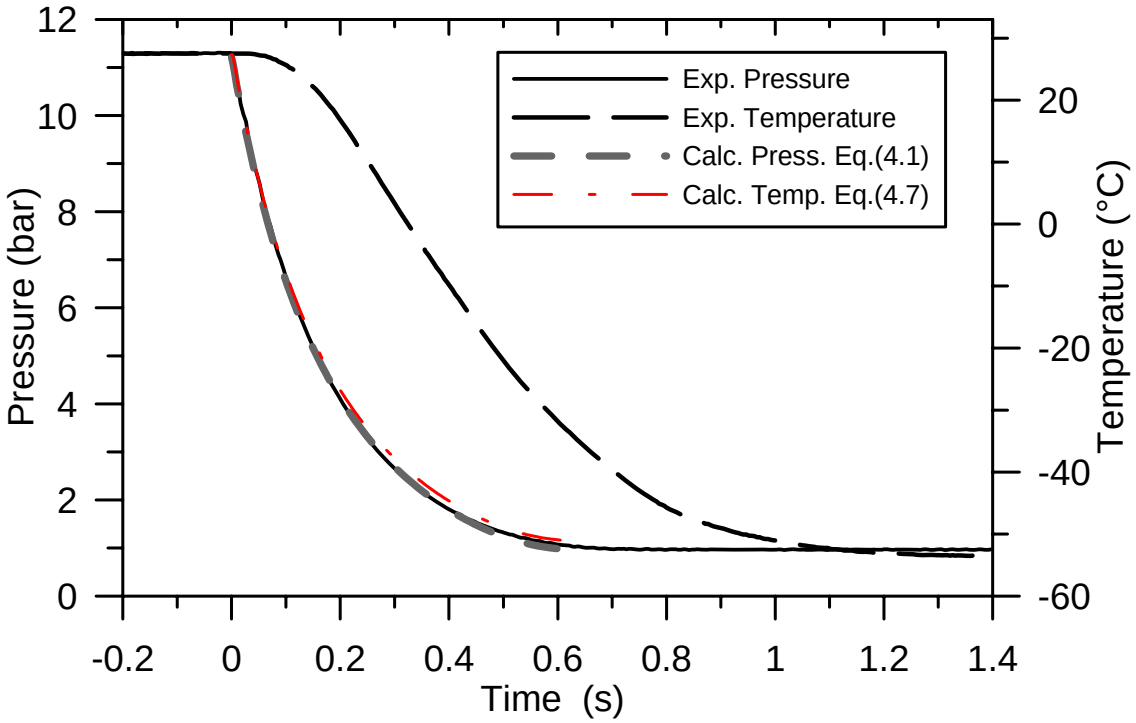

Fig. 4.1 Pressure and temperature in a gas blowdown test
(Nitrogen, 1.12 MPa, 50 mm hole diameter)

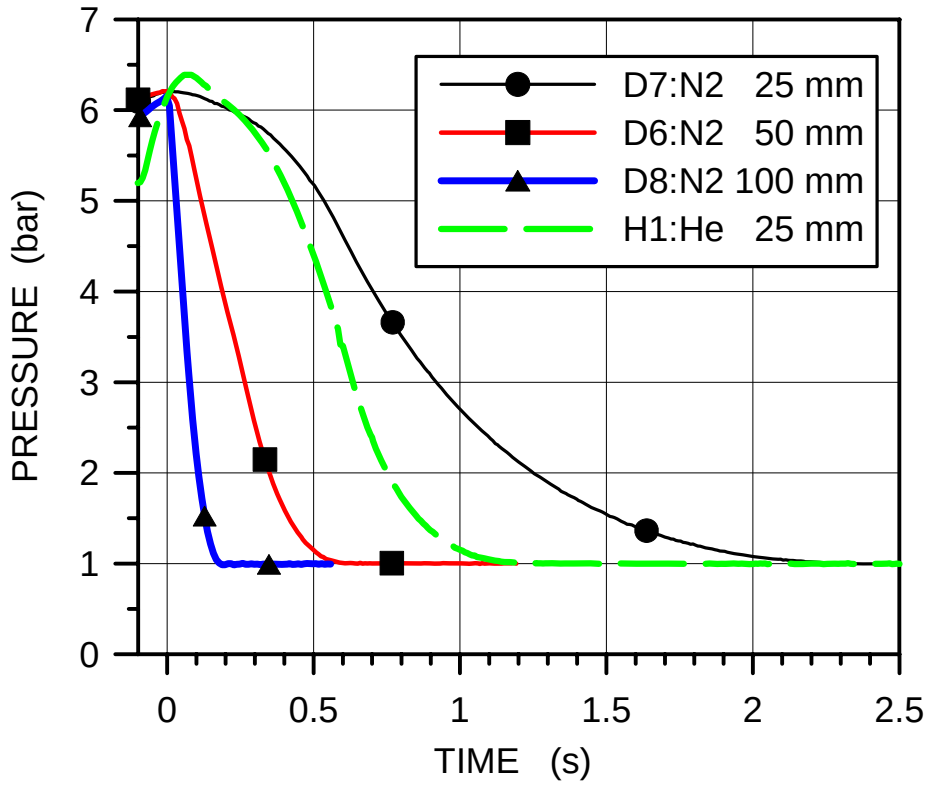

Fig. 4.2 Pressure and temperature in a gas blowdown test

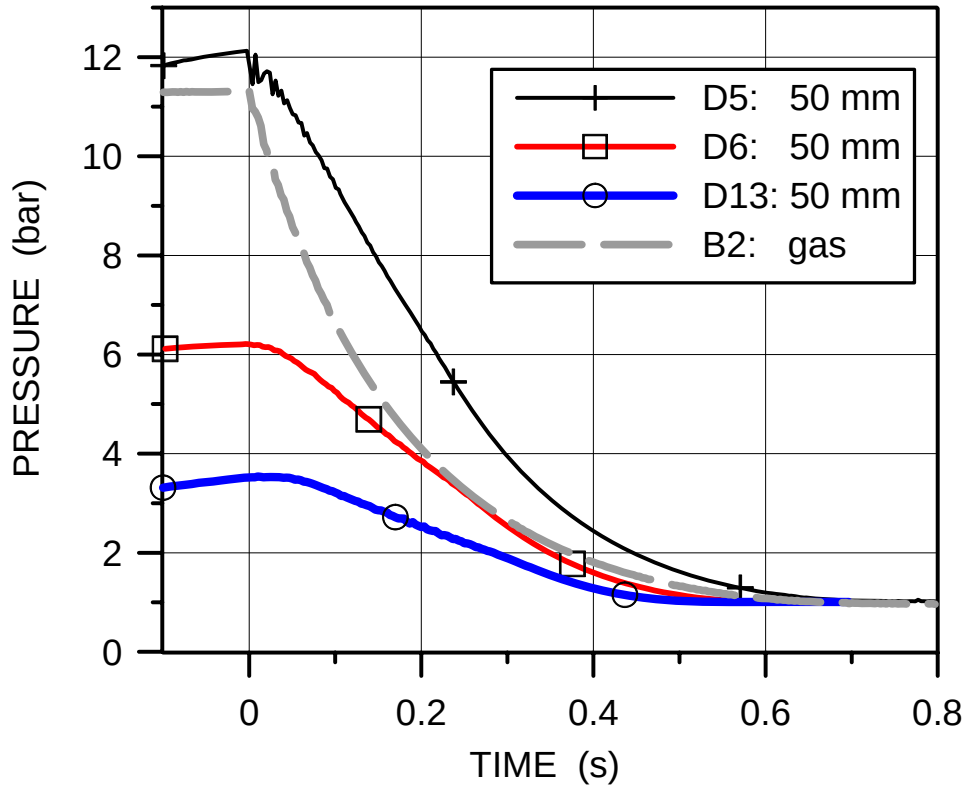

Fig. 4.3 Pressure and temperature in a gas blowdown test

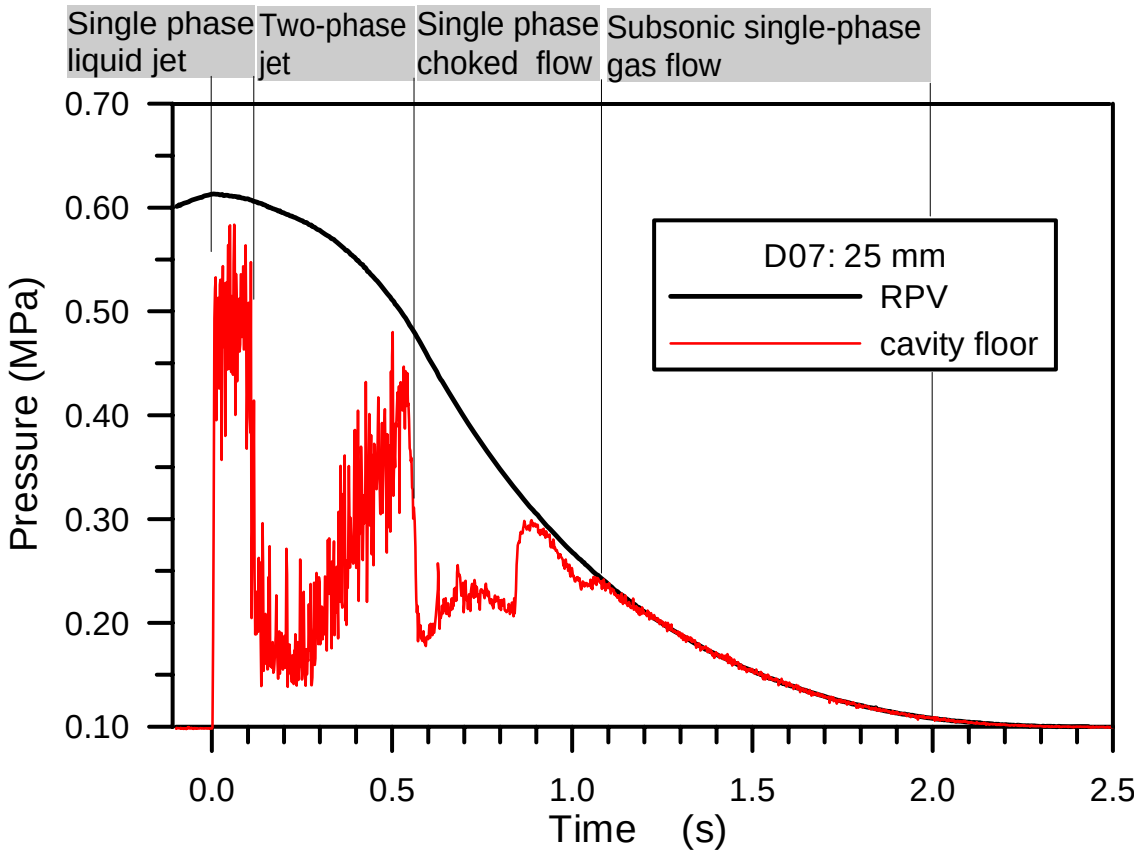

Fig. 4.4 Typical pressure history in the pressure vessel and on the cavity floor below the hole

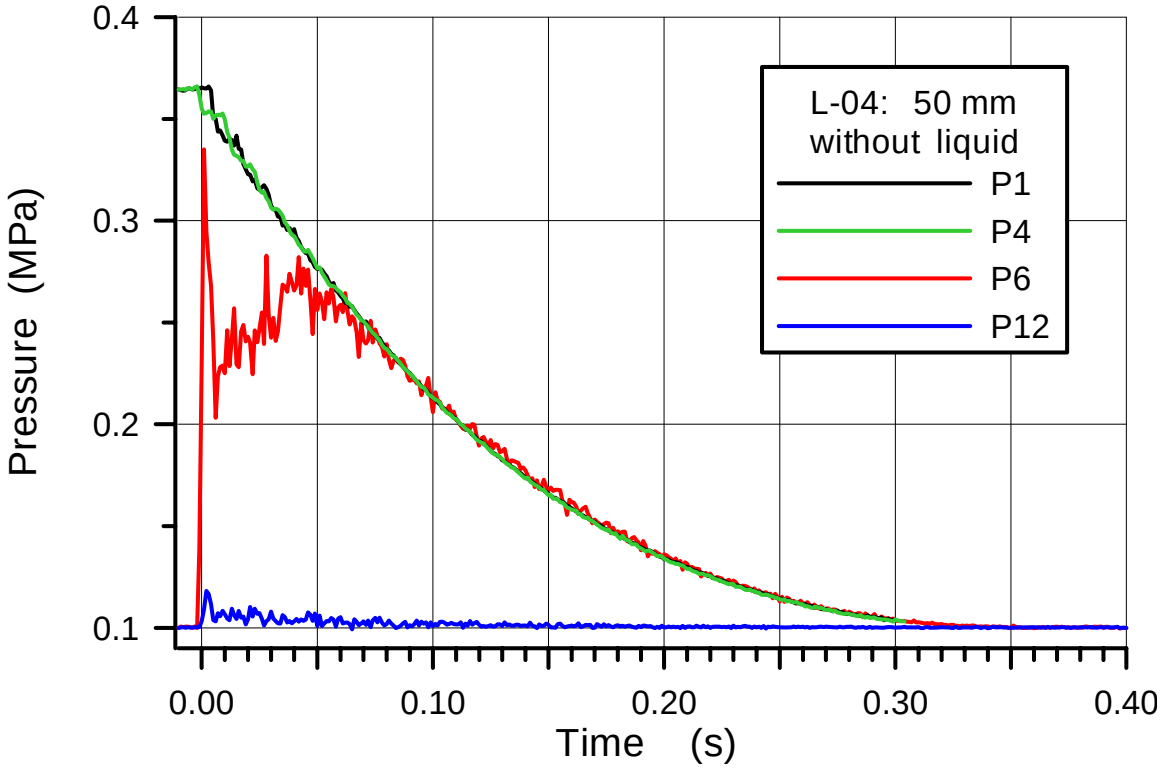

Fig. 4.5 Pressures in the vessel and the cavity in a test without liquid, L04, 50 mm hole

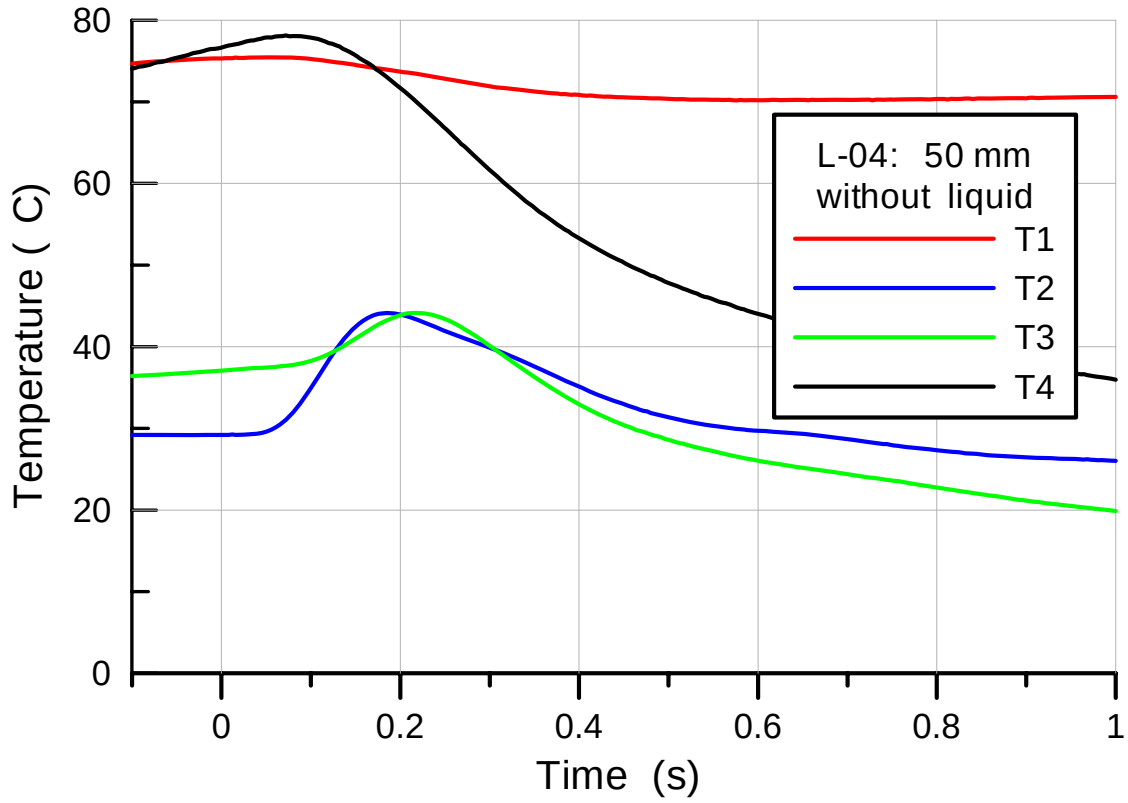

Fig. 4.6 Gas temperatures in the vessel and the cavity in a test without liquid

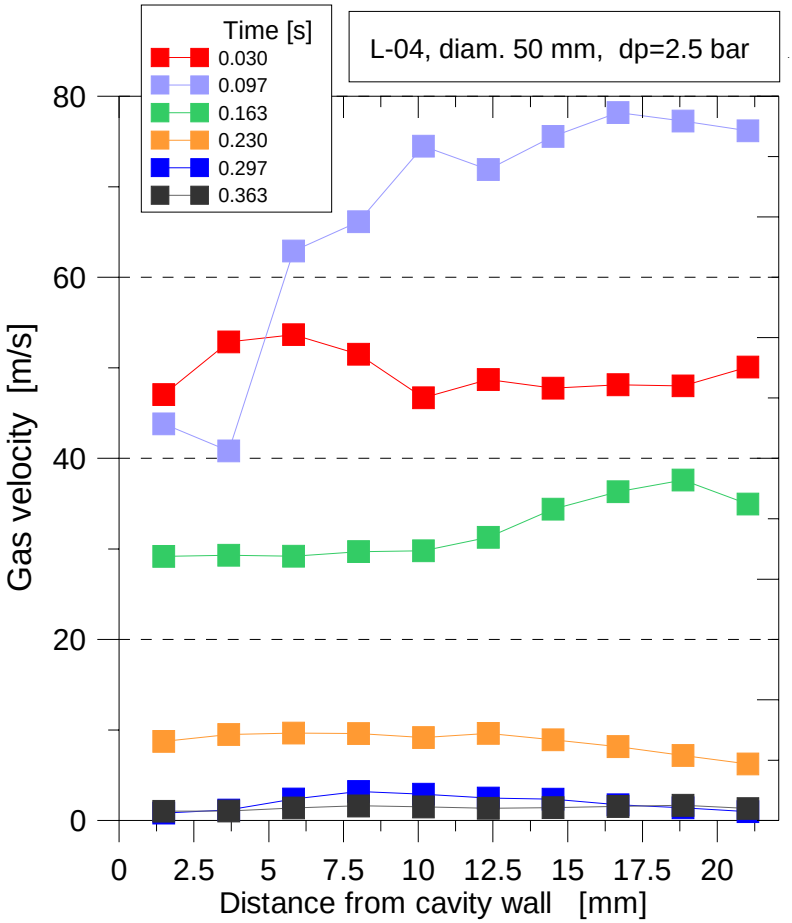

Fig. 4.7 Velocity profiles across the annular gap between cavity wall and RPV wall

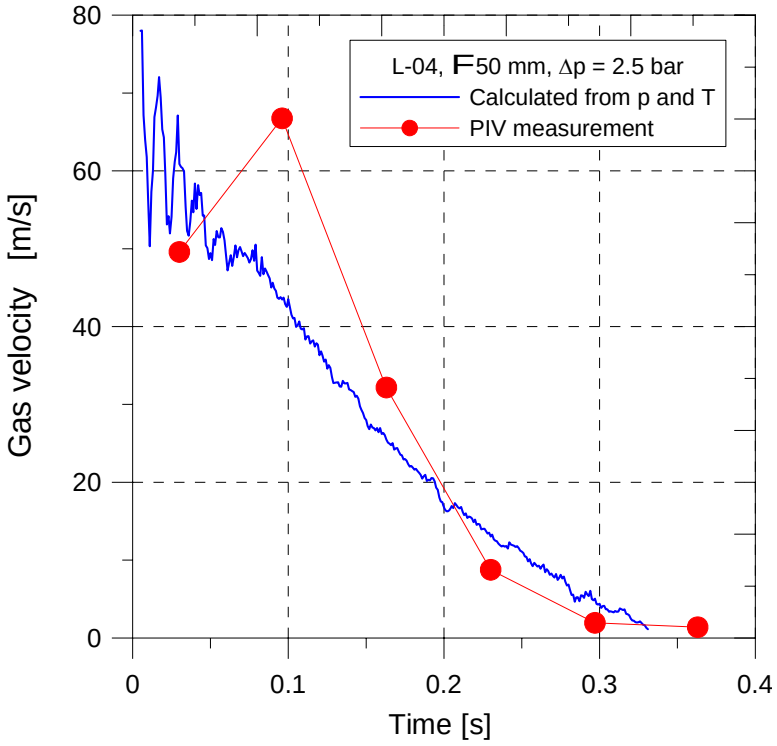

Fig. 4.8 Comparison of mean gas velocity

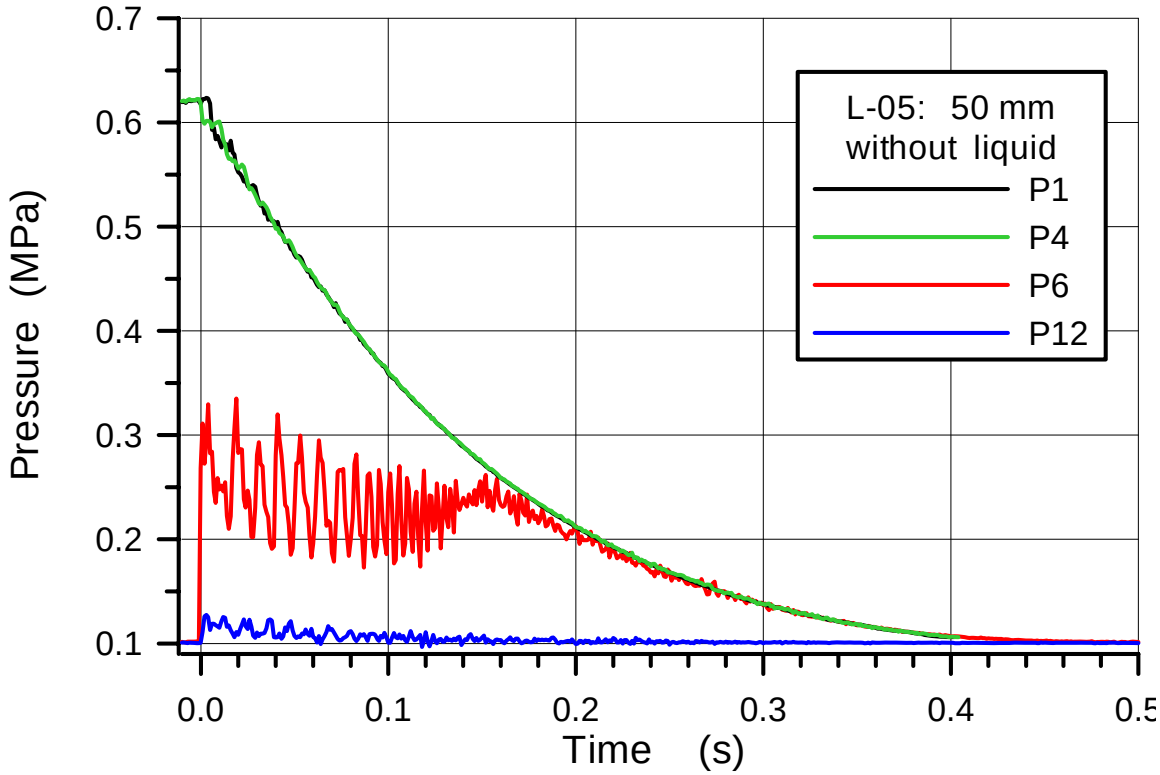

Fig. 4.9 Pressures in the vessel and the cavity in a test without liquid, L05, 50 mm hole

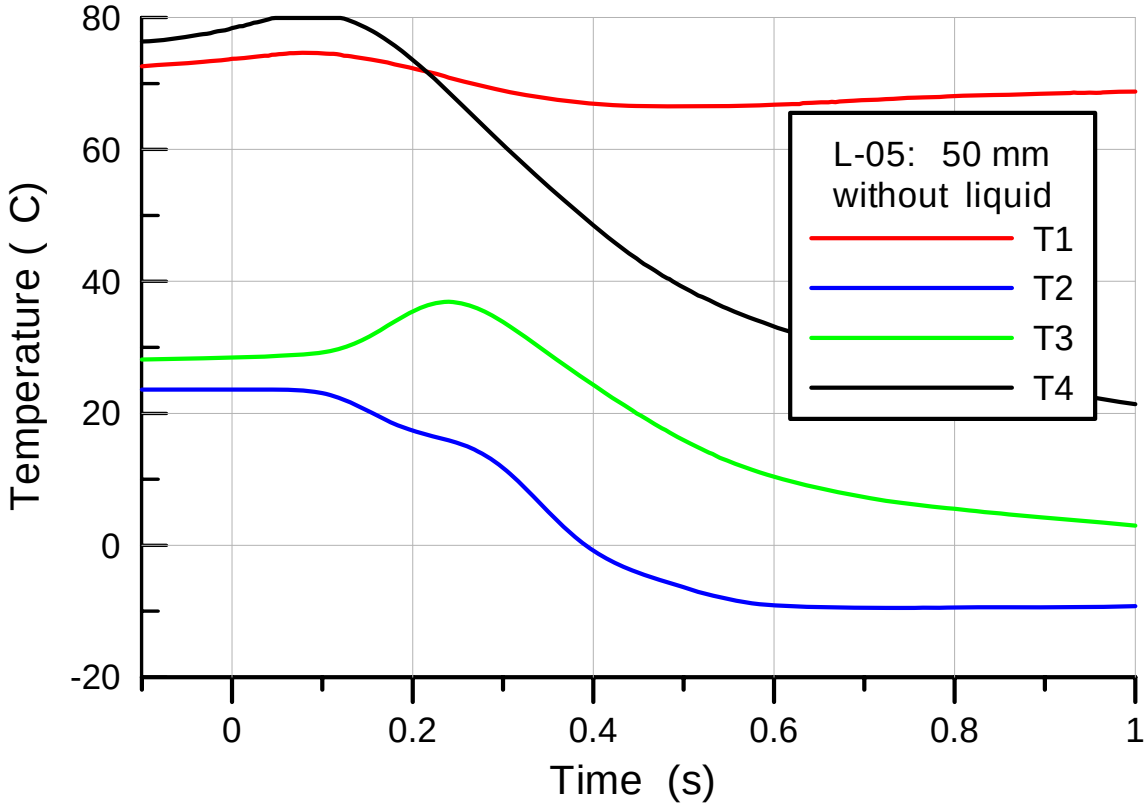

Fig. 4.10 Gas temperatures in the vessel and the cavity in a test without liquid

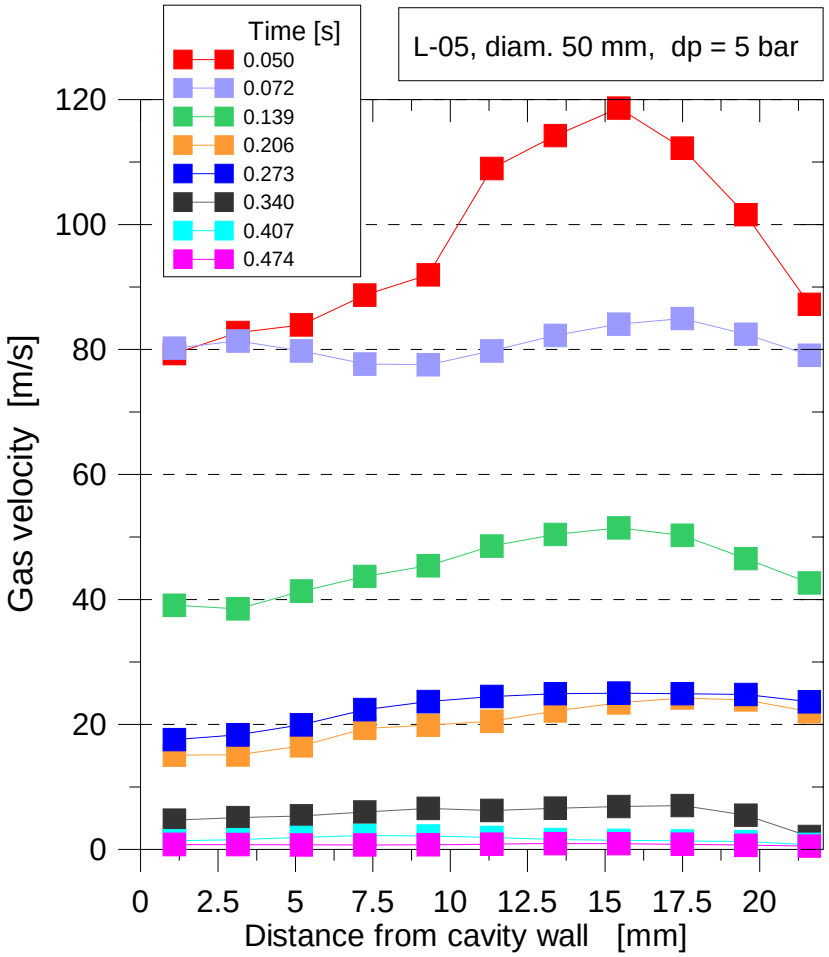

Fig. 4.11 Velocity profiles across the annular gap between cavity wall and RPV wall

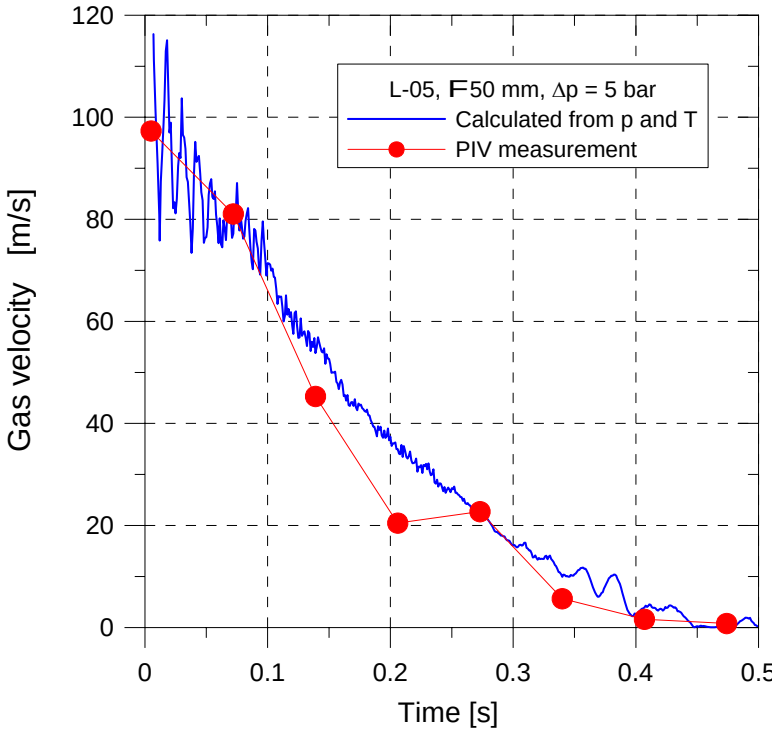

Fig. 4.12 Comparison of mean gas velocity

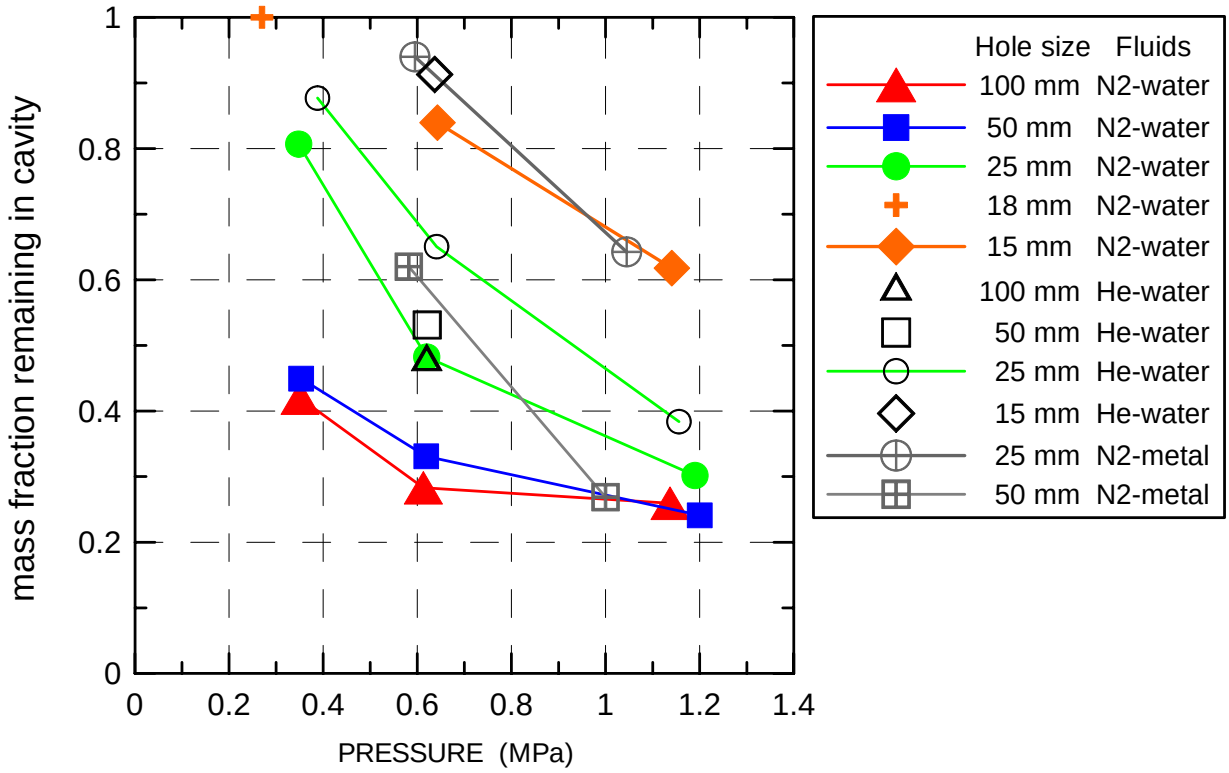

Fig. 4.13 Total liquid mass fraction remaining in the cavity for tests with central holes

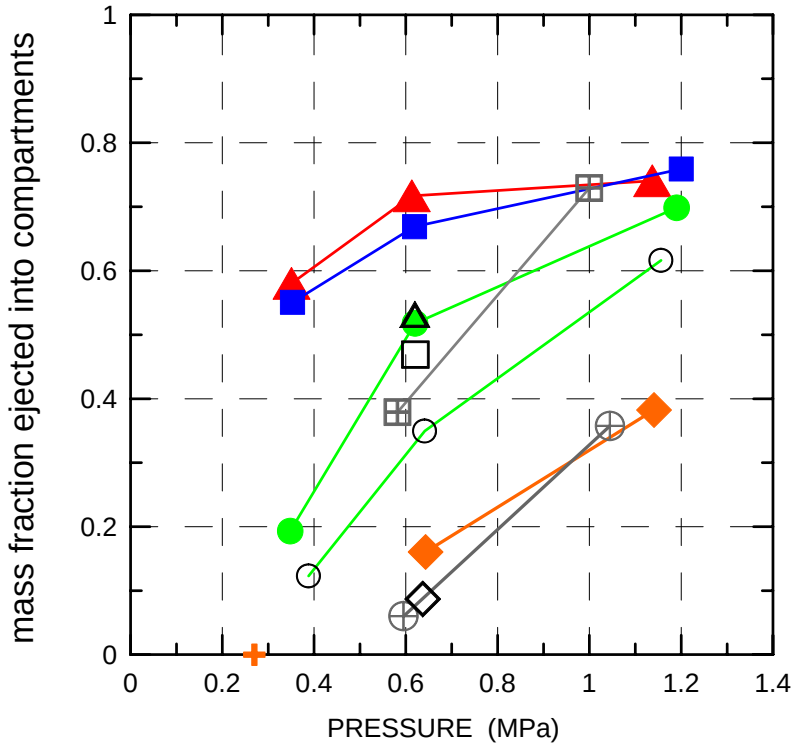

Fig. 4.14 Total liquid mass fraction ejected out of cavity for tests with central holes

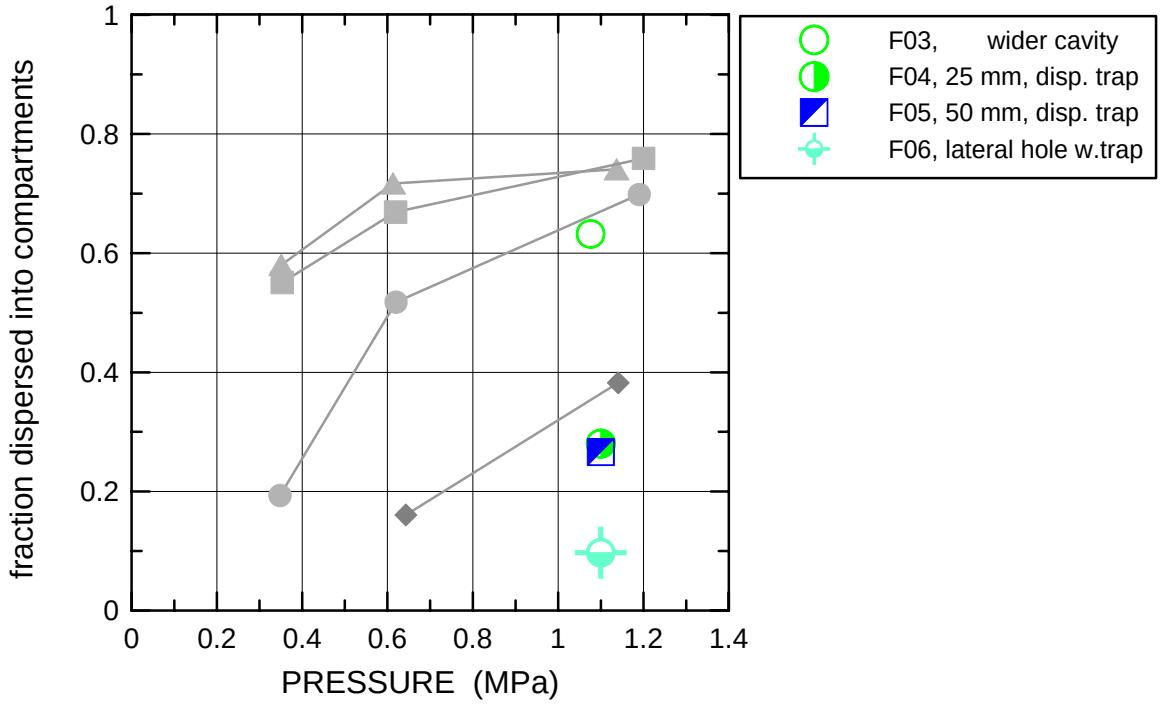

Fig. 4.15 Dispersed fractions for tests with changes in cavity geometry in comparison with results from tests with central holes.

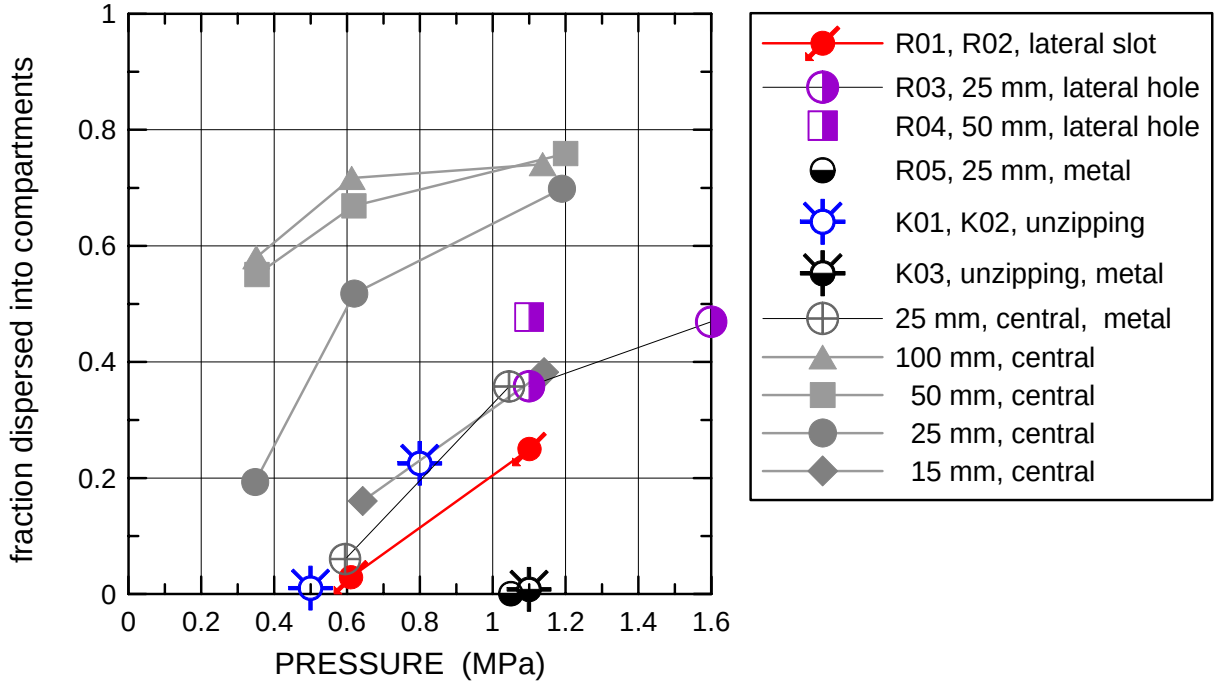

Fig. 4.16 Dispersed fractions for tests with lateral breaches in comparison with results from tests with central holes.

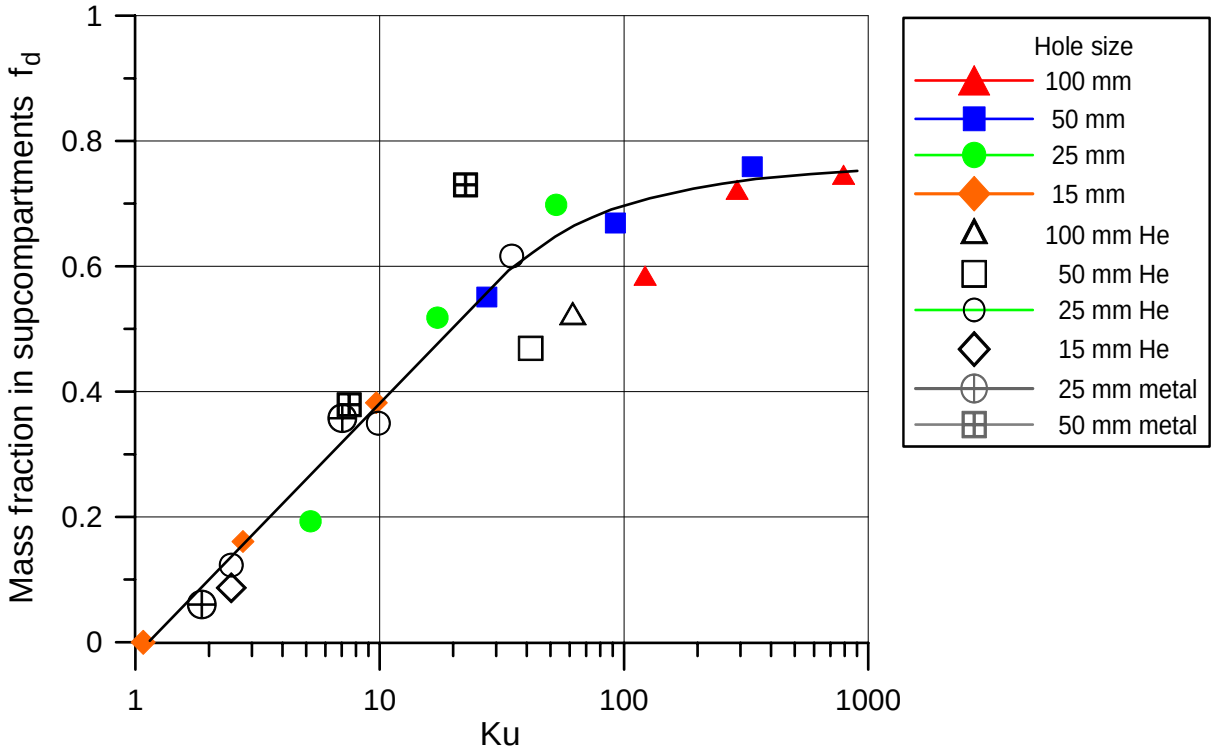

Fig. 4.17 Mass fraction ejected into compartments as function of the Kutadeladse number, for tests with central holes, and water/nitrogen (solid symbols), water/helium (open symbols) and liquid metal/nitrogen (cross symbols).

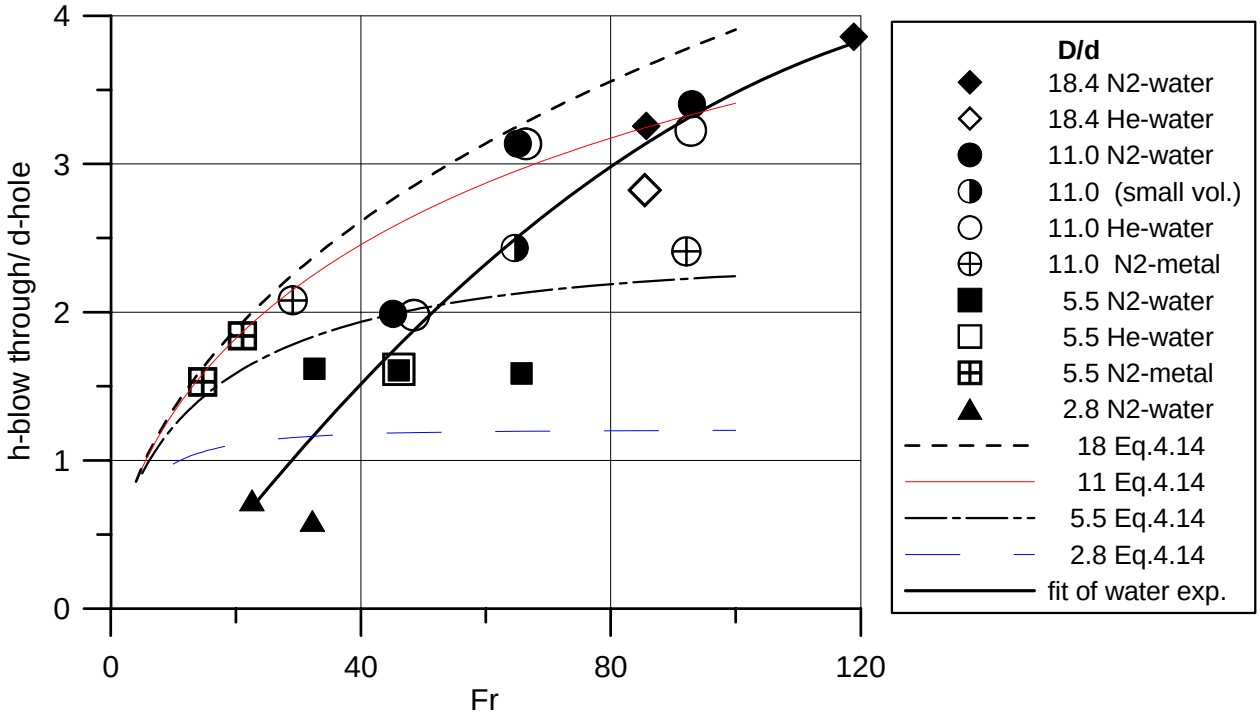

Fig. 4.18 Relative blowthrough height versus Froude number (D = 276 mm)

5 EFFECTS OF EXPERIMENTAL PARAMETERS

Figures 5.1 through 5.158 show the pressure and temperature data for all tests in the same sequence as that of table 4.3. The pressures measured inside the pressure vessel at different positions were almost identical, therefore generally only one curve is shown. Usually, no effect of the disk with the flow constricting pipes separating the RCS from the RPV volume could be detected except for very large breach sizes.

In experiments with low vessel pressures or with small holes the pressure in the subcompartments was practically unchanged (at atmospheric pressure), therefore no plot is shown in these cases. The sampling rate was 2.5 kHz, but the pressure curves shown are smoothed by the method of the running average, where necessary, especially the pressures in the cavity and the subcompartments. Care was taken, not to loose any important peaks.

5.1 Effect of fluids, hole size and pressure with central holes

5.1.1 Nitrogen-water

5.1.1.1 Nitrogen-water, hole size 15 mm (18 mm), D12, D11, D10

D12: This experiment did not run as it was intended. A 25-mm-hole size was installed with a 0.35-MPa differential pressure rupture disk. Probably because of the heat from the lights the temperature of the disk became too high and it already burst at a differential pressure of 0.27 MPa. The disk blades did not fully open, and the free cross section was equivalent to a hole size of 18 mm diameter.

The vessel pressure decreases only slightly up to t=1.3 s, which implies a single phase liquid flow through the breach (Fig. 5.1). The pressure signal below the hole, P6, is low up to that time, increases to almost vessel pressure in the time interval 1.3 s – 1.7 s and decreases parallel to the vessel pressure for t > 1.7 s. This indicates single- phase gas flow in the last period and two-phase flow for 1.3 < t < 1.7 s. The fact that the pressure P6 does not reach the height of the vessel pressure in the first stage shows that there is a high pressure loss at the hole and the water jet is diffuse, probably because of the rough edges of the hole. The theoretical velocity of the jet would be 23 m/s, but it is only approximately 15 m/s (according to the pressure data P6). The pressure change in the cavity (Fig. 5.2) is small and it is zero in the compartments.

The shape of the jet can be seen in the pictures of the high speed camera (Fig. 5.179). In the subsequent pictures a dispersed water film is formed at the cavity wall, that moves up only part of the cavity height and falls back onto the cavity bottom. The exit velocity of the water jet is less than 3 m/s. After the onset of the two-phase flow (t > 1.3 s) the water film becomes more churned but does not rise higher. The maximum gas velocity in the annular gap is only 5 m/s (s. Fig.5.159). Only 5% of the water was found at the RPV support structure and none in the subcompartments.

D11: The pressure in the pressure vessel (Fig.5.4) continued to increase for 90 ms (20 ms more than normal, because of late break wire failure) after the burst of the rupture disk. During single-phase liquid outflow the pressure drop is small up to 0.69 s. The theoretical liquid velocity is 32 m/s but the total pressure measured by the transducer P6 corresponds to only 20 m/s. The maximum gas velocity (u_{Gc}= 9 m/s, Fig. 5.159) is reached at t = 1200 ms coinciding with the second peak in the pressure P6. Probably, at this point single phase gas flow is reached, but due to the supercritical pressure ratio there is choked flow at the hole and the total pressure at gauge P6 is below the static pressure in the vessel. Only at t = 3500 ms these two pressures are the same when the gas velocity at the hole becomes subsonic. Between t = 1200 ms and t = 3500 ms the pressure signal P6 depicts two different stages, that were observed in many tests. It is not clear whether the pressure transducer is covered by liquid in the first stage and therefore cannot measure the total head of the flow or some other process changes within this time period (at t = 2100 ms). The liquid obviously is blown to the side when the pressure signal of P6 is equal to the static vessel pressure.

Thus, from the pressure signal P6 we can clearly distinguish five stages in the blowdown process:

1., the single-phase liquid flow,

2., the blowthrough with two-phase flow,

3. and 4., single-phase choked flow with two stages that could be caused by processes in the cavity, and

5., subsonic single-phase gas flow.

A low maximum pressure increase in the cavity (Fig. 5.5, P7-P12) with 1600 Pa is observed when the gas mass flow reaches its maximum (Fig. 5.159). All pressures in the lower cavity immediately swing back to a slight under pressure, the pressure difference in the annular space remains positive.

The high speed pictures (Fig. 5.177) depict the different stages of the blowdown. After 10 ms the liquid film starts to flow up the cavity walls. At t = 190 ms a steady pulsating upwards motion can be observed, that lasts until t = 740 ms, the end of single phase liquid flow. This movement breaks down until a new upwards directed film flow begins at t = 840 ms. At t = 1500 ms the liquid film starts to flow down at the upper edge of the picture and a vortex develops with upwards and downwards directed flow at different positions. These vortices are stable for approximately 200 ms, and different patterns of upwards directed flow in the lower part and downward directed flow in the upper part develop. The boundary between the two directions moves downwards until only downward film flow is present.

The video pictures (Fig. 5.178) show the flow into one subcompartment. In the first stage, up to t = 1000 ms, the water flows slowly in a stream through the cutout area for the loop piping. At t = 1040 ms the liquid flow has almost ceased. At that time droplets appear at the cut out flow cross section and a new, more violent liquid flow starts, that dies down to a stream at the bottom at t = 1440 ms. After t = 2300 ms no more water enters the subcompartment.

The first stage of liquid flow into the subcompartments is a purely inertia driven liquid flow, driven by the relatively high exit velocity of water of 24 m/s or more. The second stage is due to the two-phase flow with gas velocities in the annular cavity above 6 m/s, and maybe some entrainment of the liquid film. This entrainment stops at lower velocities. The liquid mass found

in the subcompartments was small with only 16.1 % of the total. However, 25.6 % were driven up the walls into the space at the RPV support.

D10: The higher pressure, compared to D11, does not change the blowdown characteristics much. Again five stages can be observed (Fig. 5.7). The instant of blowthrough, when gas exits the hole for the first time, is earlier. The pressure P6 indicates a total pressure corresponding to a liquid velocity of approximately 33.5 m/s versus a theoretical possible value of 45.6 m/s. The maximum gas velocity in the annular space (Fig. 5.159) is reached at the time of the second peak in P6 (t = 0.91 s), indicating the beginning of a predominant single-phase gas flow. The calculated vessel pressure according to equation (1) is in good agreement with the measured one, when the calculation is started at t = 1.0 s. That also shows that we have single-phase gas flow at that time. In the third stage, the pressure signal of P6 is very low, lower than in D11.

The pressure increase in the cavity (Fig.5.8) is not higher in D10 than in D11, but the swing into under-pressure is approximately twice as large. The pressure traces shown were heavily smoothed because they had a large noise. No pressure increase in the subcompartments was observed.

The flow into the subcompartments (Fig.5.176) shows for stages. In the first stage, up to t = 600 ms, the water flows in a stream through the cutout area. Than large droplets appear in the flow cross section. In a third stage, starting approximately at t = 760 ms, the flow is faster and the droplet flow is more uniform across the flow cross section. The transition into the fourth stage is gradual, and after t = 1200 ms the water flow dies down to a stream at the bottom with few droplets in a gas flow in the rest of the cross section. At = 5000 ms no more liquid enters the subcompartment.

As in D11, the first stage of the flow into the subcompartments corresponds to inertia driven liquid flow, the third stage is a two phase flow out of the hole in the lower head all the way into the subcompartments, and the fourth stage is a film flow driven by the gas without much droplet entrainment, except at the end of the two-phase flow stage and the beginning of single-phase gas flow with gas velocities above 13 m/s in the annular cavity cross section. 38.2 % of the liquid inventory were ejected into the subcompartments, and 23.1% remained in the space at the RPV support.

5.1.1.2 Nitrogen-water, hole size 25 mm, D15, D07, D04

D15: The blowdown time is approximately inversely proportional to the flow cross section of the hole, that is about three times larger with the 25-mm hole than with the 15-mm hole. The peak pressure is reached at t = 80 ms (Fig. 5.10). In this test the single phase liquid flow is obviously undisturbed. The total pressure indicated by P6 coincides exactly with the static pressure in the vessel, indicating a liquid velocity of 22 m/s. Only three stages can be determined from the signal P6. The peak at 710 ms probably does not indicate single-phase gas flow because the vessel pressure is still to high for a subsonic flow and the total pressure P6 should drop to a lower value. The maximum gas mass flow is reached at 800 ms (Fig. 5.160), and that is probably the time when single-phase flow begins. Again there is little pressure increase in the subcompartments.

The flow pattern at the cavity wall (Fig. 5.185 and 5.186) changes when the single phase liquid flow ends and the transition to gas flow begins. Although we see a turbulent film at the wall, only very few droplets reach the subcompartments up to t = 500 ms (Fig. 5.187). Only then, water flows in a stream and as droplets into the subcompartments. This dies down at t = 1400 ms.

The liquid exit velocity of 22 m/s is obviously not high enough to drive liquid into the subcompartments. The main part of the water in the subcompartments (19.3%) is carried by two-phase flow originating at the exit hole and liquid film driven by the gas when the velocity is higher than approximately 6 m/s (Fig. 5.160).

D07: Here again, we find five distinct stages in the blowdown process, as described for D11 and D10 (Fig. 5.14). The transducer P6 indicates a higher signal during single-phase liquid flow, than in D11 with the smaller hole. That lasts until 106 ms. The pressures in the lower cavity show the same characteristics as in the experiments with the smaller hole of 15 mm diameter (D11 and D10). The pressure near the vessel support at the cavity exit slightly increases (P13 and P14), but does not change in the compartments (Fig. 5.15).

In spite of the high liquid velocity of at least 28 m/s, only a few water droplets enter the subcompartments before t = 240 ms (Fig. 5.173). Large amounts of water enter the subcompartments between t = 300 ms and 900 ms, with the maximum between 400 and 800 ms, that is during the two-phase flow stage and shortly thereafter, when the gas velocity in the annular space of the cavity is higher than 14 m/s (Fig. 5.160).

D04: The blowdown process and the pressures in the cavity (Fig. 5.18 and 5.19) are similar to those of D07. The duration of the liquid single-phase flow is short with 48 ms, only about one third of the time it would need to drain all water in a single phase.

The photographs of the flow in the cavity do no show any interesting features and are not presented here. Pictures of the flow into the subcompartments are shown in Fig. 5.170. First droplets appear approximately 40 ms after the break of the rupture disk. At t = 160 ms a water surge with large droplets enters the box. These droplets are getting smaller while the velocity is increasing (picture at t = 360 ms). At t = 480 ms, the droplet flow fades out. This coincides with the end of the two-phase flow out of the lower head. At t =580 ms the gas velocity in the box is high enough to drive a water film up the opposite wall (in the picture on the right side). At t = 800 ms this film flows back down the wall.

5.1.1.3 Nitrogen-water, hole size 50 mm, D13, D06, D05

In the test series with the 50-mm hole the blowdown is faster by about a factor of four compared with the 25-mm hole experiments (Fig. 5.22 - Fig. 5.33). The measured total pressure below the hole (P6) is equal to the static pressure in the vessel in all three cases of initial vessel pressure. Only three stages of the blowdown process can be distinguished by the pressure P6. Between the single-phase liquid flow and the single-phase subsonic gas flow only one stage is discernible.

There is a big difference between the cavity pressures for the 25-mm hole experiments and the 50-mm hole experiments. First of all, they are higher for the larger hole by a factor of 5 for the low initial pressure experiments D13 versus D15, and by a factor of 15 for the high pressure experiments D05 versus D04. Then, different from the small hole experiments, the pres-

sure maxima are always higher in the lower cavity (P7-P10) than in the annular space (P11 and P12), and the underswing of the pressures in the lower cavity (P7-P10) after the maximum is relatively small.

For the first time, we measure a distinct pressure rise in the narrow flow cross section around the main cooling line stubs (P15 and P16, ≈ 4000 Pa) and a slight pressure increase in the subcompartments (P17 and P19, ≈ 400 Pa).

The flow in the cavity is shown in Fig. 5.180 for the low pressure experiment D13. During the single-phase liquid flow the water does not reach the cavity exit. In the time interval 50 to 300 ms the flow becomes more violent and the water film is driven up the cavity wall into the subcompartments. Later the water film is first stagnant and then flows back down again.

In the subcompartments the first droplets appear at t=80 ms (Fig. 5.181). The main water mass flow with large droplets enters the subcompartments between t = 220 ms and t = 460 ms.

For the medium pressure experiment D06 (Fig. 5.172) the first droplets appear at t= 60 ms, and the main mass flow occurs in the time interval 100 to 340 ms. The droplets are smaller than in test D13.

In the test with the highest pressure, D05 (Fig. 5.171), the first mist appears before t = 60 ms. The main liquid mass flow is between 80 and 200 ms, with very fine droplets. The two-phase jet hits the opposite wall.

5.1.1.4 Nitrogen-water, hole size 100 mm, D14, D08, D09

Again, the blow down times are shorter by approximately a factor of four corresponding to the four times larger flow cross section of the 100-mm diameter hole versus the 50-mm hole (Figs. 5.34 – 5.45). For the first time a small difference was measured between the pressure P1 and P2, that is the space above and below the disk, that separates the RPV-volume from the RCS volume within the pressure vessel (Fig. 5.42). The signal P6, showing the total pressure below the hole, has a peak for about 10 ms, but then indicates the same pressure as the static pressure in the vessel P2, for both, the low and medium pressure tests D14 and D08. This is possible because the pressure in the cavity is high and so the critical pressure ratio is not reached. In test D09 the transducer P6 was defect.

The maximum pressure increase in the cavity (P7-P10) is approximately one half (1/2) of the initial overpressure in the vessel. For the experiments with the 50-mm hole this was only between 1/20 and 1/50. The flow area of the 100-mm hole is less than one half of the smallest flow area in the cavity (hole area A_H = 0.00785 m^2, flow constriction at the vessel support A_{min} = 0.01890 m^2).

The maximum pressure rise in the narrow flow cross section around the main cooling line stubs (P15 and P16) is 7 kPa for the low pressure test D14 and 80 kPa for the high pressure test D09. The pressure increase in the subcompartments (P17 – P22) is zero in tests D14 and D08 and about 5 kPa in test D09.

The flow in the cavity is shown in Fig. 5.182 and 5.183 for the low pressure experiment D14. The opening of the rupture disk takes about 5 ms. No separate stages of the blowdown process can be distinguished. The flow looks similar for the higher pressure tests, but the liquid

front reaches the upper edge of the cavity earlier, about 5 ms earlier in the high pressure test D09 than in test D14. The flow of liquid into the subcompartments consists of a droplet flow with very small droplets, and lasts about 100 ms in test D14 (Fig. 5.184) and about 80 to 90 ms in test D09.

5.1.2 Helium-water

5.1.2.1 Helium-water, hole size 25 mm, H01, H02, H03

The most obvious difference to the nitrogen-water experiments D07, D15, and D04 is the much shorter blowdown time with helium (Fig. 5.46 – 5.57). On the other hand, the blow-through times, that is the duration of the single phase liquid flow, and the duration of the two-phase flow stages are almost identical for the corresponding tests. The reason for the shorter blow down times is the higher sound velocity of helium by approximately a factor of three compared to nitrogen (s. Table 4.2).

5.1.2.2 Helium-water, hole size 50 mm, H04

This experiment (Fig. 5.58 -5.61) should be compared to the nitrogen-water test D06 (Fig. 5.26 -5.29). As for the 25-mm-hole size the blow down time with helium is shorter and the blow through time is similar. The pressures in the cavity are higher than with nitrogen.

5.1.2.3 Helium-water, hole size 15 mm, H05

This experiment (Fig. 5.62-5.65) should be compared to the nitrogen-water test D11 (Fig. 5.4–5.6). As for the other helium tests the blow down time is shorter and the blow through time is similar.

5.1.2.4 Helium-water, hole size 100 mm, H06

This experiment (Fig. 5.66-5.69) should be compared to the nitrogen-water test D08 (Fig. 5.38-5.41). As for the other helium tests the blow down time is shorter. The pressures in the cavity are almost identical to those in D08.

5.1.3 Nitrogen-metal

The experiments were performed with liquid metal (Bismuth-alloy, density 9 times higher than water, dynamic viscosity approximately 60% higher than water, surface tension approximately 5 times that of water, (see table 4.2) and nitrogen. The volume of liquid metal used was similar as in the water tests, scaling to 20 m^3 or approximately 160 t of corium.

Because of the high density, the liquid metal is blown out of the RPV at low velocities. The velocities of the liquid at the hole were between 10 and 14 m/s, while for water they were be-

tween 30 and 46 m/s, at the two initial pressures (s. Table 4.4). Accordingly, the blowthrough occurred later. Additionally to the longer discharge time of liquid metal, the height of the liquid pool in the lower head at which gas blowthrough occurs is lower because it is a function of the Froude number (Eq. 4.12). Consequently, the period of single-phase liquid flow is much longer (by a factor of approximately 10) for liquid metal than for water (Figs. 5.70, 5,74, 5.77, 5.81).

The vessel pressure decreases more slowly compared to the water tests and thereby the gas velocities in the annular gap between vessel and cavity wall are lower with metal than with water (Figs. 5.164 and 5.165). This is especially true for the large 50 mm holes. Here the velocity of the two-phase jet is much lower than with water. During the two-phase flow stage the velocity increases up to a maximum when single-phase gas flow sets in. The maximum is determined by the choked flow conditions at the hole, i.e. the velocity of sound and the density of the gas, and the pressure in the cavity. The pressure in the cavity is increased, because the flow cross section at the RPV-support is constricted and the flow has to take a 90–degree turn to enter the compartments.

With pictures taken by the high speed camera from the cavity and the compartments we can try to characterize the blow down process, that shows the three distinct stages, and compare water and liquid metal behavior (Fig. 5.203 through 5.205). In the first stage, the single-phase liquid flow is driven by the static pressure in the vessel with the liquid velocity u_L. The jet impacts on the cavity floor, spreads on the floor and is diverted upwards at the cavity corner (Fig. 5.203). The liquid moves up the cavity walls by its inertia and can reach the compartments before any gas has left the vessel (Fig. 5.204). Because of the higher surface tension of liquid metal a uniform liquid film on the cavity wall is formed, while with water the film is fragmented and rough. During the second stage, the two-phase flow, the liquid is accelerated by the gas, within the jet as a dispersed droplet flow and in the cavity by shear force along the liquid film. This stage is important in the reactor case, because the thermal and chemical interaction between steam and melt is high due to the large liquid surface area. Liquid is easily carried out of the pit during this stage, especially near its end when the velocity is high. The third stage is characterized by high gas velocities in the reactor pit, and if the mass flow rate of the gas is high enough large fractions of the liquid will be carried into the compartments. The entrainment of liquid droplets in the cavity is smaller for liquid metal due to the higher density and the higher surface tension.

The flow into the compartments near the nozzles is shown in Fig.5.209. Generally two different liquid flow structures occur. In one extreme the liquid flows in a stream through the nozzle into the compartments. On the other end there is a dispersed droplet flow. In most cases these two flow types occur in one test at different times, but mixed flow forms also occur. The parameters determining the flow type are the hole size, the pressure and the type of liquid used. With small hole sizes and low pressures liquid enters the compartments only as a stream. With any of the two parameters increasing, the gas velocity increases as well and generates a droplet flow. This starts usually near the end of the two-phase outflow, when the velocity reaches its maximum. The higher the gas velocity in the tests becomes, the smaller are the droplets. At the end of the blowdown liquid flows into the compartments as a rivulet again. With the largest holes or high pressure there is only the dispersed flow during the whole blow-down. With metal as liquid, the droplets are larger compared to water tests with the same hole size and same initial pressure.

Series of pictures showing the flow in the cavity and the compartment for a 25- mm-hole and a 50-mm-hole can further give insight in the flow processes (Figs.5.206 through 5.209). In both cases the maximum liquid flow into the compartments occurs during the single-phase gas blow down. No or only little liquid can be seen on the cavity walls during that period. Thus, the liquid entering the compartments must be liquid that was already near the RPV support. One part of that liquid is blown into the compartments, one part flows back into the lower cavity and some is trapped at the support.

5.2 Effect of pool depth, T01 / D18, T02 / D19

To investigate the effect of different initial liquid pool depths or the effect of the early blow through, the standard amount of liquid (3400 cm³) was filled into a standpipe (Fig.2.4) in tests T01 and T02. Thereby we get only two distinct stages of blow down, first the liquid jet and than the gas jet, practically without a stage of a two-phase jet in between. The two experiments should be compared with tests D18 and D19 (or D06 and D07). In the pressure curve of the vessel pressure in test D18 the early blow through (at t = 0.025 s) and the long lasting two-phase flow stage can be seen, with the almost linear pressure drop up to t = 0.3 s (Fig. 5.85 and Fig. 5.101). In test T01, on the other hand (Fig. 5.93), there is little pressure drop up to t = 0.08 s, but from that time on the pressure curve has the form that is typical for single phase gas blow down. In the tests with the smaller hole, D19 and T02 (Fig. 5.89, 5.97 and 5.102), blow through times are 0.105 s and 0.245 s, respectively, and in T02 the single phase gas flow starts immediately after that, while in D19 a long period of two-phase flow follows, up to about t = 0.6 s. The total duration of the blow down is about 20% shorter for the tests with the water in the standpipe. The maximum gas velocity in the annular space is about 40% higher in test T01 (50-mm-hole) than in D18 or D06 (Fig. 5.162). In the tests with the 25-mm-hole the maximum velocities are the same in both cases, but the duration of the high velocity is longer in the test T02 with the water in standpipe (Fig.5.160). For both hole sizes the dispersed liquid fractions are higher in the tests with the water initially in the standpipe, about 12% for the 50-mm-hole and 8% for the 25-mm-hole (s. Table 4.2). This is probably due to the higher gas velocity, respectively the longer lasting maximum velocity in the second case. Code calculations have produced similar results [17].

5.3 Effect of melt mass, D17 / D07, D20 / D04

The effect of different melt masses was investigated for the nitrogen/water combination with 25-mm-holes at two pressures, 0.6 and 1.1 MPa. The water mass was reduced from 3400 cm³ to 1800 cm³ in tests D17 and D20. The mass fractions ejected into the compartments were reduced, from 70% to 55% in the 1.1 MPa tests (D04/D20) and from 52% to 41% in the 0.6 MPa tests (D07/D17) (s. Table 4.2). The ratio of the total masses was m_{07}/m_{17} = 1.89 (3400/1800) and the ratio of the masses ejected into the compartments was m_{d07}/m_{d17} = 2.4 for both pressures. This fact enables us to interpolate the dispersed melt fractions for intermediate values of pressures and masses. Naturally, due to the smaller liquid mass, the duration of the single-phase liquid flow is shorter than with the higher mass (compare figures 5.101 and 5.14).

5.4 Effect of lateral breaches

5.4.1 Lateral Holes, R03, R04, R05, R06

When the breaches are not at the center but on the side of the lower head, only part of the liquid blocks the flow cross section, depending on the liquid inventory and the vertical position of the upper and lower edges of the holes. In all tests with lateral holes the liquid volume was 1800 cm³, the liquid level being 67 mm above the bottom of the calotte and near the upper edge of the holes. With the 25-mm-hole the level was 8.2 mm above the upper edge and with the 50-mm-hole it was 0.6 mm below the edge (s. Figs. 2.8 and 2.9).

In these experiments we do not have the pressure signal P6 as an indicator of the different phases of the blowdown, especially for the determination of the blowthrough time. From the vessel pressure curves (Fig.5.110, 5.113, 5.116) and the gas velocity curves (Fig. 5.167 and 5.168) we can deduce that the blowthrough occurs very early (approximately at $t \leq 0.1$ s). In Fig. 5.116 and Fig. 5.117 we see that the theoretical pressure curves for single phase gas flow are steeper than the experimental ones for test R03 and R04 at early times. Therefore we can assume that the flow through the hole is two-phase even at times later than t = 0.1 s, however, with a lower liquid fraction than in test D05, where we have an almost linear pressure decrease up to t = 0.3 s.

Figs. 5.210 and 5.211 show the pictures of the flow in the cavity. The main direction of the flow is not vertical as with the central holes but in an angle of approximately 45 degree. Therefore, the velocities in the annular space determined from the measured pressures deviate more from the actual ones.

The ejected liquid was found mainly in the compartments opposite to the position of the hole. Not all of the liquid was ejected out of the RPV (s. Table 4.3). The main parameter determining the fraction that remains in the lower head is of course the vertical position of the lower edge of the hole. It is, however, interesting to see how much lower than this edge the water level is after the test. This number is a measure for the magnitude of the entrainment. Table 5.1 lists the data for the lower edge, the liquid level and the difference between the two. Although there is less water left in the calotte in R04 with the larger hole than in R03 with the small hole, the entrainment was somewhat smaller in R04. There are two effects reducing the entrainment. With the large hole the blowdown time is shorter, and because the water level is already lower the surface area is smaller. The entrainment in test R05 is much smaller with the high density liquid metal than with water. The fractions ejected into the compartments are smaller than in the experiments with central holes (D04 and D05). Due to the smaller total mass we could expect a somewhat lower dispersed mass fraction (compare D07 with D17), but the differences between R03 and D04, and between R04 and D05 are much larger. Even if the dispersed fraction is determined in relation to the mass that was ejected out of the RPV, the difference is still in the order of 0.3 (f_d^* in table 5.1). In the tests D04 and D05 practically no liquid remained on the cavity bottom while in R03 and R04 approximately 30% of the ejected water was found there.

The test R05 with liquid metal can be compared with test M01. In test M01 with the central hole the metal mass fraction ejected into the compartments was 36%, and 21% was captured

at the RPV support. With the lateral hole practically no metal was found in the compartments and at the RPV support.

5.4.2 Slots, R01, R02

Two tests with a small horizontal slot were performed (for geometrical data see chapter 2.3). The only difference between test R02 (slot) and R03 (round hole) is the shape and the vertical position of the opening in the lower head. The flow cross section of the slot is equivalent to a 25-mm-hole.

The vessel pressure curves of the slot and the hole tests are almost identical (Fig. 5.110 and 5.113) and therefore the gas velocities are the same also (Fig. 5.167).

Due to the higher location of the lower edge of the slot more water remains in the calotte. The difference between post test water level and lower edge, however, is larger, and therefore the entrained amount of water. The reasons could be the larger surface area of the water pool in the calotte at this higher position, and the wider flow cross section of the slot versus a round hole. The dispersed liquid fraction is smaller with the slot. In relation to the total amount of water ejected out of the RPV, it is 34% for the slot and 40% for the hole (Table 5.1). The dispersed fraction at lower pressure (R01) is small with less than 5%. The correlation to the burst pressure is similar as that for small central holes (Fig.4.16). At lower pressure more water remains in the lower head, because the entrainment is smaller at lower gas velocity, lower density and shorter blowdown time.

5.4.3 Unzipping of lower head, K01, K02, K03

To model the horizontal rip propagating around the circumference of the lower head, the calotte was a separate part that was held in position by a steel rod from below at its center. When it was released the lower head moved down on one side and was held by a hinge on the opposite side. It was stopped by crushing material on the four pedestals (Fig.2.9). Two different heights of pedestals were used to obtain different flow cross sections. The maximum drop height was h = 56 mm in K01, and h = 16 mm in K02 and K03. The drop height at the side of the hinge was not zero but varied between 0.5 mm and 2 mm. The total cross section for test K01 was 220 cm², for K02 and K03 it was approximately 70 cm³. For comparison, the cross section of the 100-mm-hole is 79 cm² and for the 50-mm-hole it is 20 cm².

Corresponding to the large flow cross section with the high drop height of the calotte in test K01, the time for depressurization is extremely short with 0.08 seconds (Fig. 5.124). The other two tests, K02 and K03, with a drop height of 16 mm show a similar blowdown curve as tests D08 and D09, with the 100-mm-hole (compare figures 5.128 and 5.132 with figures 5.38 and 5.42). This time the pressure gauges in the vessel show distinct differences. The gauge P4 near the lower head is the first to respond, then P2 and P1 indicate the depressurization wave traveling upwards with the speed of sound ($a = (\kappa RT)^{1/2}$, a = 383 m/s, T = 353 K). The pressure P1 remains above the other pressures up to t = 0.4 s. The same effect was observed in the tests with the 100-mm-hole. The maximum values of the cavity pressures in test K01 are comparable with those of test D08. However, the pressures of the tests K02 and K03 in the cavity and in the subcompartments are lower than those in tests D08 and D09, respectively

(compare figures 5.126 and 5.130 with figures 5.39 and 5.43). Regarding the similar blowdown curves, this is peculiar.

As for the lateral holes and slots liquid remains in the lower head after the blowdown (Tab. 5.1). The amount of liquid depends on the tilt angle of the calotte, that is higher for K01 than for the other two experiments, and on the entrainment. For test K02 compared to K01 the entrainment is larger, and therefore the liquid level below the lowest edge of the tilted calotte is lower, because of the higher pressure and the larger surface area of the remaining water. With liquid metal (K03) the entrainment is much less due to its high density.

The liquid fraction dispersed out of the cavity is very small for test K01, with f_d = 0.011. With the central 100-mm-hole at an even lower pressure it was f_d = 0.580 (D14). The large break cross section does not lead to high dispersion rates, because the gas does not accelerate the liquid with the lateral break and the entrainment is small because of the extremely short blow down time. With a smaller drop height (smaller flow cross section) and a somewhat higher burst pressure of 0.8 MPa in test K02 the reduced dispersed fraction is higher (f_d^* = 0.277), but still less than half of that of central holes with similar cross section (D08, f_d = =0.717). Because the entrainment process plays the major role in the case of lateral breaches, the dispersed fraction with metal is very small (K03), even at the higher pressure of 1.1 MPa.

5.5 Effect of geometry changes

All parameter variations discussed up to now were related to the conditions of and in the RPV. In this section we will describe the effect of geometry variations in the reactor pit.

5.5.1 Changes at RPV-support, D06 / D18, D07 / D19, D17/D21

As described in chapter 2.1, the constriction at the RPV support below the main cooling lines was modeled by a conical ring that contained 16 holes (s. Fig.2.2). Behind that ring liquid collected and could not flow back into the pit. In the first test with liquid metal the metal solidified in that space and it was difficult to remove. Therefore, this space was filled with silicon rubber up to the lower edge of the holes in all subsequent tests. Thereby less liquid mass was collected behind the conical ring. To study the effect of this modification tests D18 and D19 were performed to be compared with D06 and D07. There was no effect on the mass fraction ejected into the compartments, the differences were –0.7% and +1.2%. The only difference was in the distribution of liquid between pit and space behind the ring. With the filling about 10% of the liquid flowed back into the pit.

A second modification relates to the minimum flow cross section at the support girder. The annular cross section between outer RPV wall and the conical ring is 0.0104 m² and the total cross section of the 16 holes in the ring amounts to 0.0085 m². In test D21 these holes were closed, so the minimum flow cross section reduced from 0.0189 m² to 0.0104 m². The effect on the mass fraction ejected into the compartments is small. With the holes closed we get 2.25% less mass in the compartments and practically no difference behind the ring (0.12%). The maximum pressure in the cavity, however, rises by 10 kPa, while in D17 it rises by less than 2 kPa (s. Figs. 5.156 and 5.104).

5.5.2 Venting channel, S01 /D04

The four openings in the lower part of the pit (see. Chapter 2.4, Table 2.1 and Fig. 2.14) had a total flow cross section of approximately ¼ of the minimum flow cross section below the RPV support girder. The four holes with the diameter of 38 mm take up 14% of the circumference of the pit. One test (S01) with a initial pressure of 1.1 MPa and a central hole of 25 mm diameter was performed, similar as test D04. No liquid was found in the melt spreading room and only 1.3 % of the liquid was in the circumferential venting channel after the test. The other results are listed in table 4.3. The slightly higher fraction (71.3 versus 69.8 %) of liquid in the compartments compared with test D04 is within the range of reproducibility of the tests. The pressure curves shown in Figs. 5.137 through 5.139 are similar to those of D04. The time of blow through is somewhat later, maybe due to the lower initial pressure (9% less than in D04).

5.5.3 Wider cavity (larger annular flow cross section), F03 / D04

The diameter of the cavity was changed from 342 mm to 386 mm for test F03 (see Fig. 2.9, without the dispersion preventing device). In a wider cavity the average gas velocity is lower due to the larger flow cross section. The minimum flow cross section below the nozzles was kept constant. Comparison with tests D04 and S01 shows that the mass fraction ejected into the compartments was reduced from 70% to 63%. The maximum average gas velocity changed from 38 m/s to 17 m/s (Fig. 5.169).

5.5.4 Dispersion trap, F04, F05, F06

In these tests it could be observed, that the cylinder separates the liquid at the cavity wall from the gas. The gas can flow into the compartments, while the liquid is trapped between the cylinder and the cavity wall. However, the liquid falls back into the lower cavity as soon as the top of the gap is reached and can be entrained by the gas, but at lower gas velocities. This reduces the dispersion substantially (s. Table 4.3). With central holes of 25 or 50 mm diameter (1.1 MPa burst pressure) the reduction was from 63 % or 77%, respectively, with a wider cavity without trap, to 28 % with trap for both cases. With a lateral hole of 25 mm diameter (F06, 1.1 MPa) the reduction was from 36% to 10%. The corresponding pressure curves are shown in Figs. 5.140 through 5.154.

Table 5.1 Lateral breaks data on post test water level in the lower head and reduced dispersed fraction f_d^*

Test	diameter or drop height [mm]	liquid	P [MPa]	lower edge	water level	Diff. [mm]	Diff. $f_{entr.}$	f_{RPV}	f_d	f_d^*
R-01	slot 25 equiv.	water	0.6	56	39	17	0.355	0.363	0.029	0.045
R-02	slot 25 equiv.	water	1.1	56	33	23	0.455	0.262	0.250	0.339
R-03	25	water	1.1	41	21	20	0.290	0.111	0.358	0.403
R-04	50	water	1.1	32	14	18	0.200	0.048	0.477	0.501
R-05	25	metal	1.1	41	39	3	0.036	0.336	0.0005	0.0008
K-01	56	water	0.5	-	-	15	0.180	0.095	0.011	0.012
K-02	16	water	0.8	-	-	25	0.410	0.187	0.225	0.277
K-03	16	metal	1.1	-	-	10	0.190	0.413	0.008	0.013

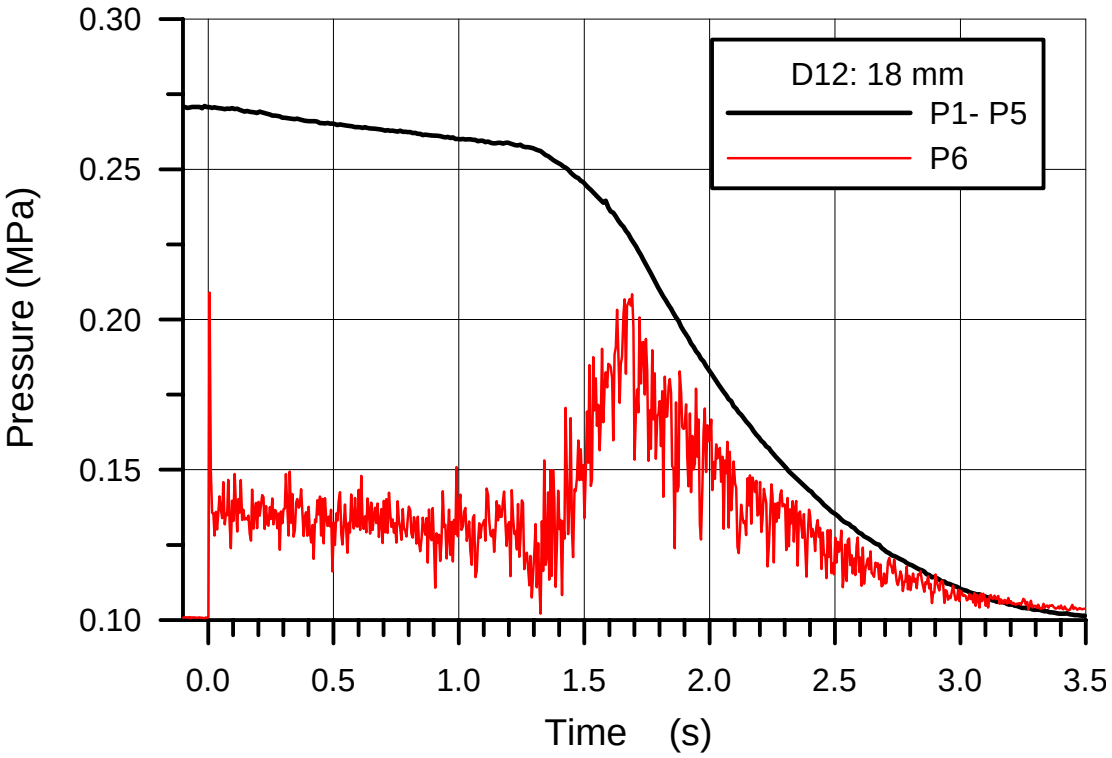

Fig. 5.1 D12 Blow down pressure in the RPV and total pressure on the cavity floor below the hole

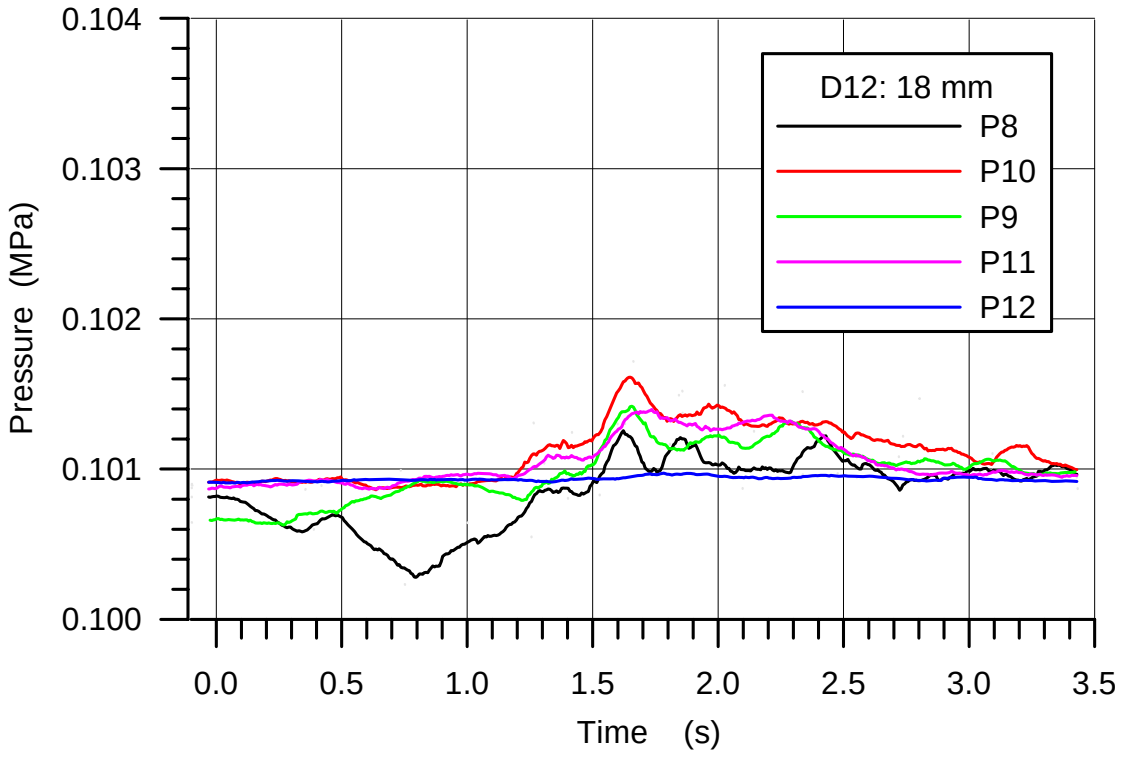

Fig. 5.2 D12 Pressures in the cavity

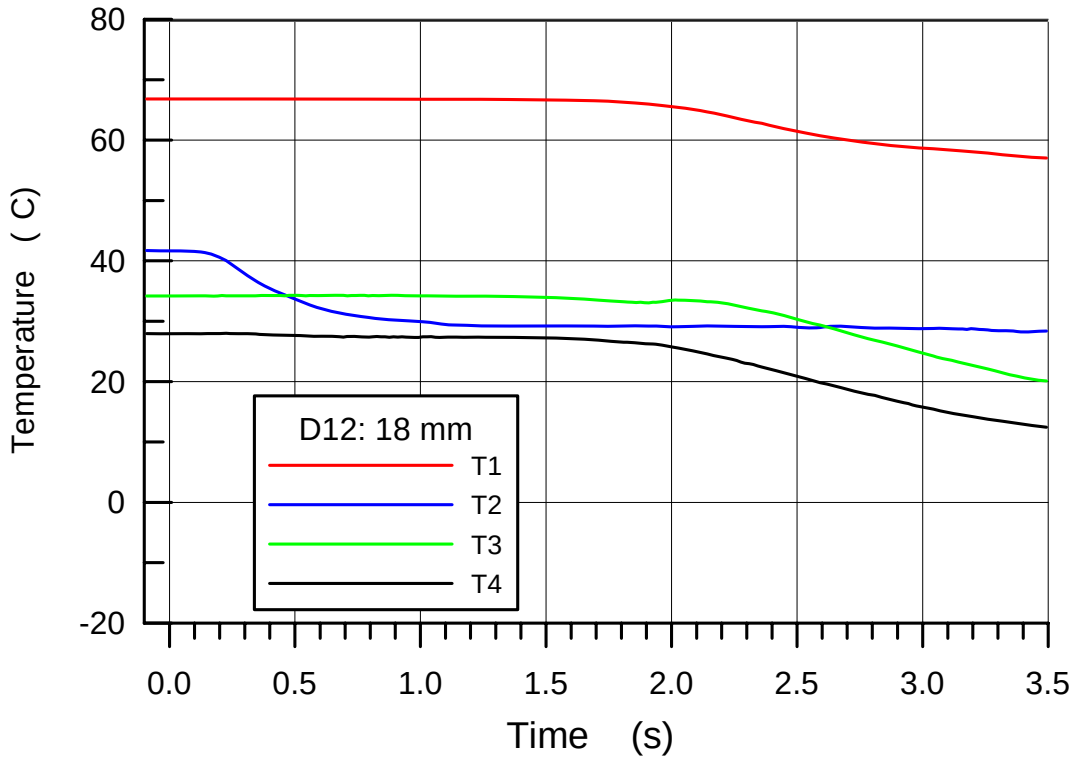

Fig. 5.3 D12 Gas temperatures in the RPV and the cavity

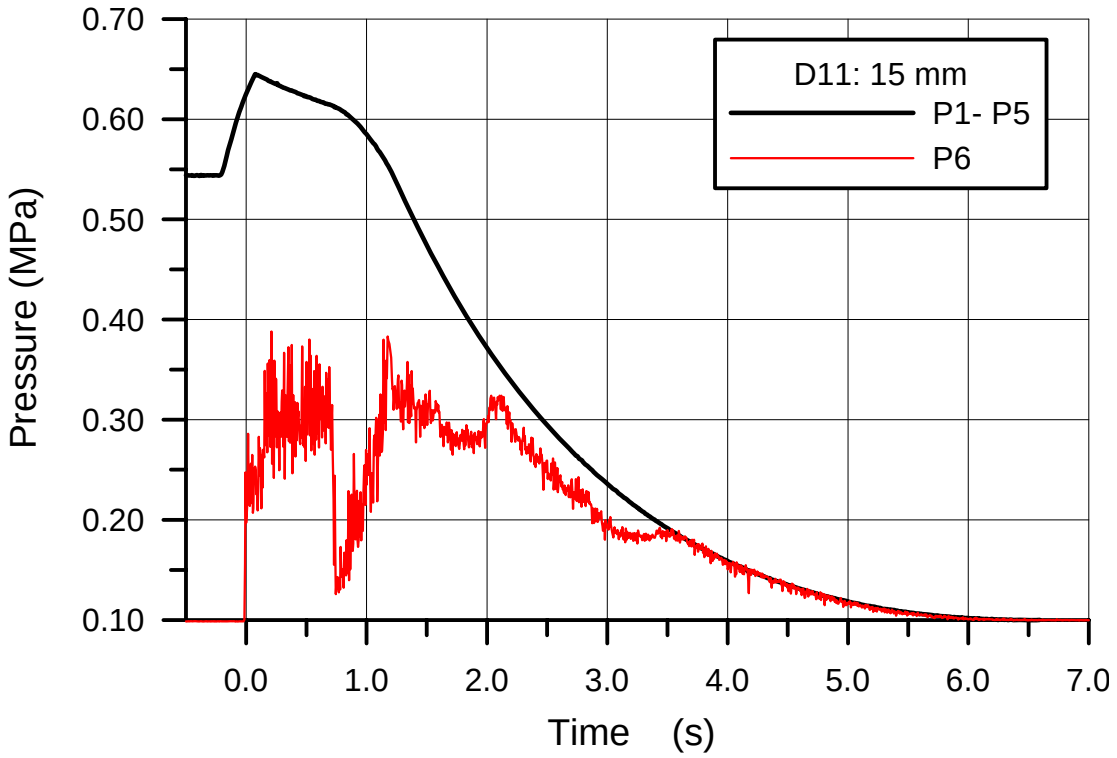

Fig. 5.4 D11 Blow down pressure in the RPV and total pressure on the cavity floor below the hole

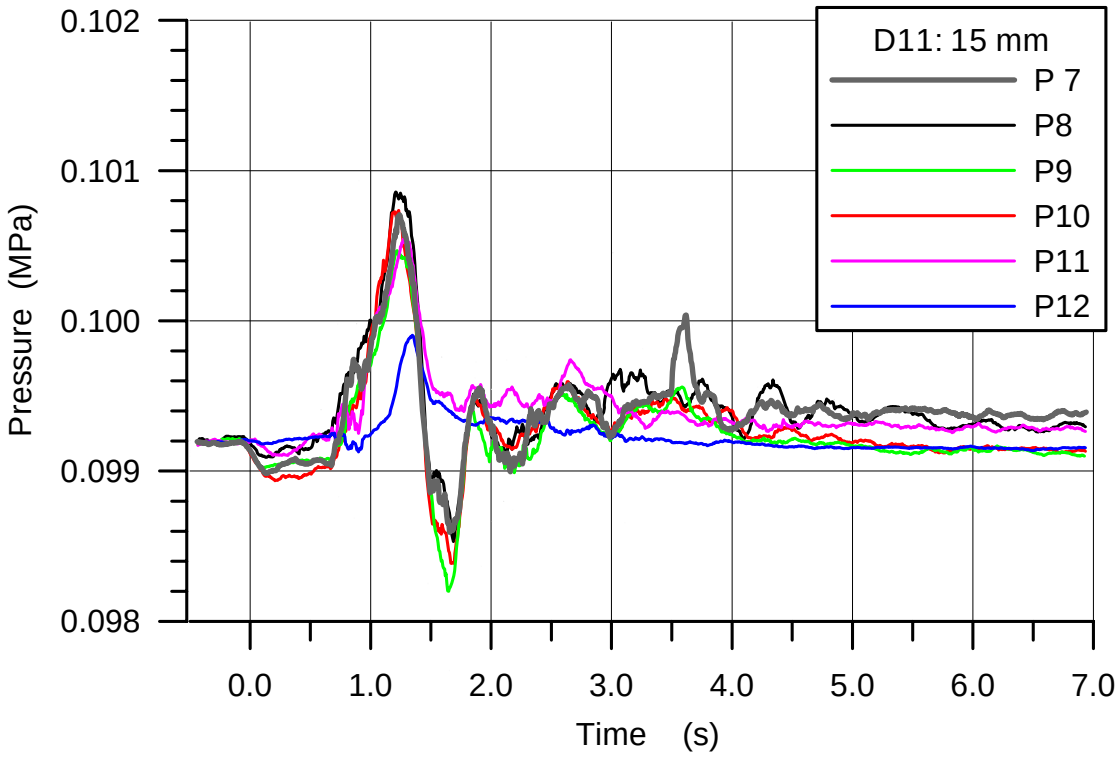

Fig. 5.5 D11 Pressures in the cavity

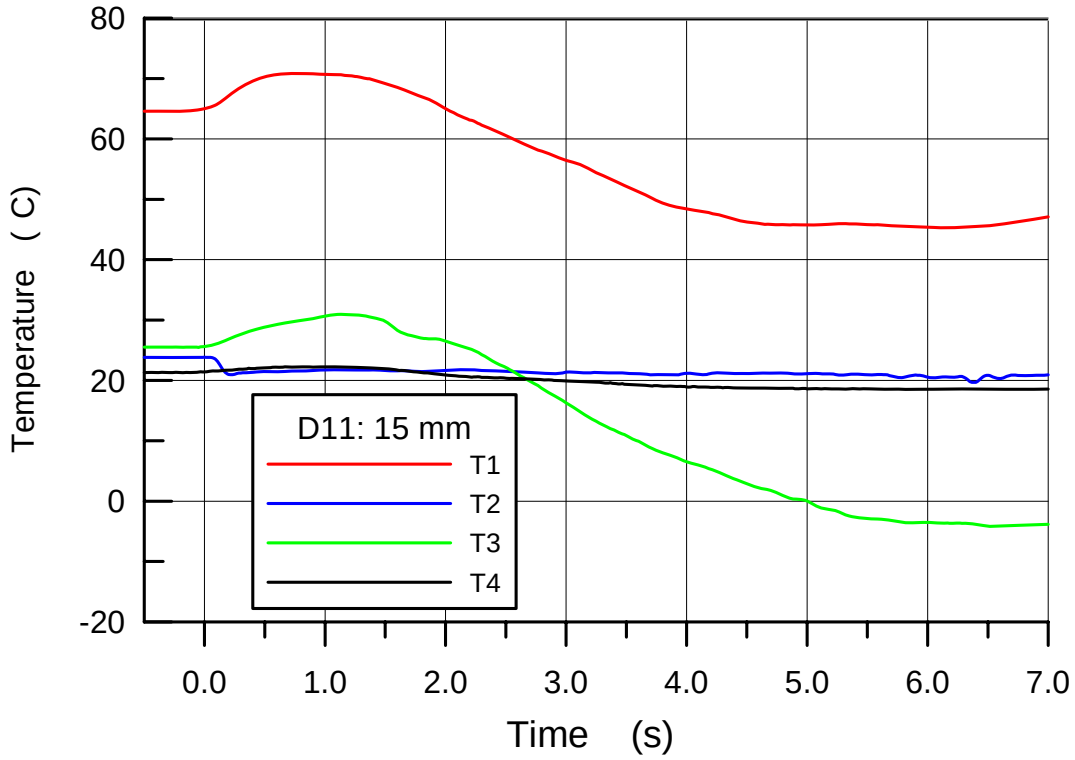

Fig. 5.6 D11 Gas temperatures in the RPV and the cavity

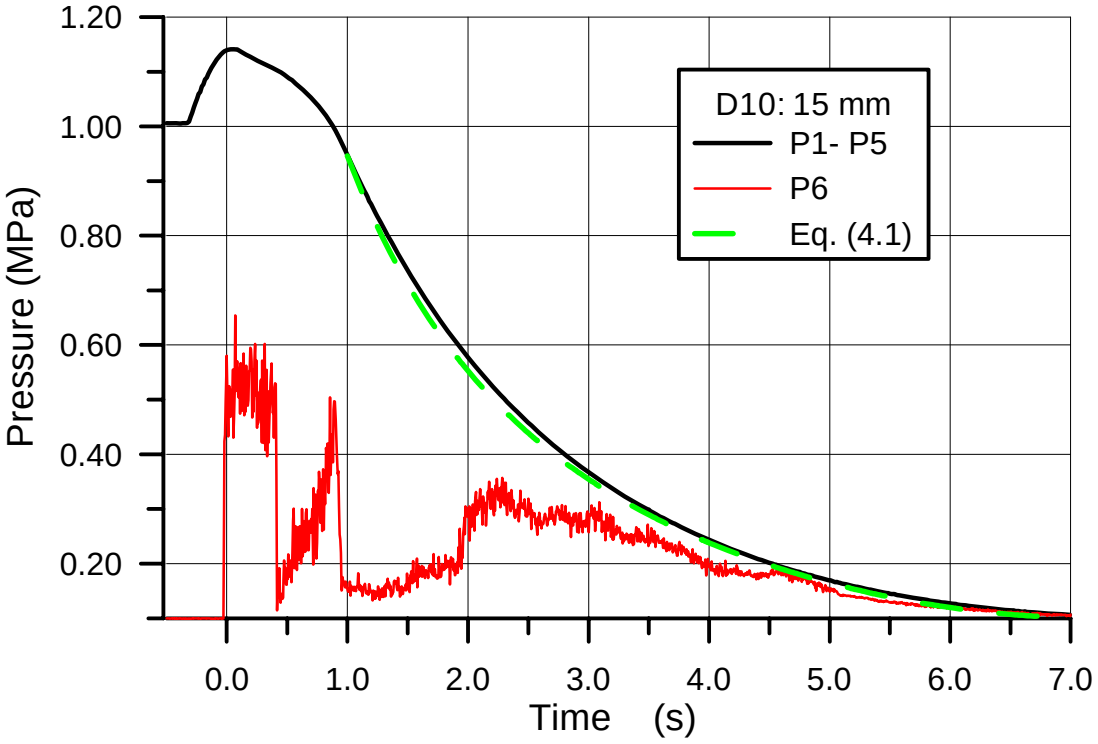

Fig. 5.7 D10 Blow down pressure in the RPV and total pressure on the cavity floor below the hole.
Shown is also the blow-down pressure for a single phase gas blow down calculated with equation 4.1, starting at t = 1.0 s.

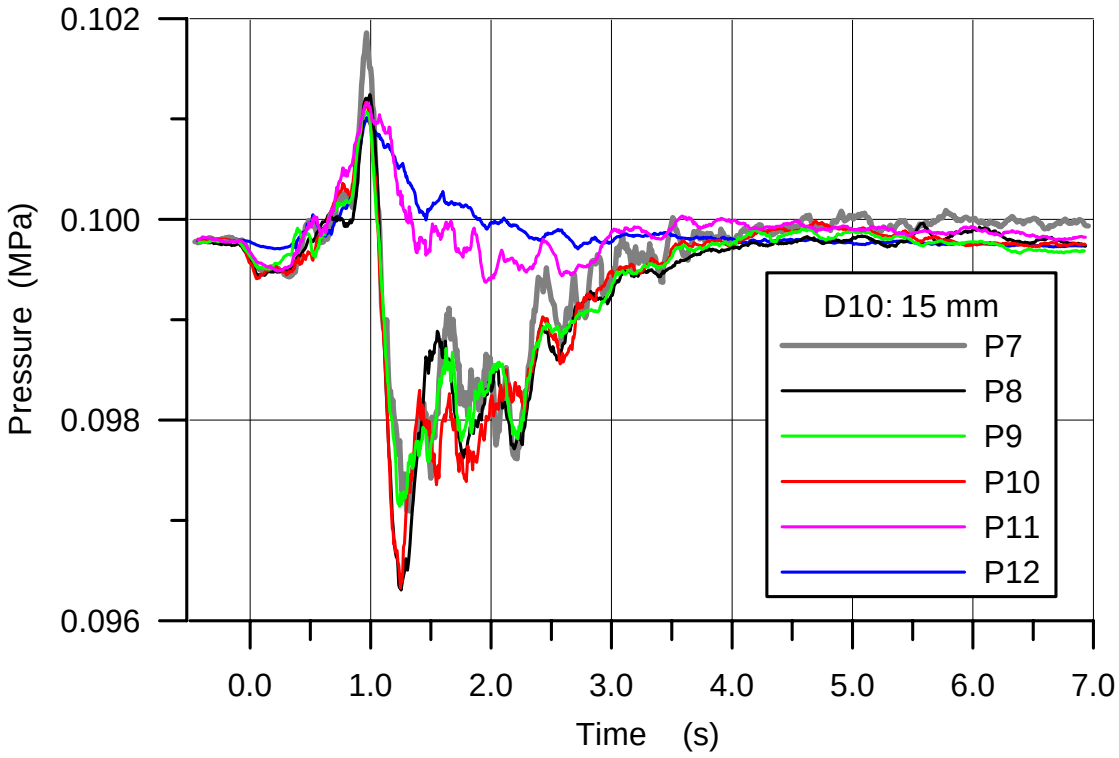

Fig. 5.8 D10 Pressures in the cavity

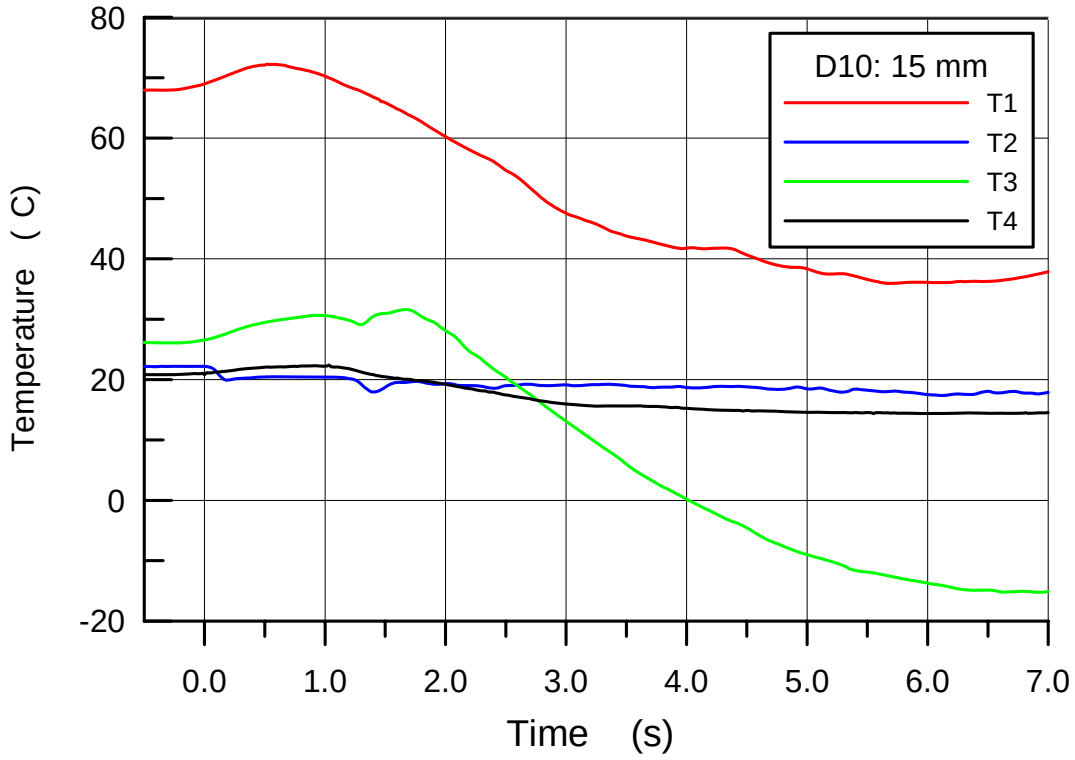

Fig. 5.9 D10 Gas temperatures in the RPV and the cavity

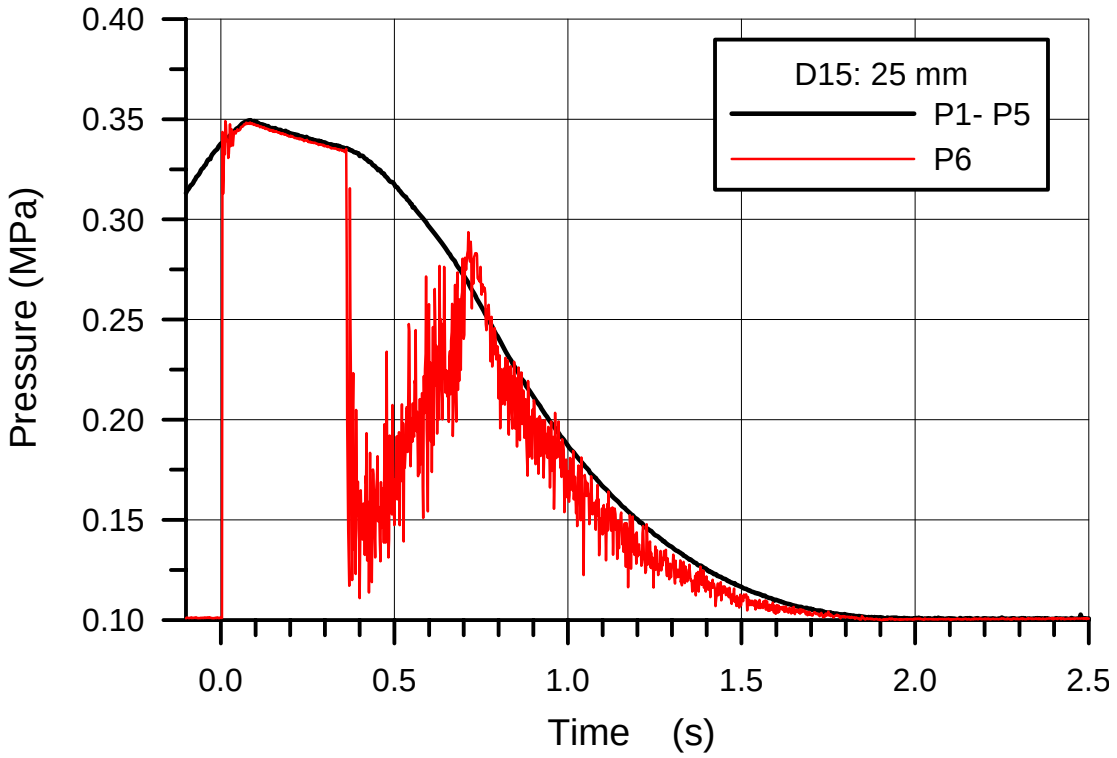

Fig. 5.10 D15 Blow down pressure in the RPV and total pressure on the cavity floor below the hole

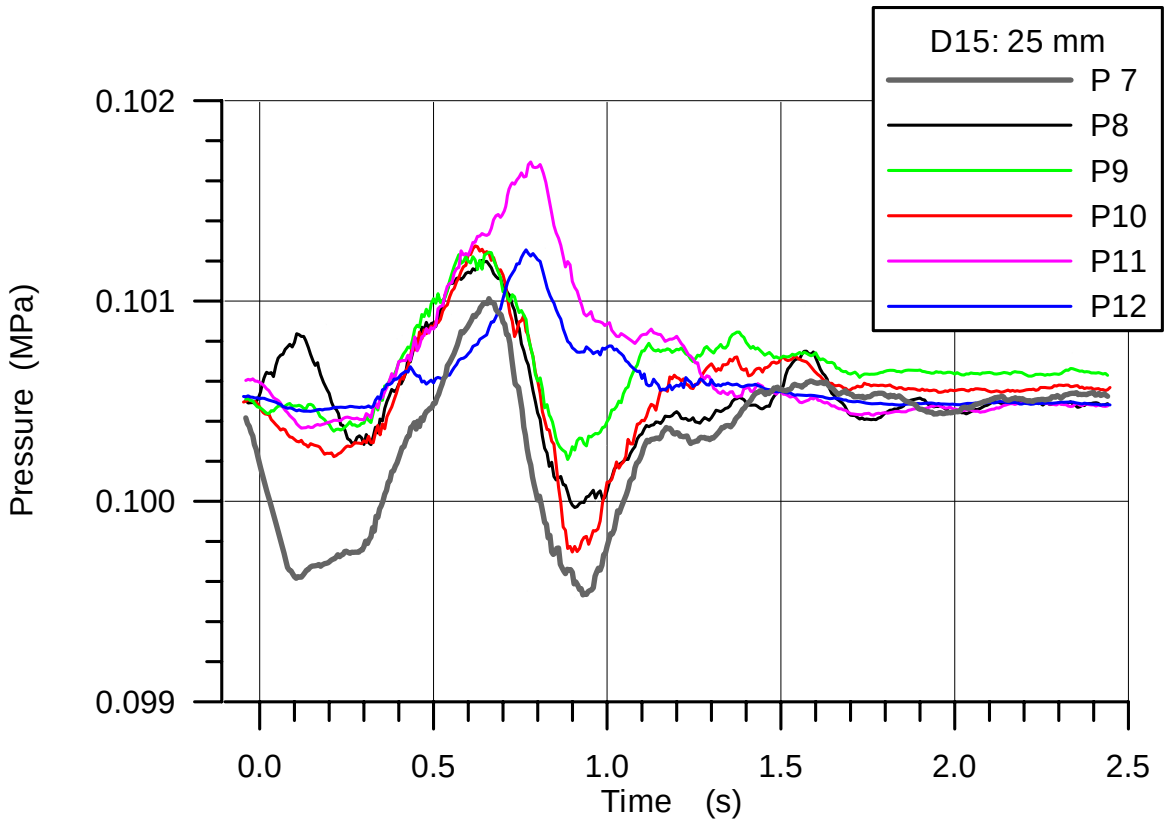

Fig. 5.11 D15 Pressures in the cavity

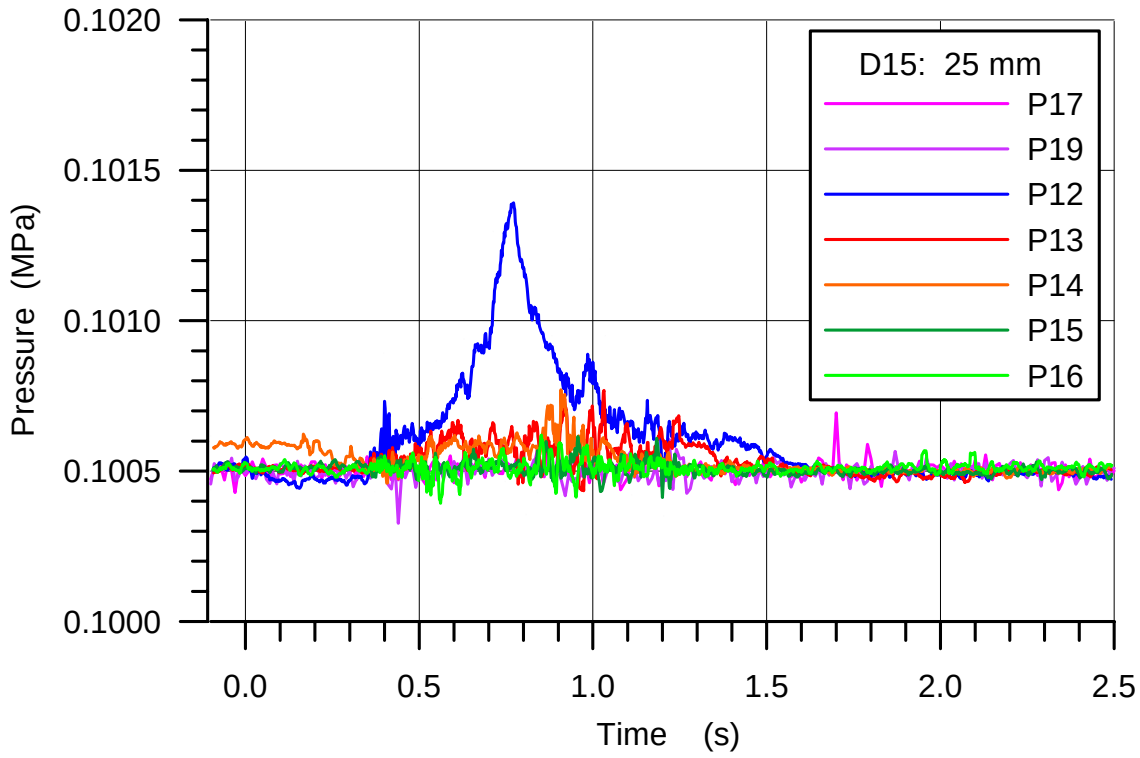

Fig. 5.12 D15 Pressure in the space at the RPV support and in the subcompartments

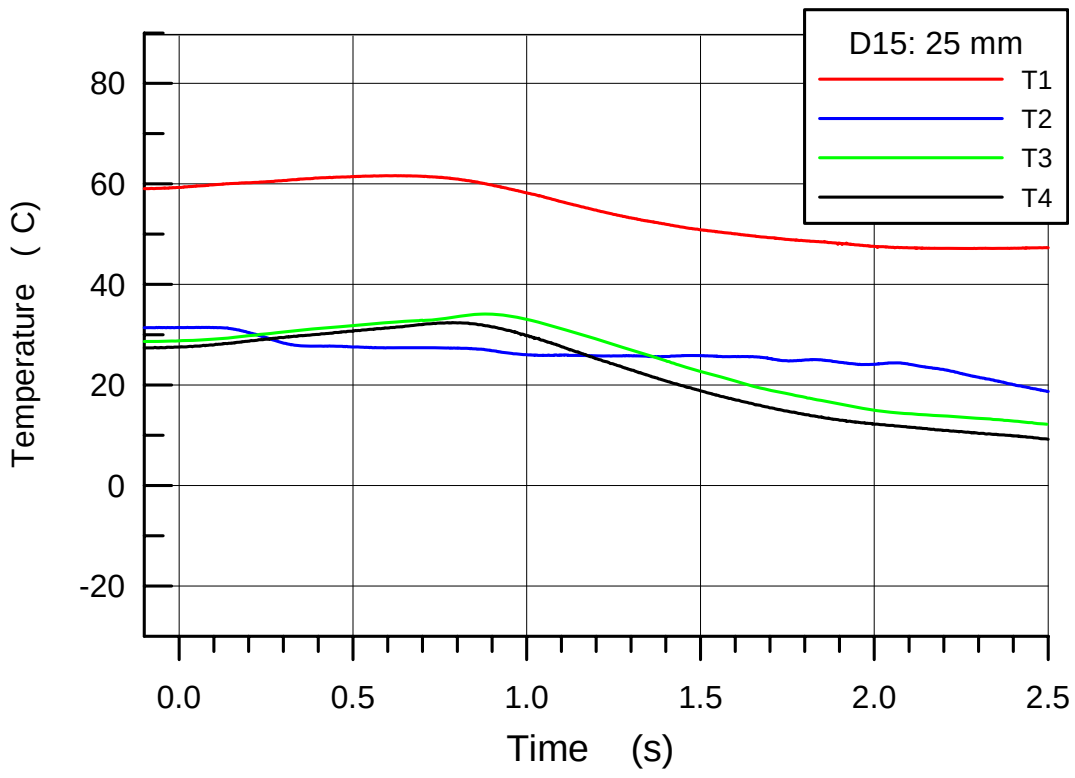

Fig. 5.13 D15 Gas temperatures in the RPV and the cavity

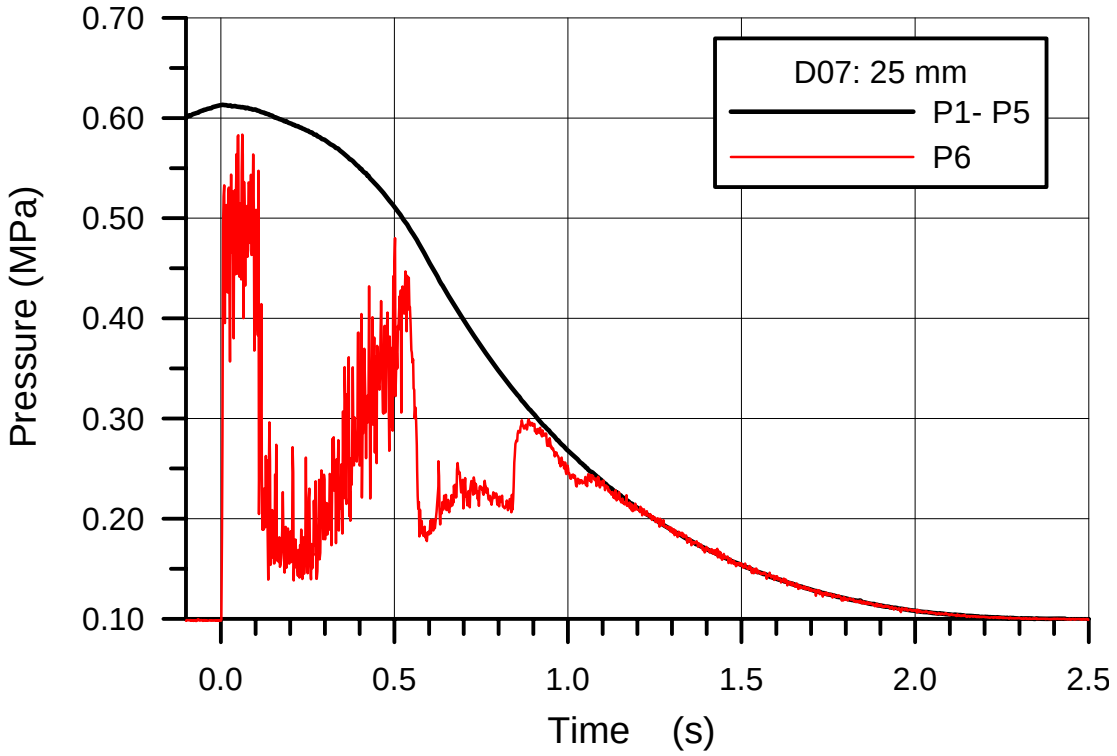

Fig. 5.14 D07 Blow down pressure in the RPV and total pressure on the cavity floor below the hole

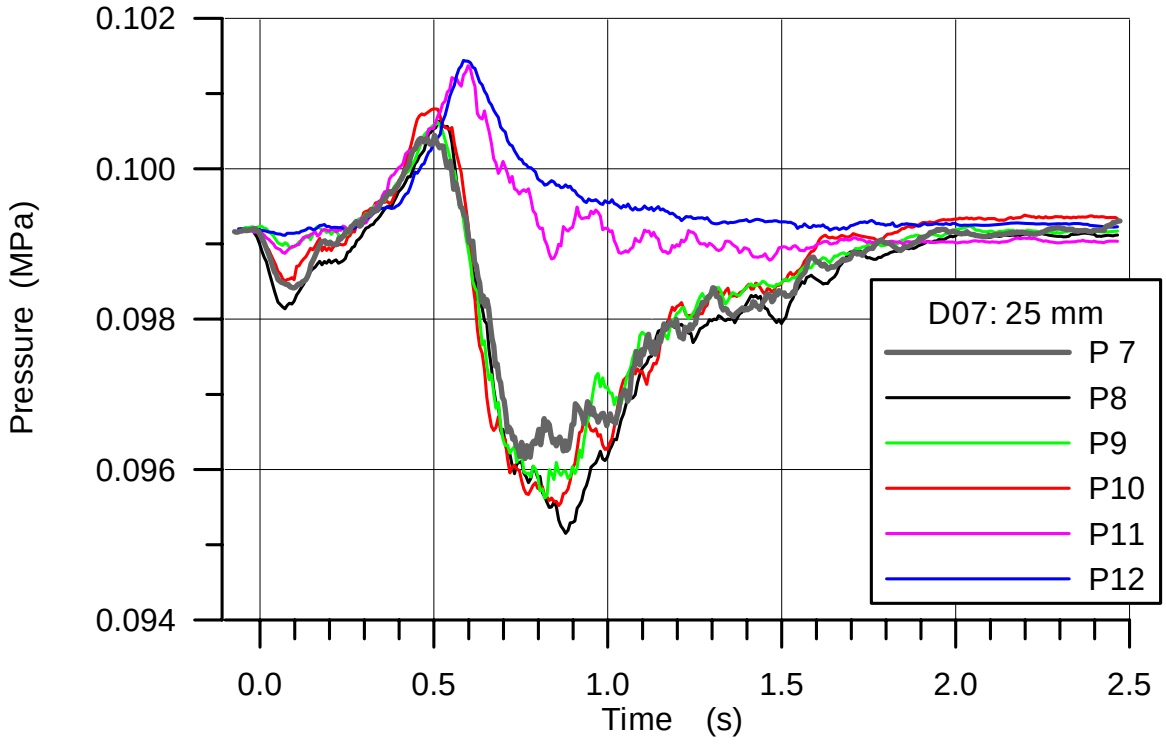

Fig. 5.15 D07 Pressures in the cavity

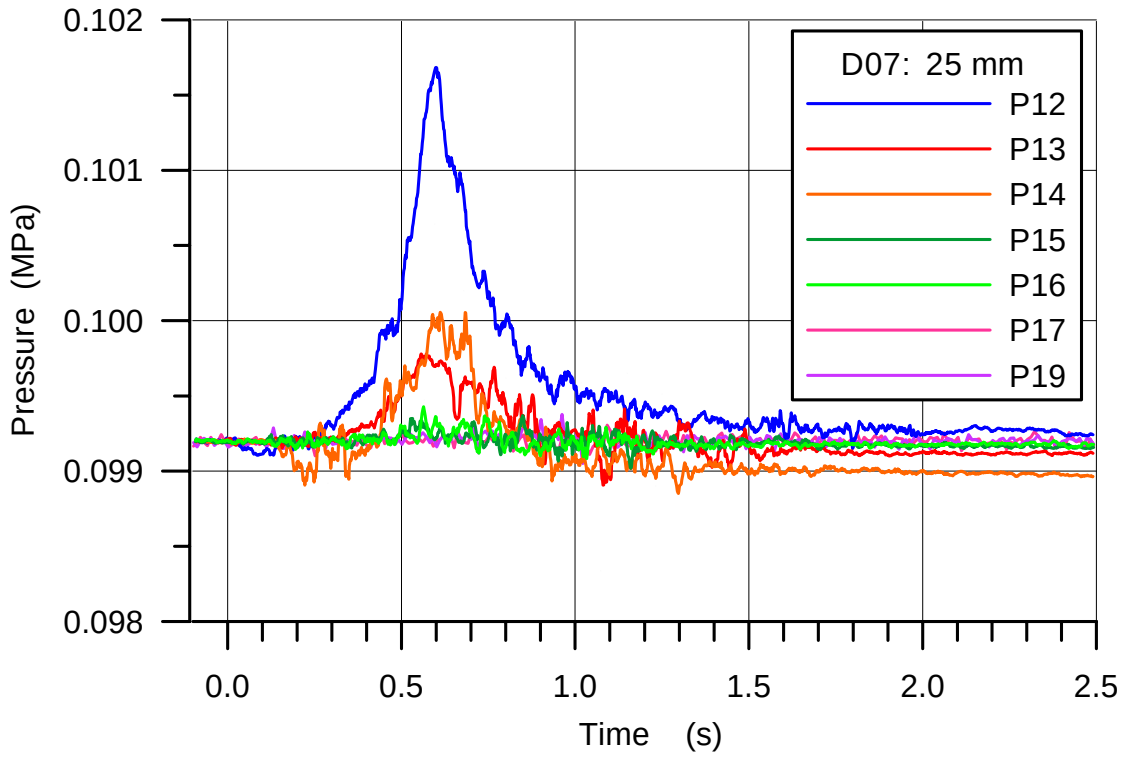

Fig. 5.16 D07 Pressure in the space at the RPV support and in the subcompartments

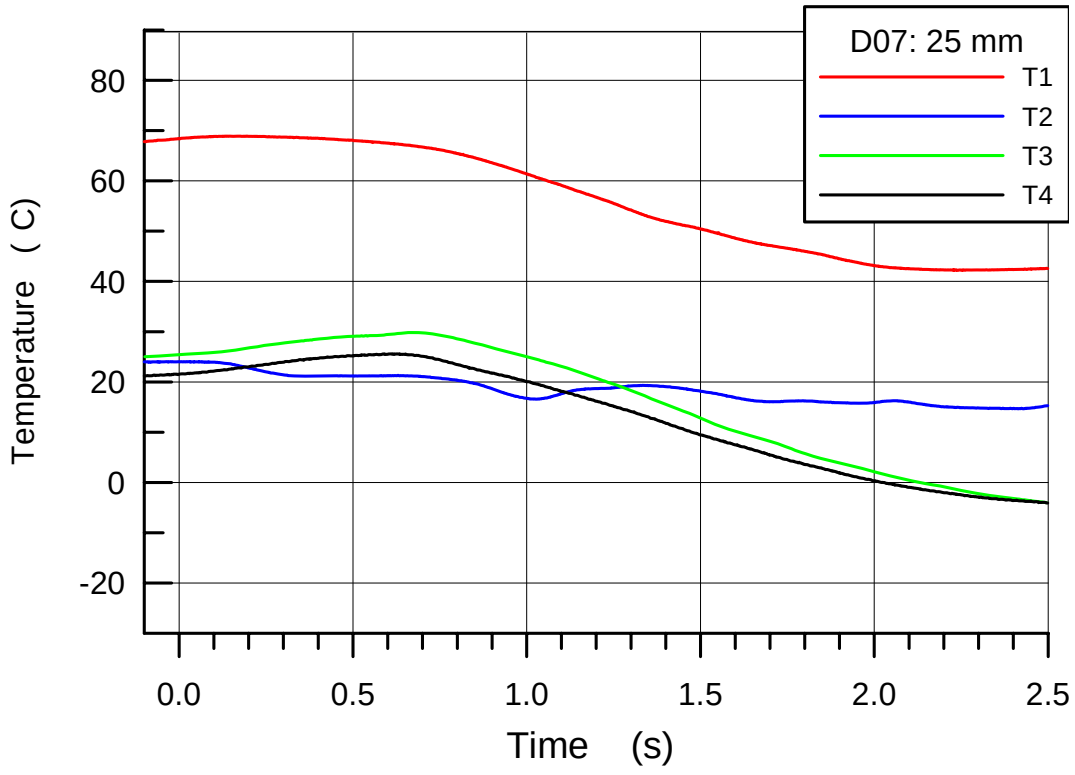

Fig. 5.17 D07 Gas temperatures in the RPV and the cavity

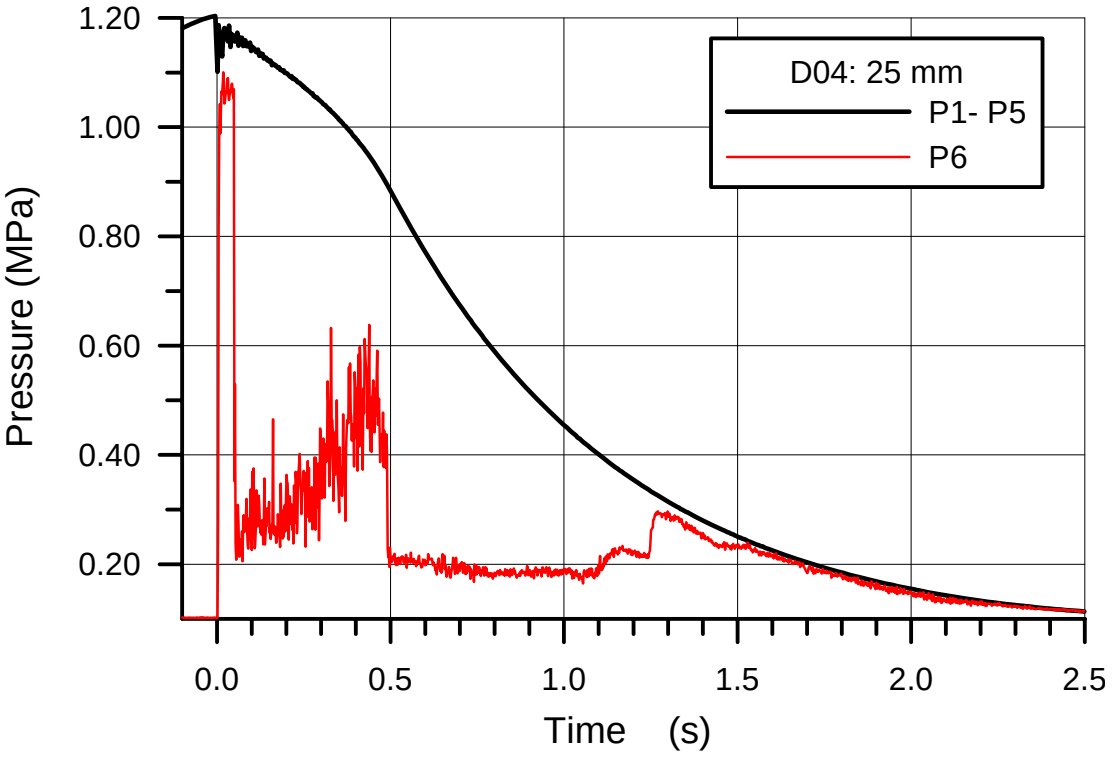

Fig. 5.18 D04 Blow down pressure in the RPV and total pressure on the cavity floor below the hole

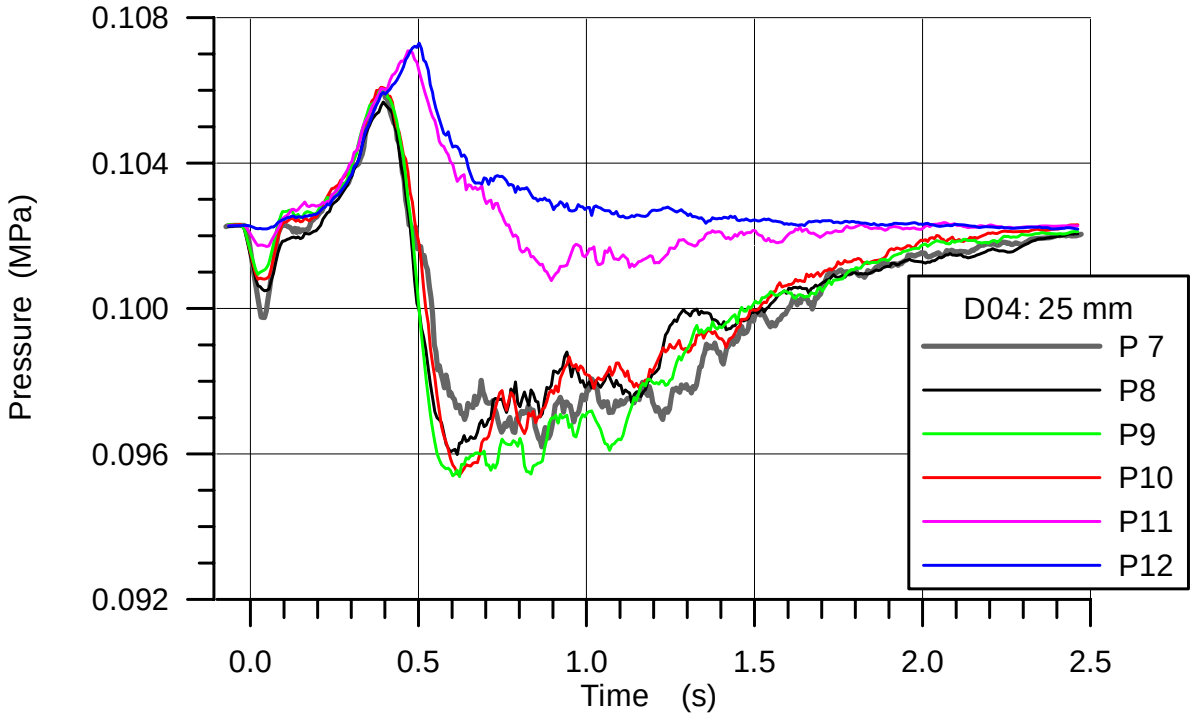

Fig. 5.19 D04 Pressures in the cavity

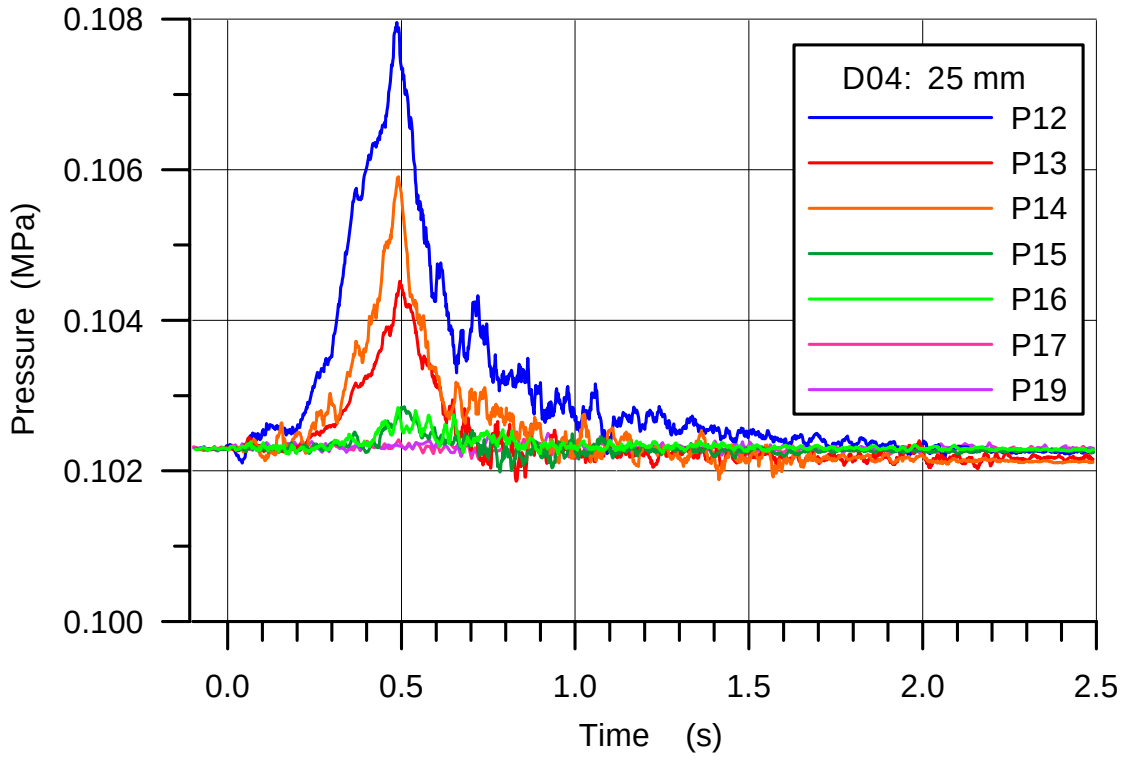

Fig. 5.20 D04 Pressure in the space at the RPV support and in the subcompartments

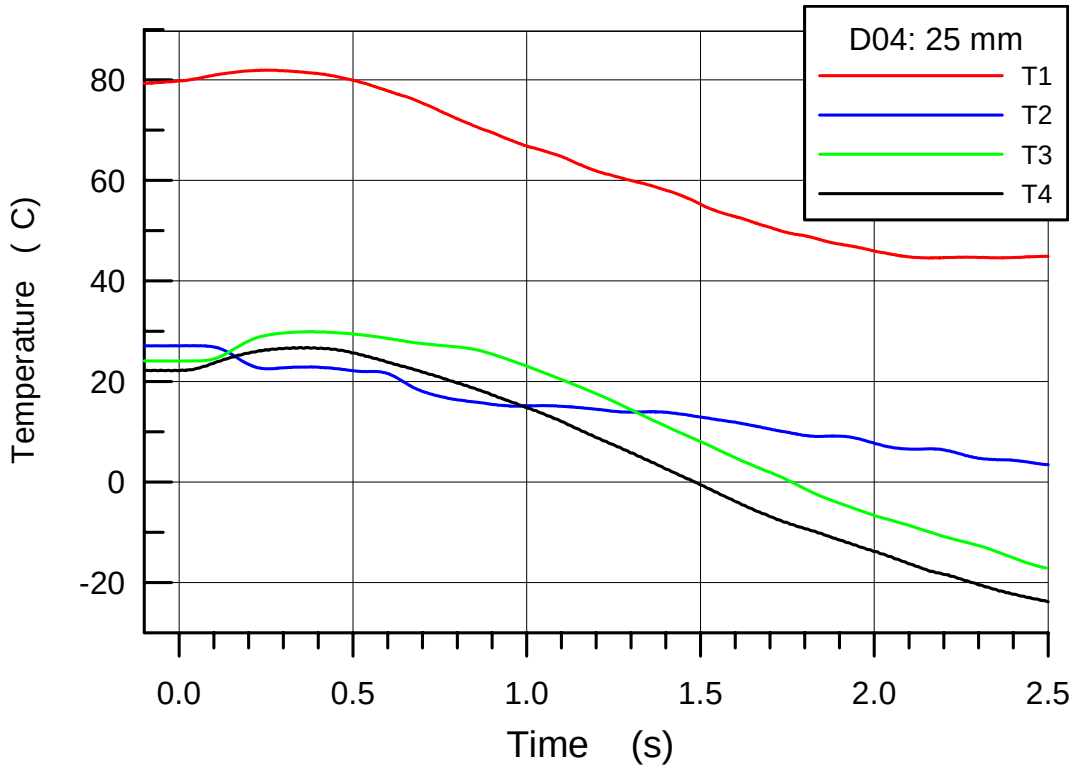

Fig. 5.21 D04 Gas temperatures in the RPV and the cavity

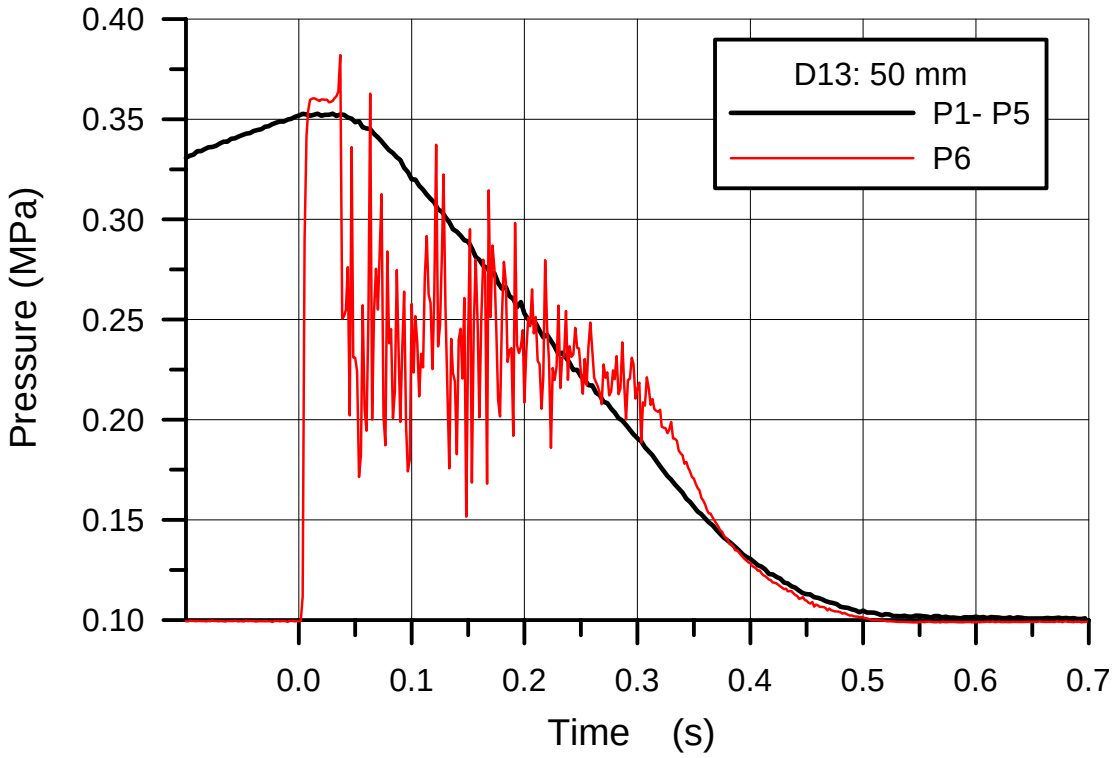

Fig. 5.22 D13 Blow down pressure in the RPV and total pressure on the cavity floor below the hole

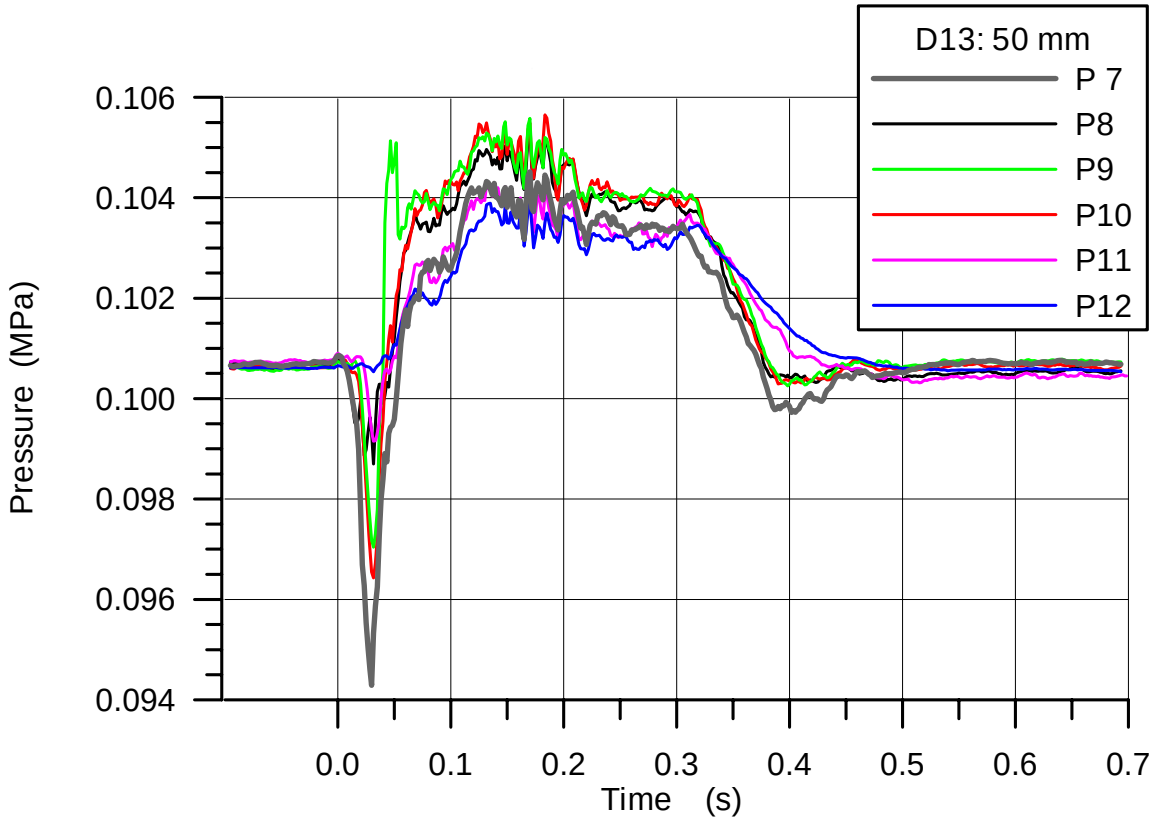

Fig. 5.23 D13 Pressures in the cavity

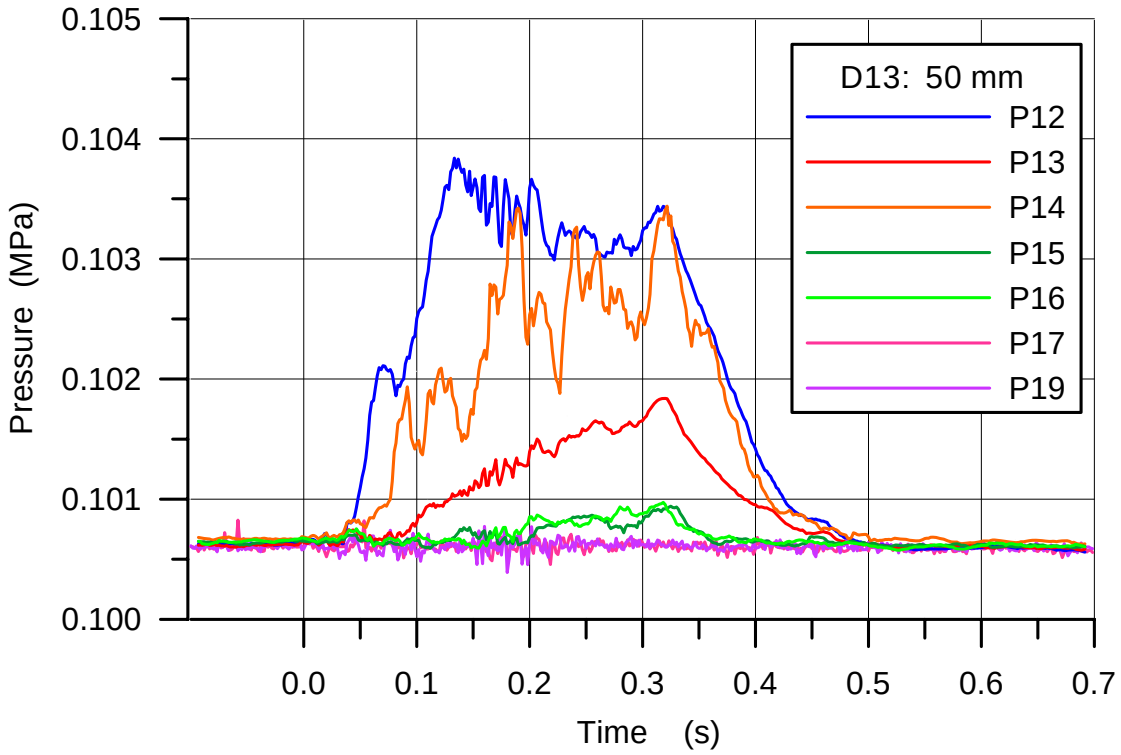

Fig. 5.24 D13 Pressure in the space at the RPV support and in the subcompartments

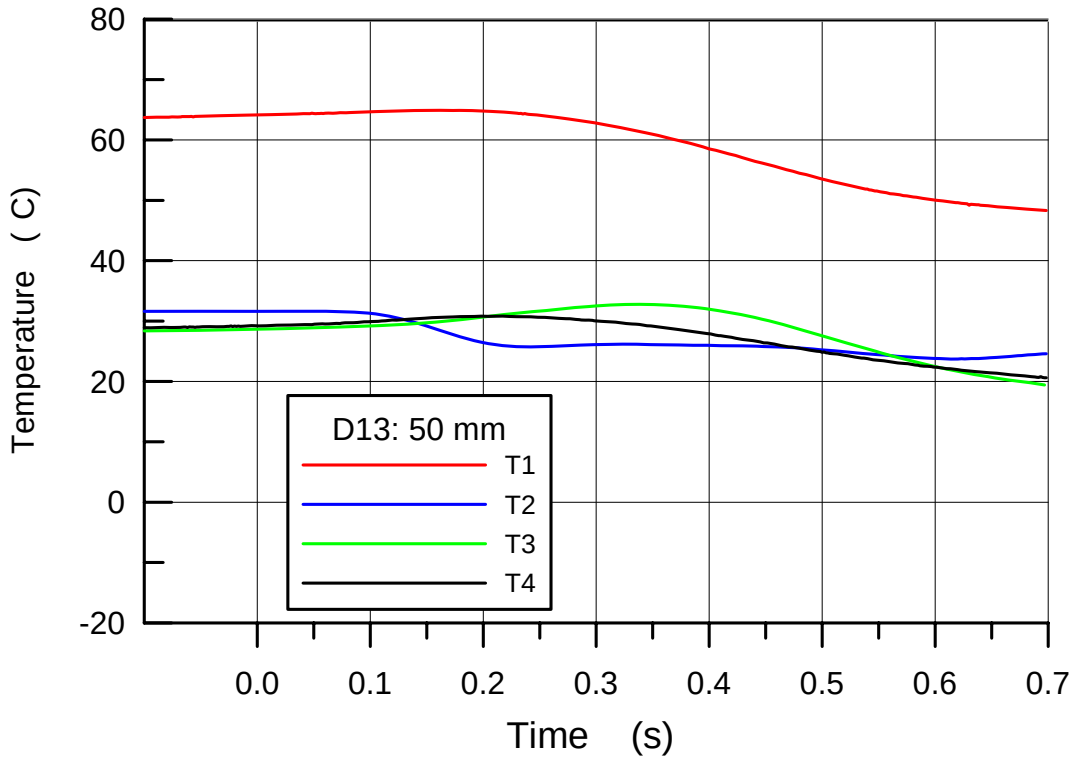

Fig. 5.25 D13 Gas temperatures in the RPV and the cavity

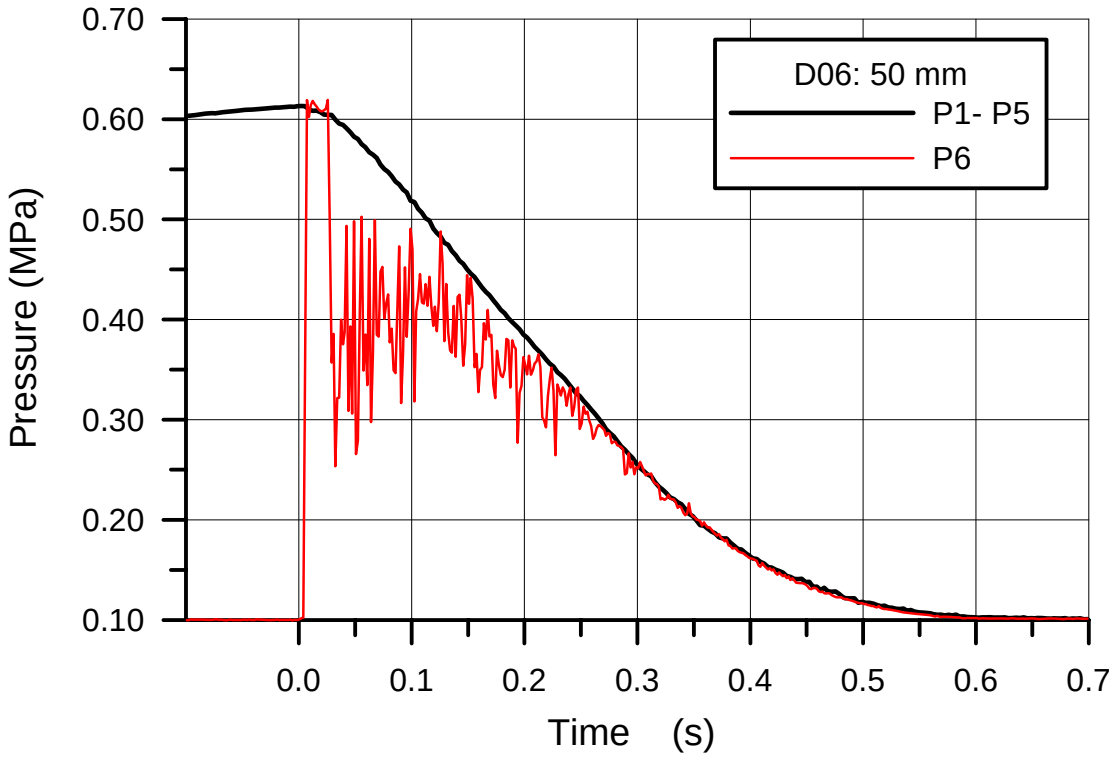

Fig. 5.26 D06 Blow down pressure in the RPV and total pressure on the cavity floor below the hole

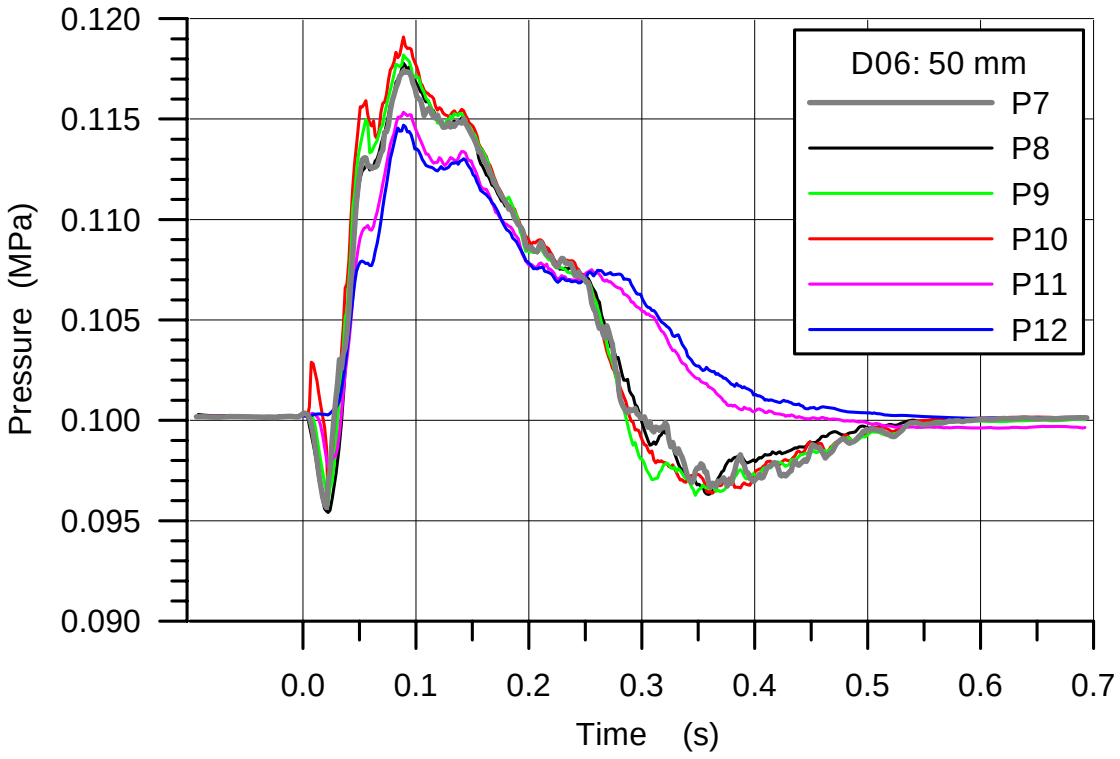

Fig. 5.27 D06 Pressures in the cavity

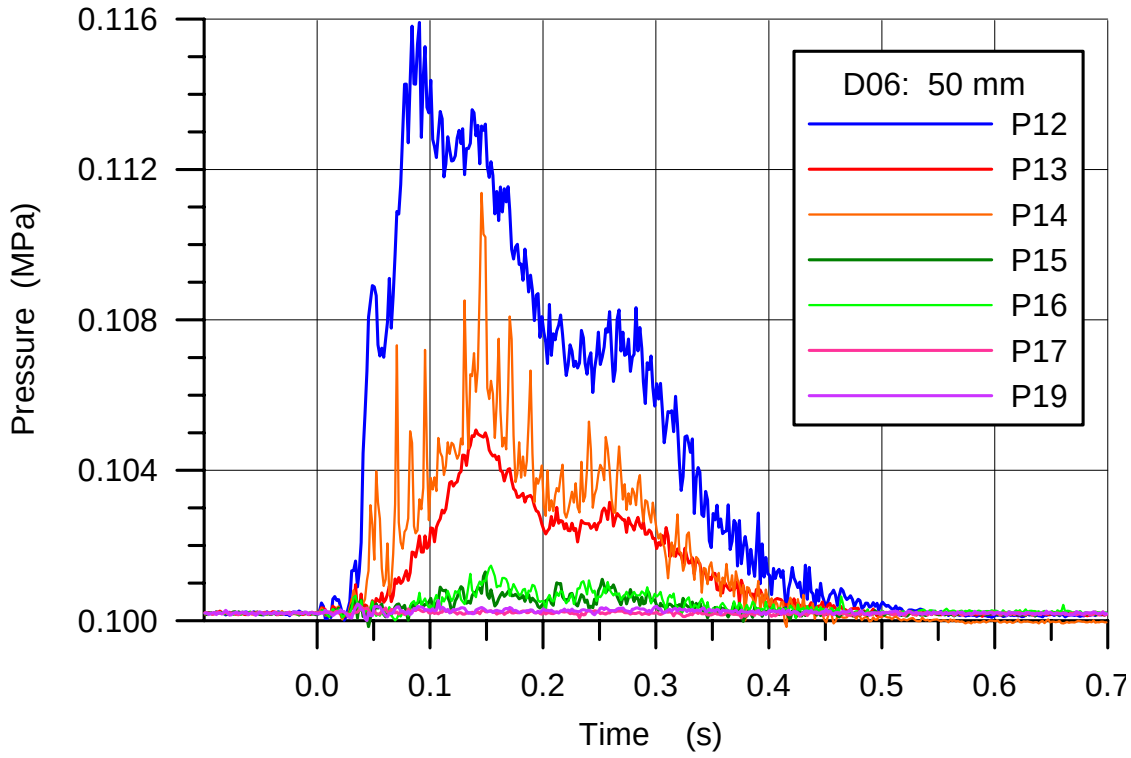

Fig. 5.28 D06 Pressure in the space at the RPV support and in the subcompartments

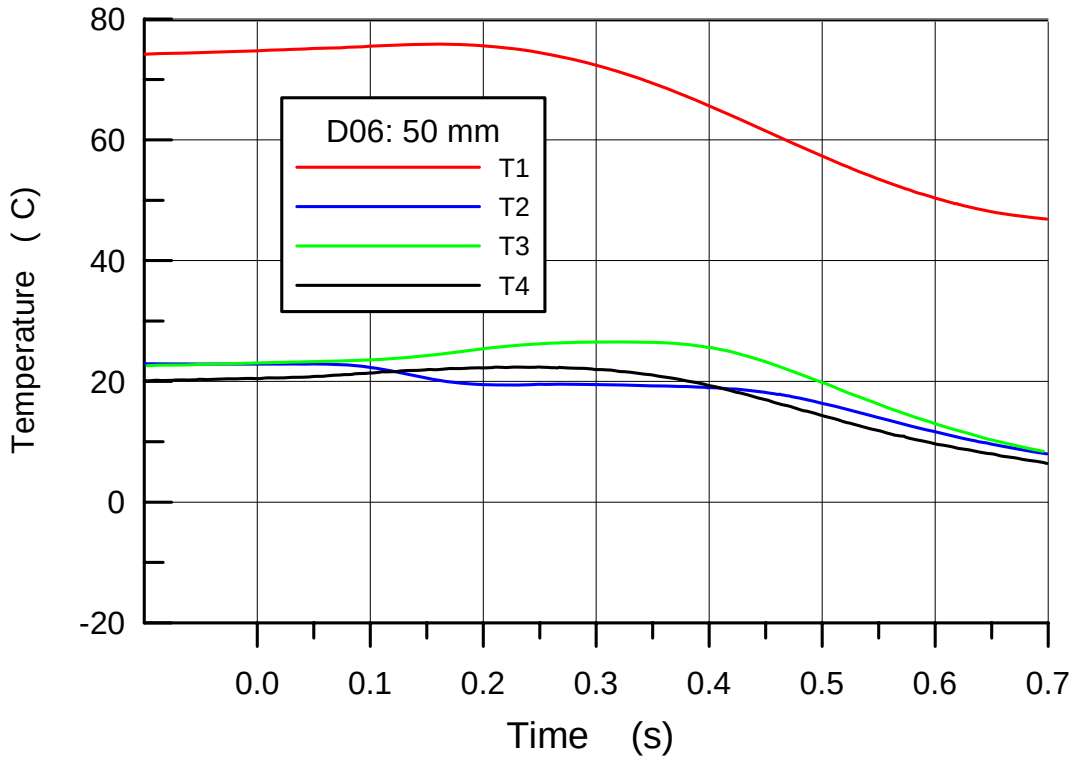

Fig. 5.29 D06 Gas temperatures in the RPV and the cavity

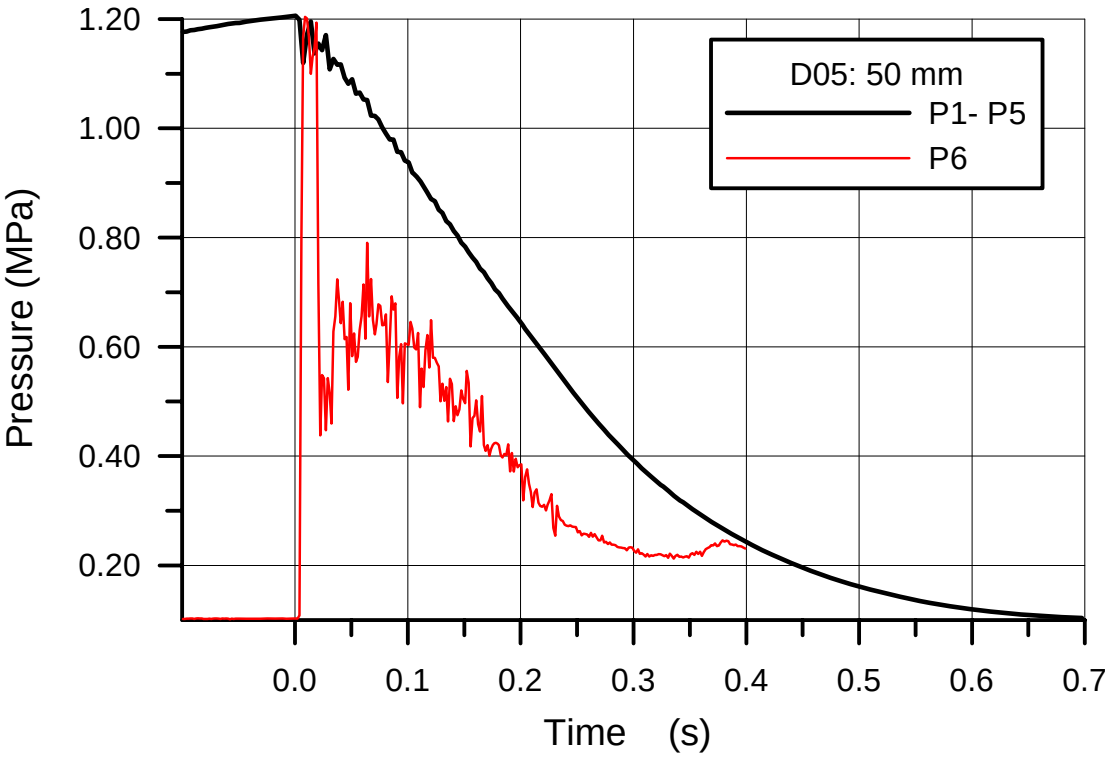

Fig. 5.30 D05 Blow down pressure in the RPV and total pressure on the cavity floor below the hole

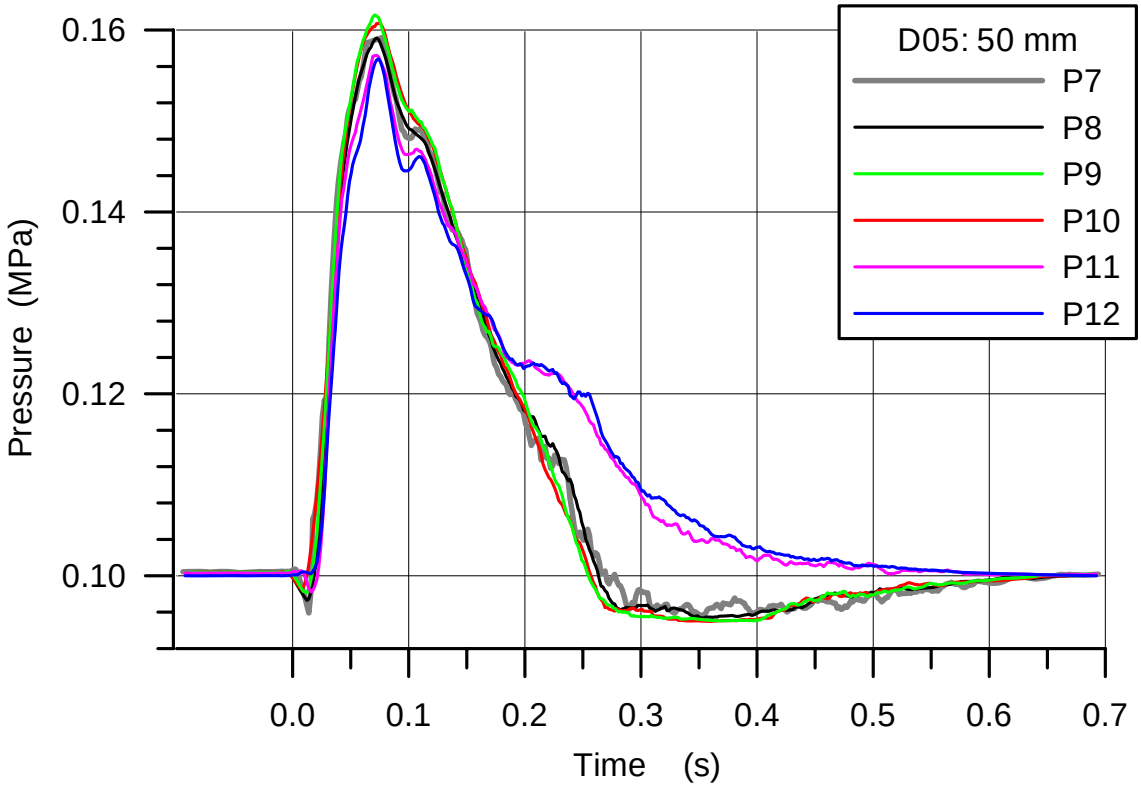

Fig. 5.31 D05 Pressures in the cavity

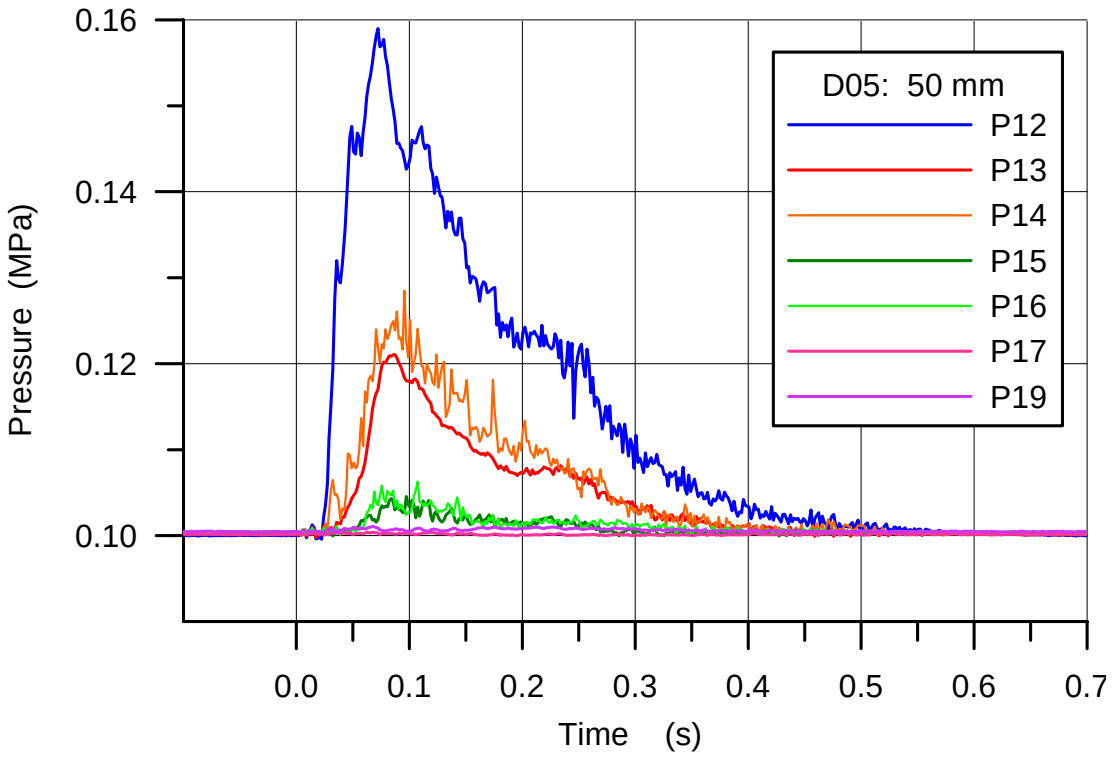

Fig. 5.32 D05 Pressure in the space at the RPV support and in the subcompartments

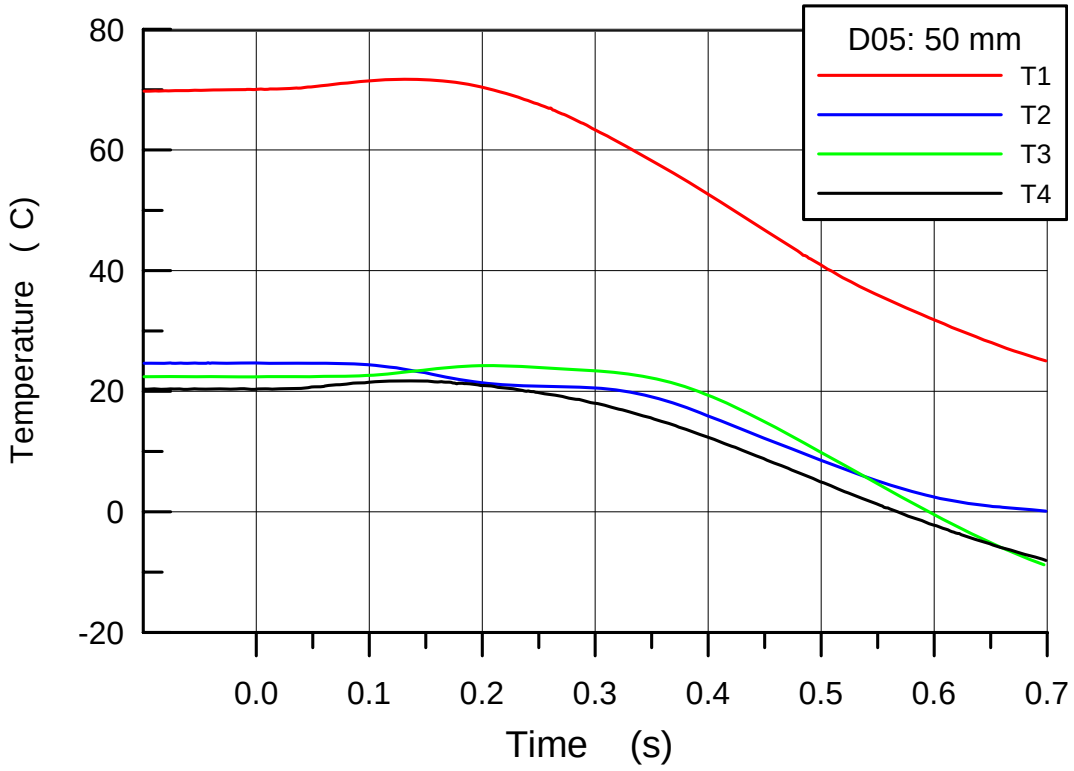

Fig. 5.33 D05 Gas temperatures in the RPV and the cavity

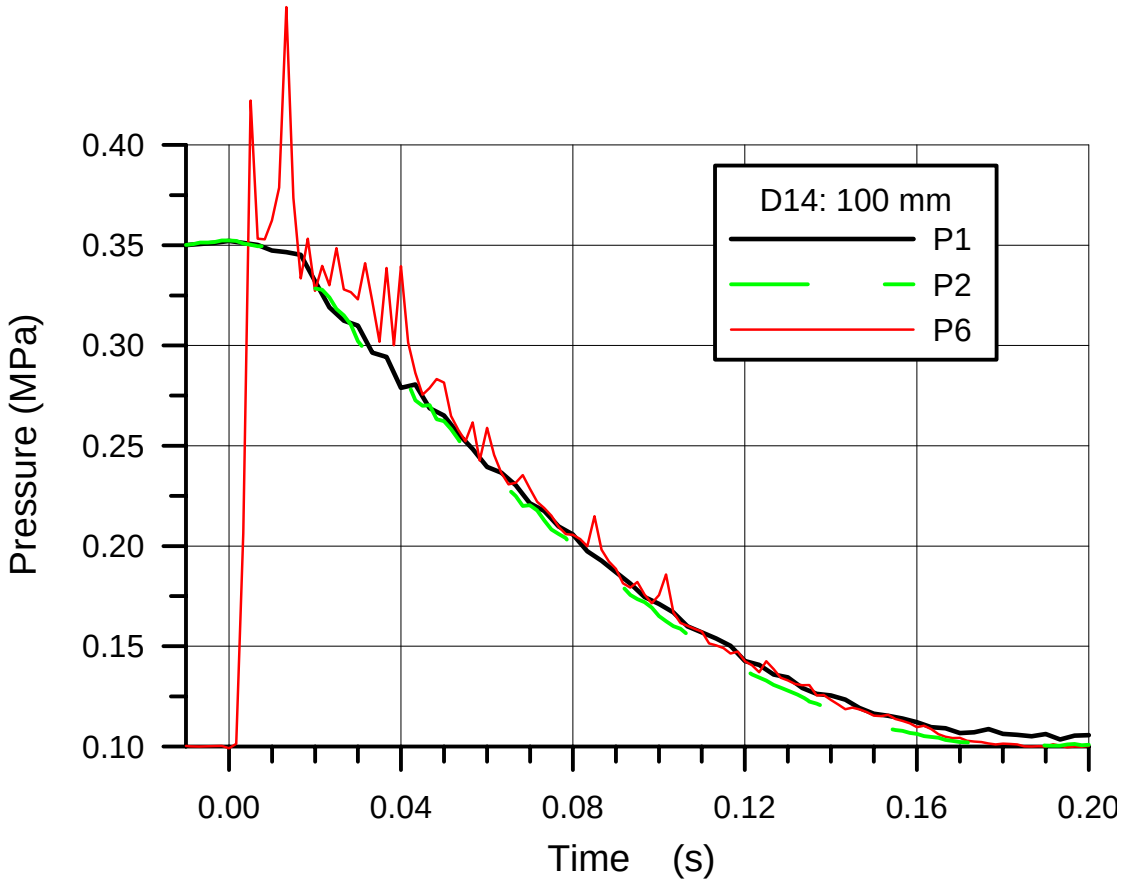

Fig. 5.34 D14 Blow down pressure in the RPV and total pressure on the cavity floor below the hole

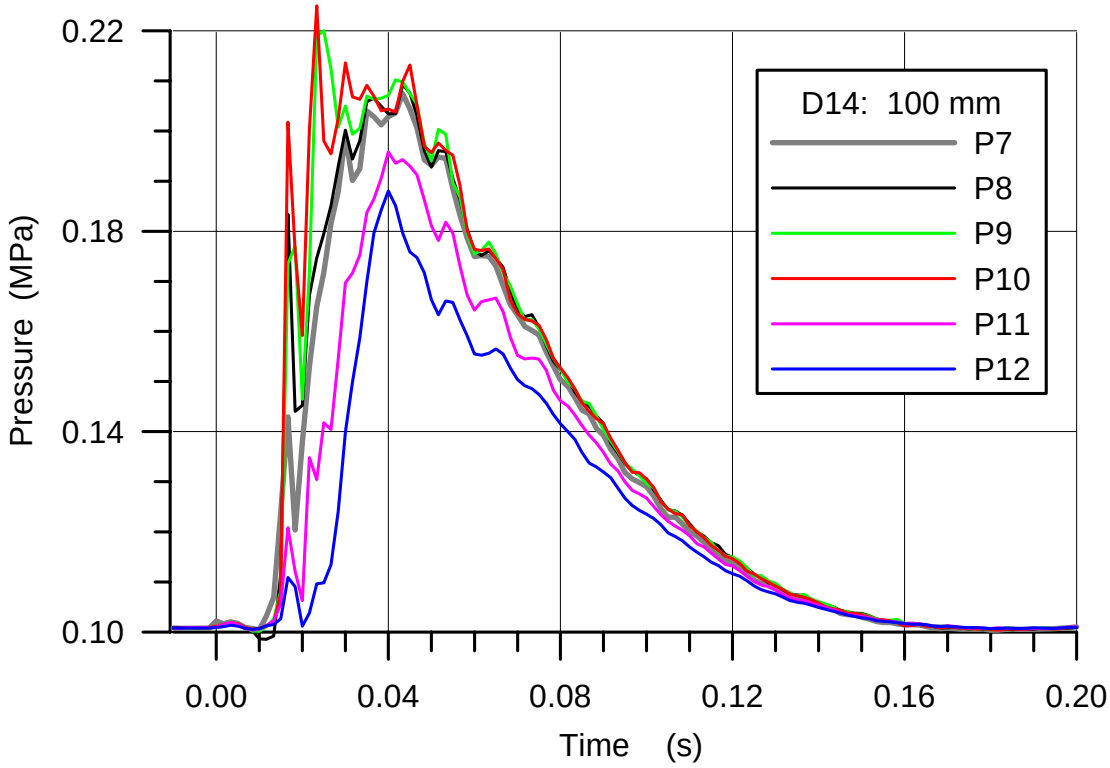

Fig. 5.35 D14 Pressures in the cavity

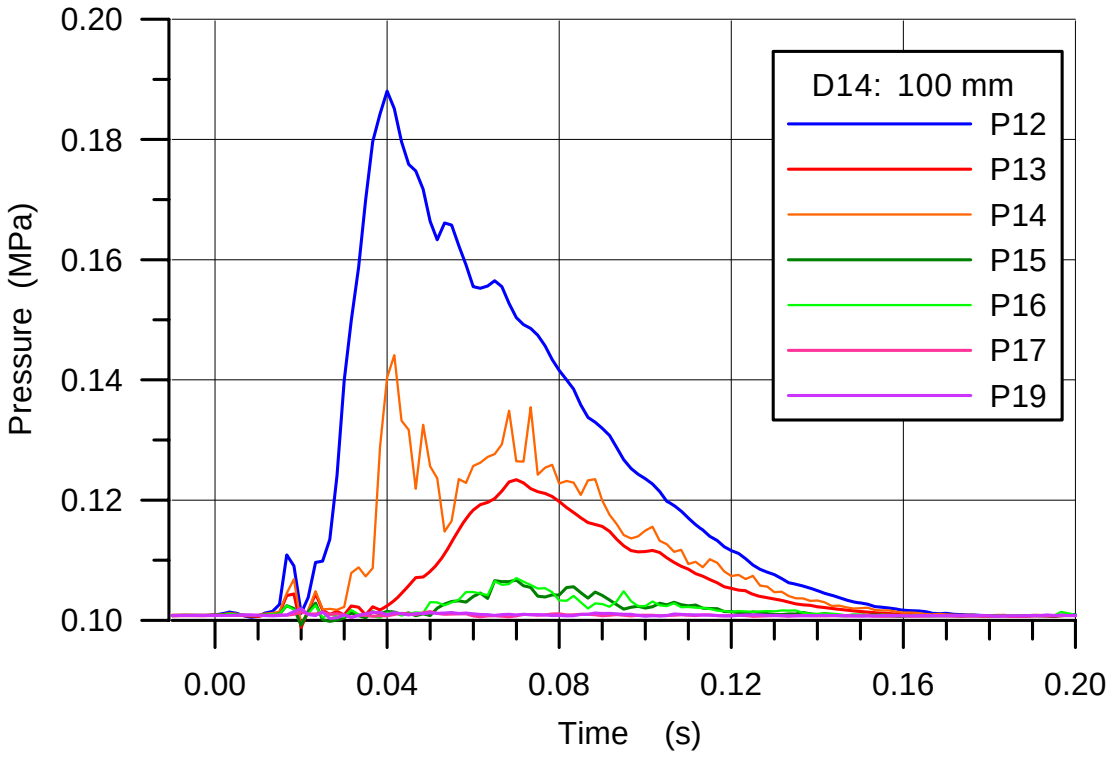

Fig. 5.36 D14 Pressure in the space at the RPV support and in the subcompartments

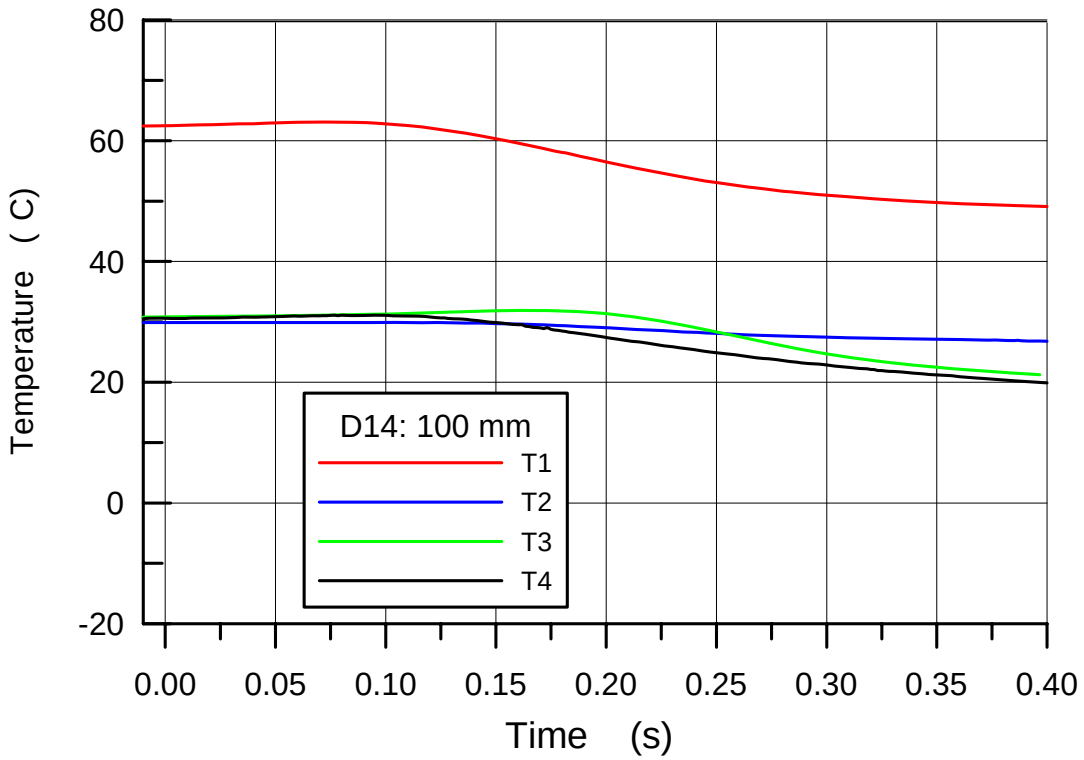

Fig. 5.37 D14 Gas temperatures in the RPV and the cavity

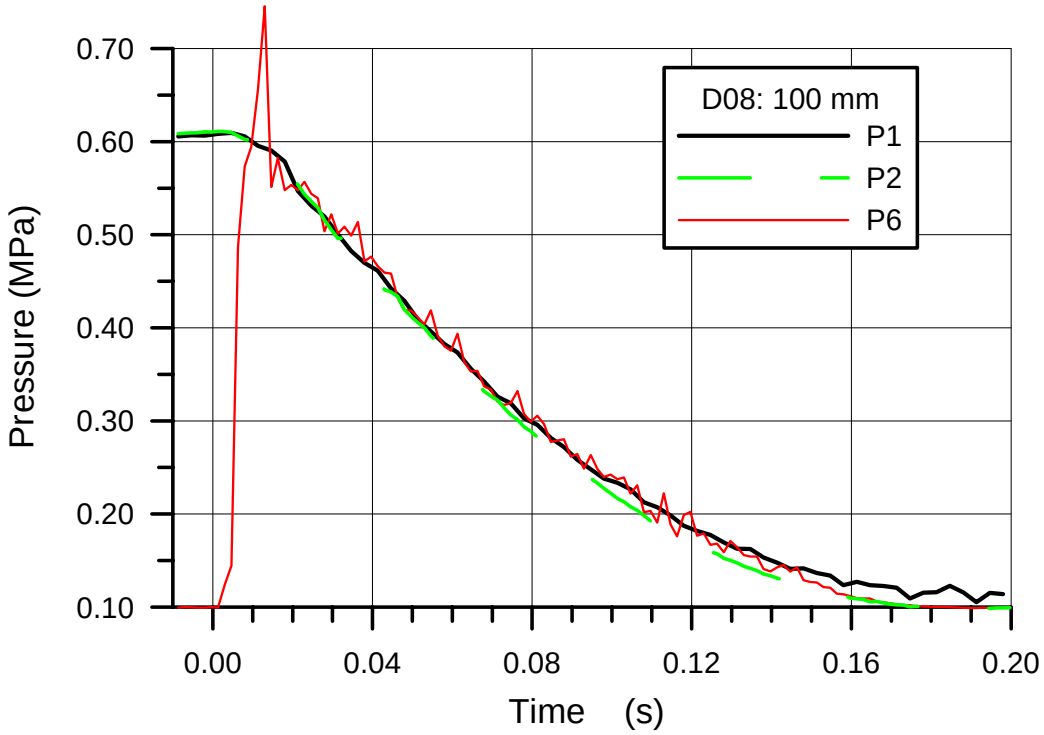

Fig. 5.38 D08 Blow down pressure in the RPV and total pressure on the cavity floor below the hole

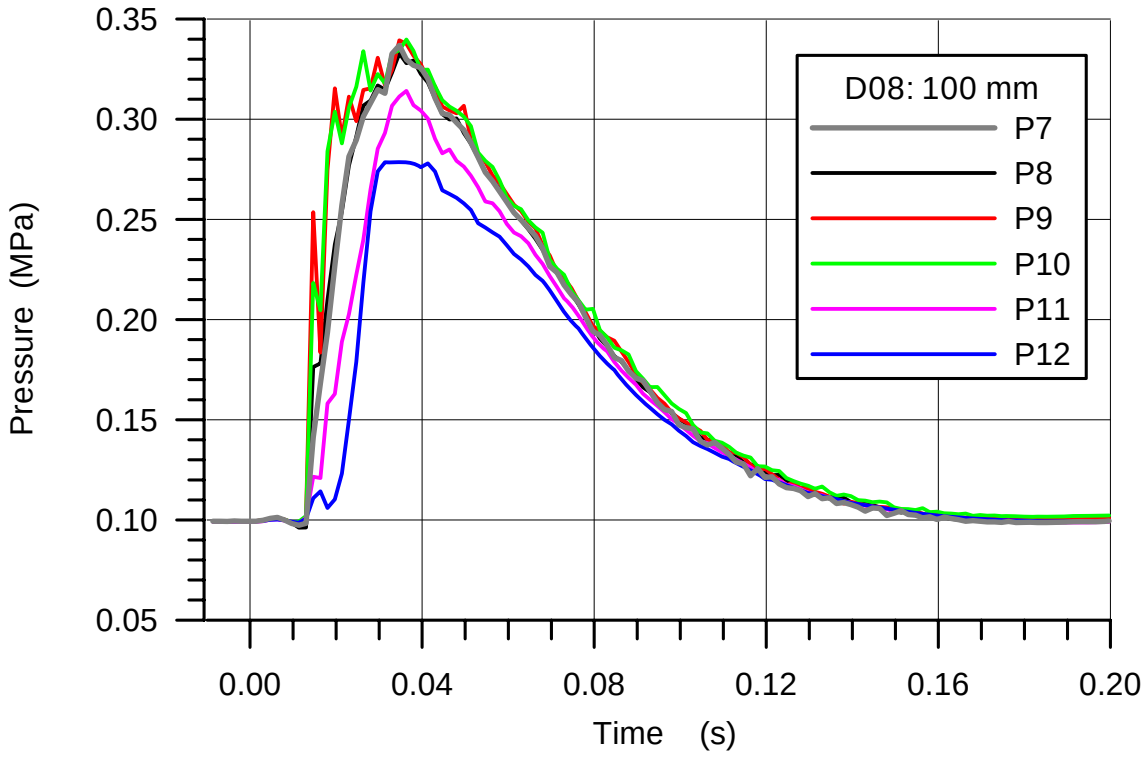

Fig. 5.39 D08 Pressures in the cavity

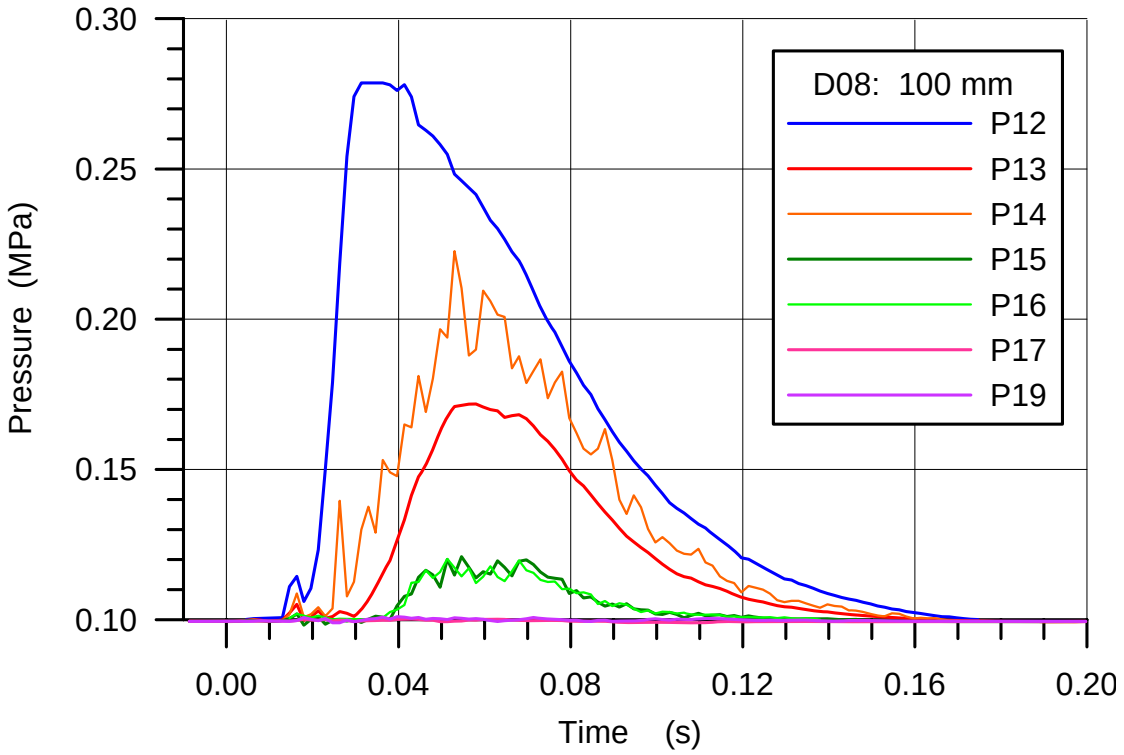

Fig. 5.40 D08 Pressure in the space at the RPV support and in the subcompartments

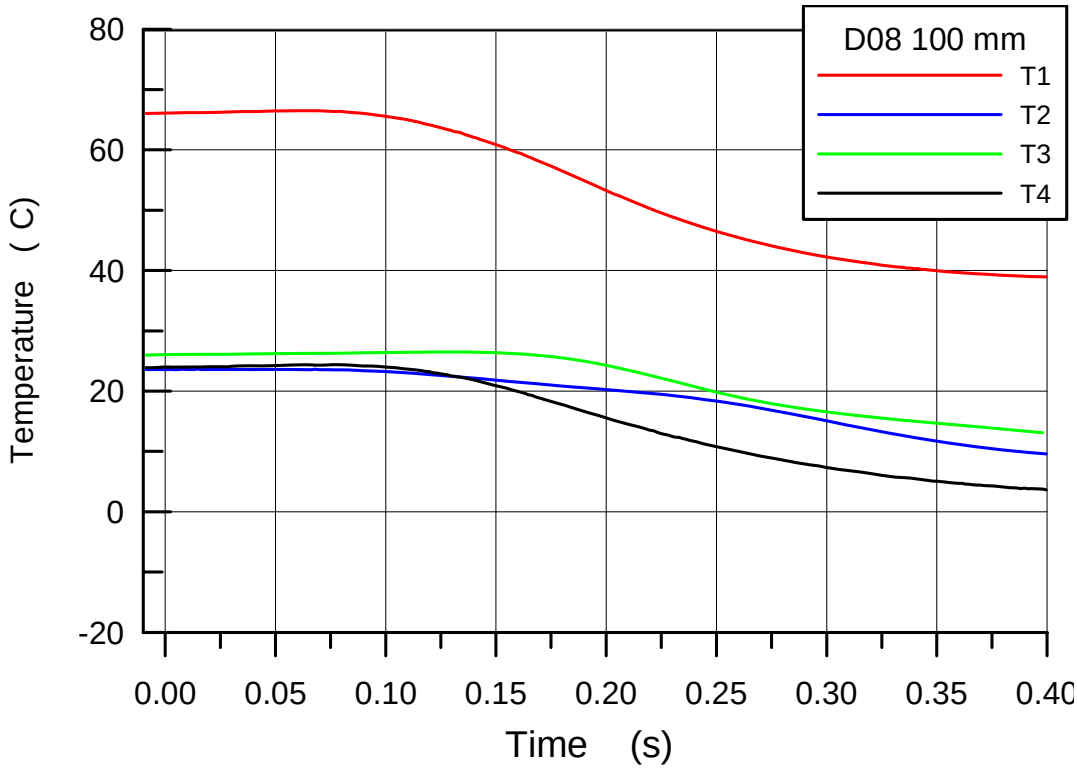

Fig. 5.41 D08 Gas temperatures in the RPV and the cavity

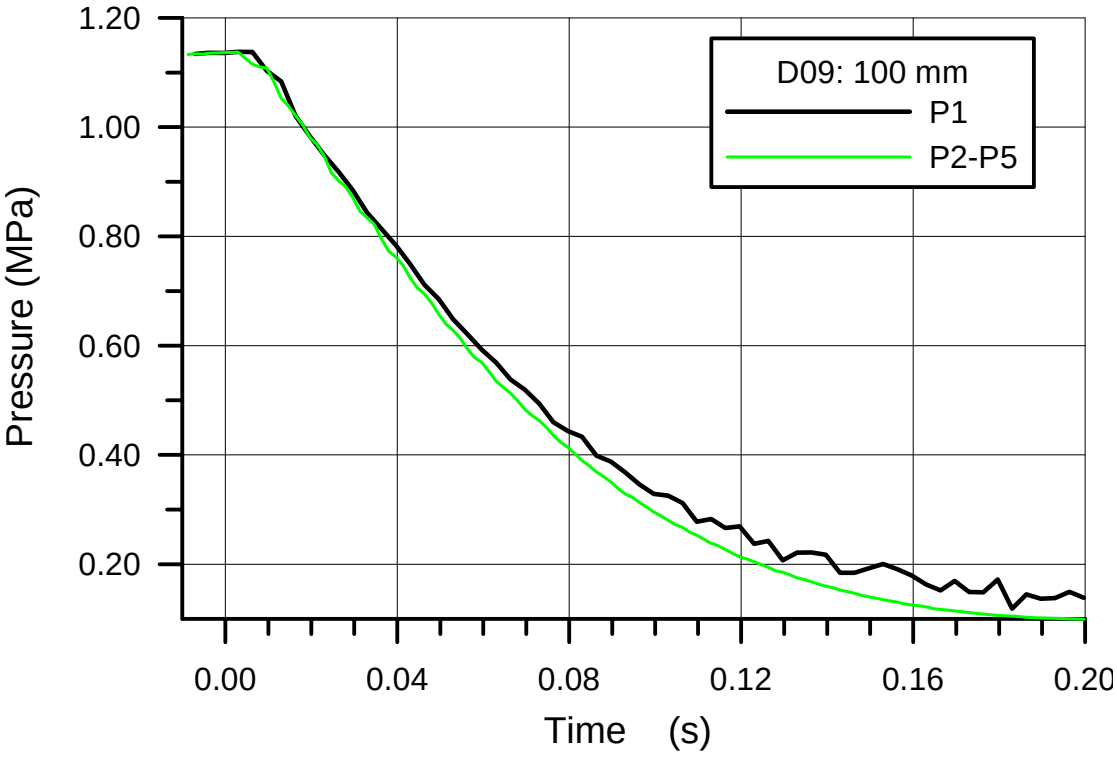

Fig. 5.42 D09 Blow down pressure in the RPV

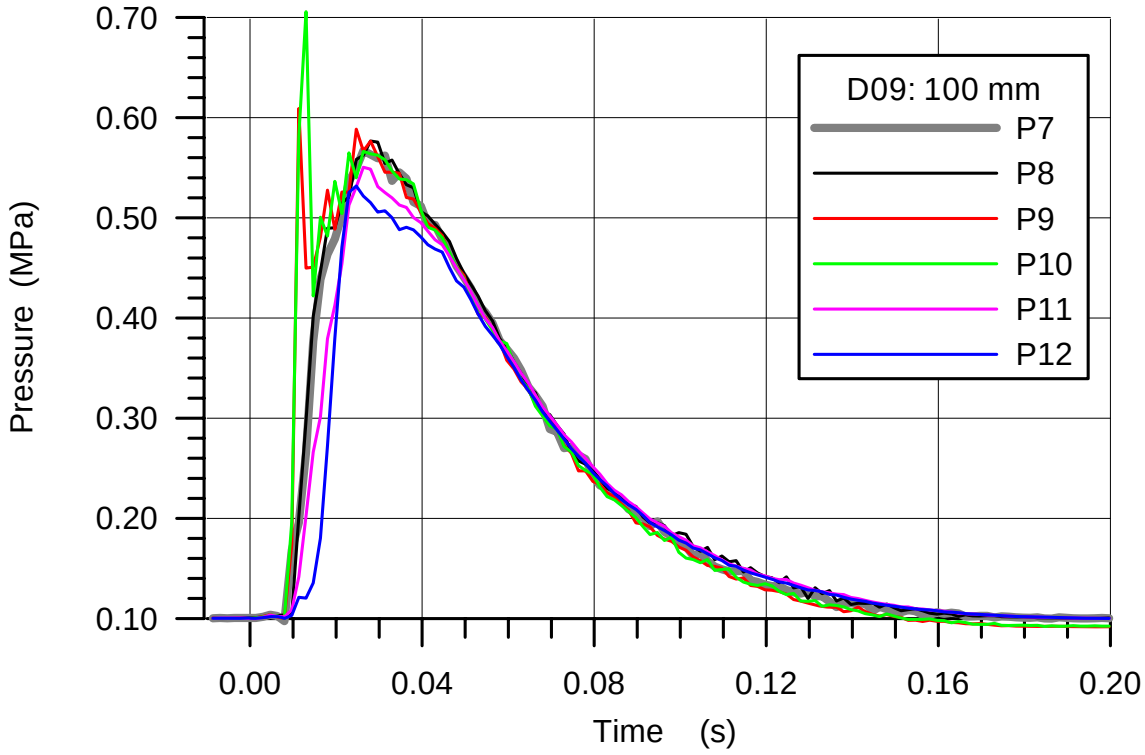

Fig. 5.43 D09 Pressures in the cavity

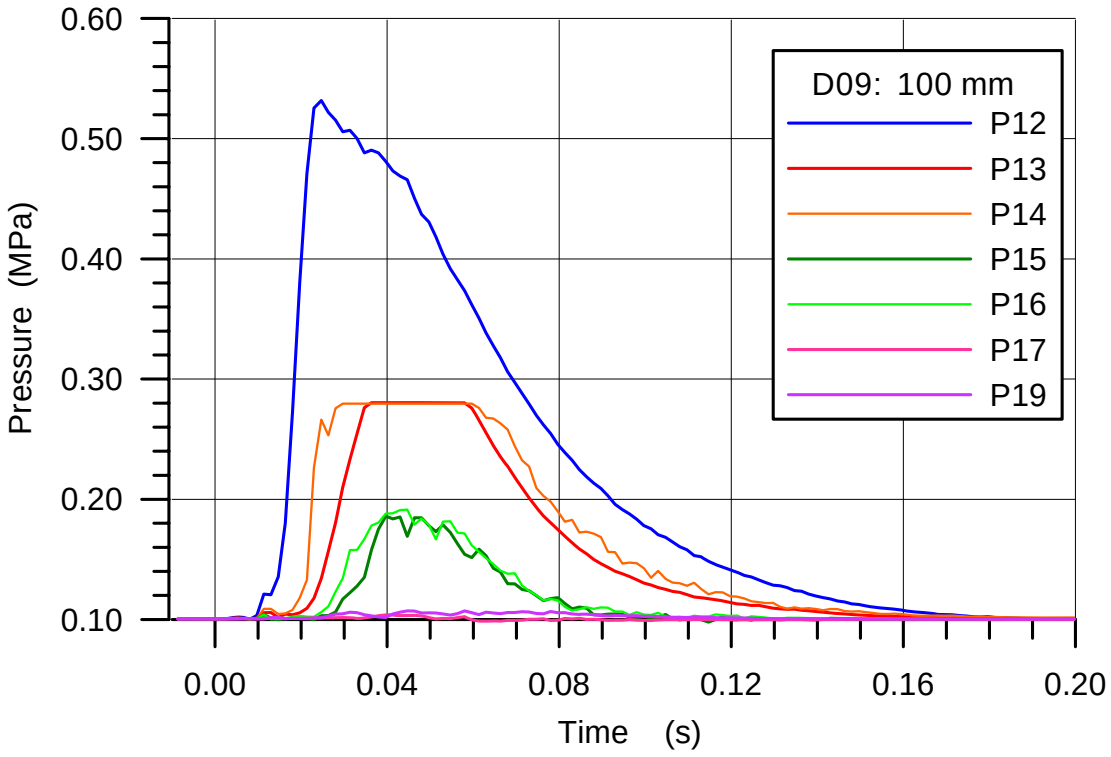

Fig. 5.44 D09 Pressure in the space at the RPV support and in the subcompartments (P13 and P14 exceeded measuring range)

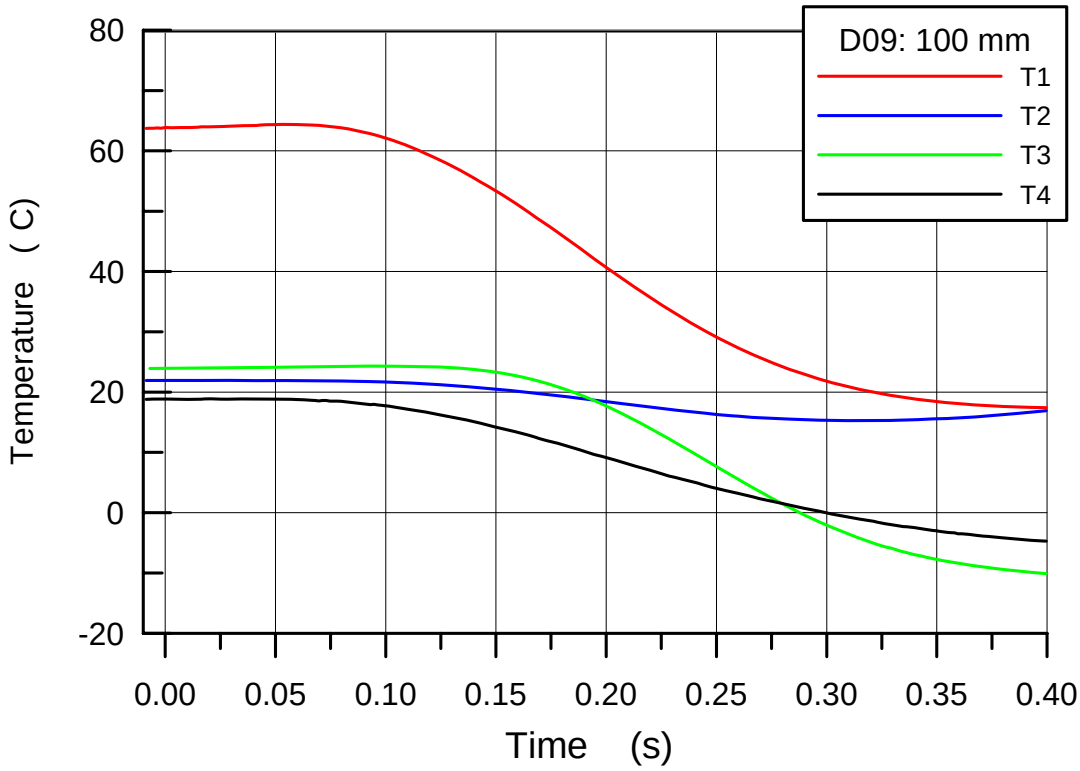

Fig. 5.45 D09 Gas temperatures in the RPV and the cavity

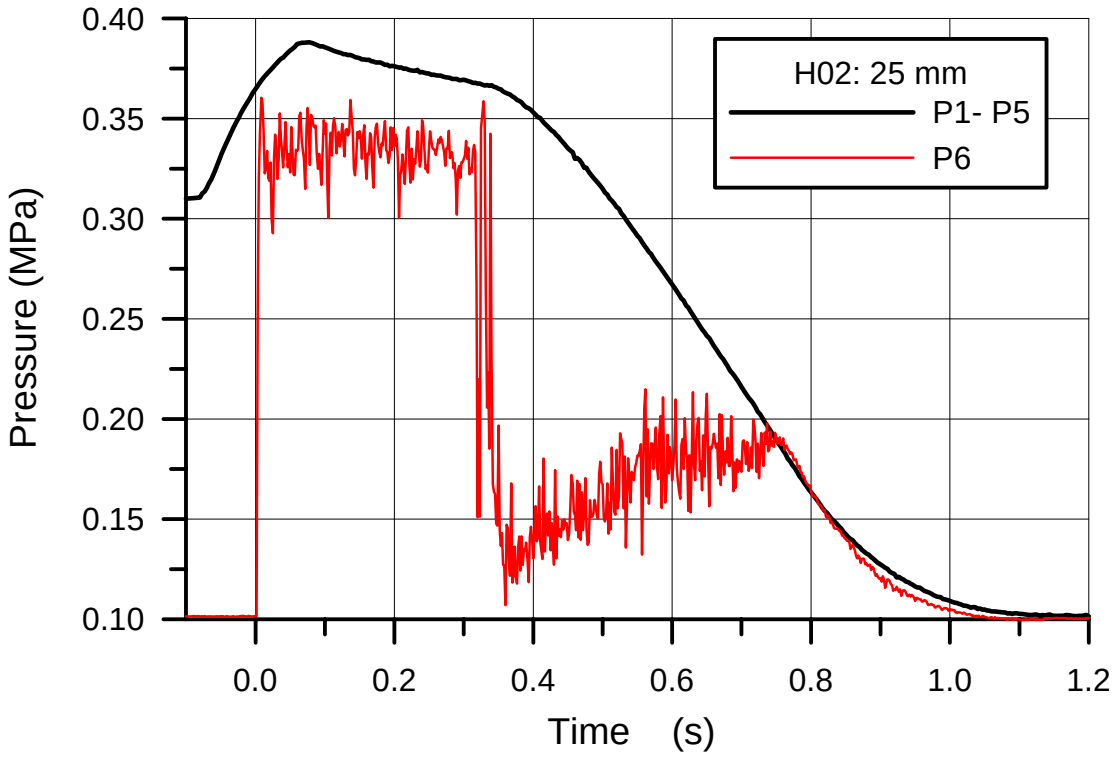

Fig. 5.46 H02 Blow down pressure in the RPV and total pressure on the cavity floor below the hole

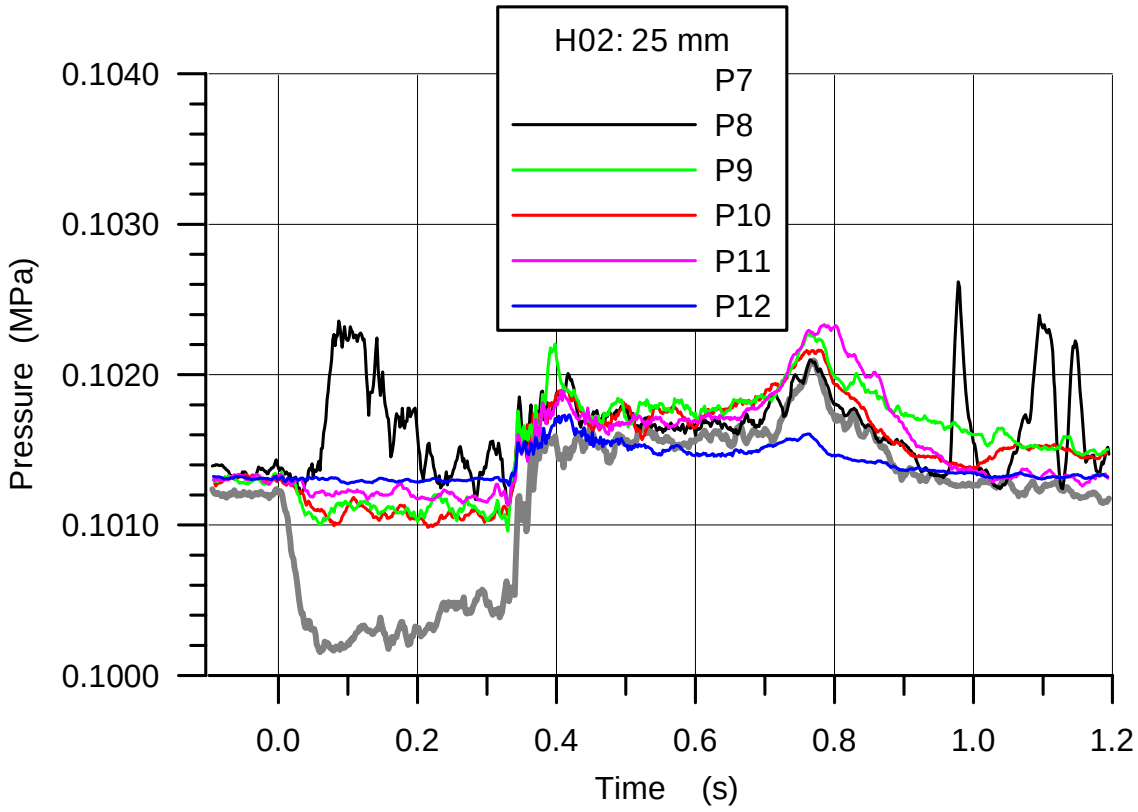

Fig. 5.47 H02 Pressures in the cavity

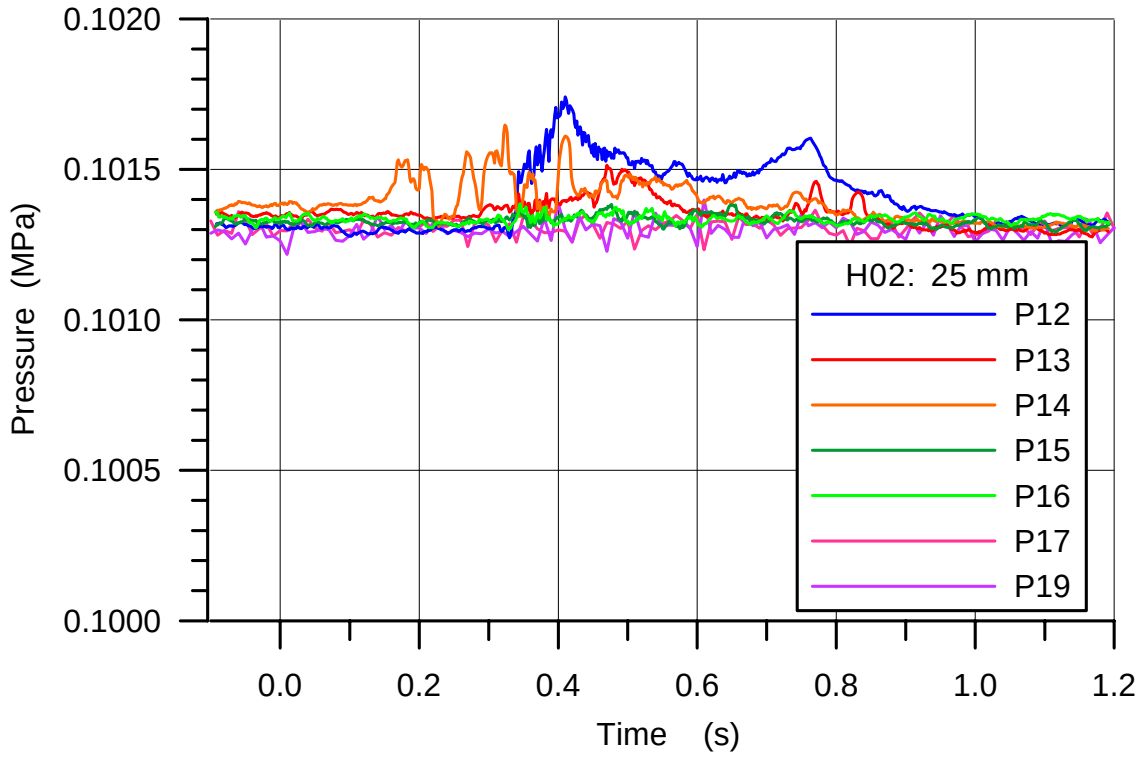

Fig. 5.48 H02Pressure in the space at the RPV support and in the subcompartments

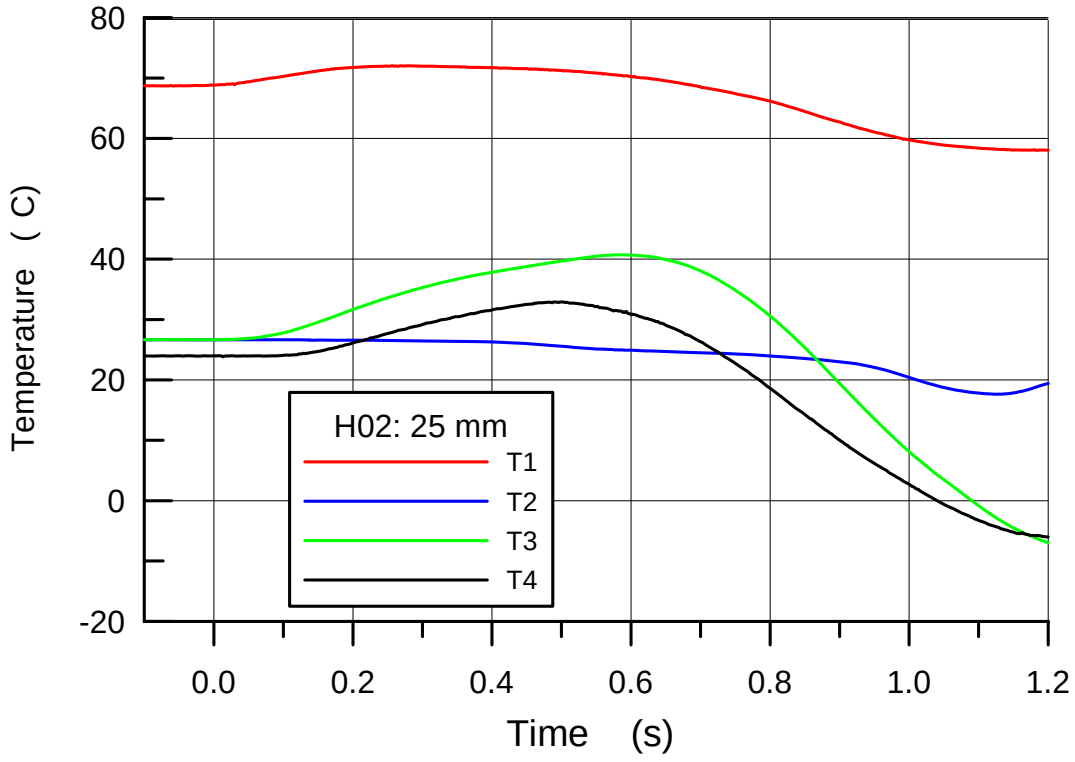

Fig. 5.49 H02Gas temperatures in the RPV and the cavity

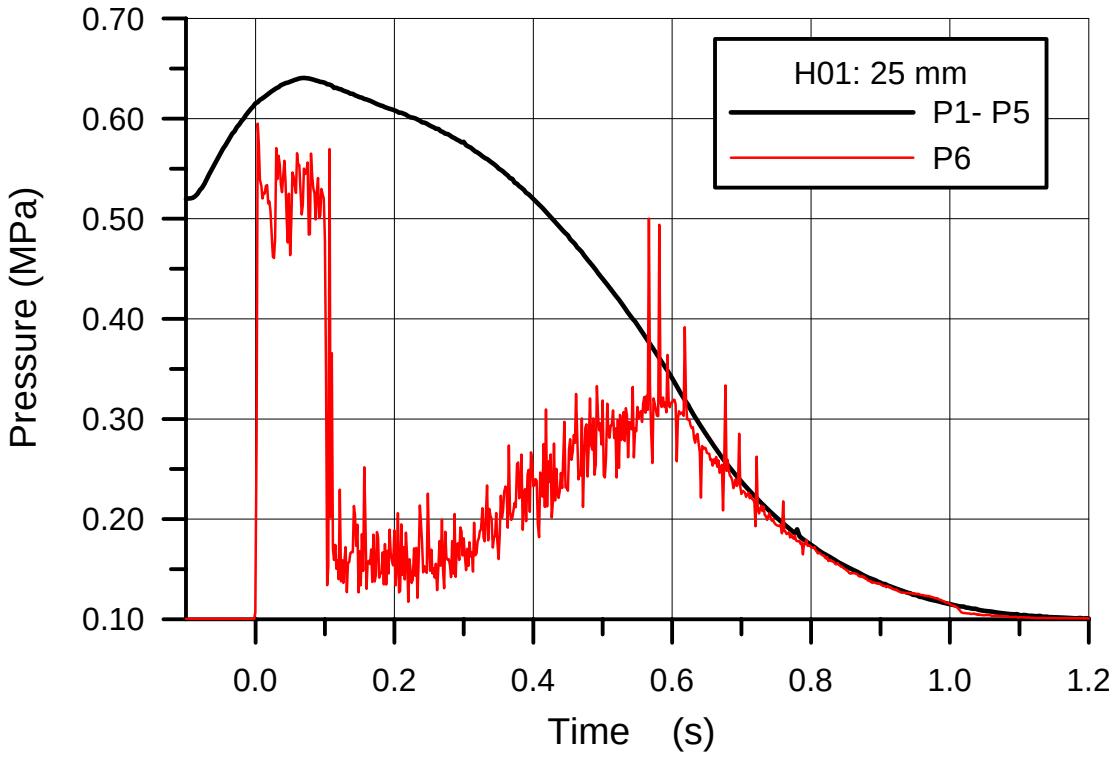

Fig. 5.50 H01 Blow down pressure in the RPV and total pressure on the cavity floor below the hole

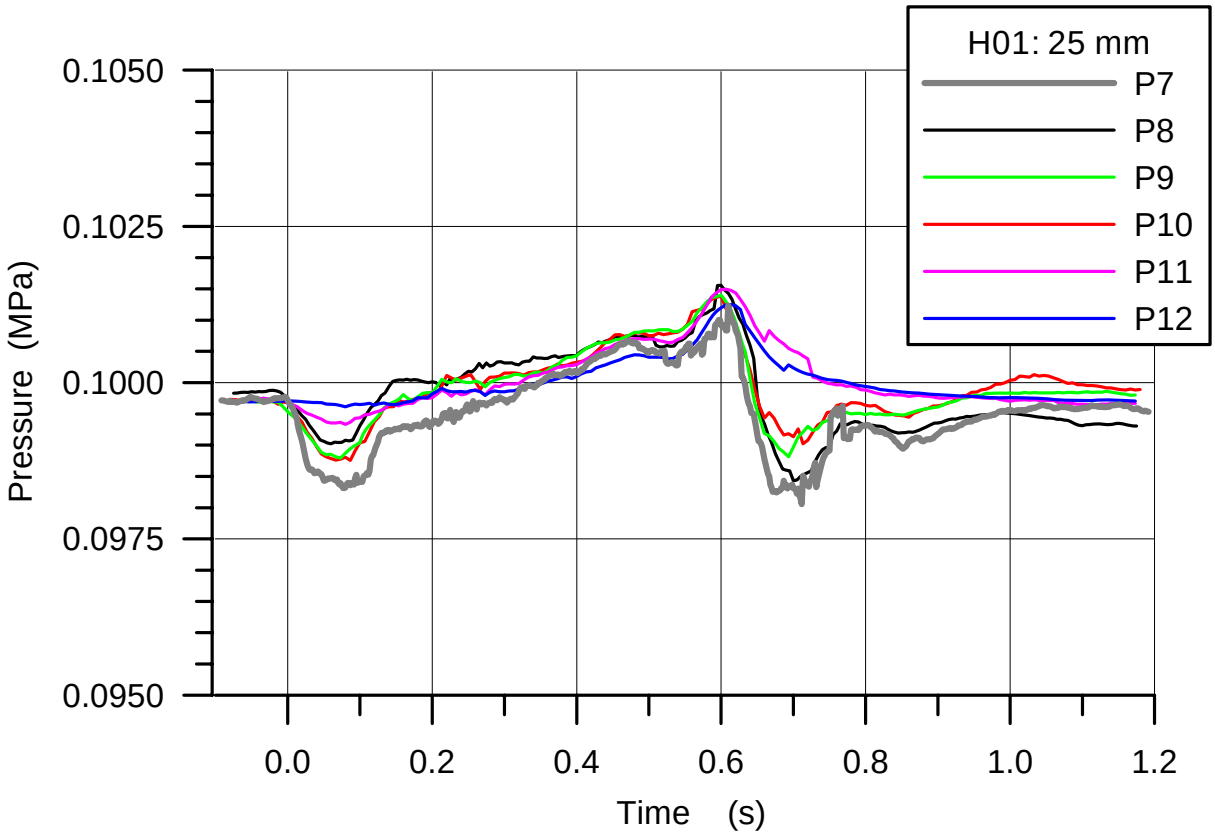

Fig. 5.51 H01 Pressures in the cavity

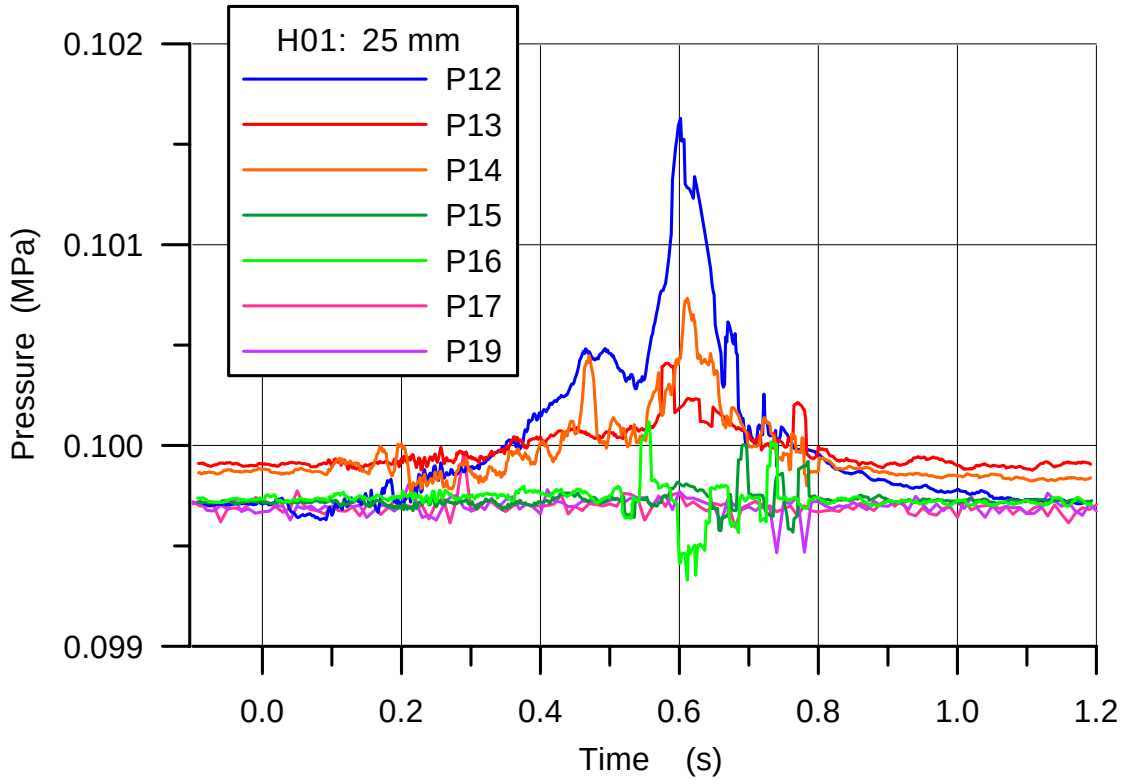

Fig. 5.52 H01 Pressure in the space at the RPV support and in the subcompartments

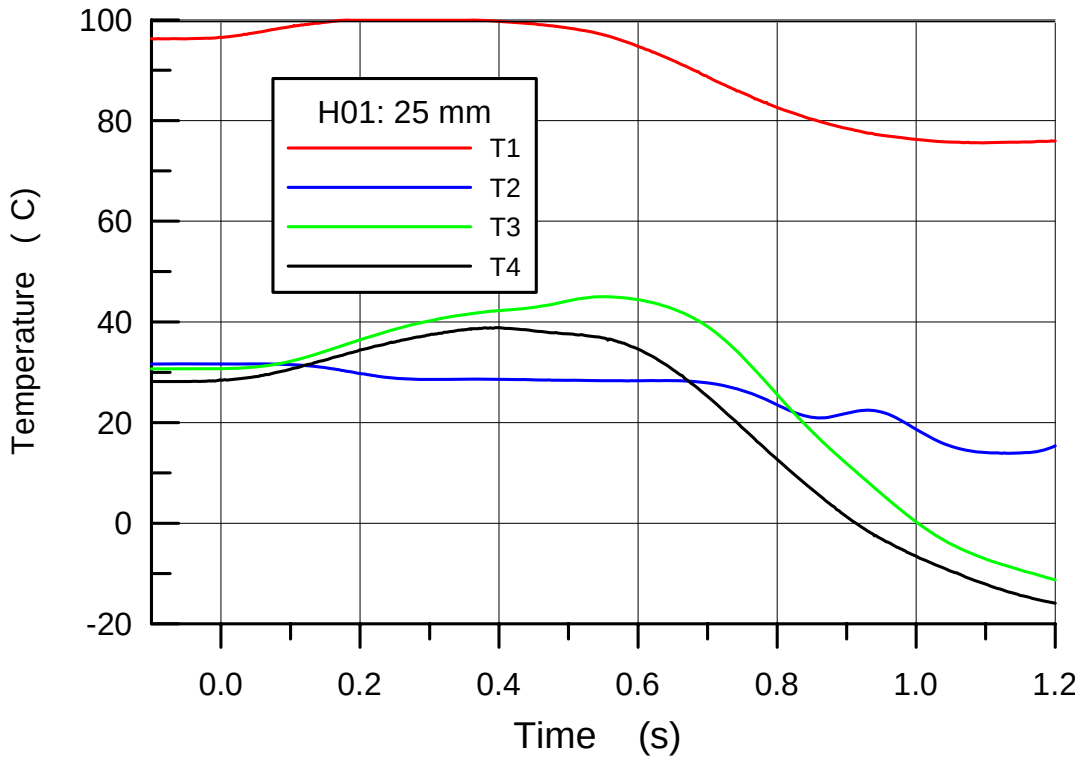

Fig. 5.53 H01 Gas temperatures in the RPV and the cavity

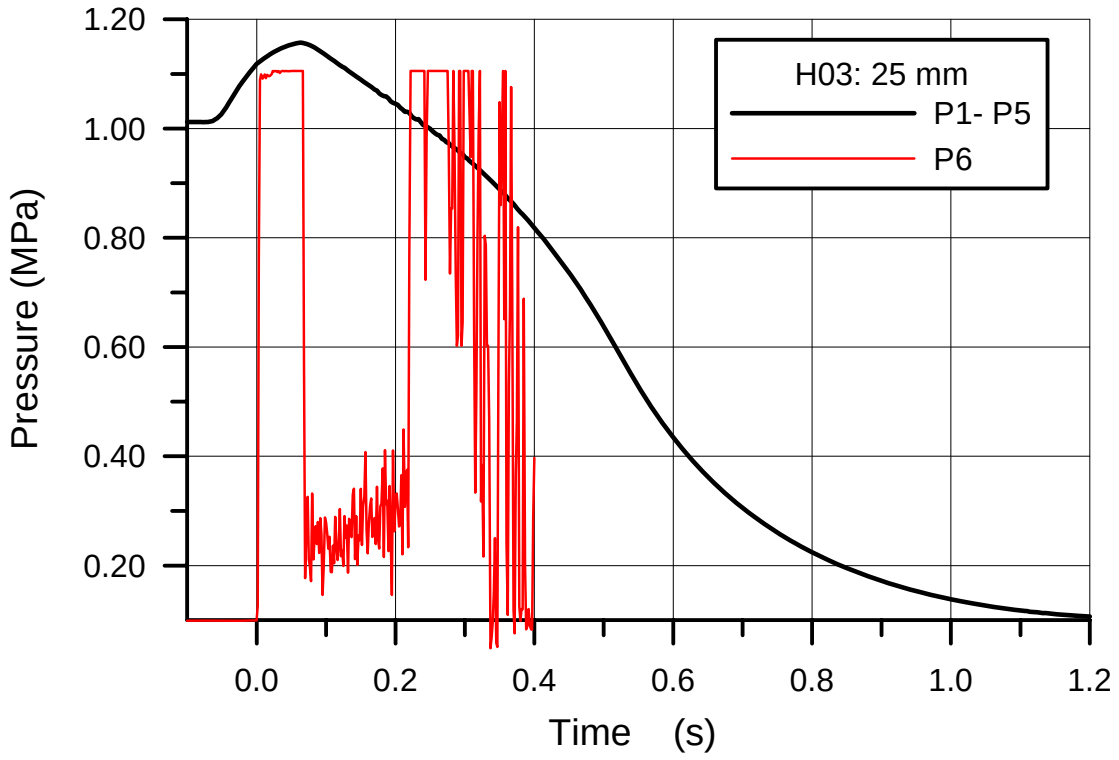

Fig. 5.54 H03 Blow down pressure in the RPV and total pressure on the cavity floor below the hole

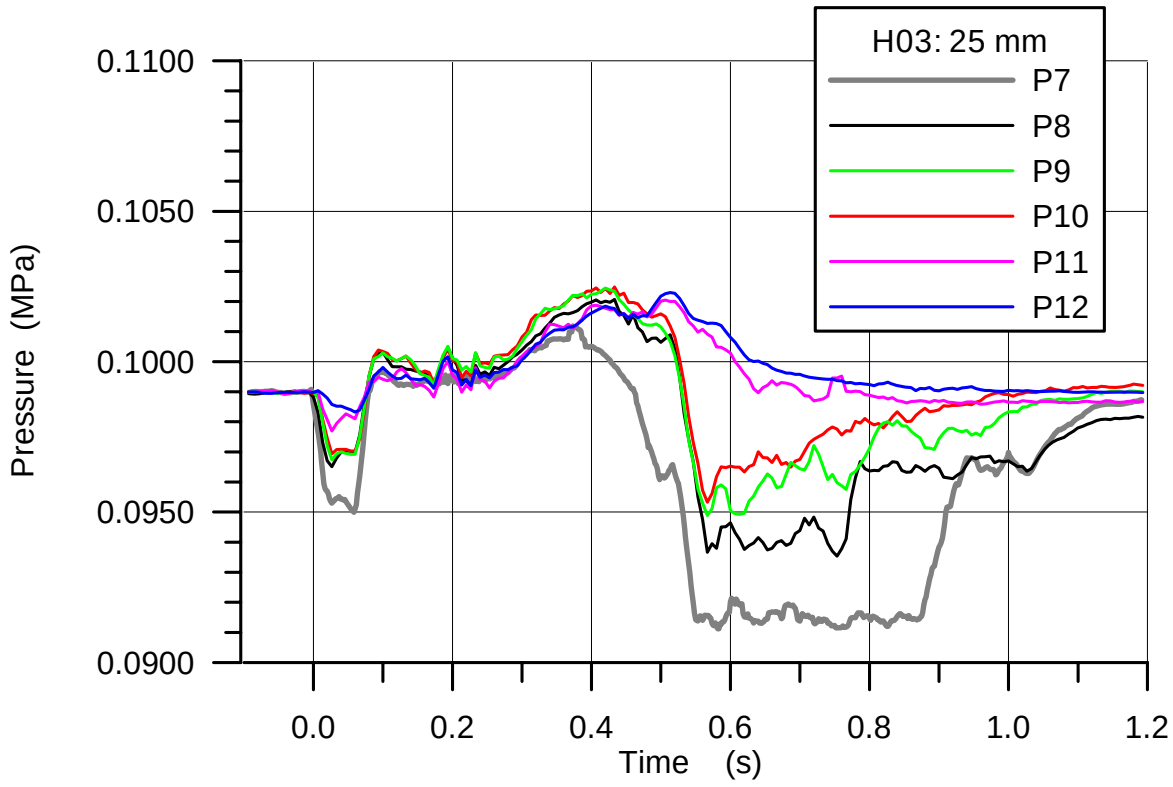

Fig. 5.55 H03 Pressures in the cavity

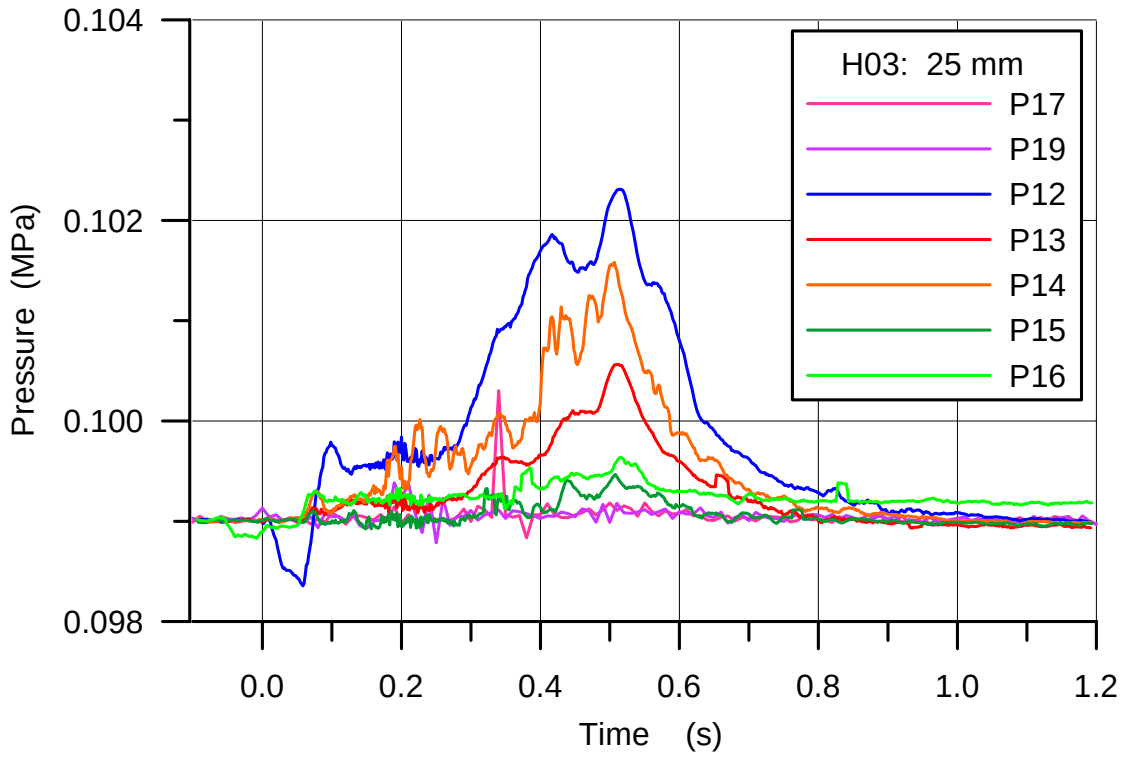

Fig. 5.56 H03 Pressure in the space at the RPV support and in the subcompartments

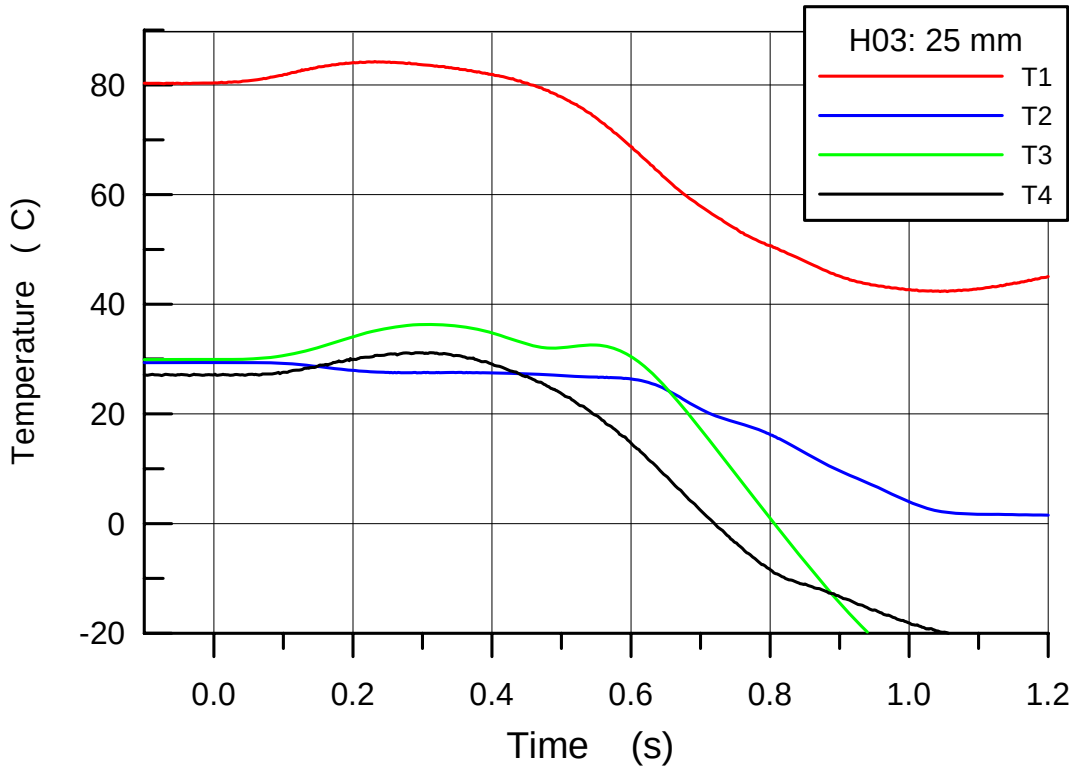

Fig. 5.57 H03 Gas temperatures in the RPV and the cavity

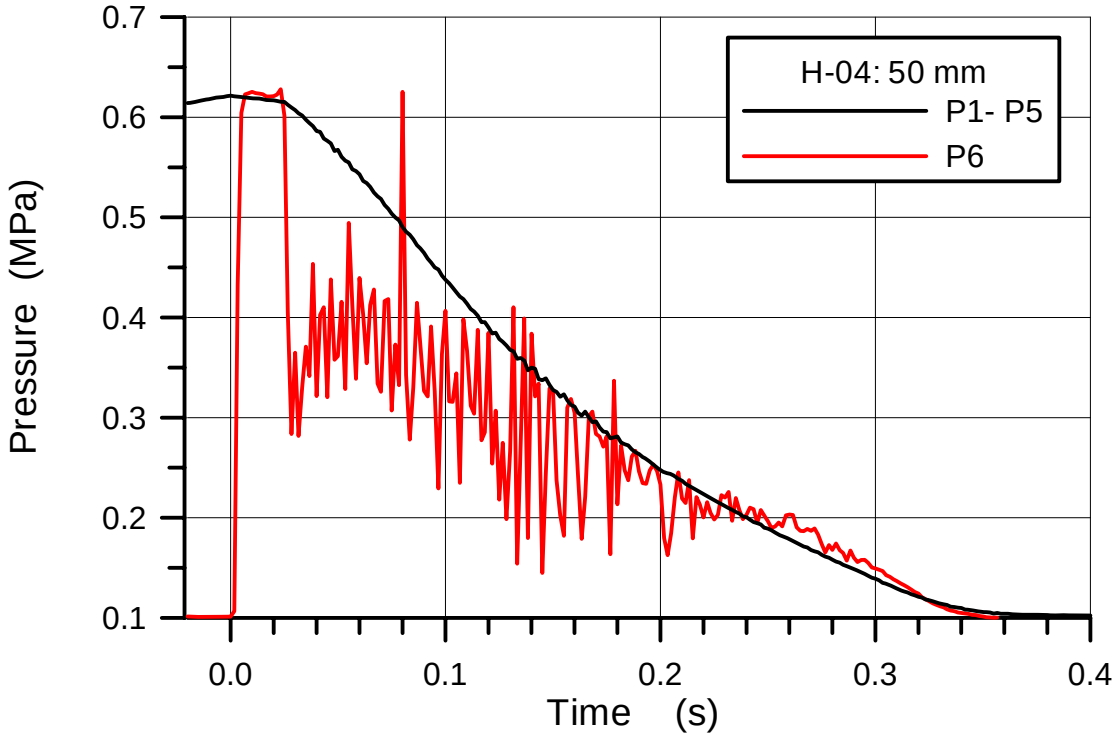

Fig. 5.58 H04 Blow down pressure in the RPV and total pressure on the cavity floor below the hole

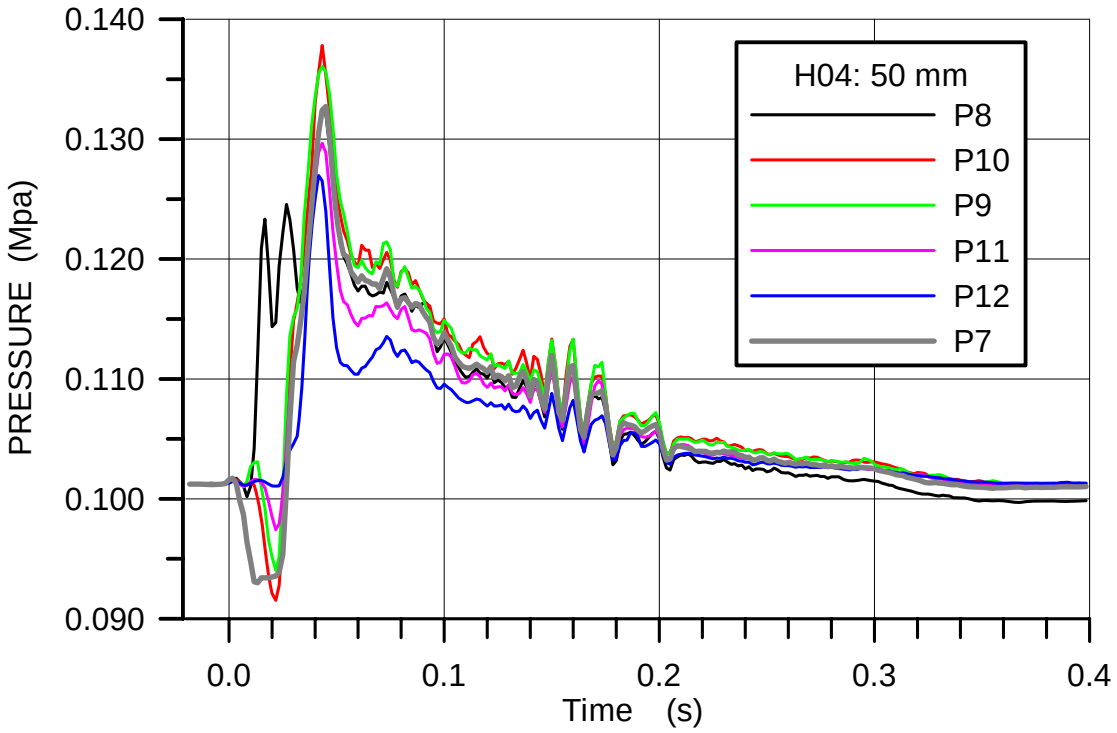

Fig. 5.59 H04 Pressures in the cavity

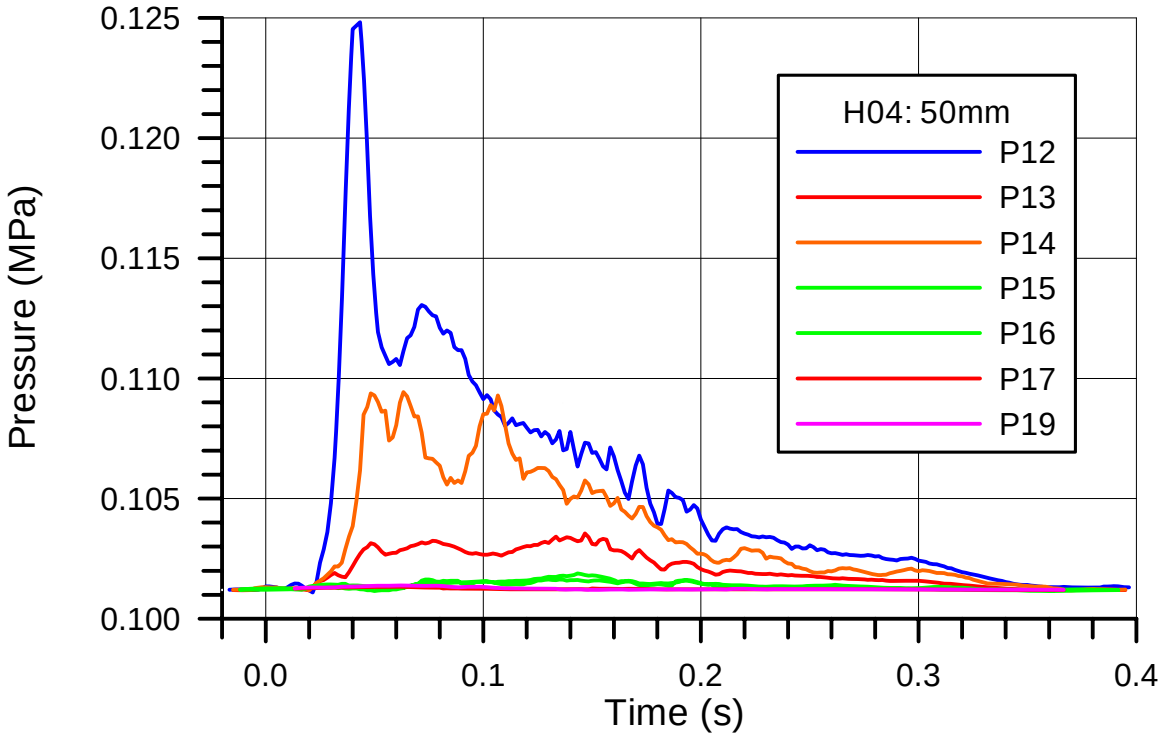

Fig. 5.60 H04 Pressure in the space at the RPV support and in the subcompartments

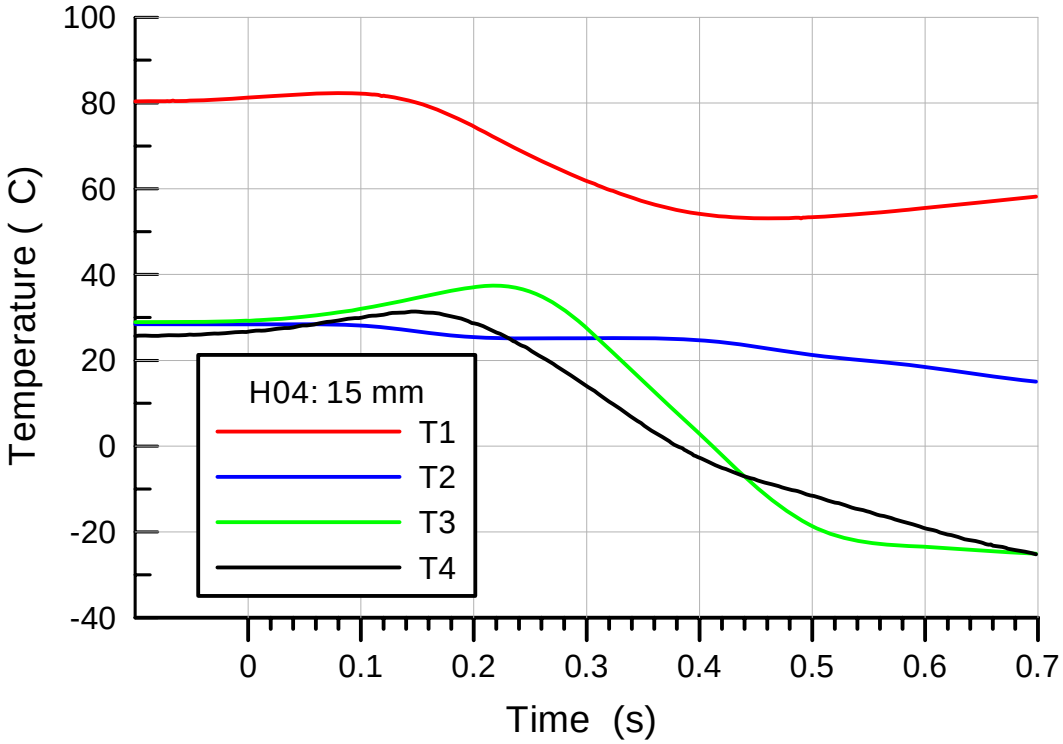

Fig. 5.61 H04Gas temperatures in the RPV and the cavity

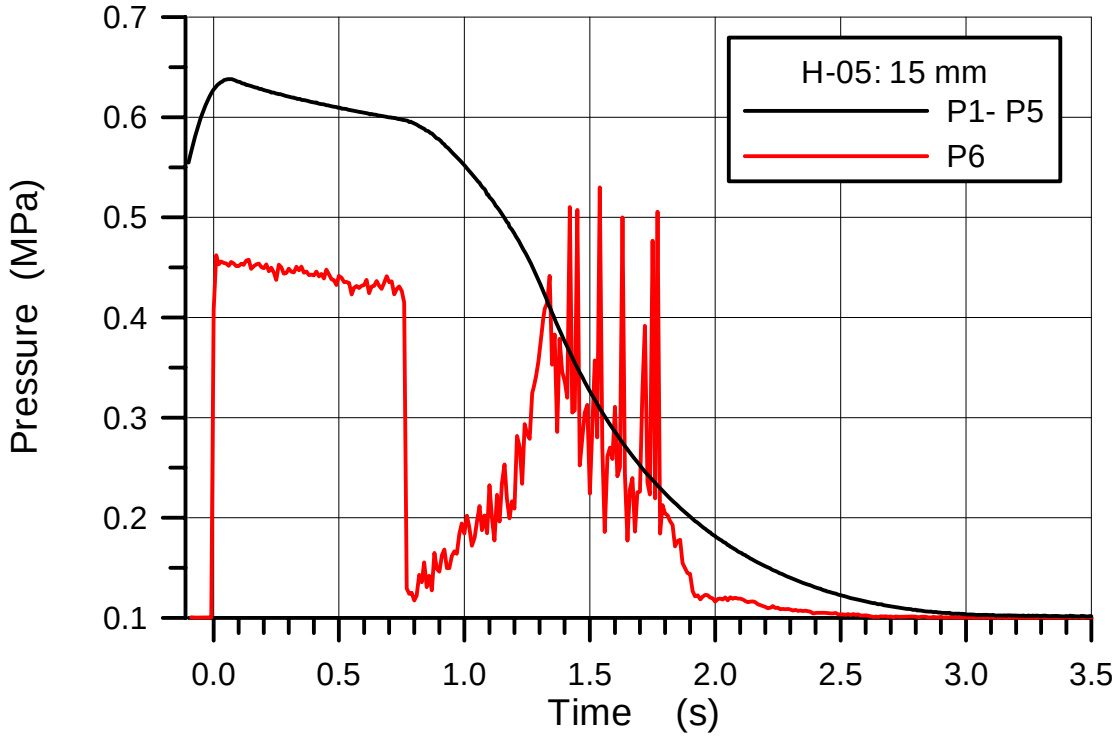

Fig. 5.62 H05 Blow down pressure in the RPV and total pressure on the cavity floor below the hole

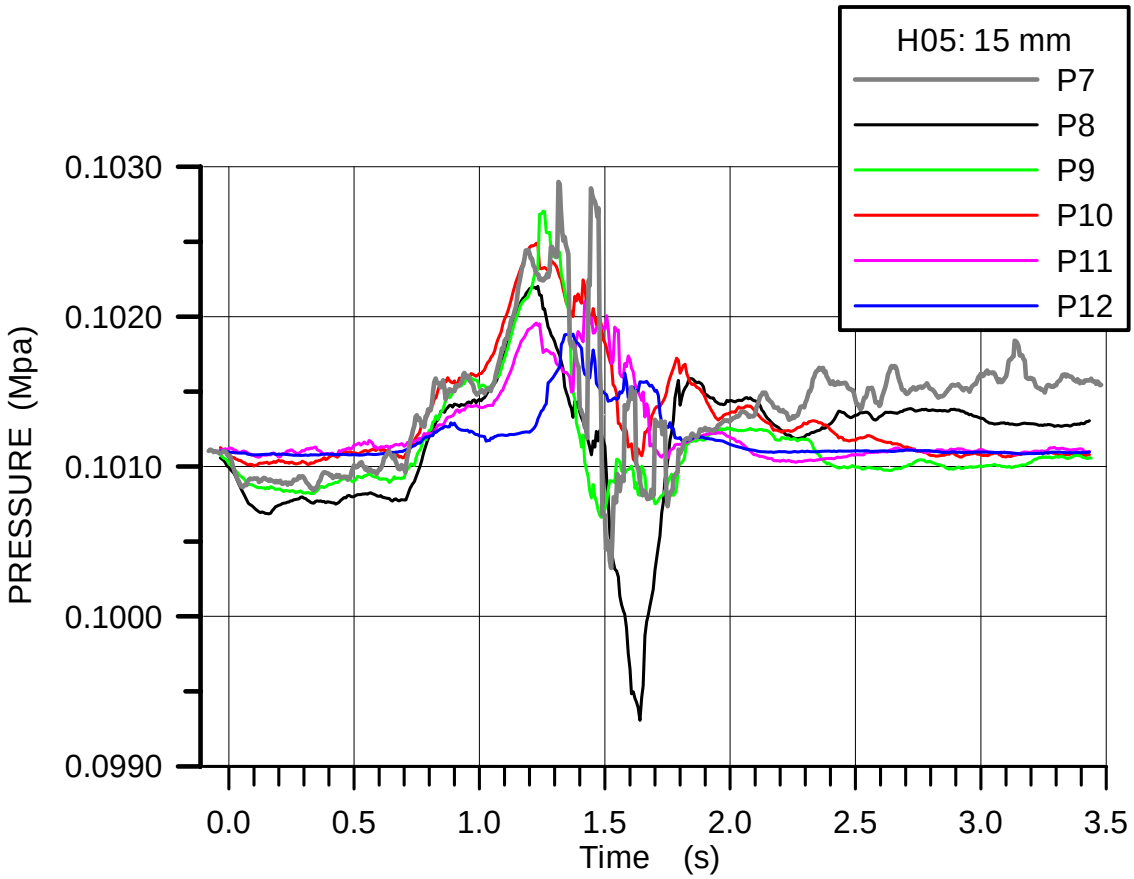

Fig. 5.63 H05 Pressures in the cavity

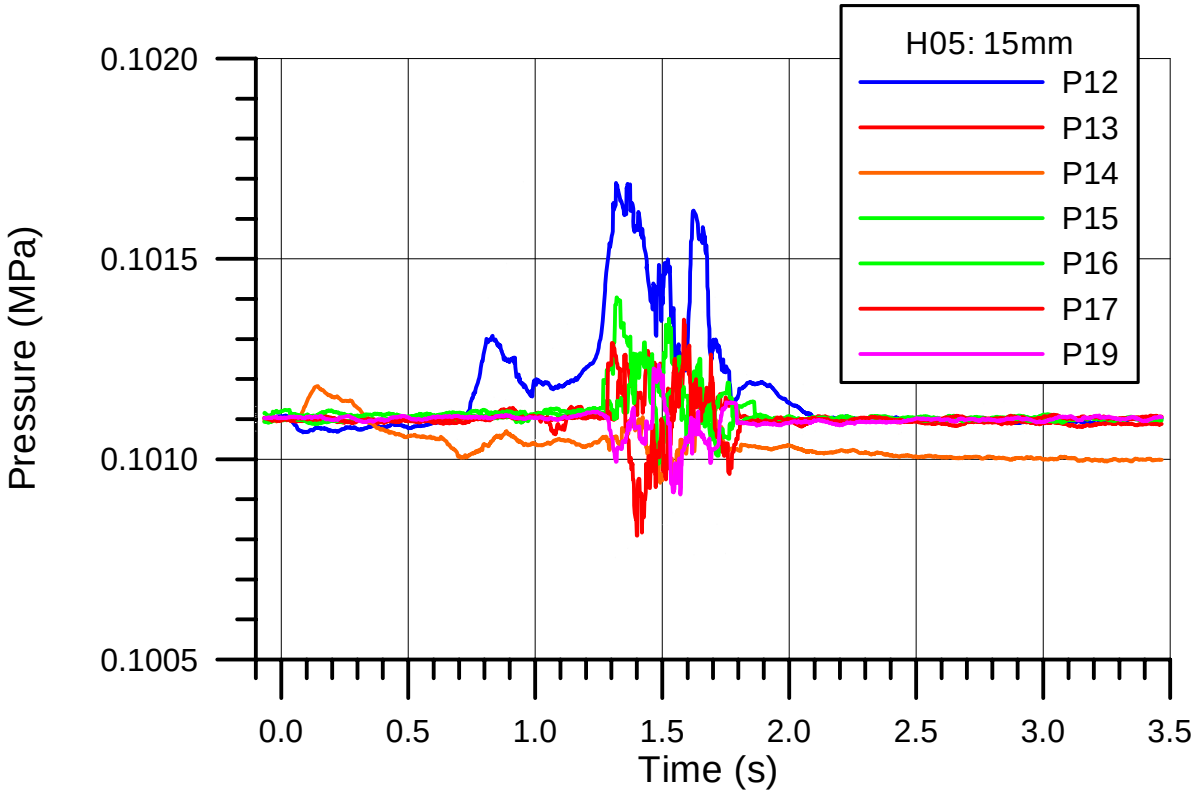

Fig. 5.64 H05 Pressure in the space at the RPV support and in the subcompartments

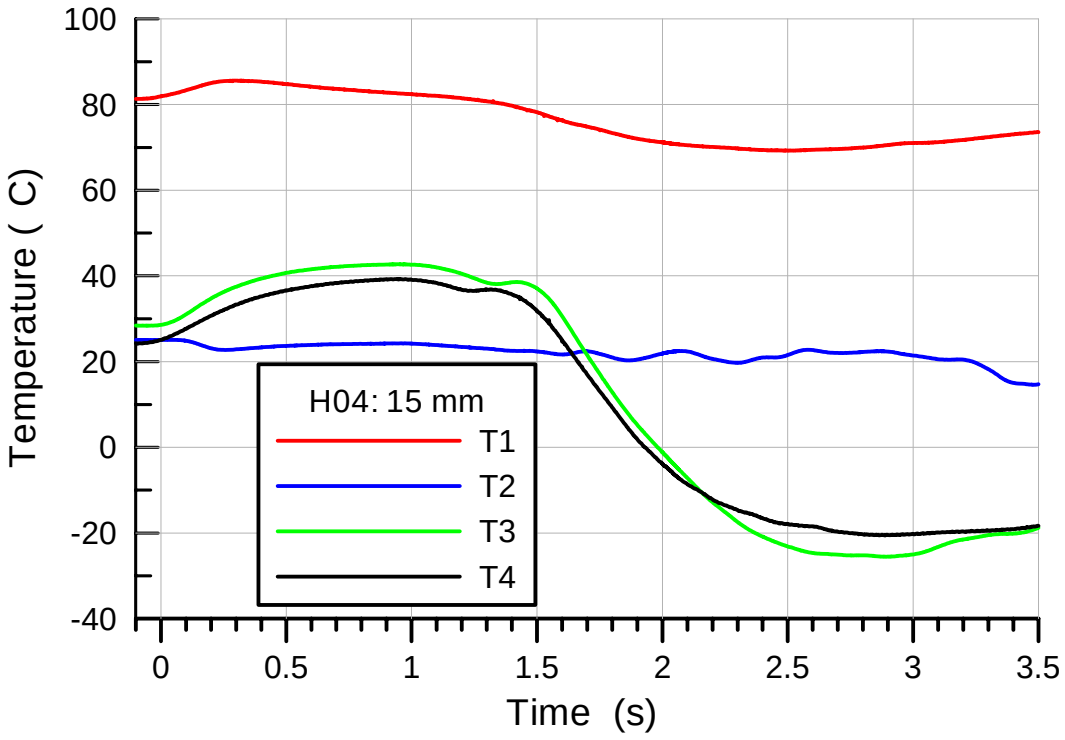

Fig. 5.65 H05 Gas temperatures in the RPV and the cavity

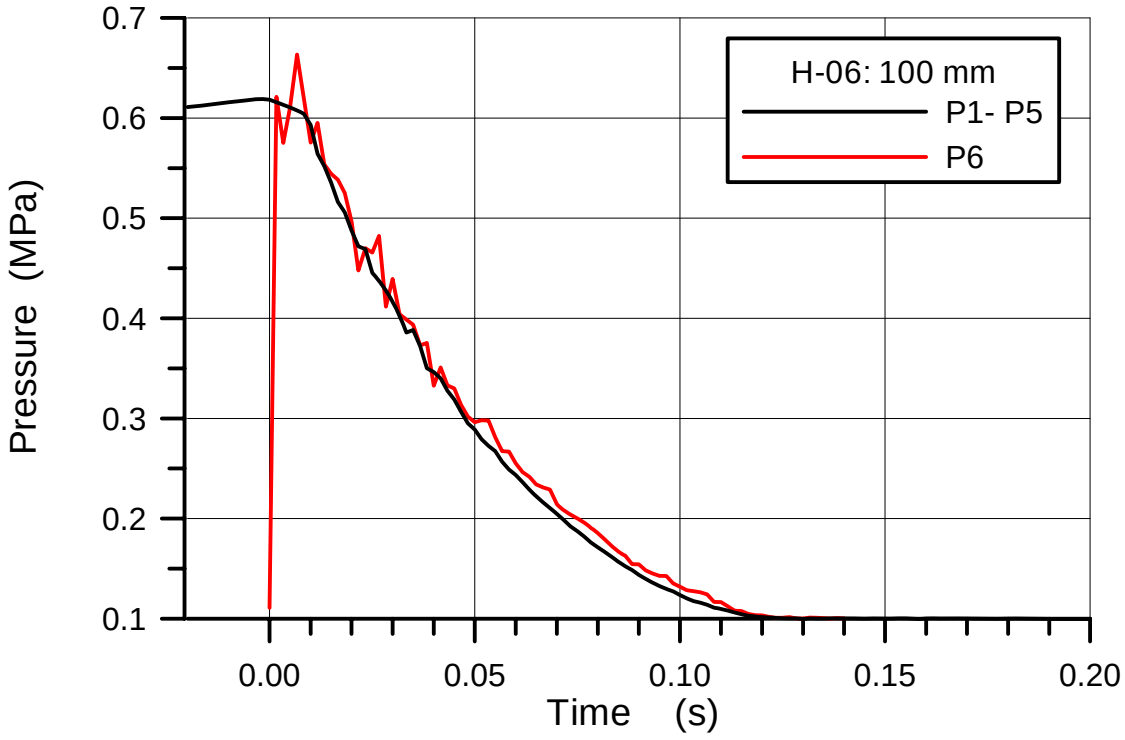

Fig. 5.66 H06 Blow down pressure in the RPV and total pressure on the cavity floor below the hole

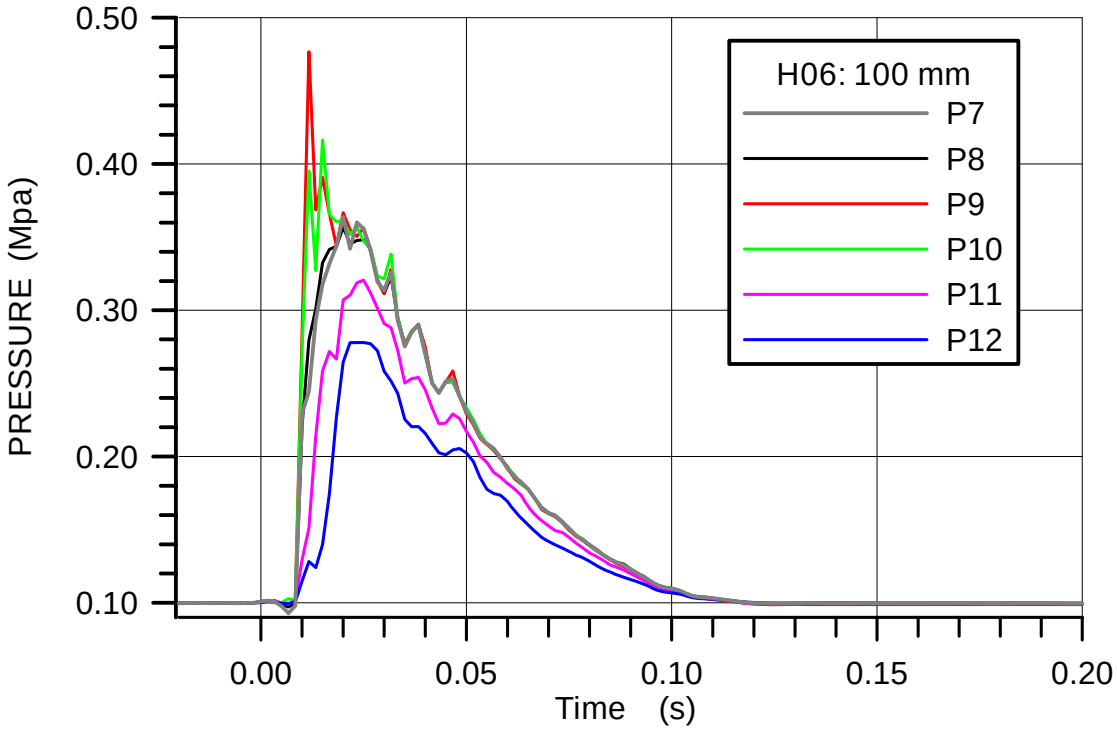

Fig. 5.67 H06 Pressures in the cavity

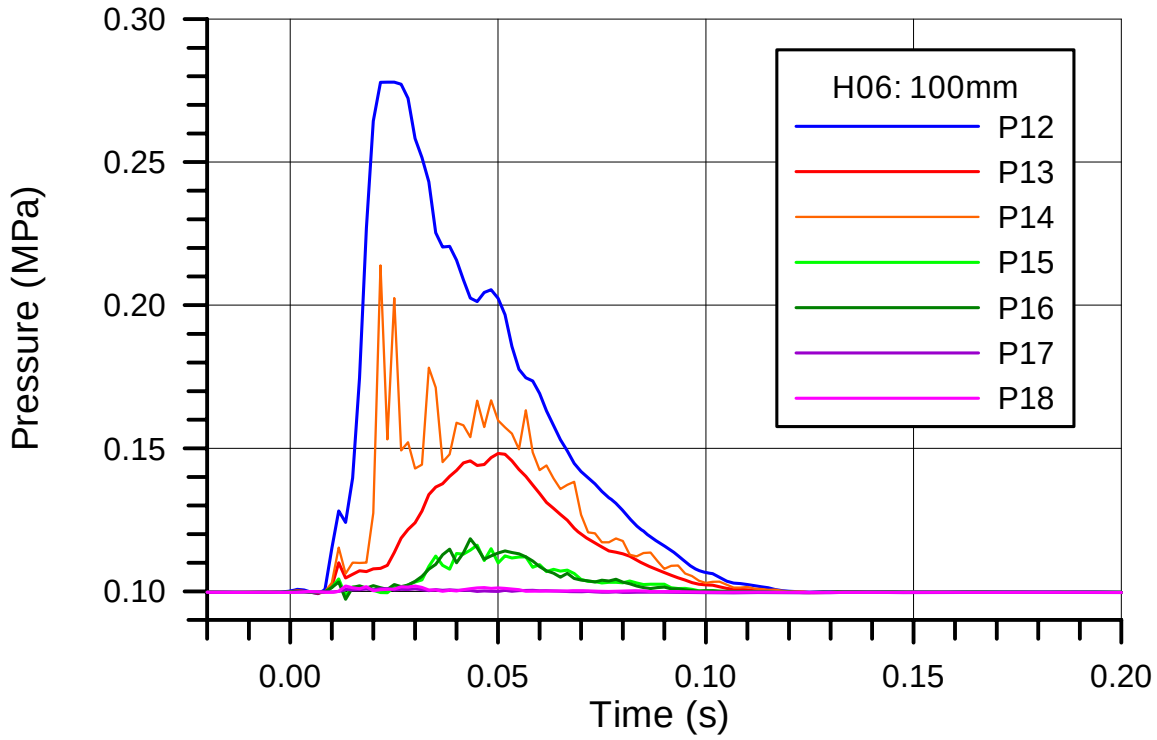

Fig. 5.68 H06 Pressure in the space at the RPV support and in the subcompartments

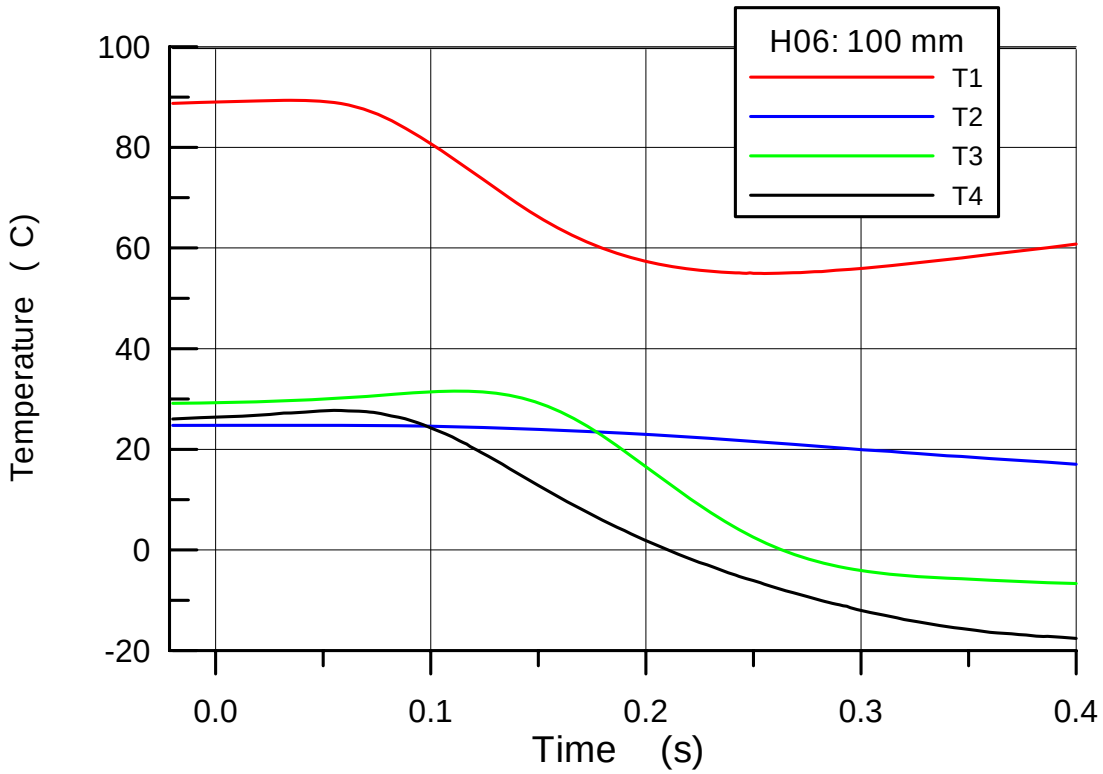

Fig. 5.69 H06 Gas temperatures in the RPV and the cavity

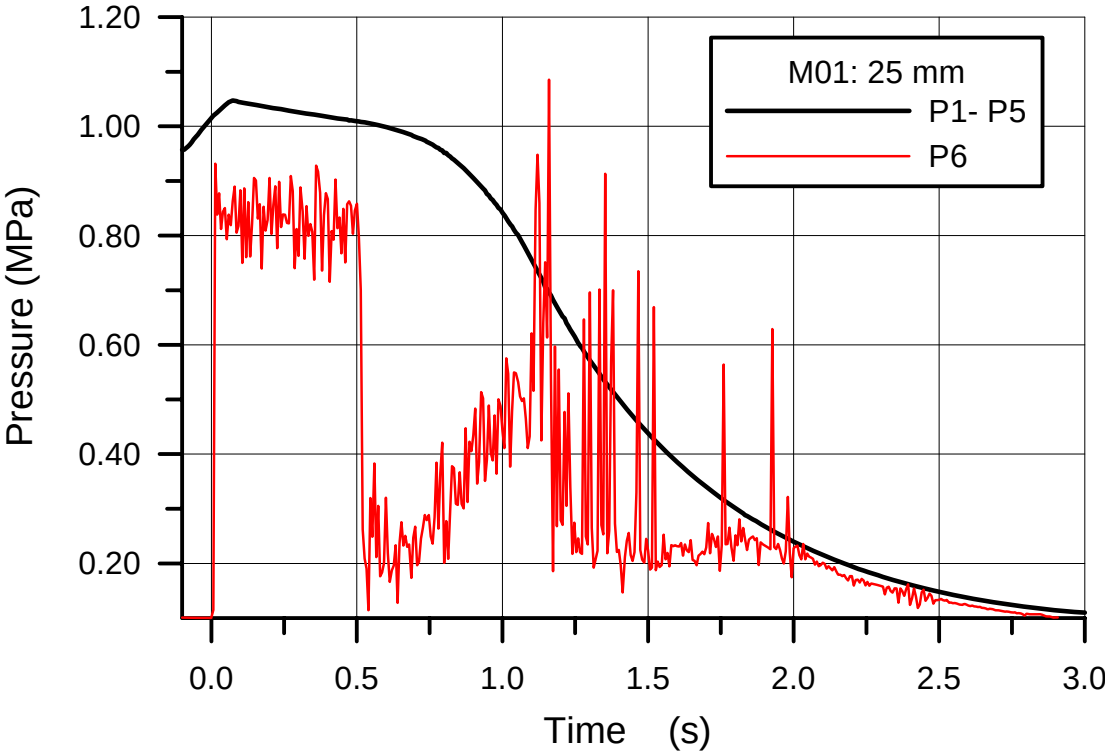

Fig. 5.70 M01 Blow down pressure in the RPV and total pressure on the cavity floor below the hole

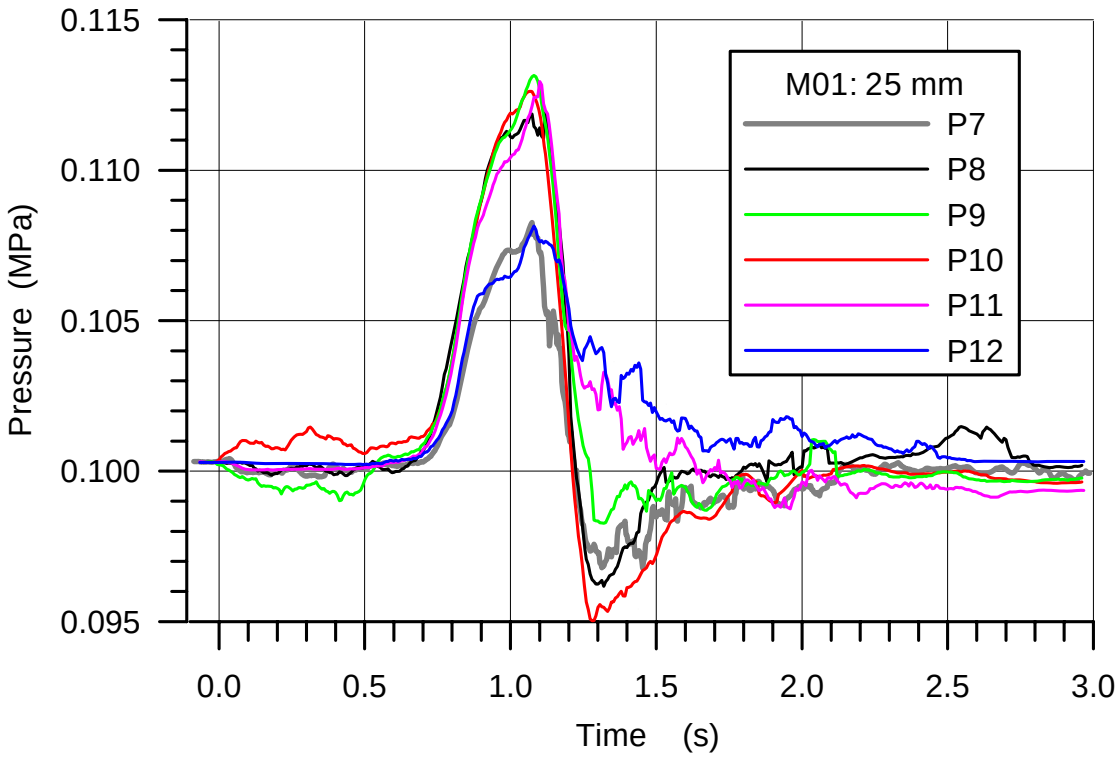

Fig. 5.71 M01 Pressures in the cavity

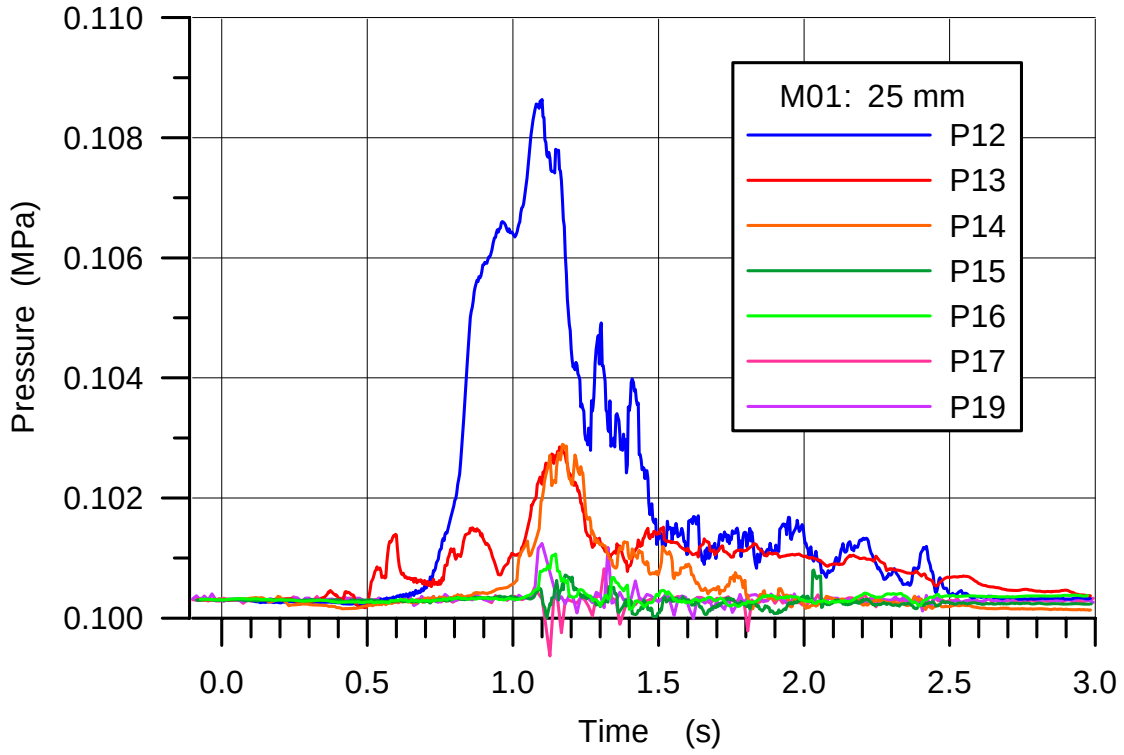

Fig. 5.72 M01 Pressure in the space at the RPV support and in the subcompartments

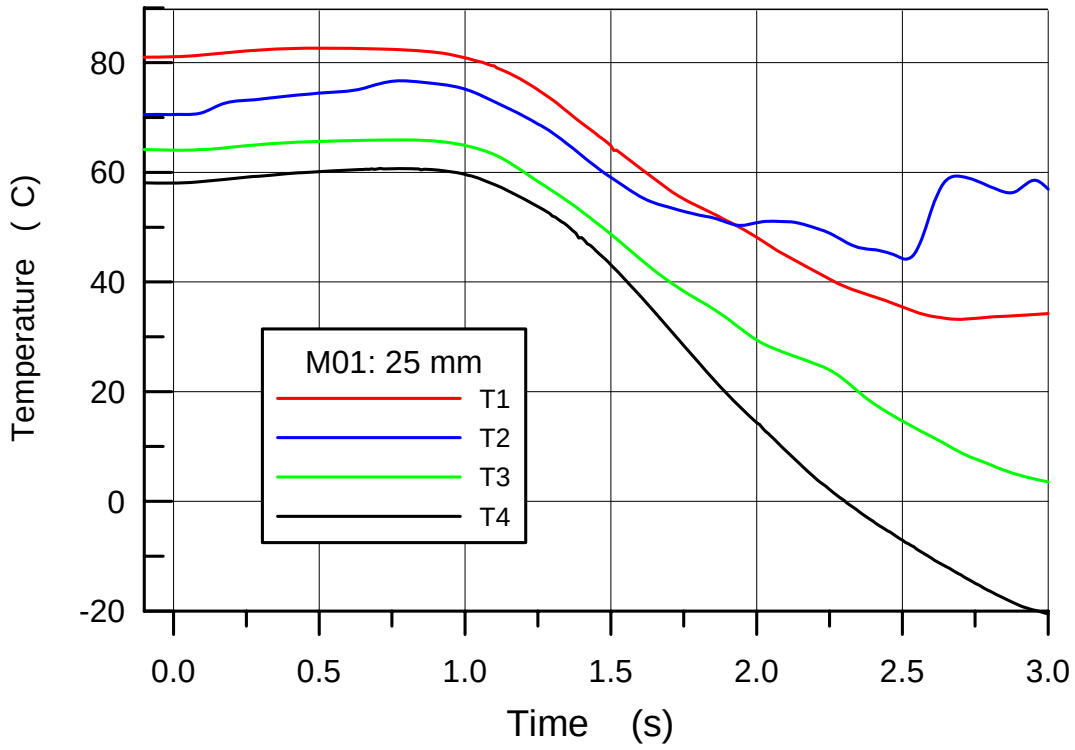

Fig. 5.73 M01 Gas temperatures in the RPV and the cavity

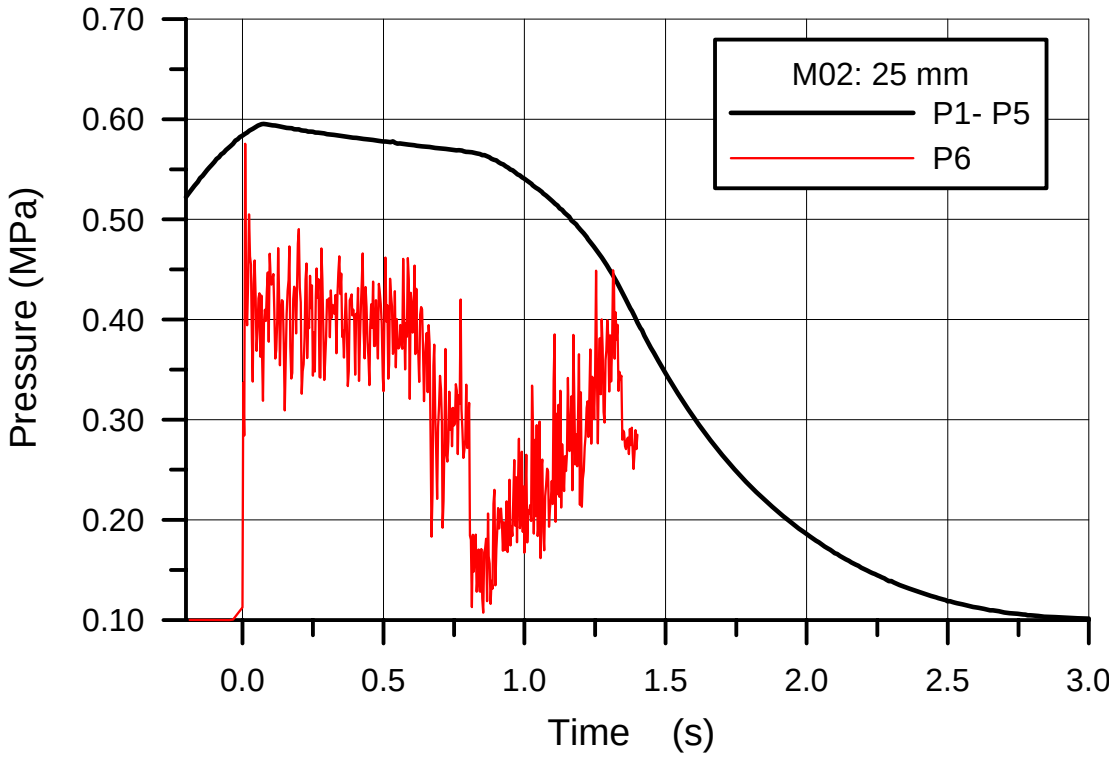

Fig. 5.74 M02 Blow down pressure in the RPV and total pressure on the cavity floor below the hole

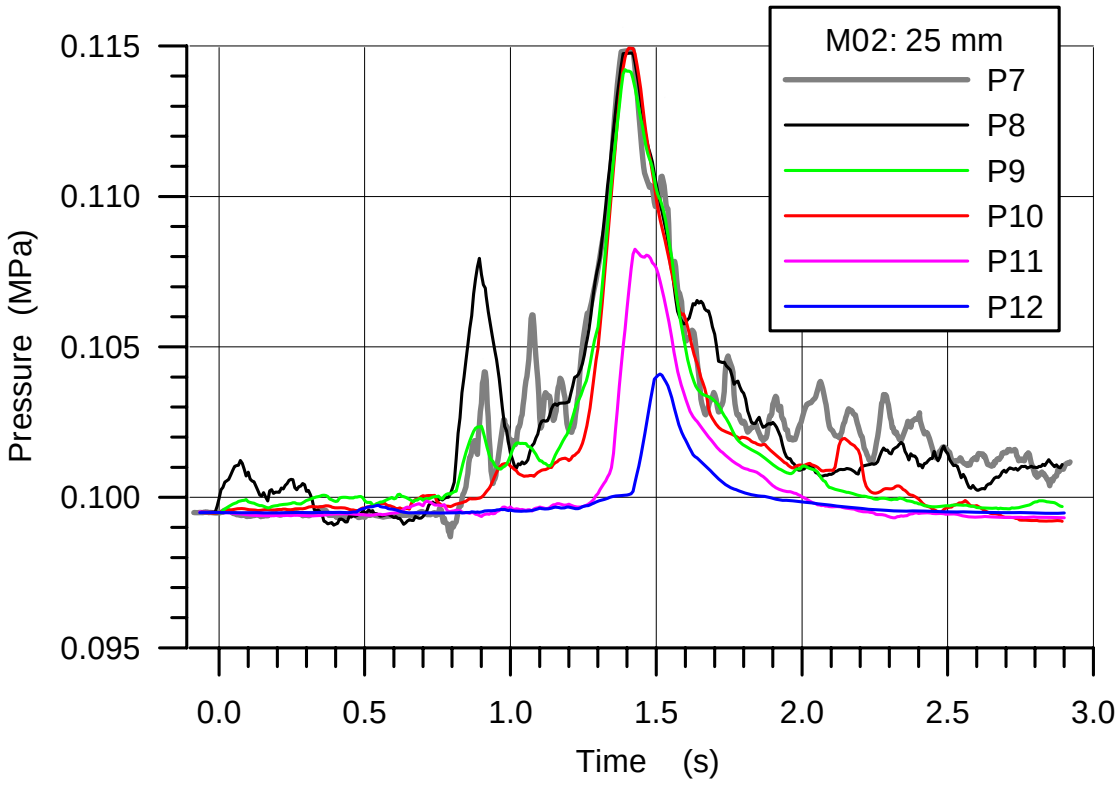

Fig. 5.75 M02 Pressures in the cavity

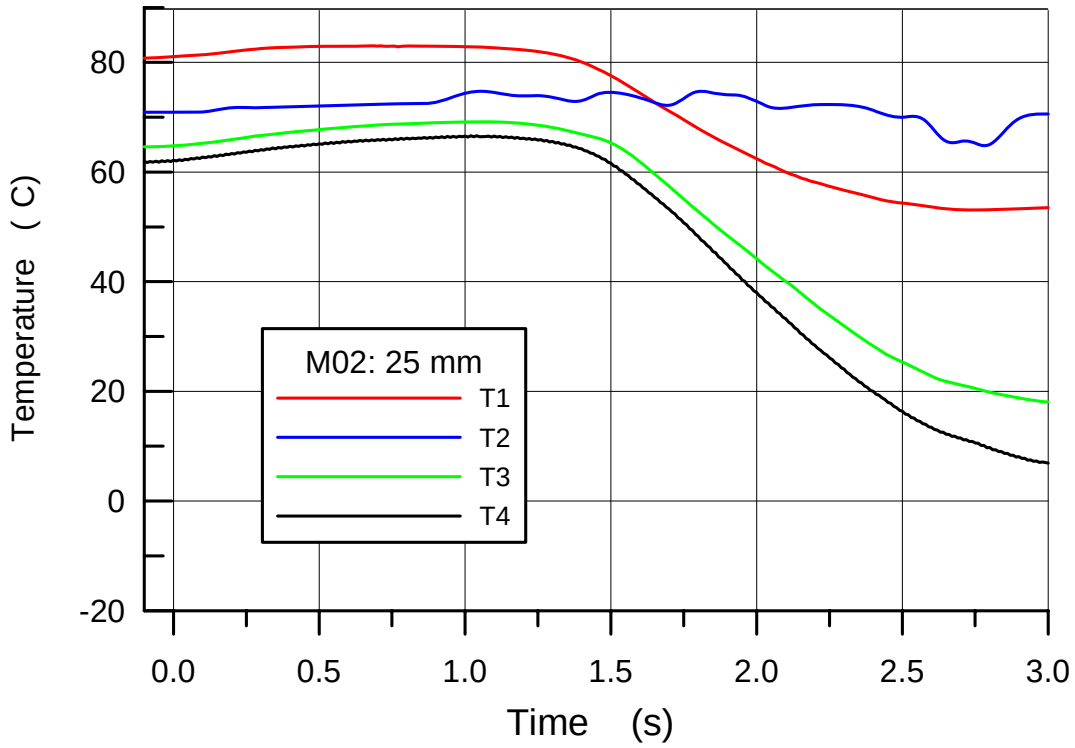

Fig. 5.76 M02 Gas temperatures in the RPV and the cavity

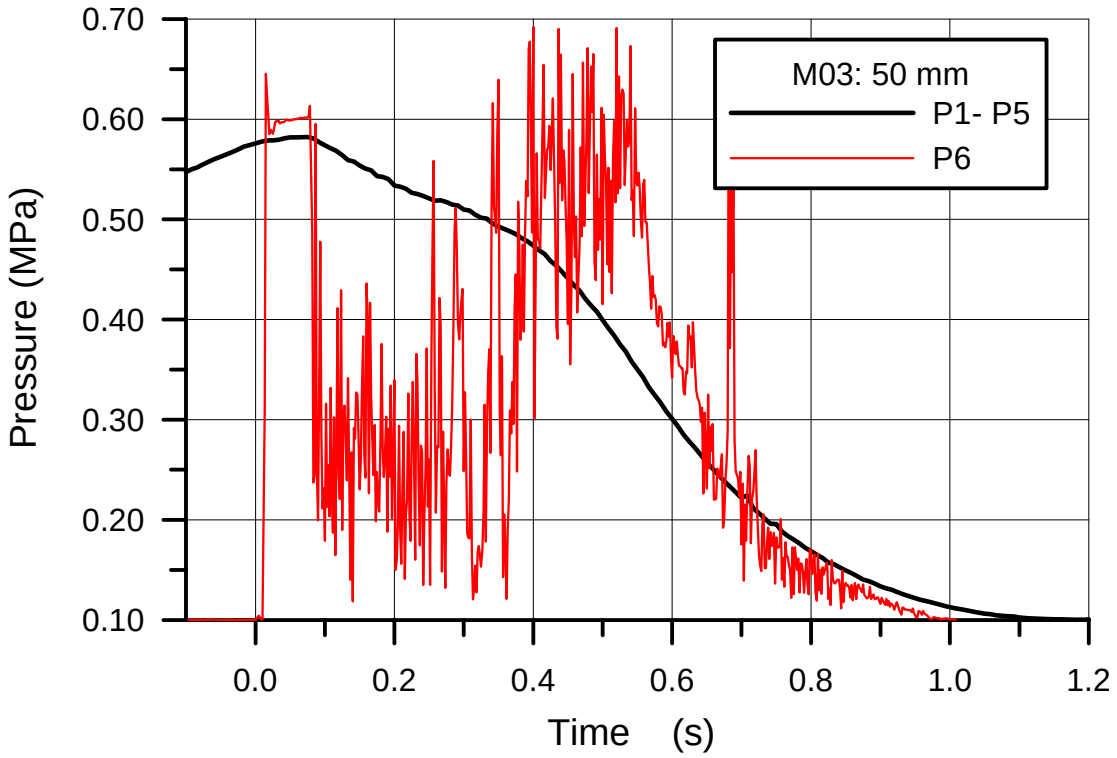

Fig. 5.77 M03 Blow down pressure in the RPV and total pressure on the cavity floor below the hole

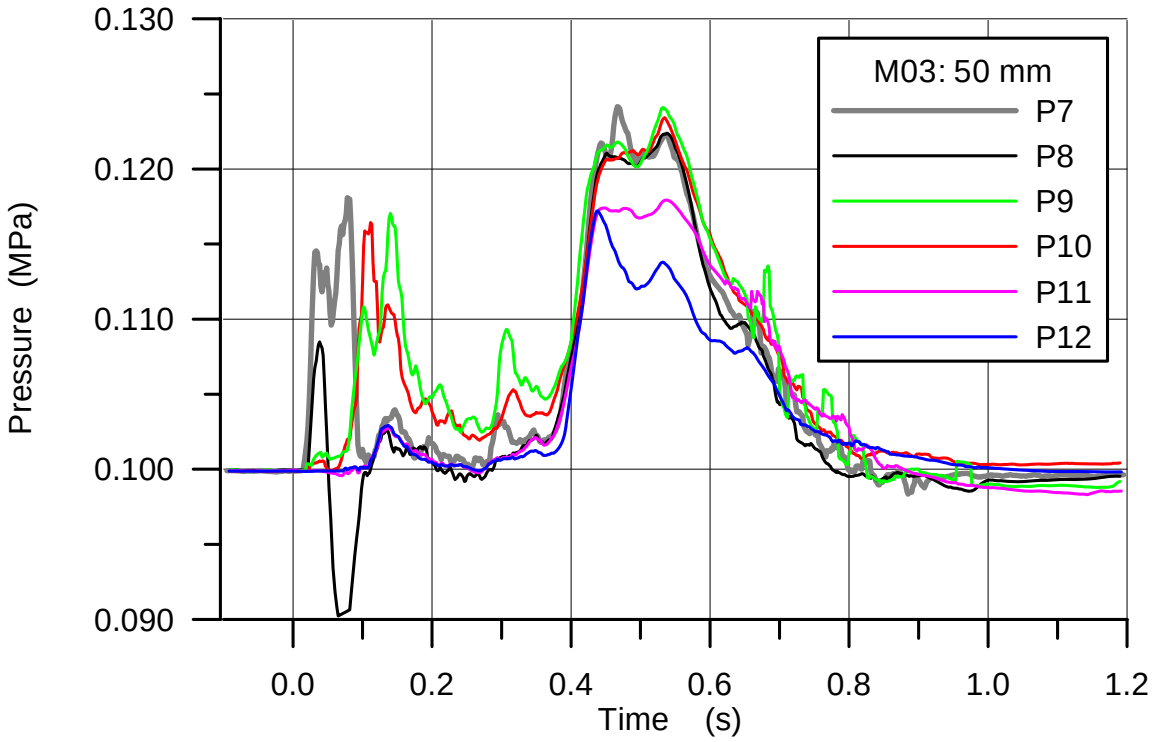

Fig. 5.78 M03 Pressures in the cavity

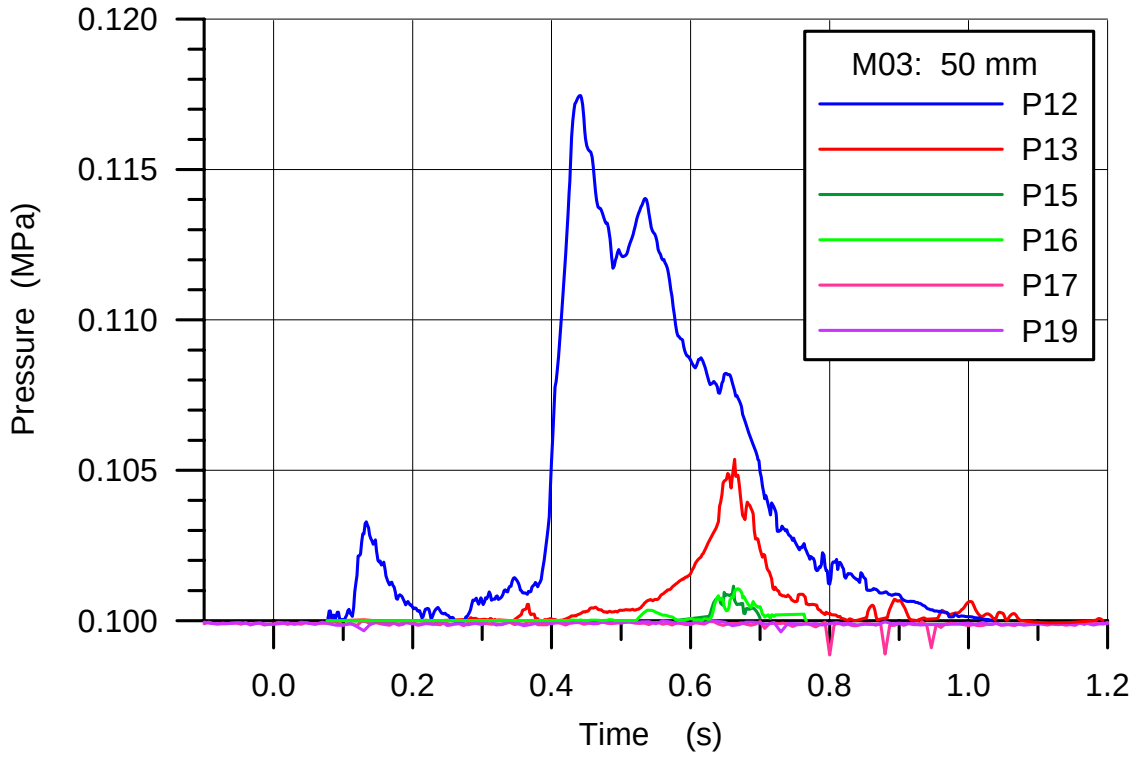

Fig. 5.79 M03 Pressure in the space at the RPV support and in the subcompartments

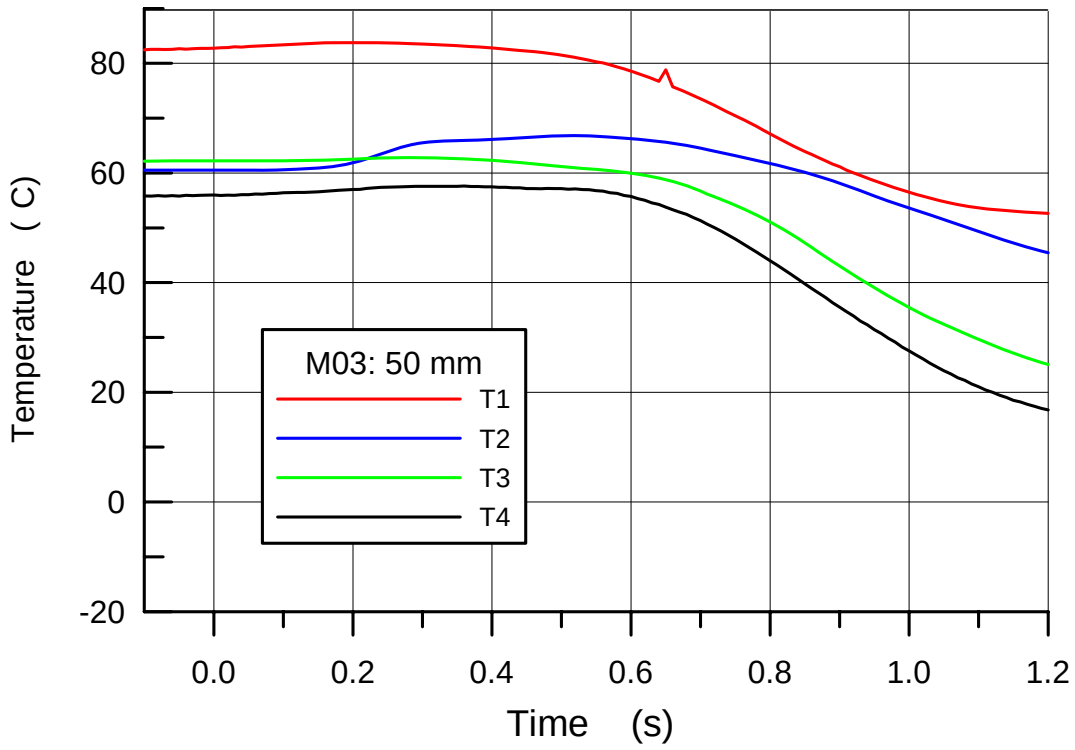

Fig. 5.80 M03 Gas temperatures in the RPV and the cavity

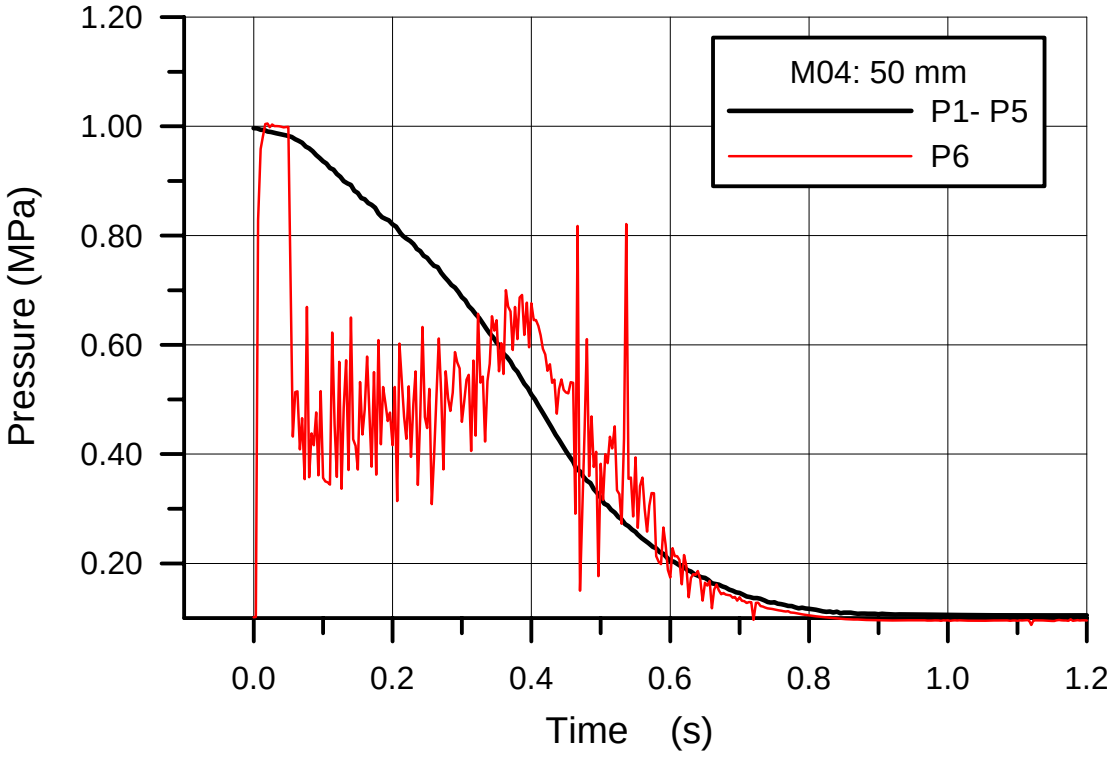

Fig. 5.81 M04 Blow down pressure in the RPV and total pressure on cavity floor below hole

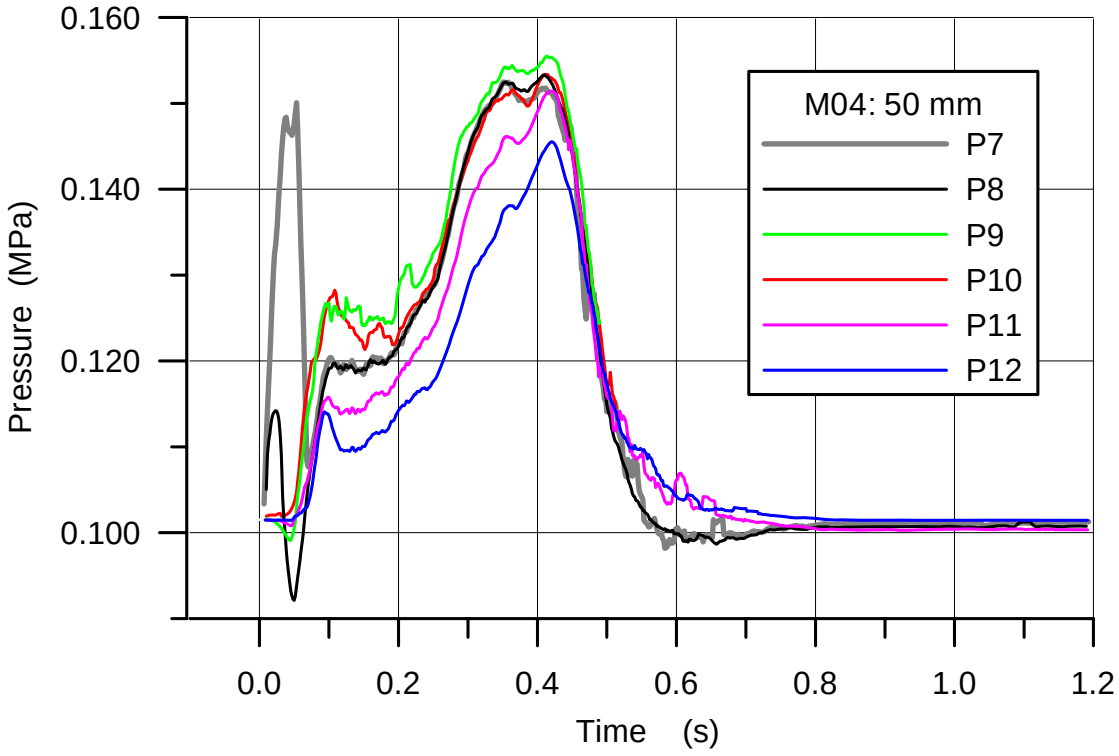

Fig. 5.82 M04 Pressures in the cavity

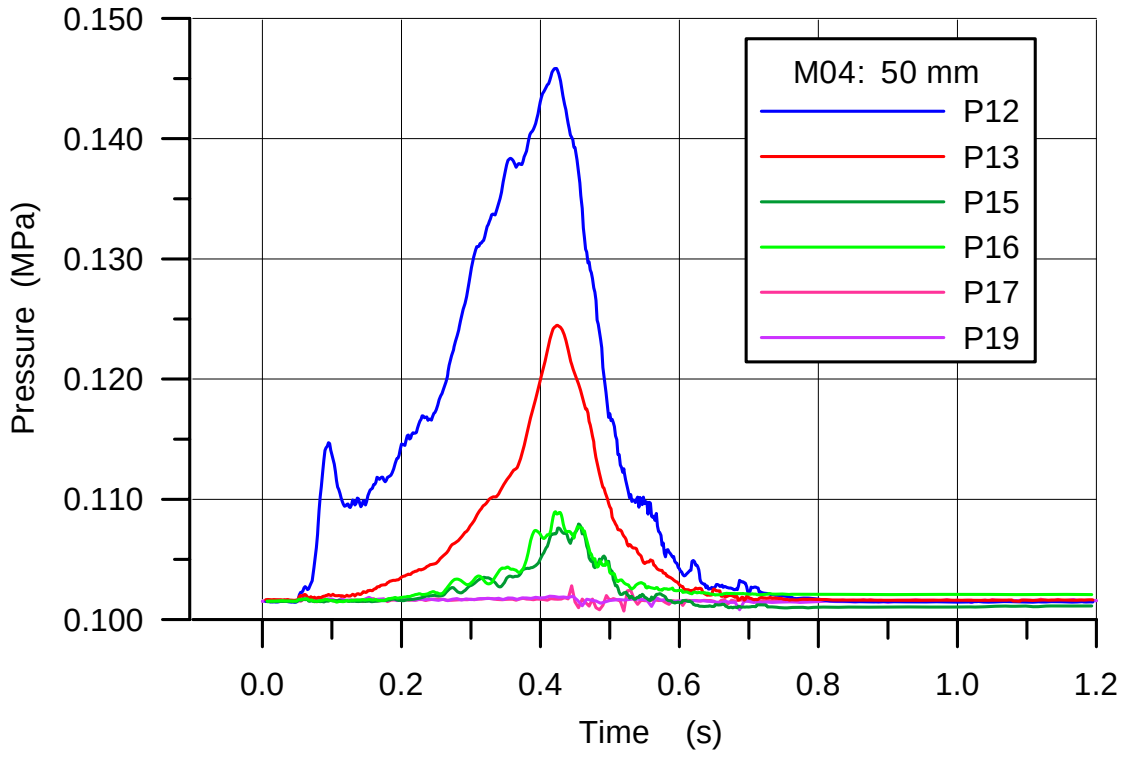

Fig. 5.83 M04 Pressure in the space at the RPV support and in the subcompartments

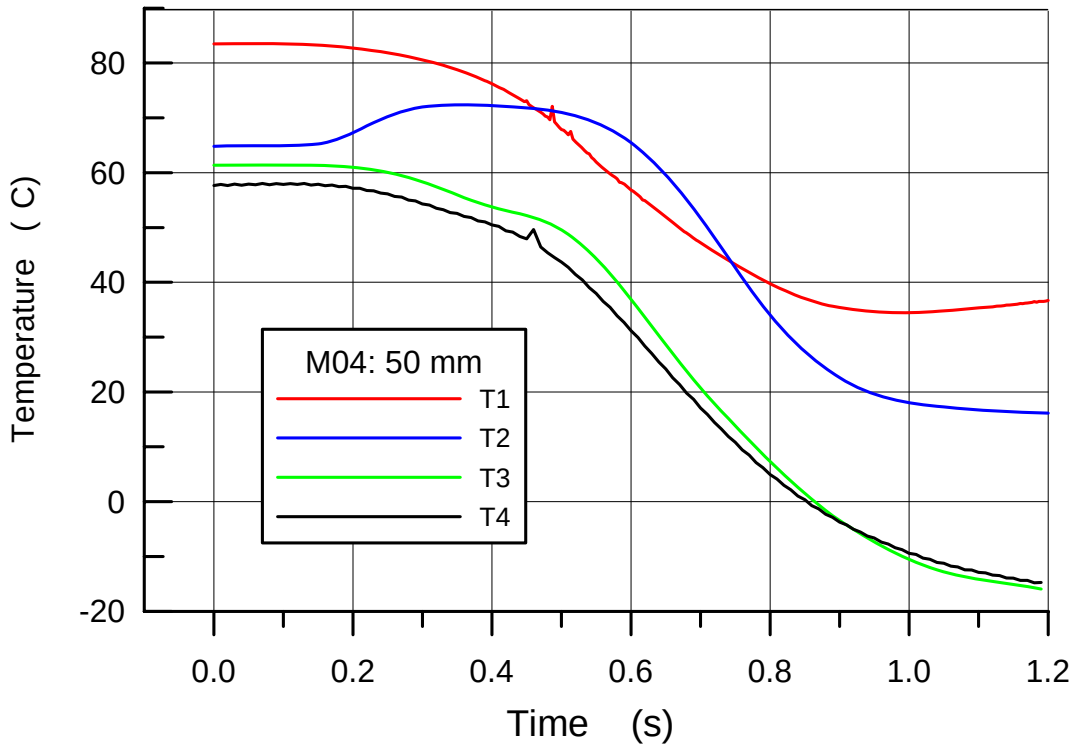

Fig. 5.84 M04 Gas temperatures in the RPV and the cavity

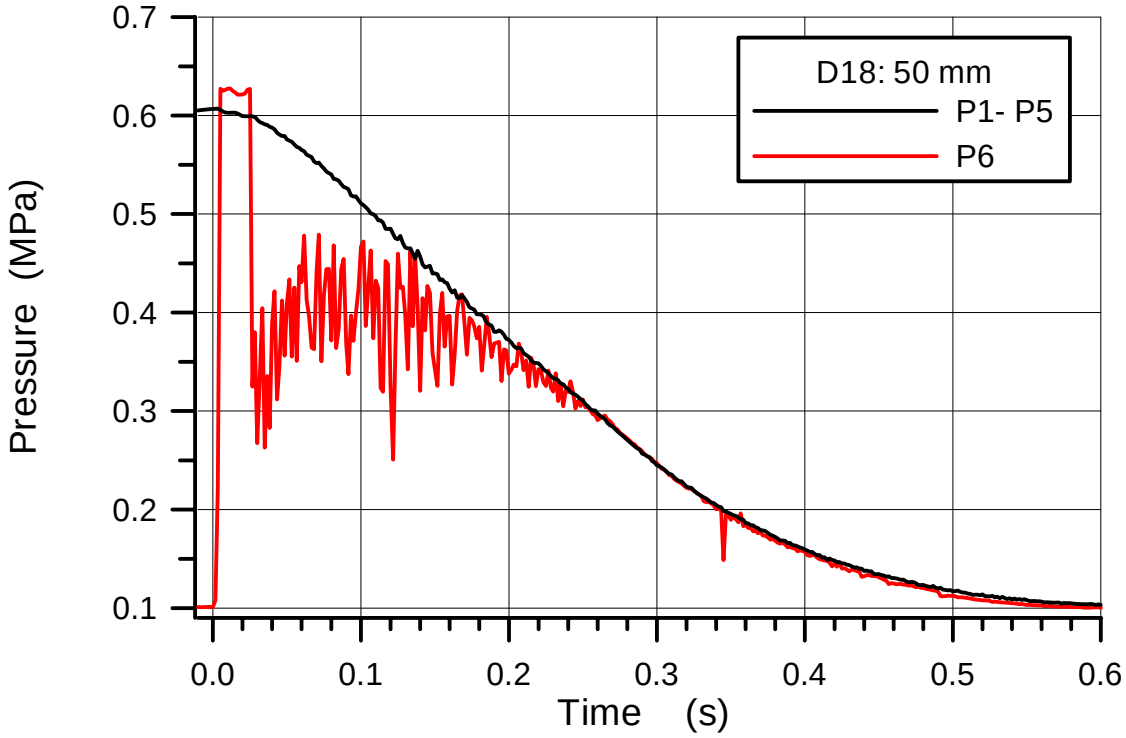

Fig. 5.85 D18 Blow down pressure in the RPV and total pressure on cavity floor below hole

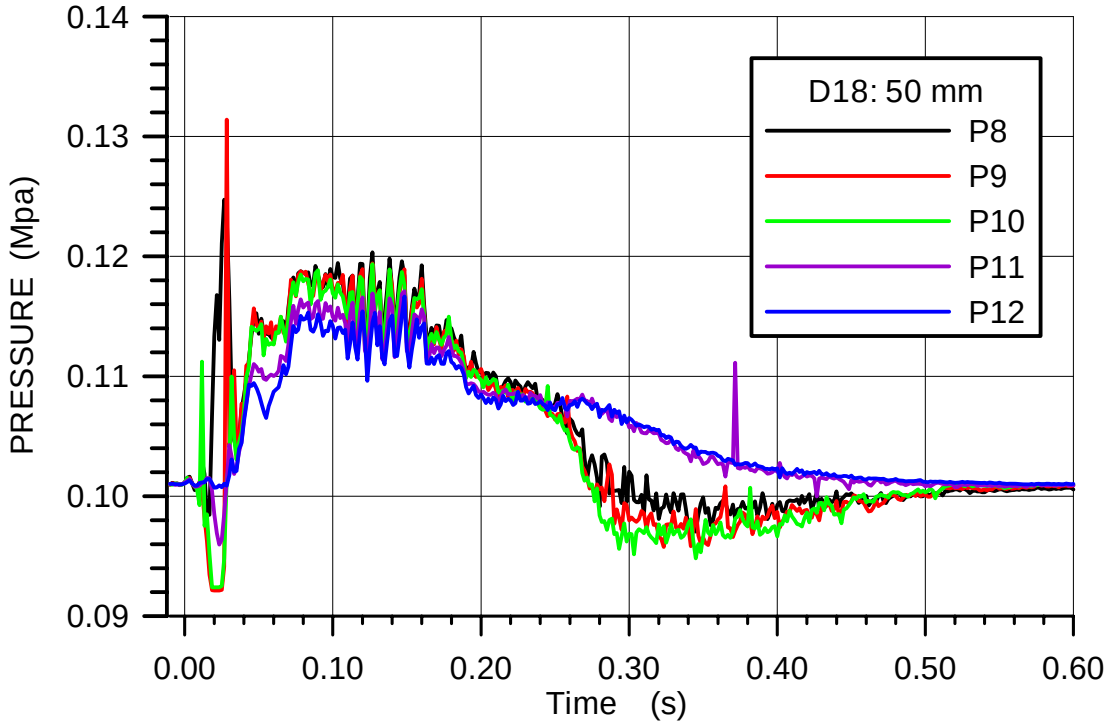

Fig. 5.86 D18 Pressures in the cavity

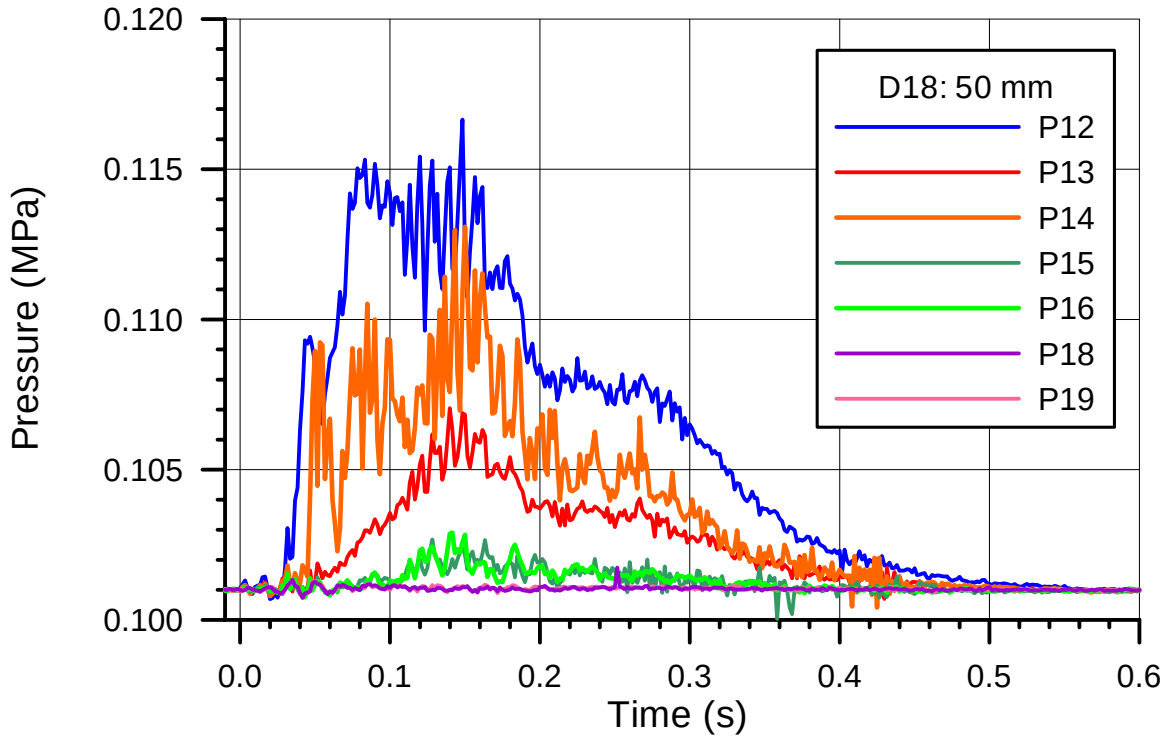

Fig. 5.87 D18 Pressure in the space at the RPV support and in the subcompartments

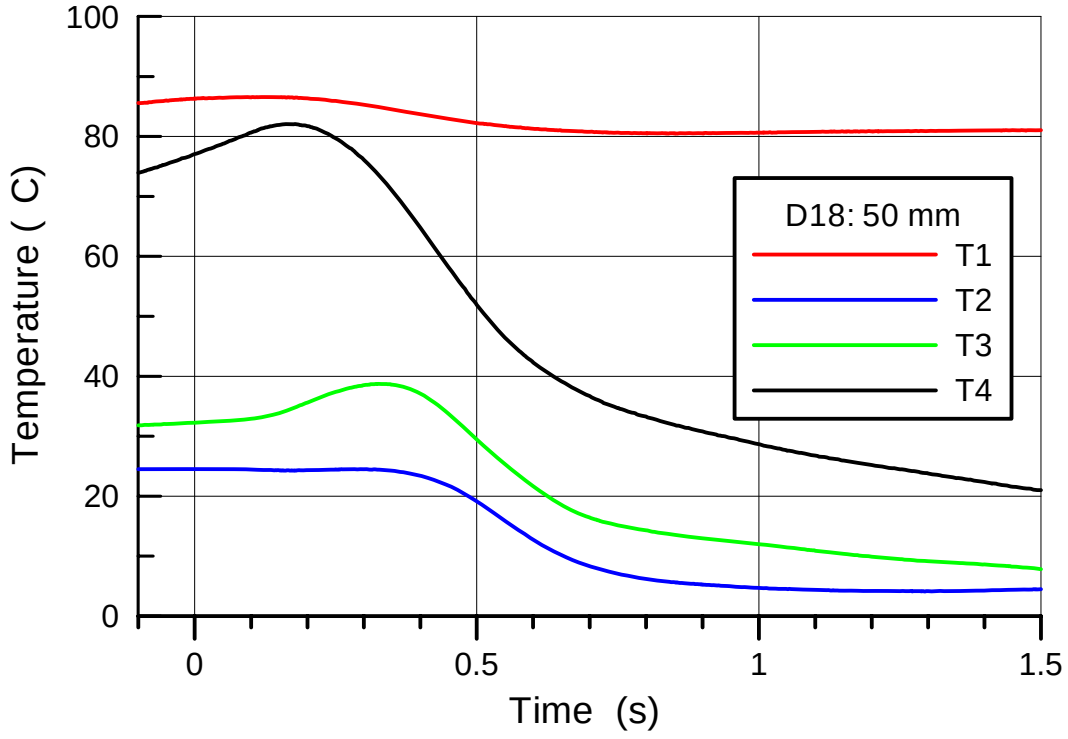

Fig. 5.88 D18 Gas temperatures in the RPV and the cavity

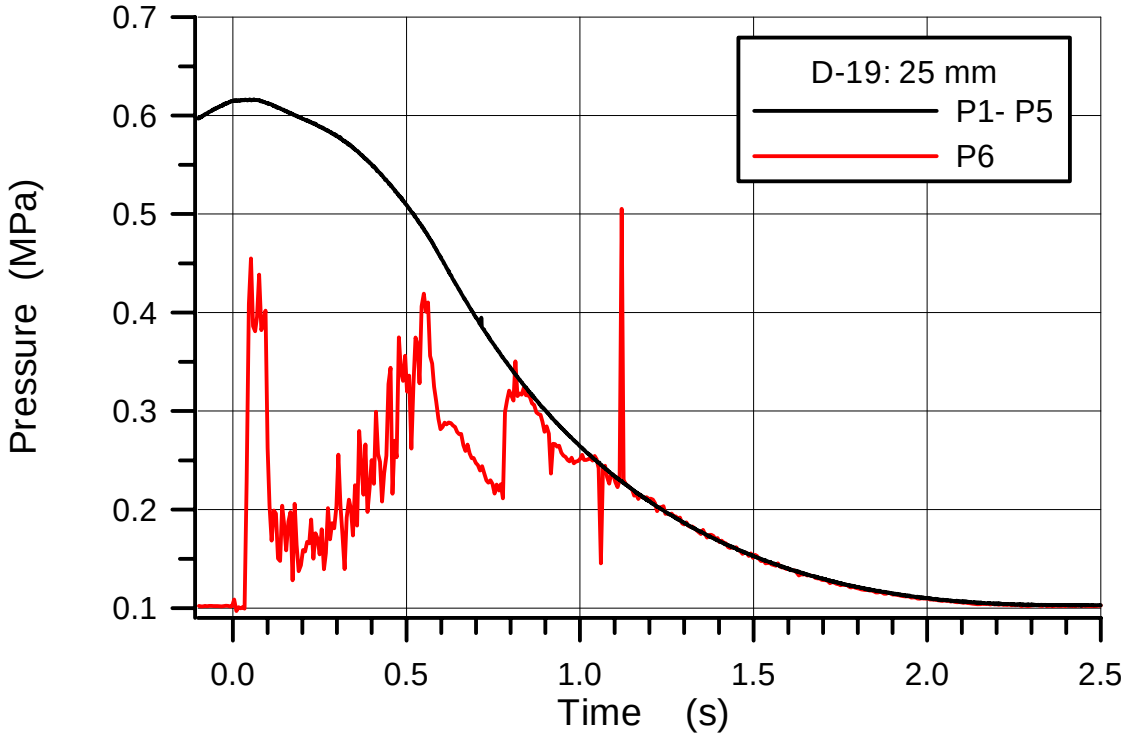

Fig. 5.89 D19 Blow down pressure in the RPV and total pressure on cavity floor below hole

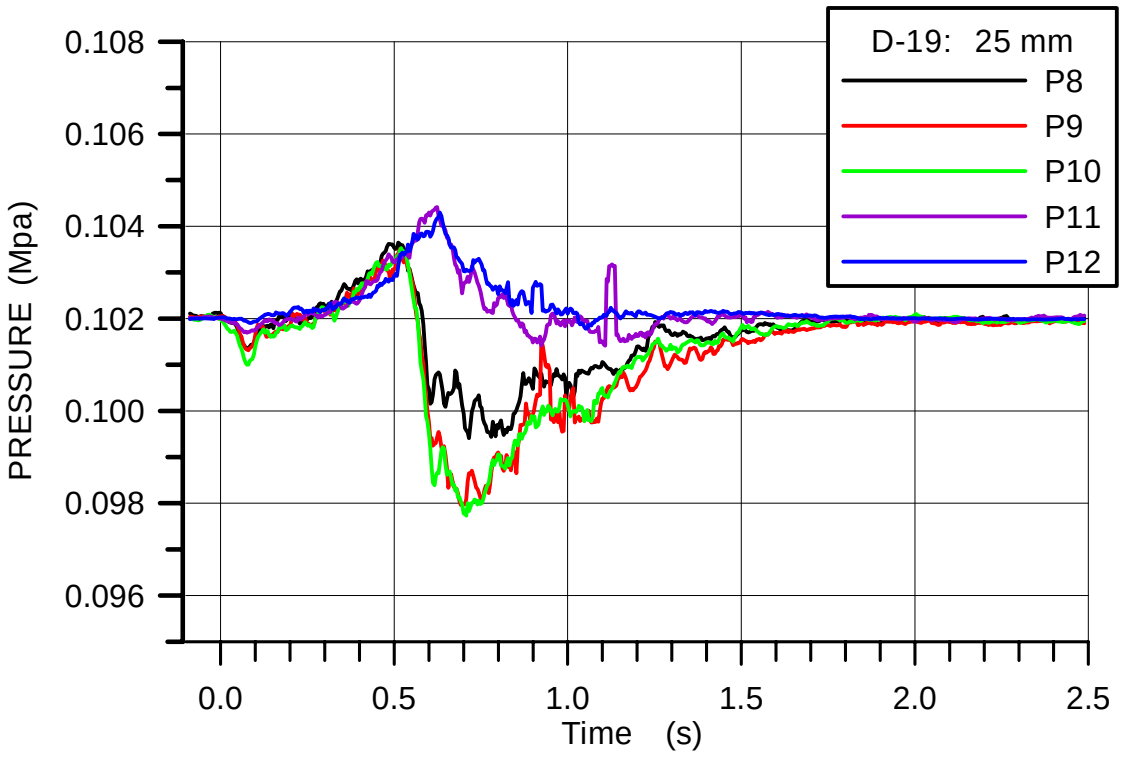

Fig. 5.90 D19 Pressures in the cavity

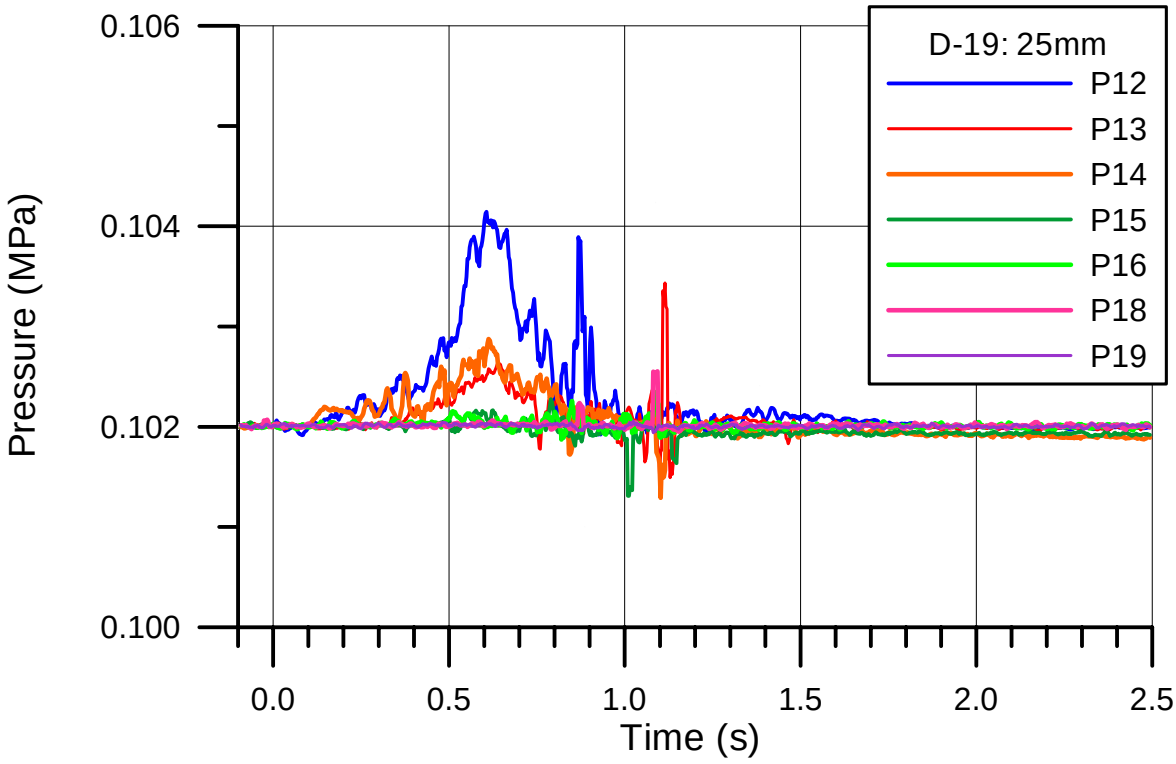

Fig. 5.91 D19 Pressure in the space at the RPV support and in the subcompartments

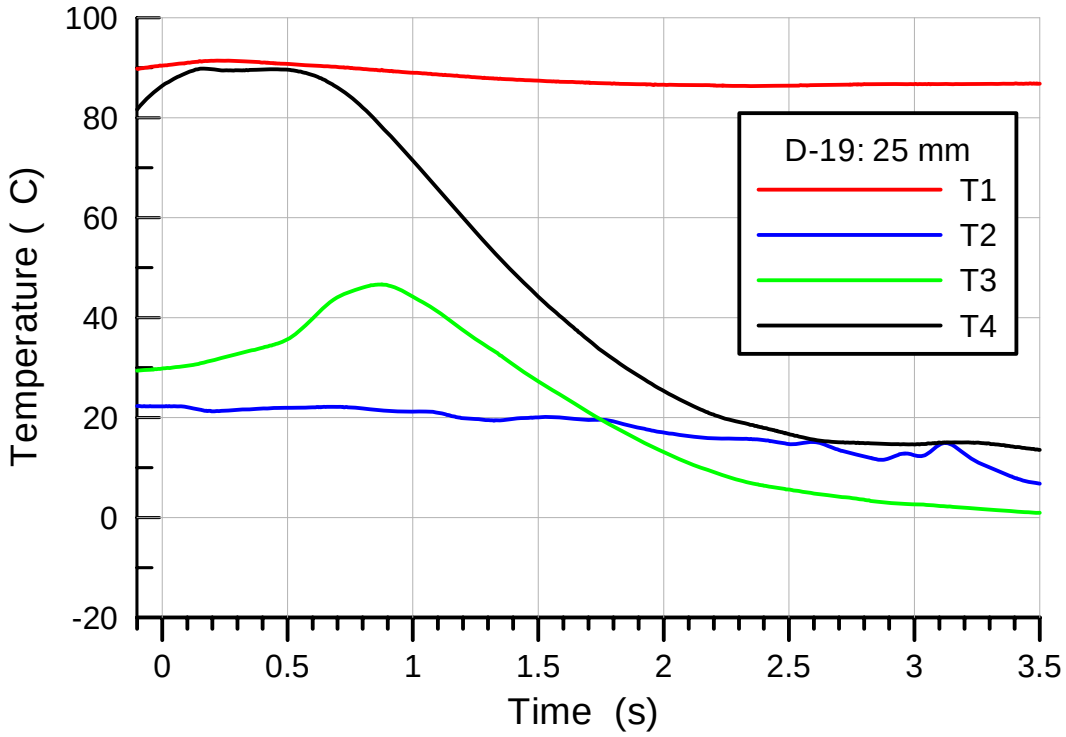

Fig. 5.92 D19 Gas temperatures in the RPV and the cavity

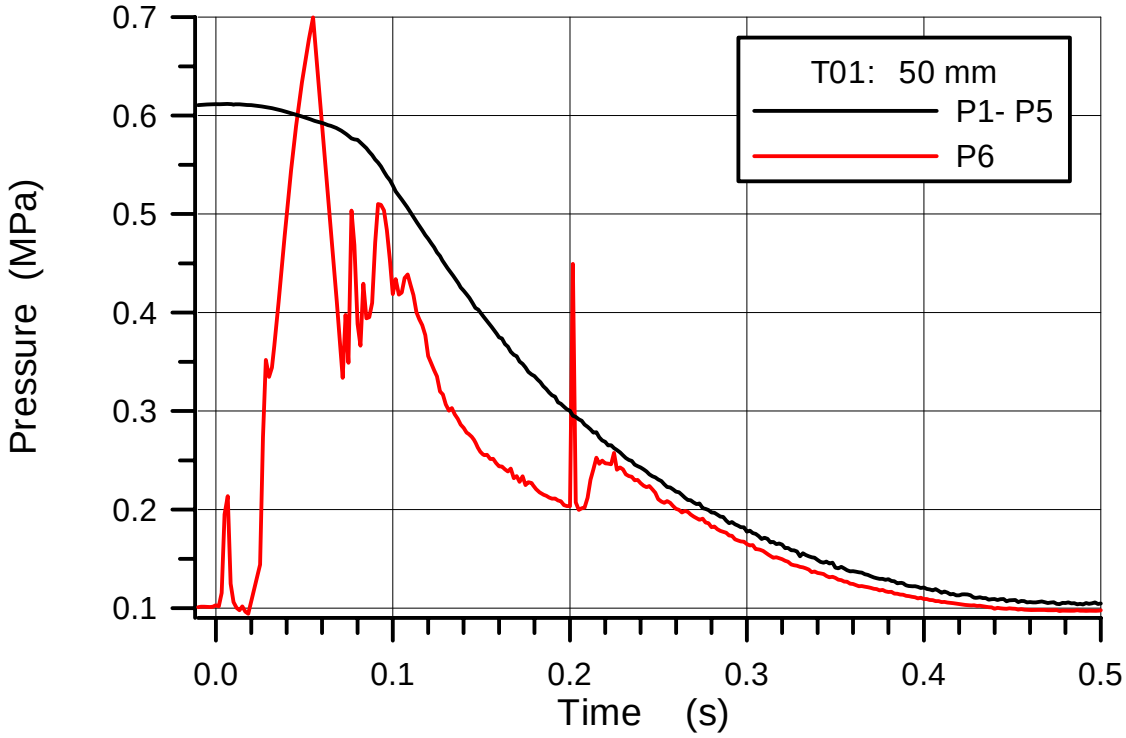

Fig. 5.93 T01 Blow down pressure in the RPV and total pressure on cavity floor below hole

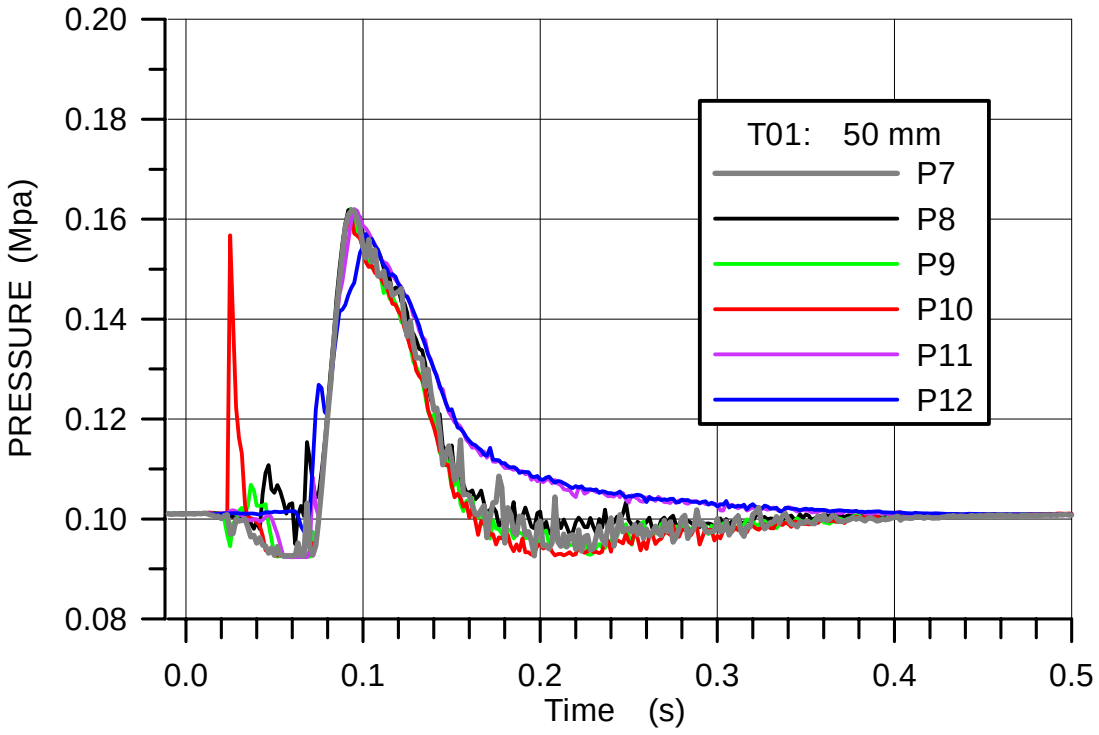

Fig. 5.94 T01 Pressures in the cavity

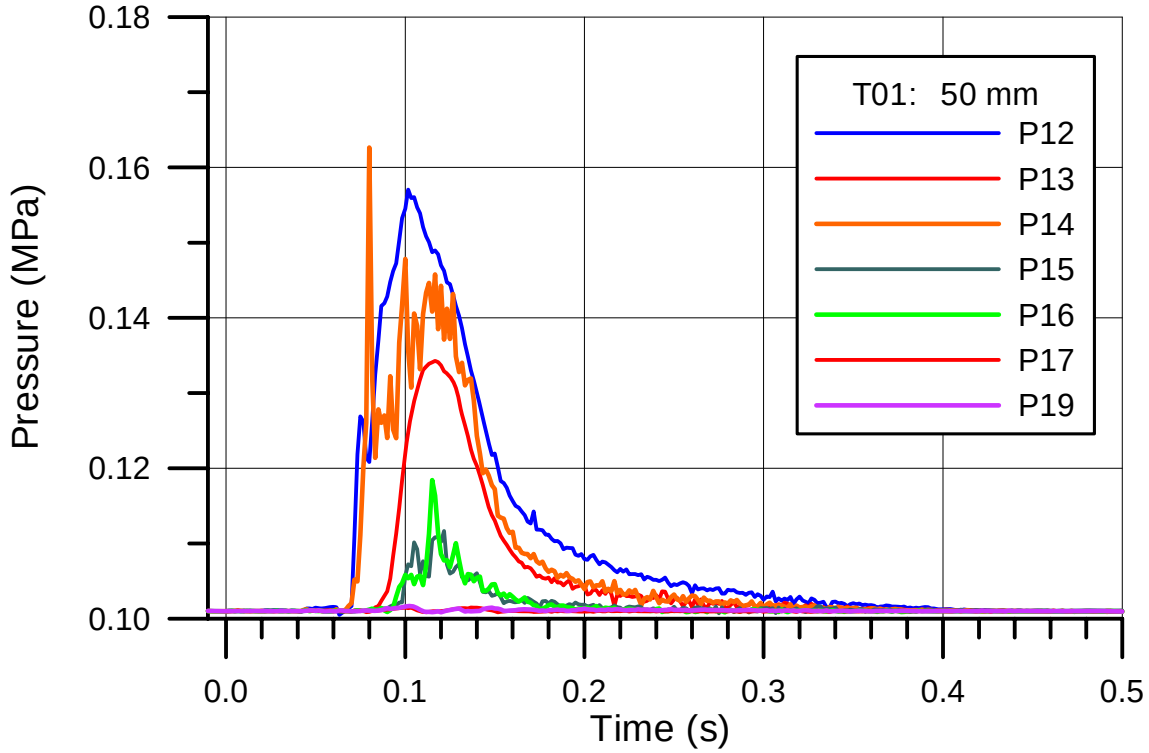

Fig. 5.95 T01 Pressure in the space at the RPV support and in the subcompartments

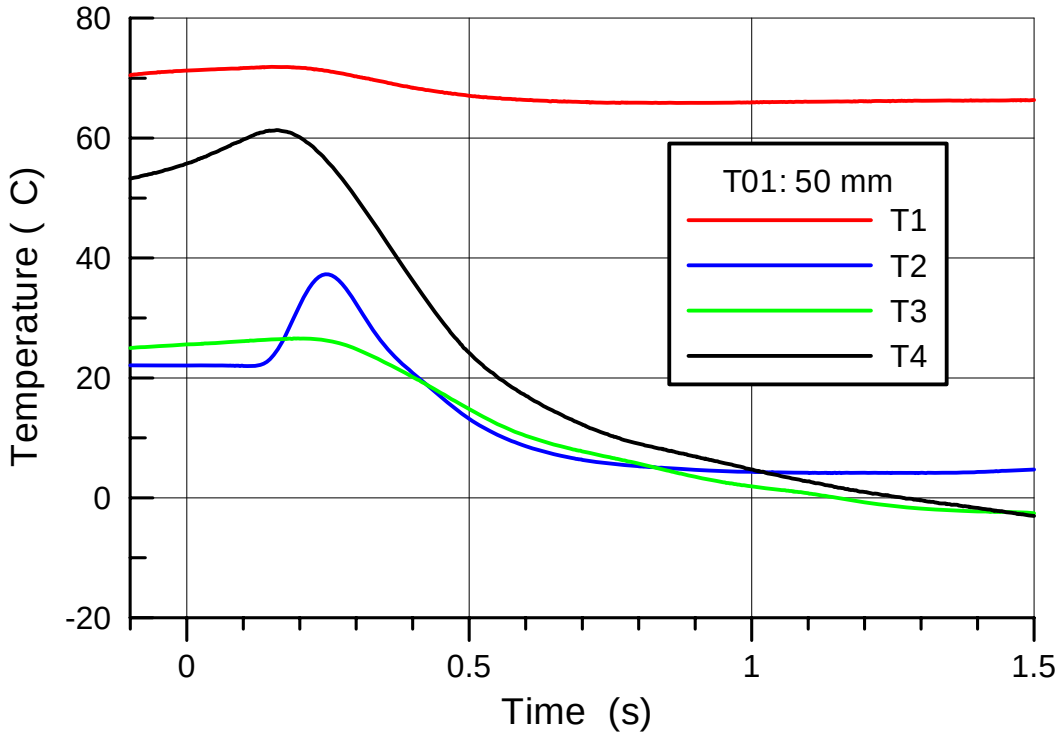

Fig. 5.96 T01 Gas temperatures in the RPV and the cavity

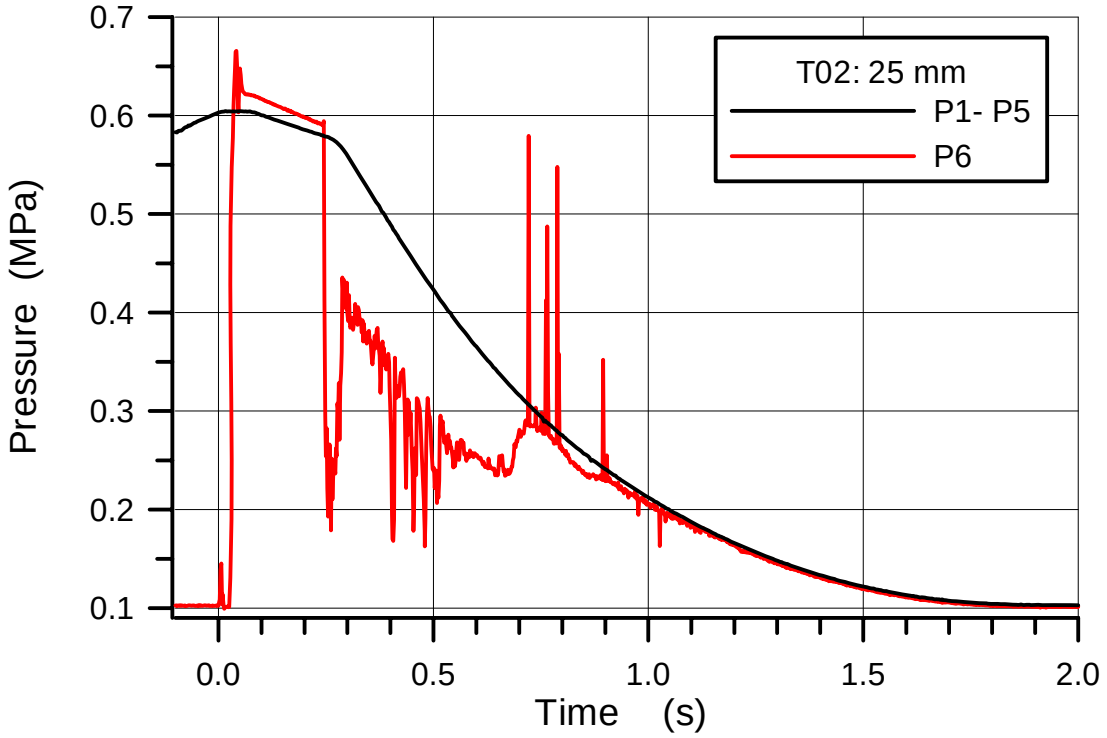

Fig. 5.97 T02 Blow down pressure in the RPV and total pressure on cavity floor below hole

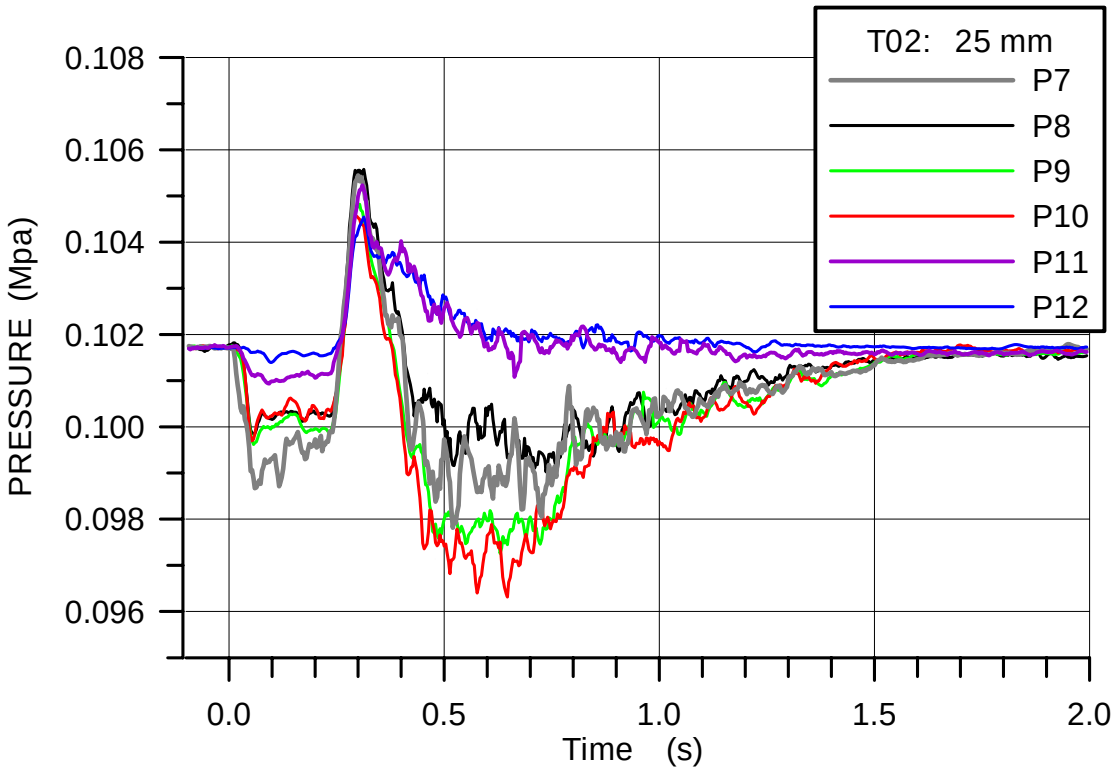

Fig. 5.98 T02 Pressures in the cavity

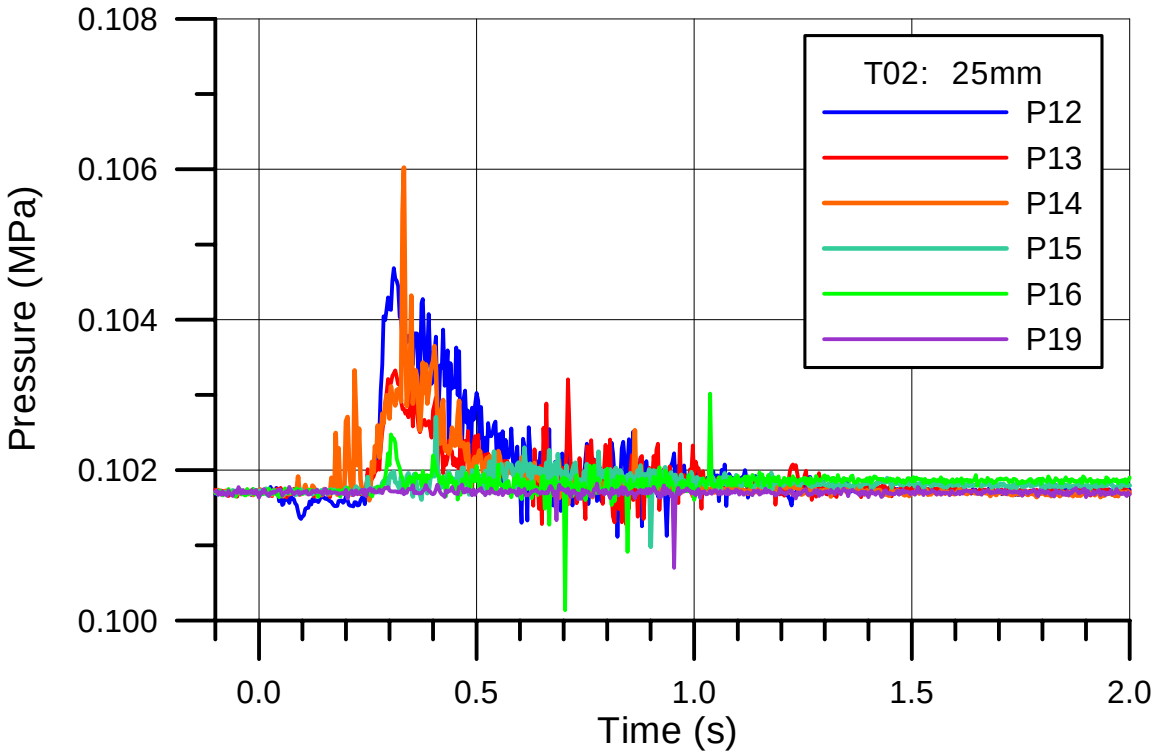

Fig. 5.99 T02 Pressure in the space at the RPV support and in the subcompartments

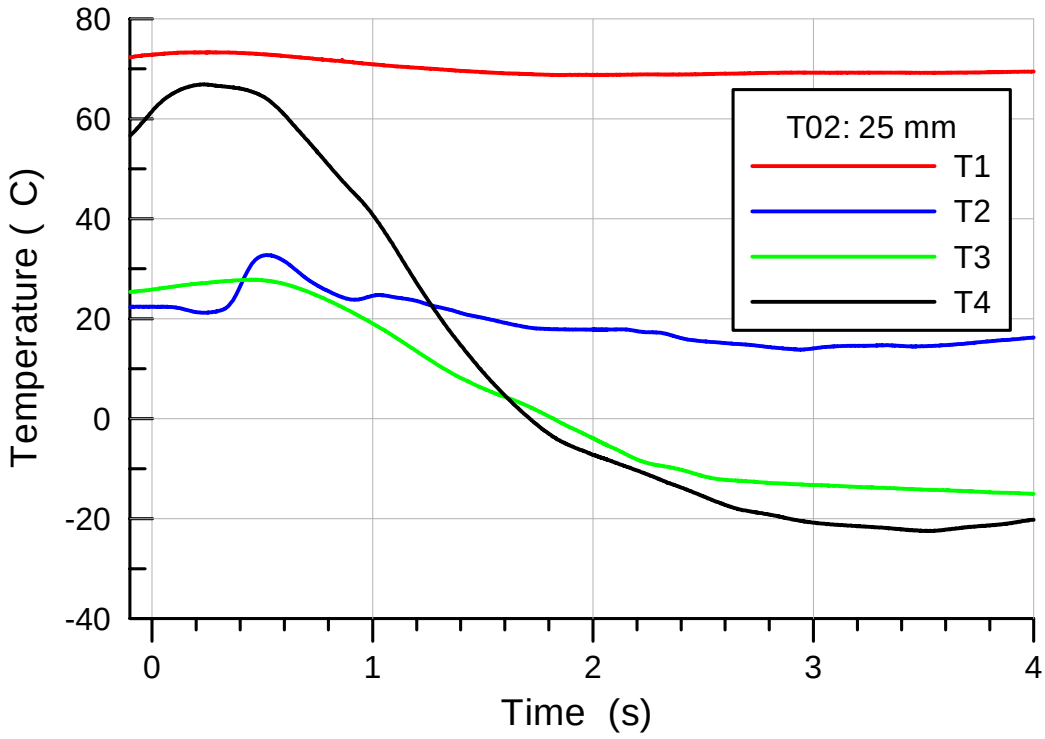

Fig. 5.100 T02 Gas temperatures in the RPV and the cavity

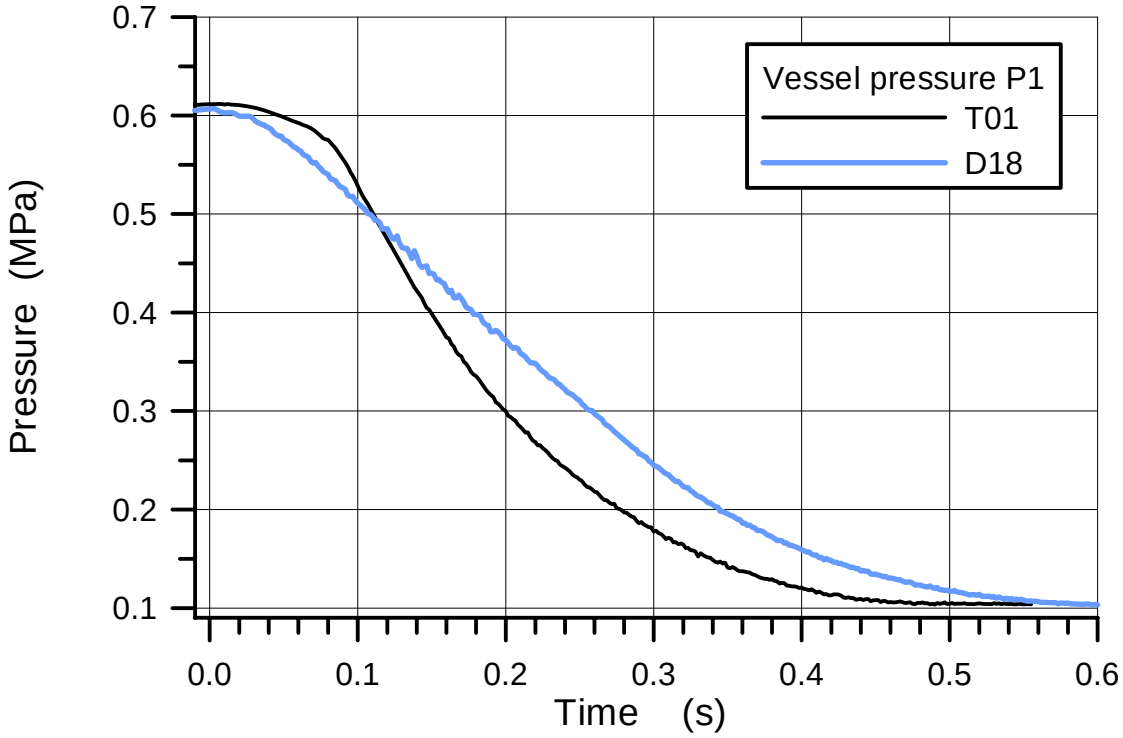

Fig. 5.101 Blow down pressure in test with liquid in lower head (D18) and liquid in standpipe (T01), d = 50 mm.

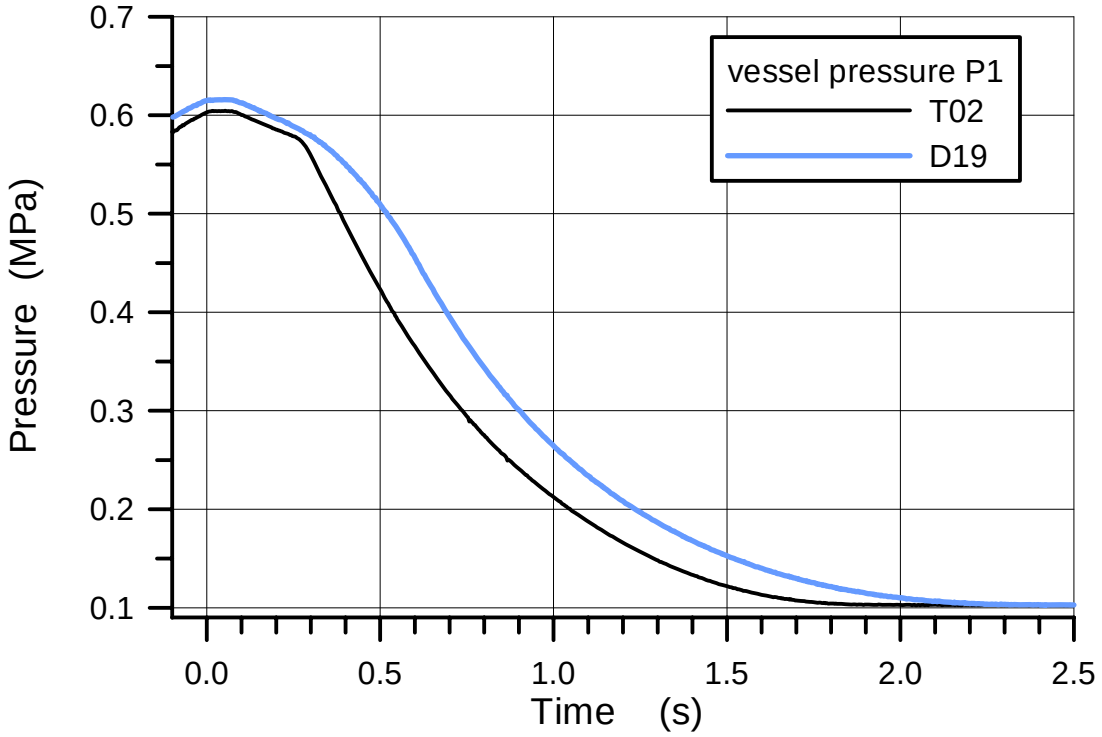

Fig.5.102 Blow down pressure in test with liquid in lower head (D19), and liquid in standpipe (T02), d = 25 mm.

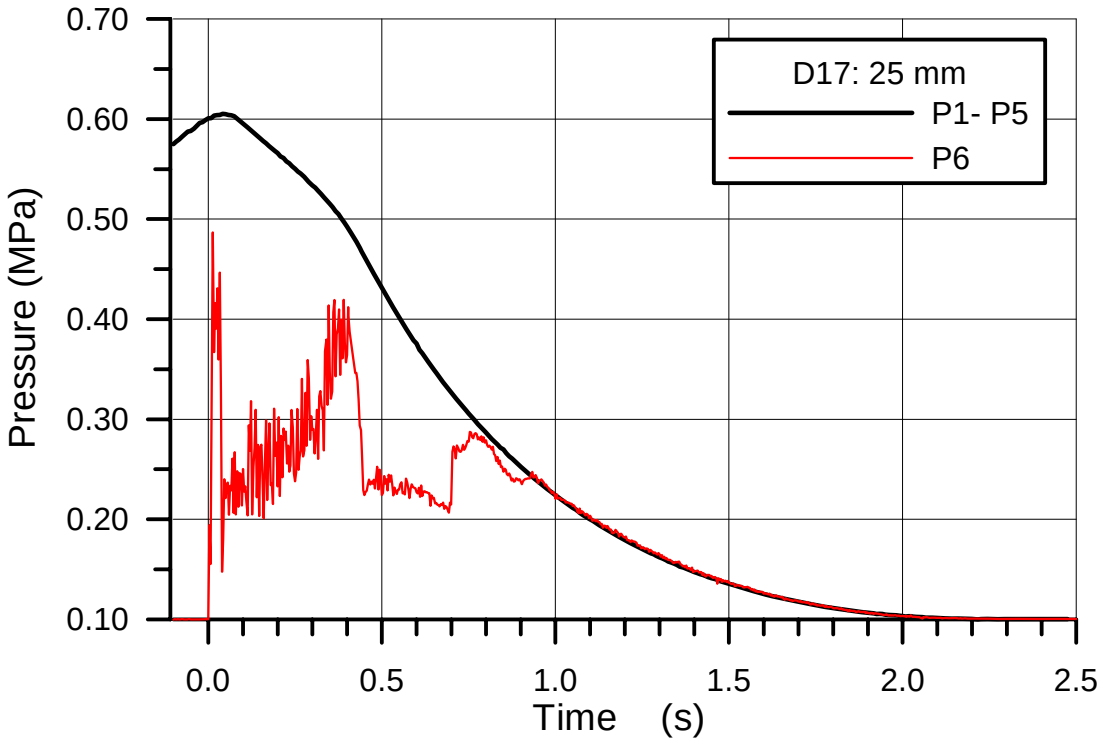

Fig. 5.103 D17 Blow down pressure in the RPV and total pressure on cavity floor below hole

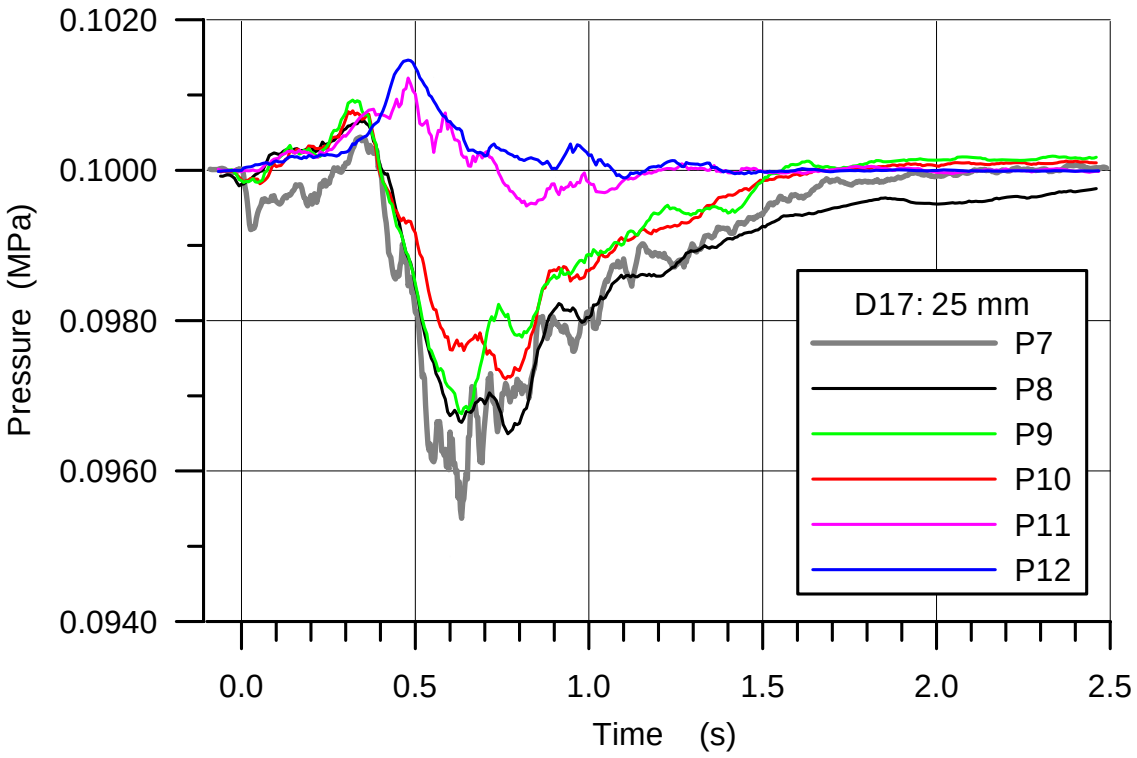

Fig. 5.104 D17 Pressures in the cavity

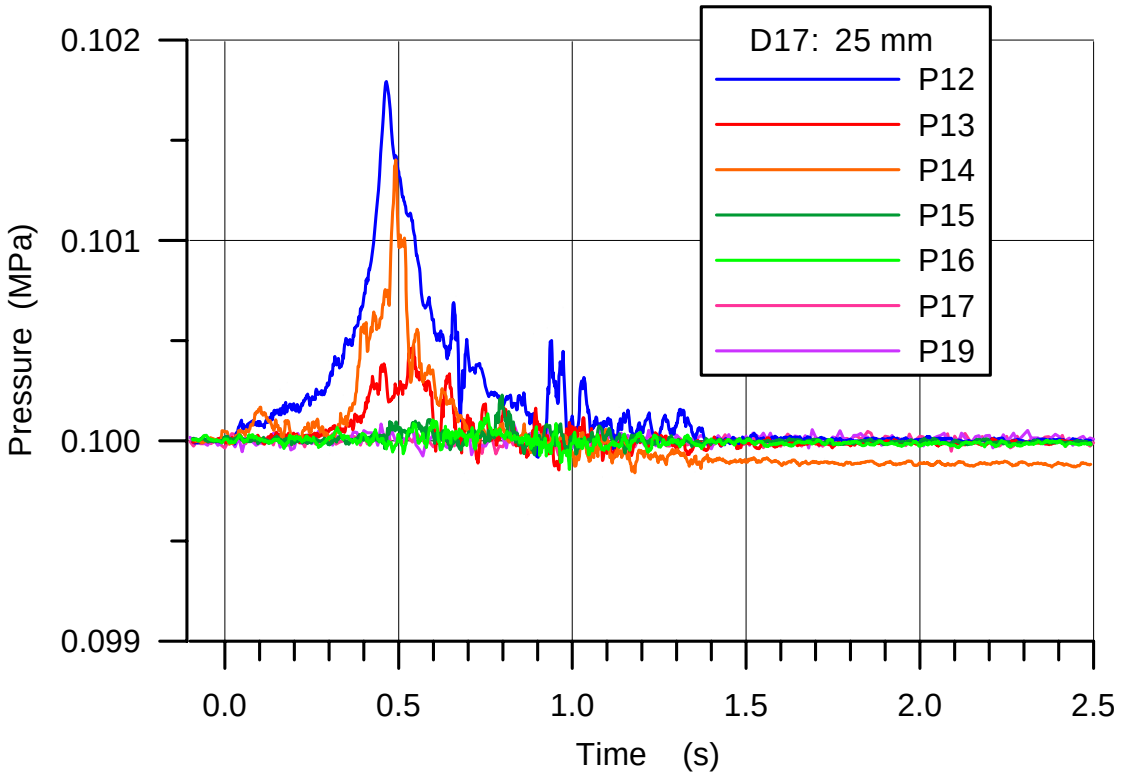

Fig. 5.105 D17 Pressure in the space at the RPV support and in the subcompartments

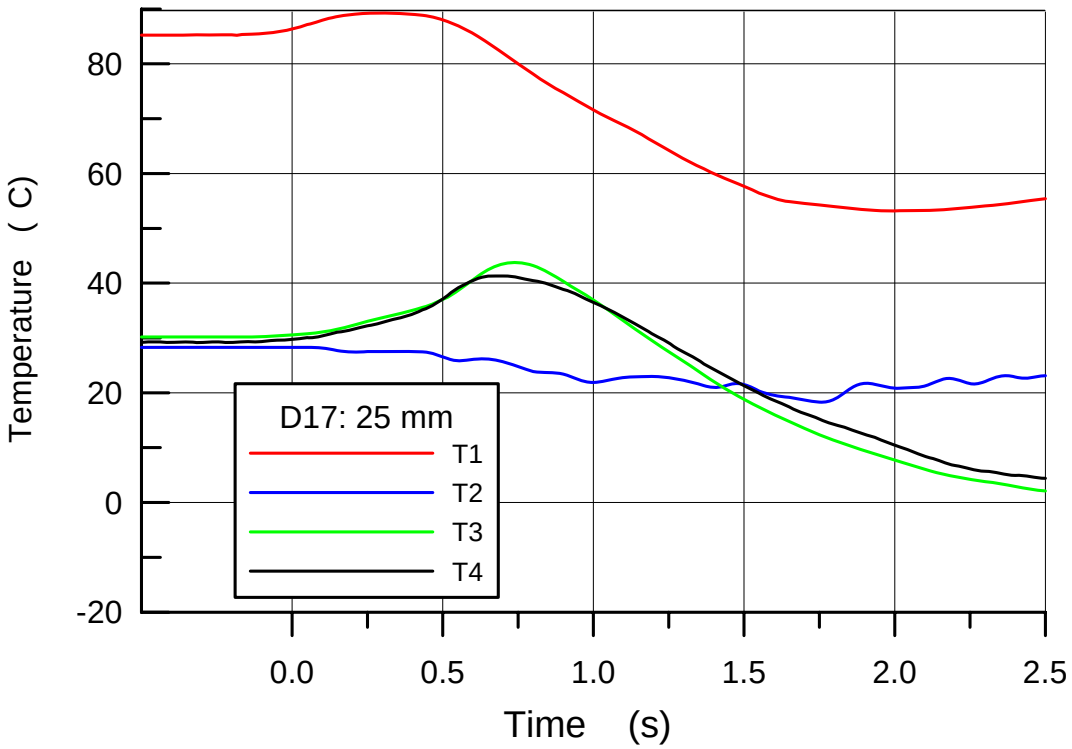

Fig. 5.106 D17 Gas temperatures in the RPV and the cavity

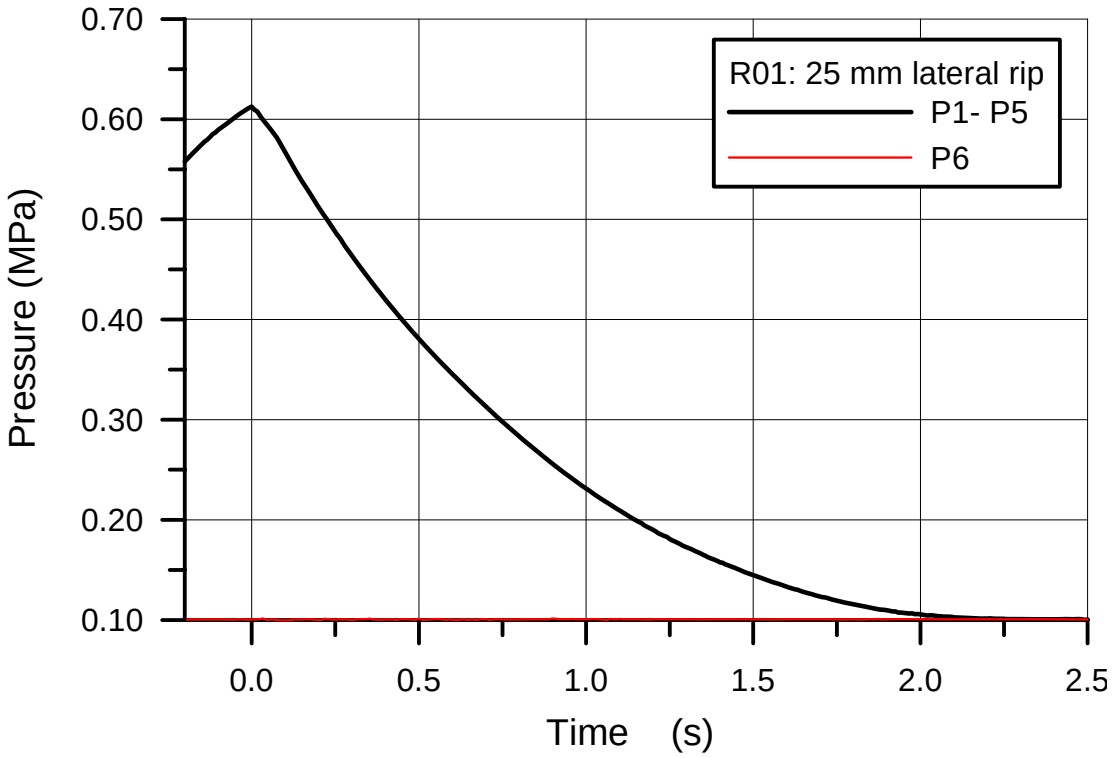

Fig. 5.107 R01 Blow down pressure in the RPV

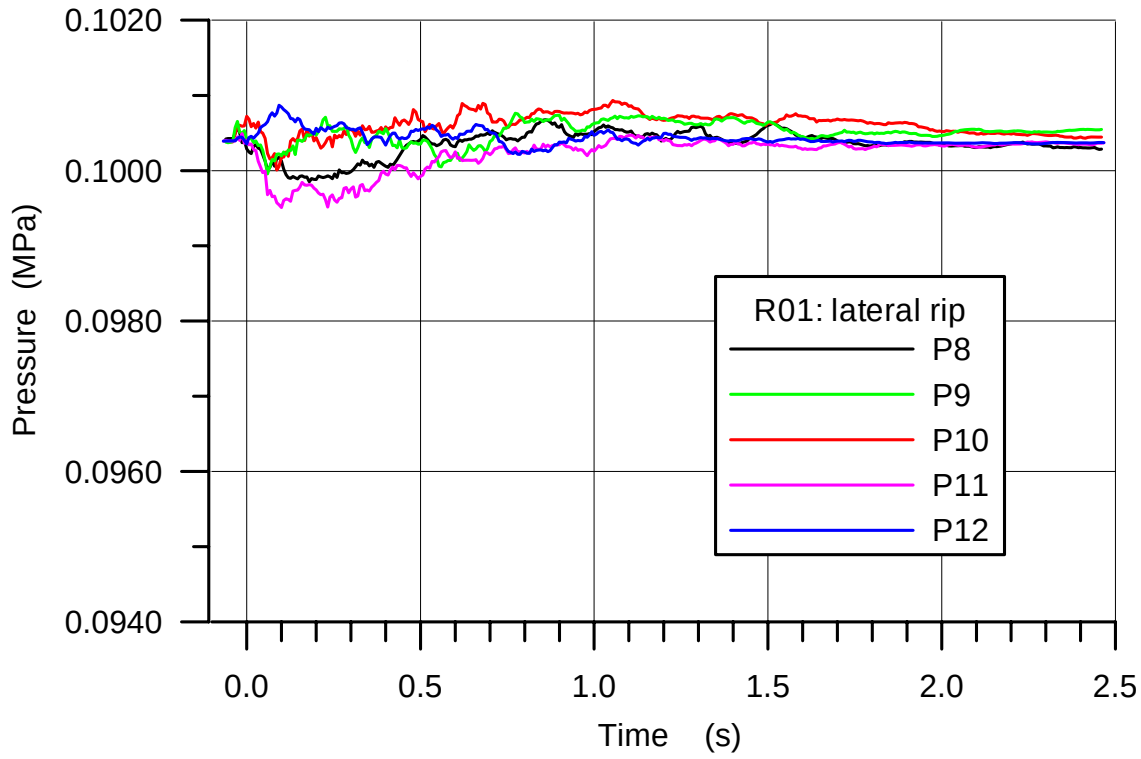

Fig. 5.108 R01 Pressures in the cavity

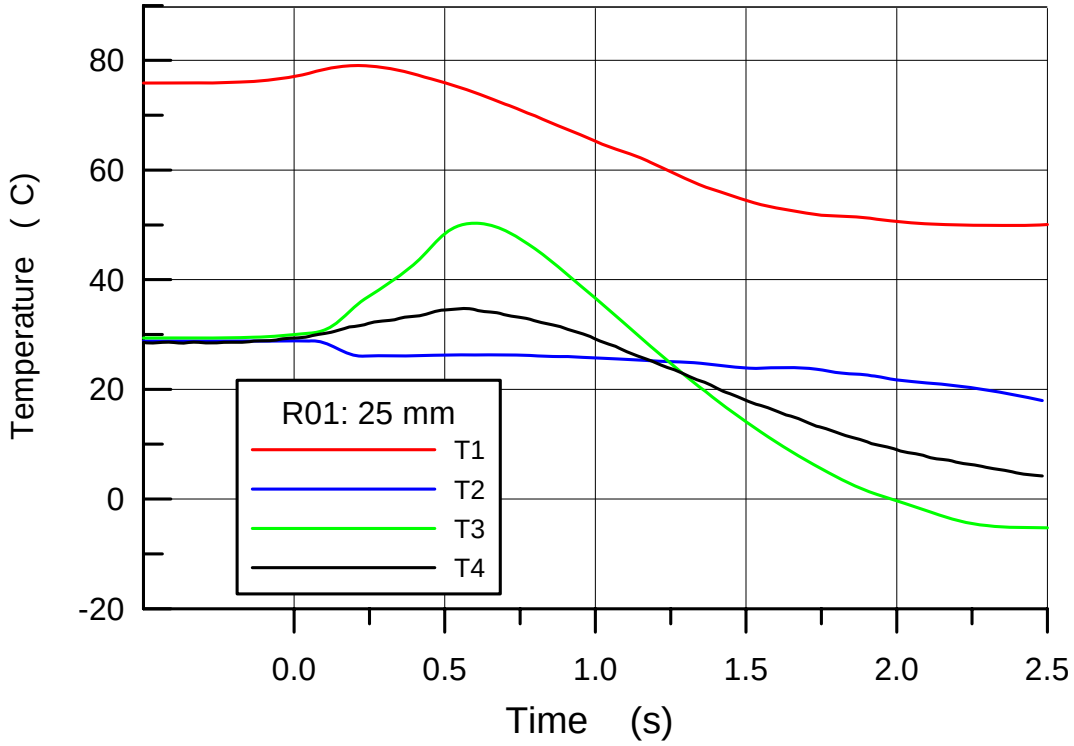

Fig. 5.109 R01 Gas temperatures in the RPV and the cavity

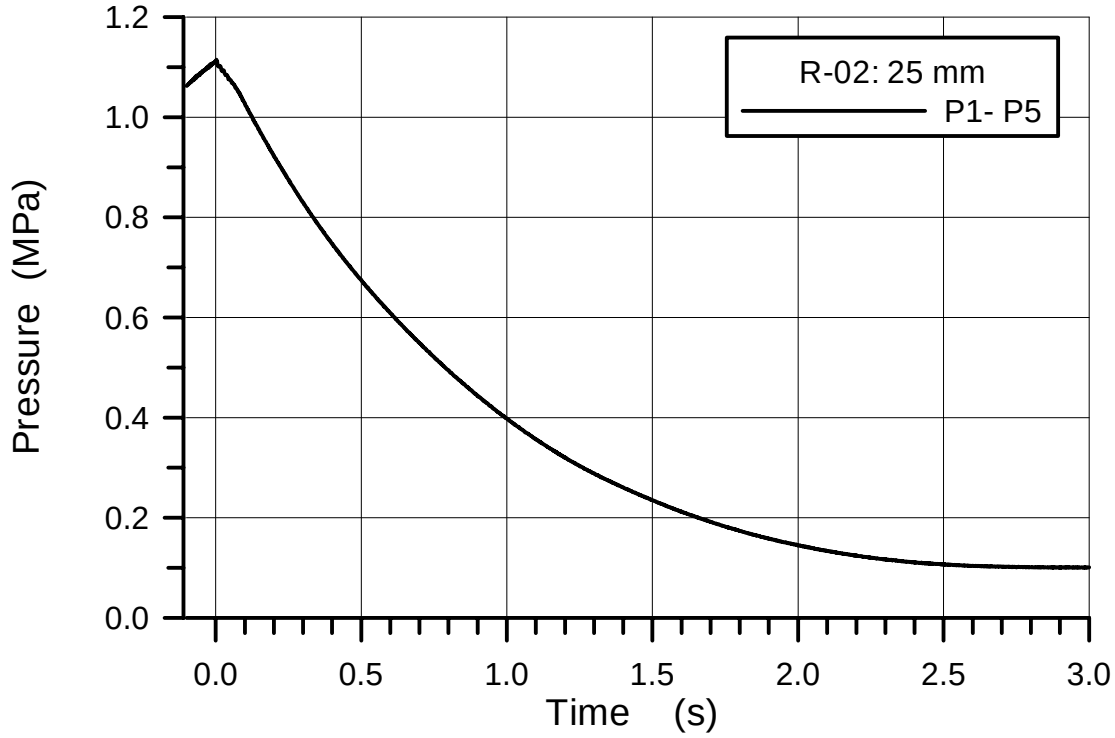

Fig. 5.110 R02 Blow down pressure in the RPV

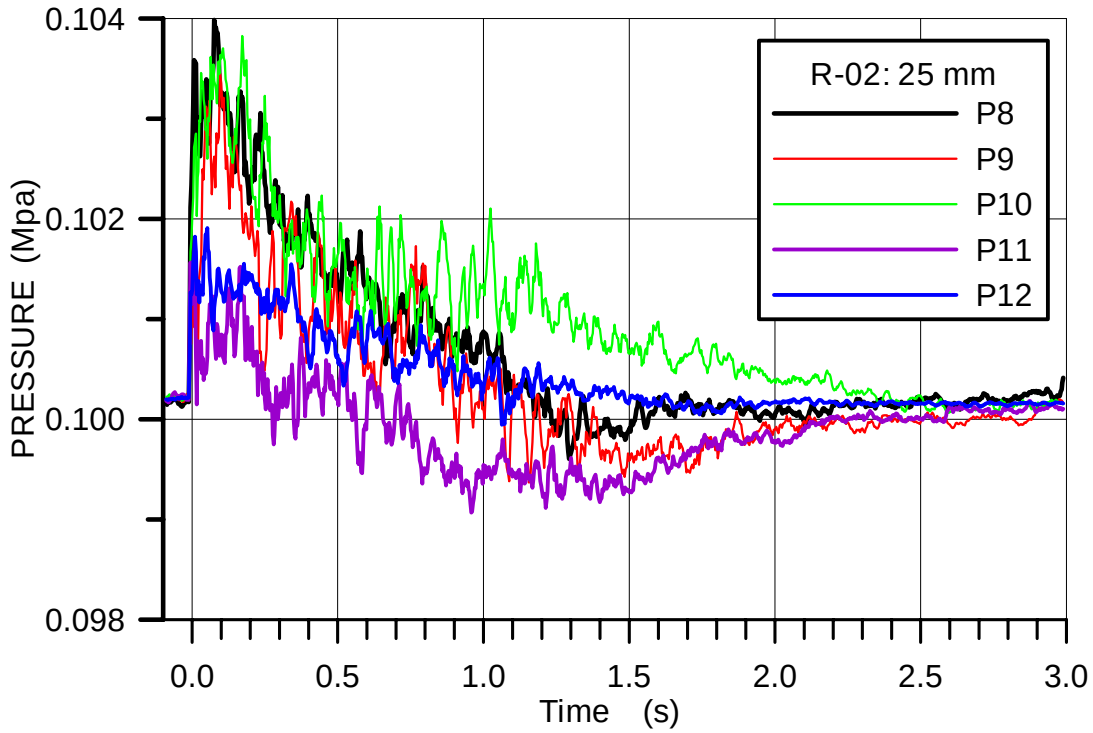

Fig. 5.111 R02 Pressures in the cavity

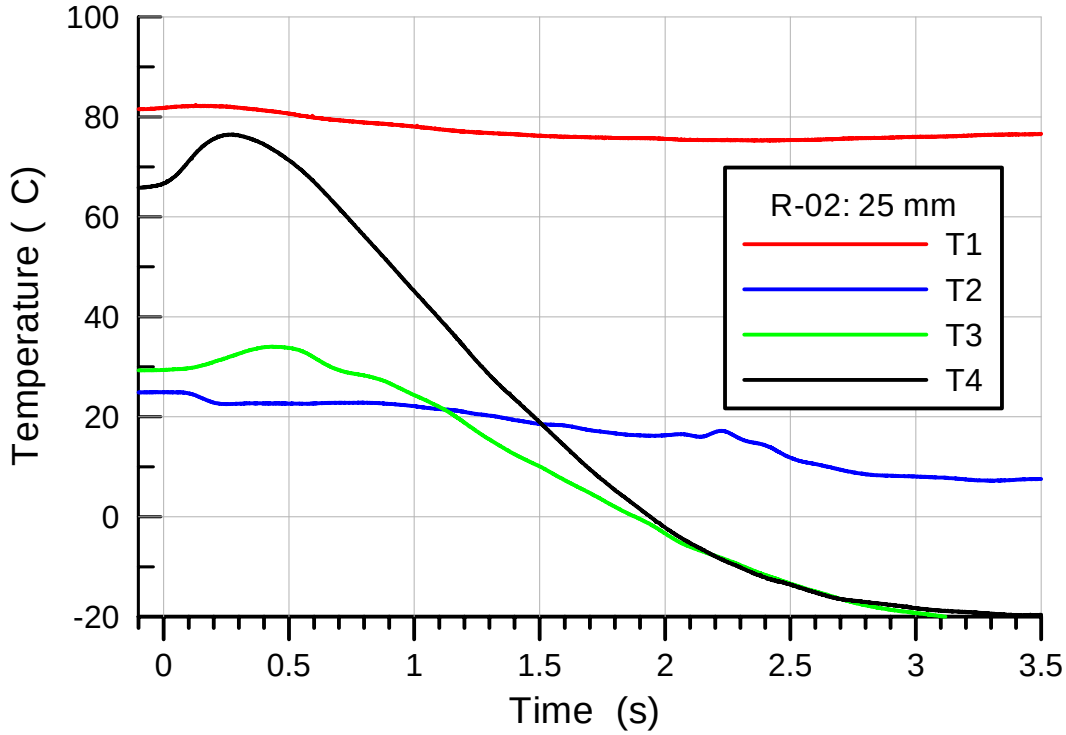

Fig. 5.112 R02 Gas temperatures in the RPV and the cavity

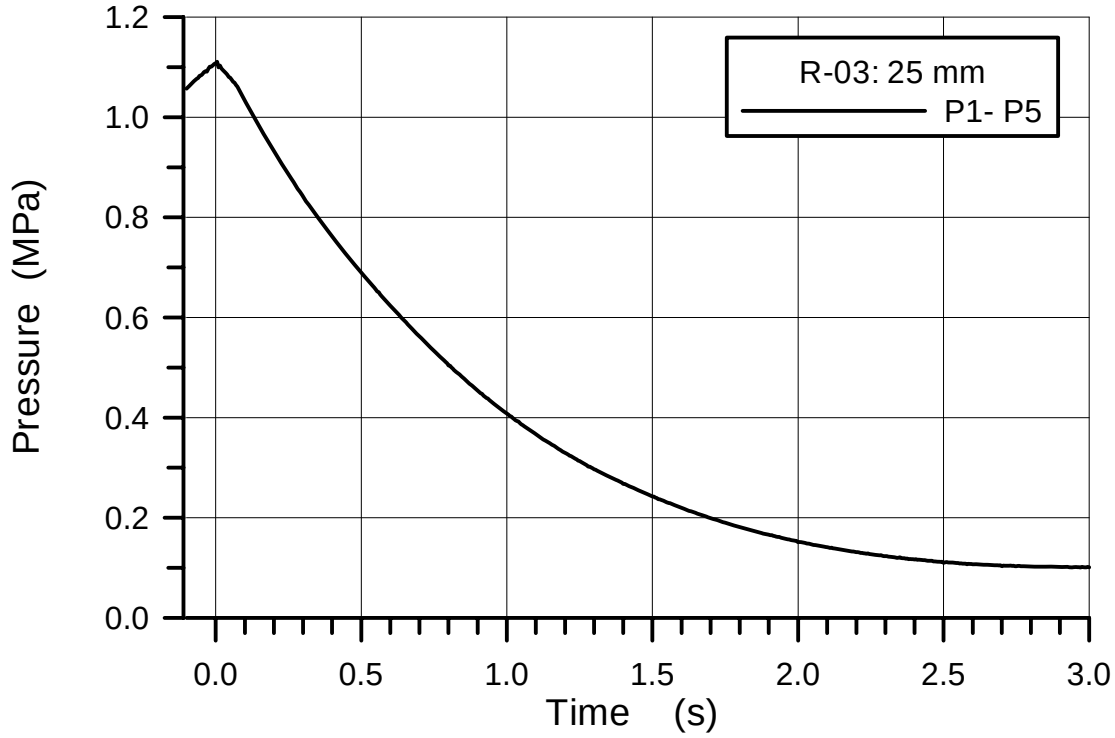

Fig. 5.113 R03 Blow down pressure in the RPV

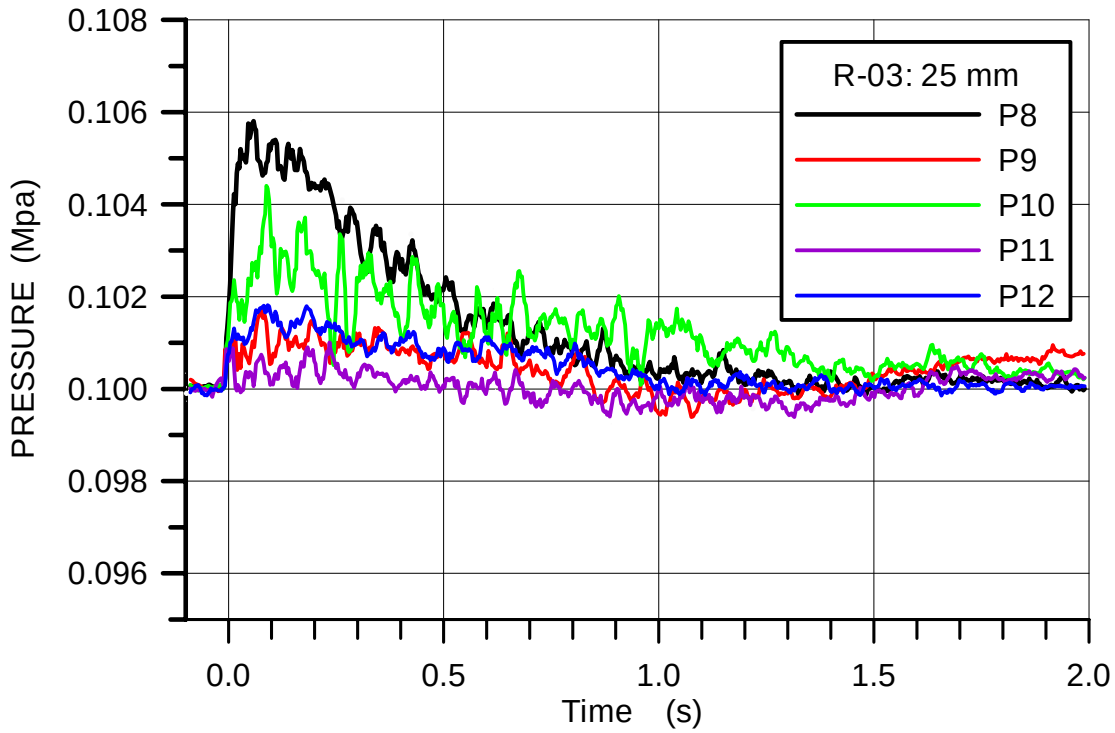

Fig. 5.114 R03 Pressures in the cavity

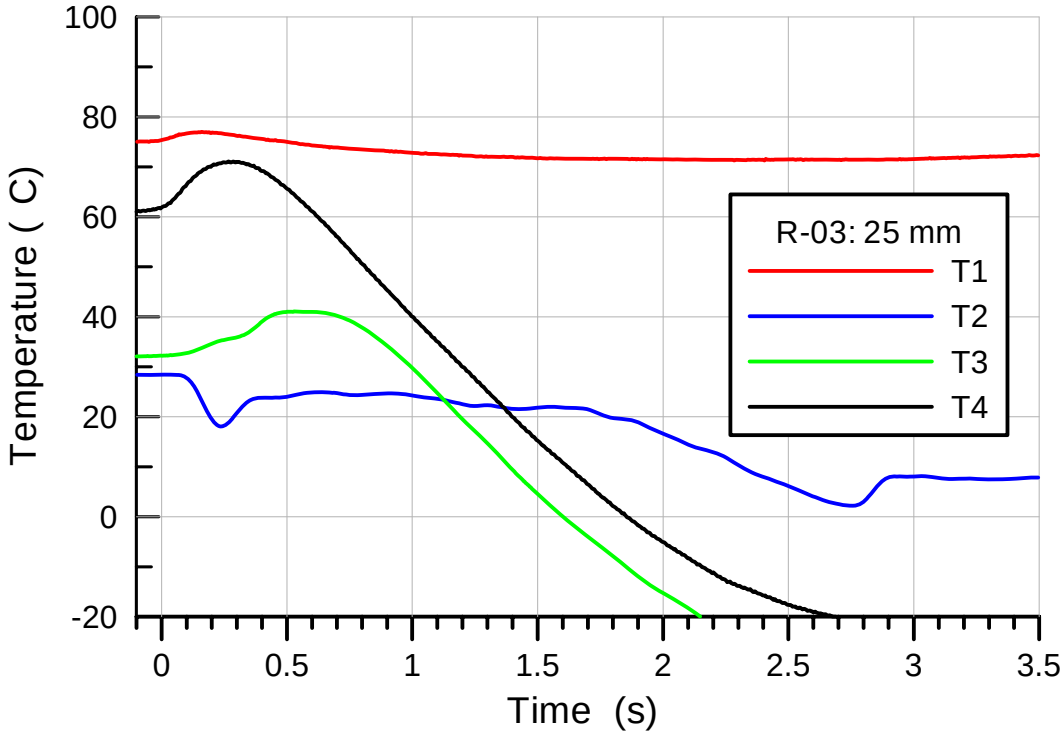

Fig. 5.115 R03 Gas temperatures in the RPV and the cavity

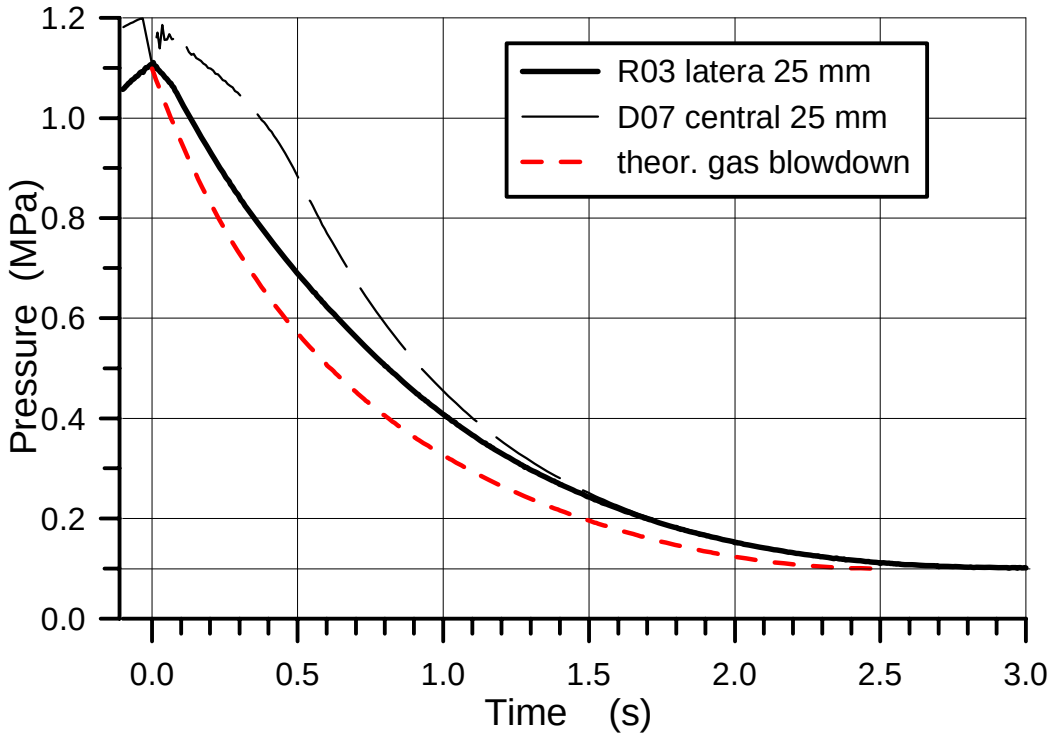

Fig. 5.116 Comparison of blowdown pressure of experiments with central hole (D07) and lateral hole (R03), and with single-phase gas blowdown calculated by Eq. 4.1

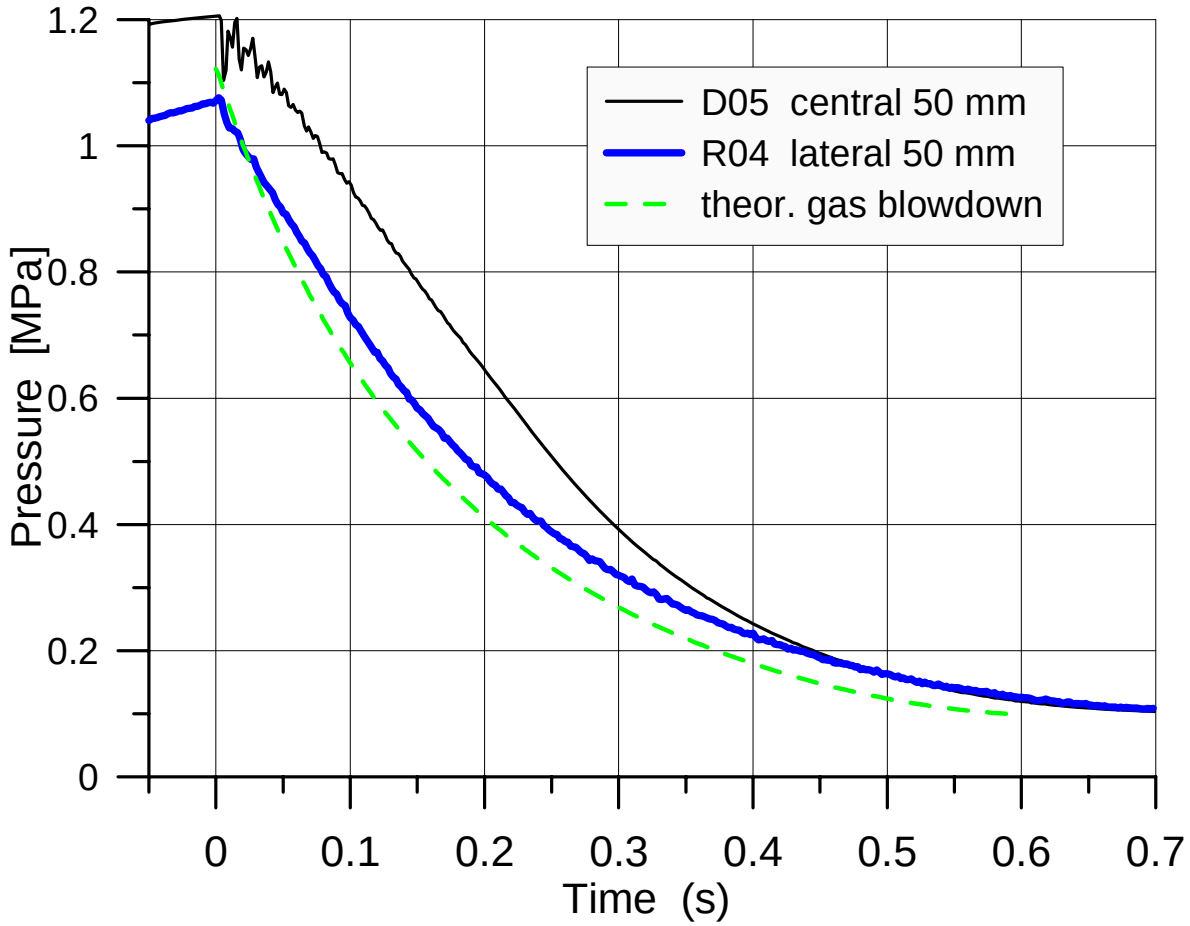

Fig. 5.117 R04 Blow down pressure in the RPV in comparison with theoretical single phase gas blow down calculated by Eq. 4.1

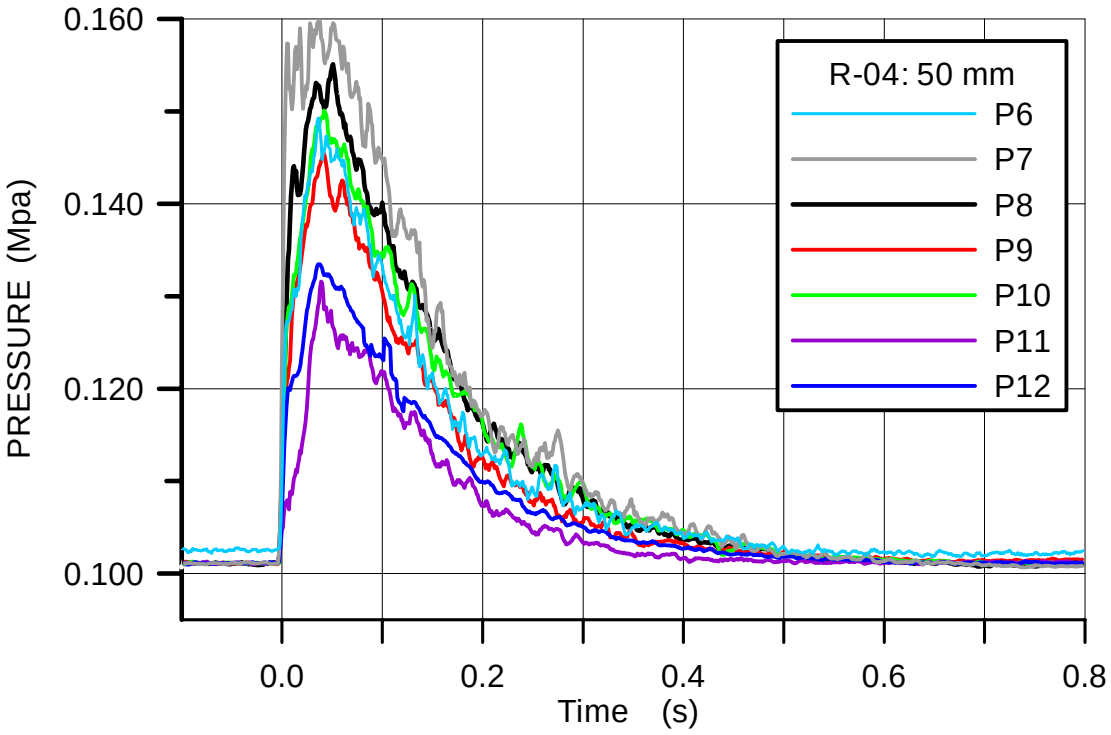

Fig. 5.118 R04 Pressures in the cavity

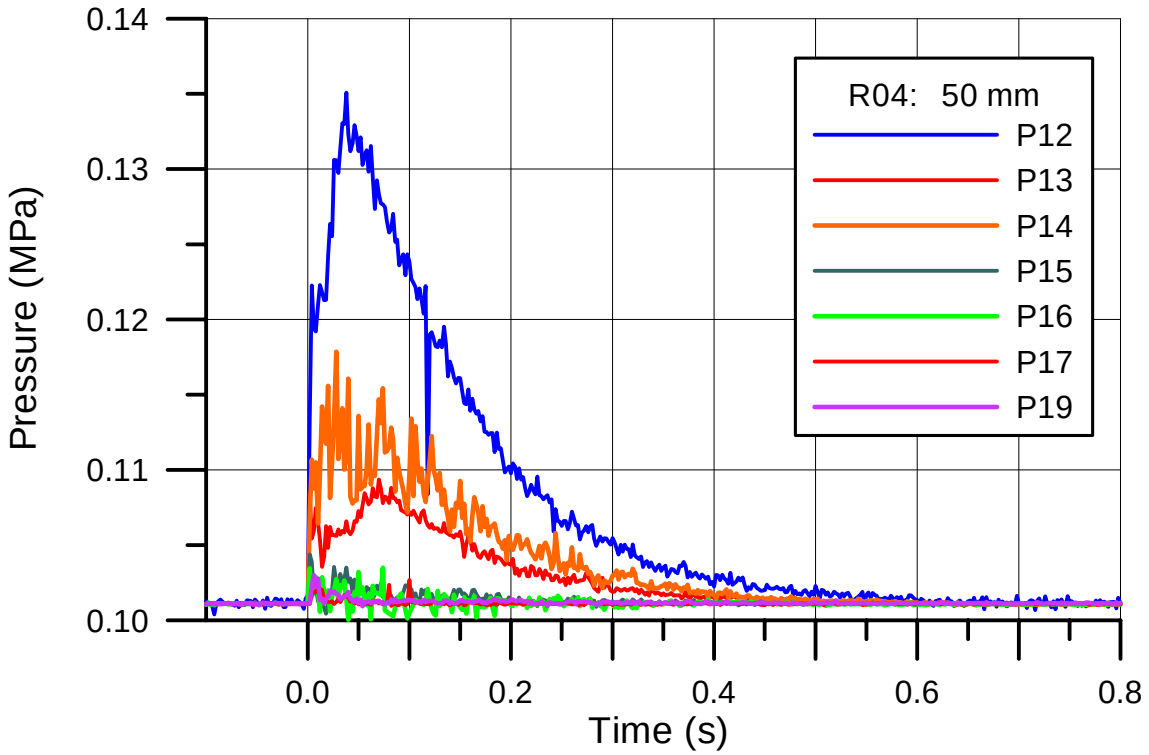

Fig. 5.119 R04 Pressure in the space at the RPV support and in the subcompartments

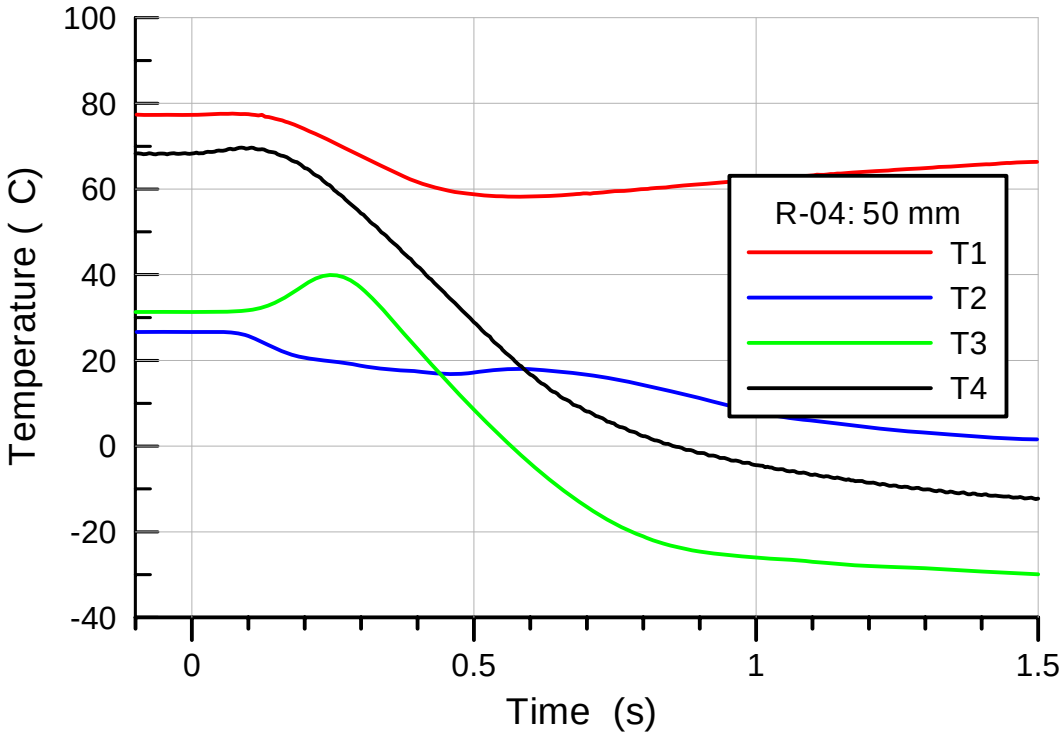

Fig. 5.120 R04 Gas temperatures in the RPV and the cavity

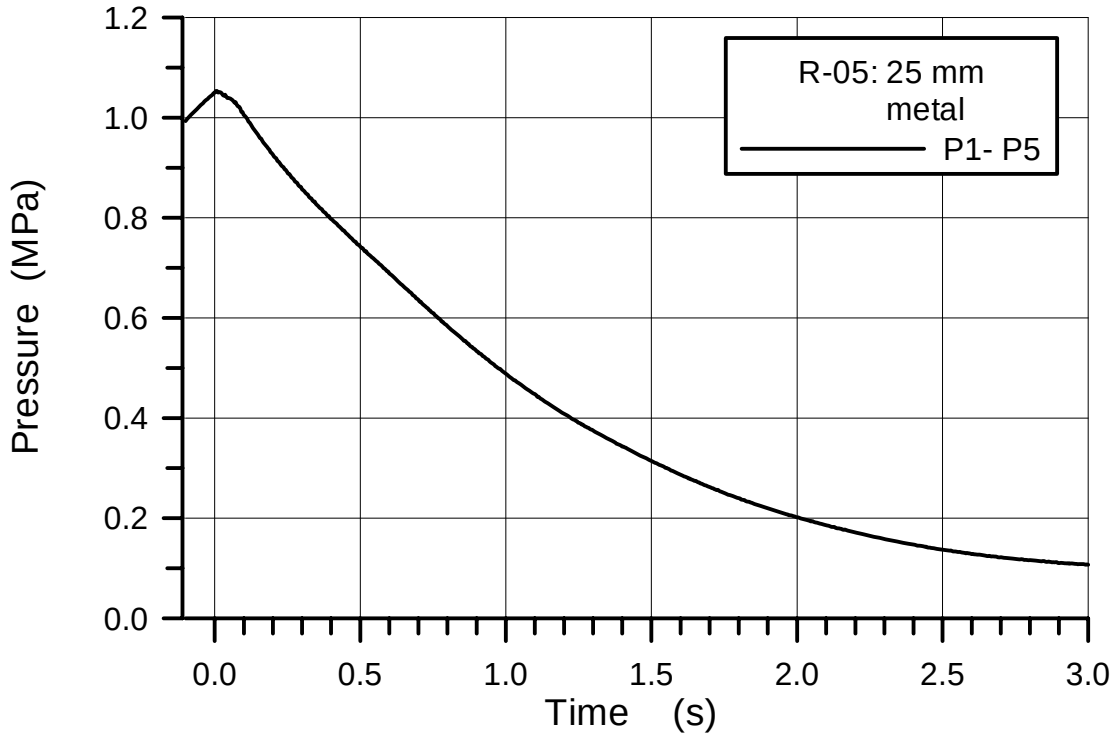

Fig. 5.121 R05 Blow down pressure in the RPV

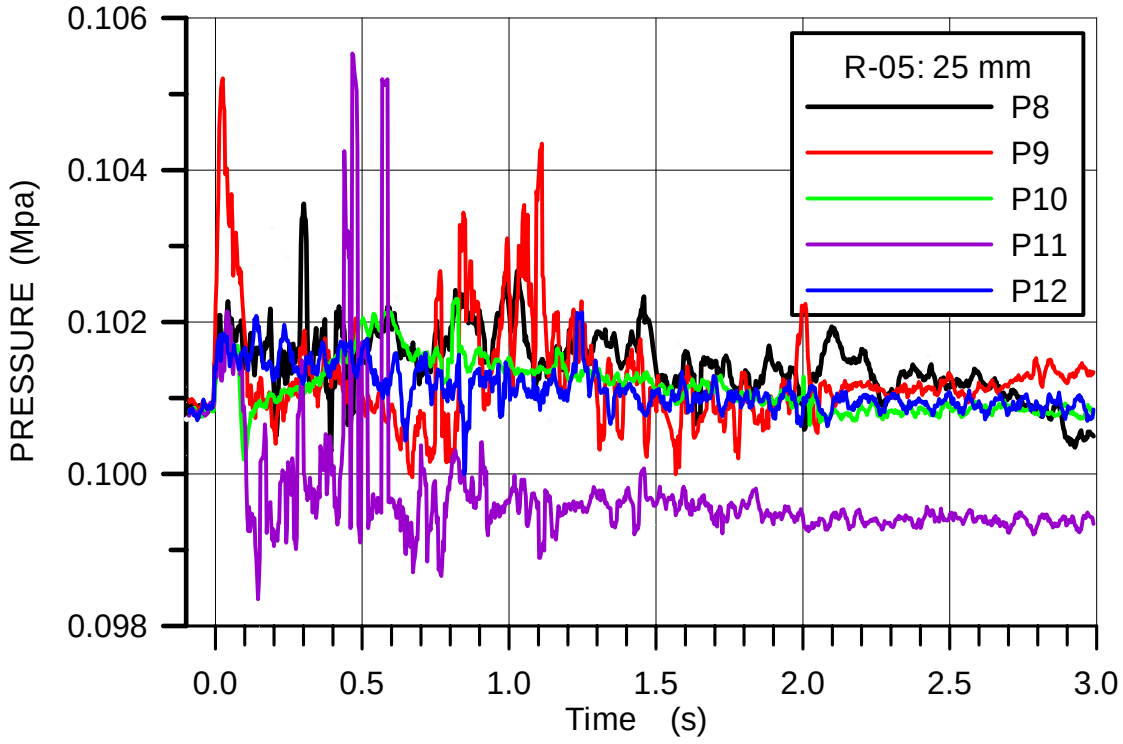

Fig. 5.122 R05 Pressures in the cavity

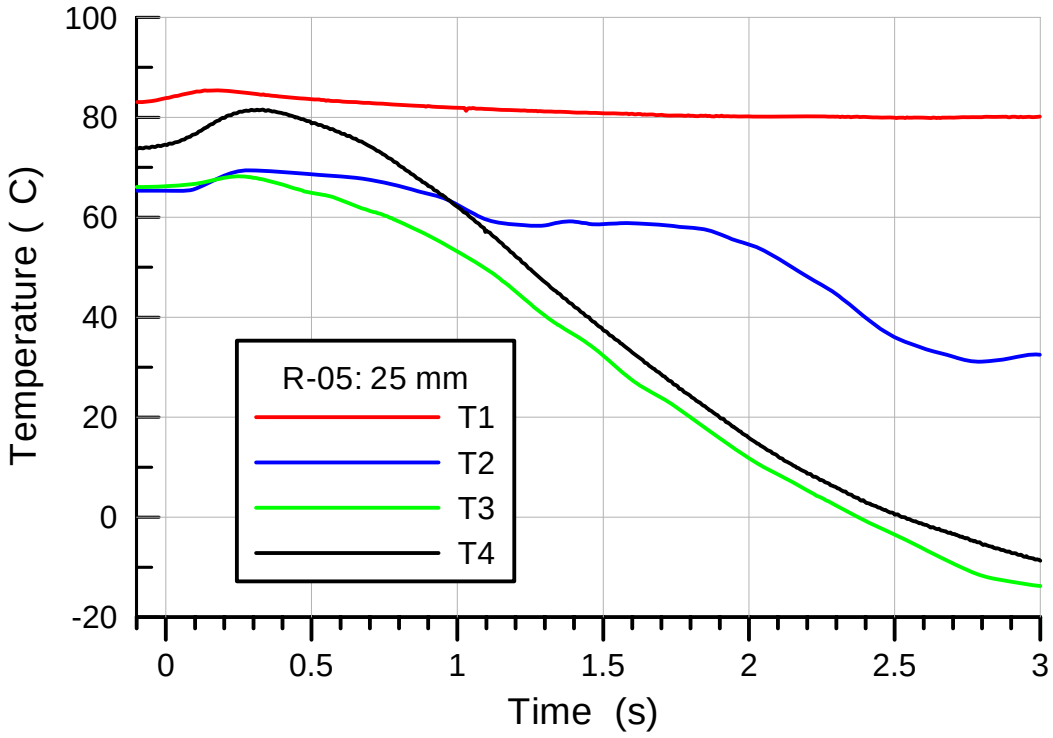

Fig. 5.123 R05 Gas temperatures in the RPV and the cavity

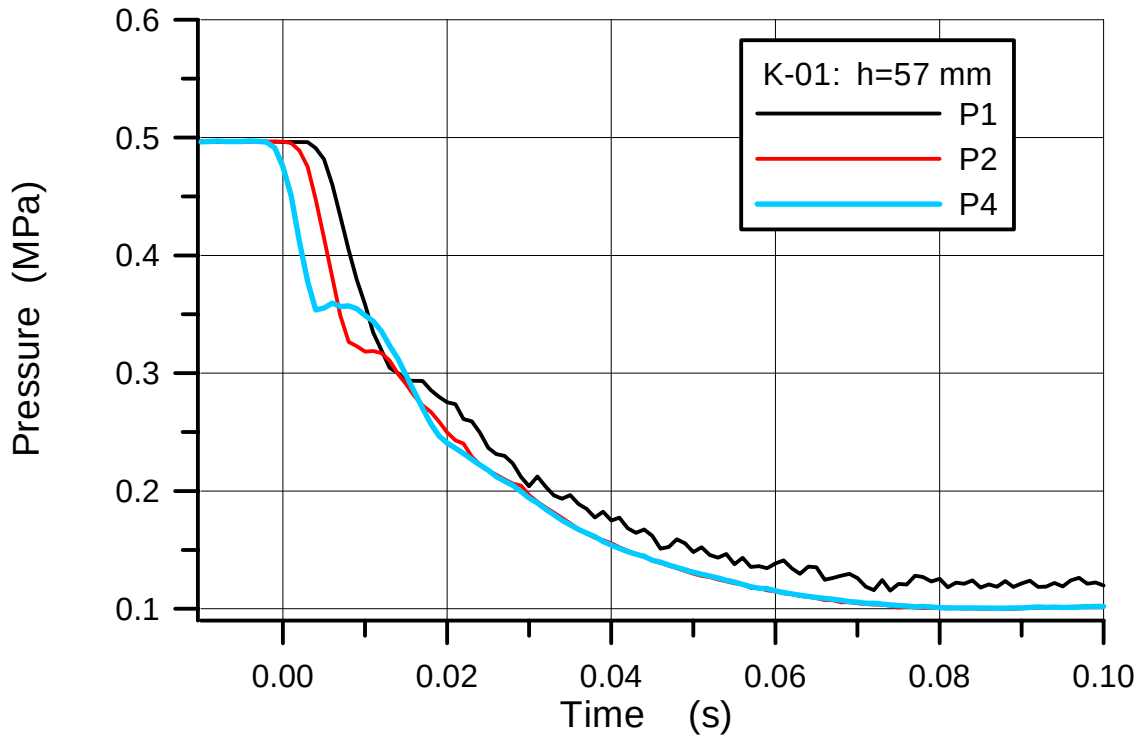

Fig. 5.124 K01 Blow down pressure at different positions in the RPV

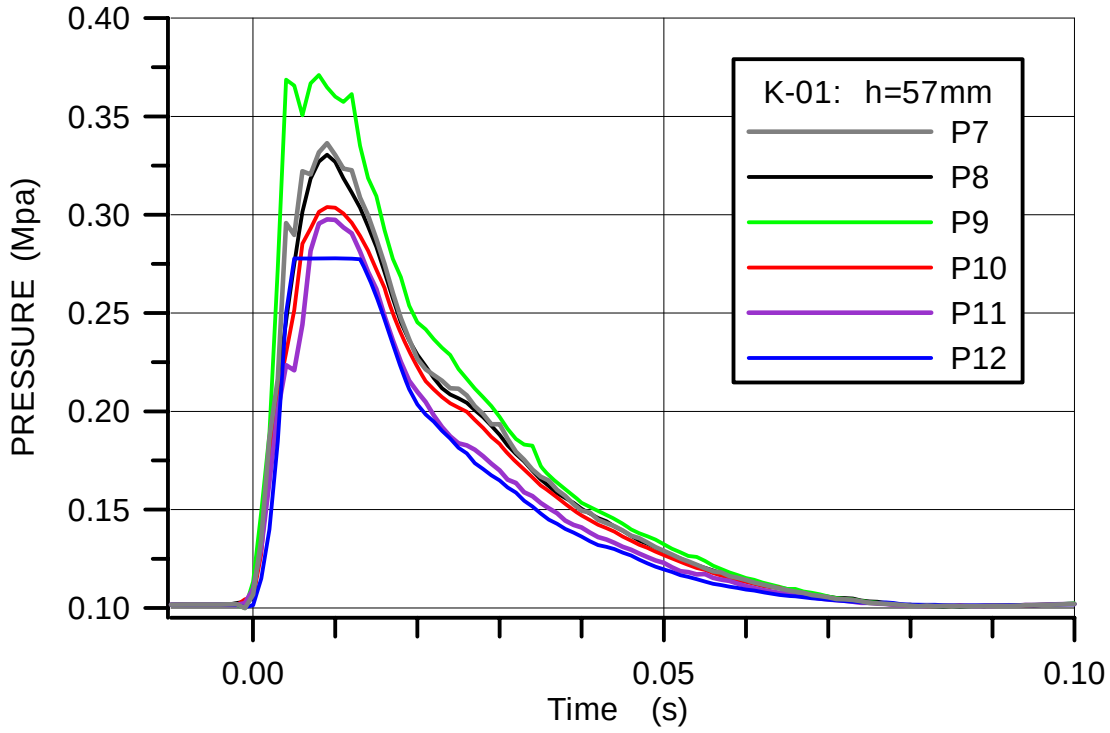

Fig. 5.125 K01 Pressures in the cavity

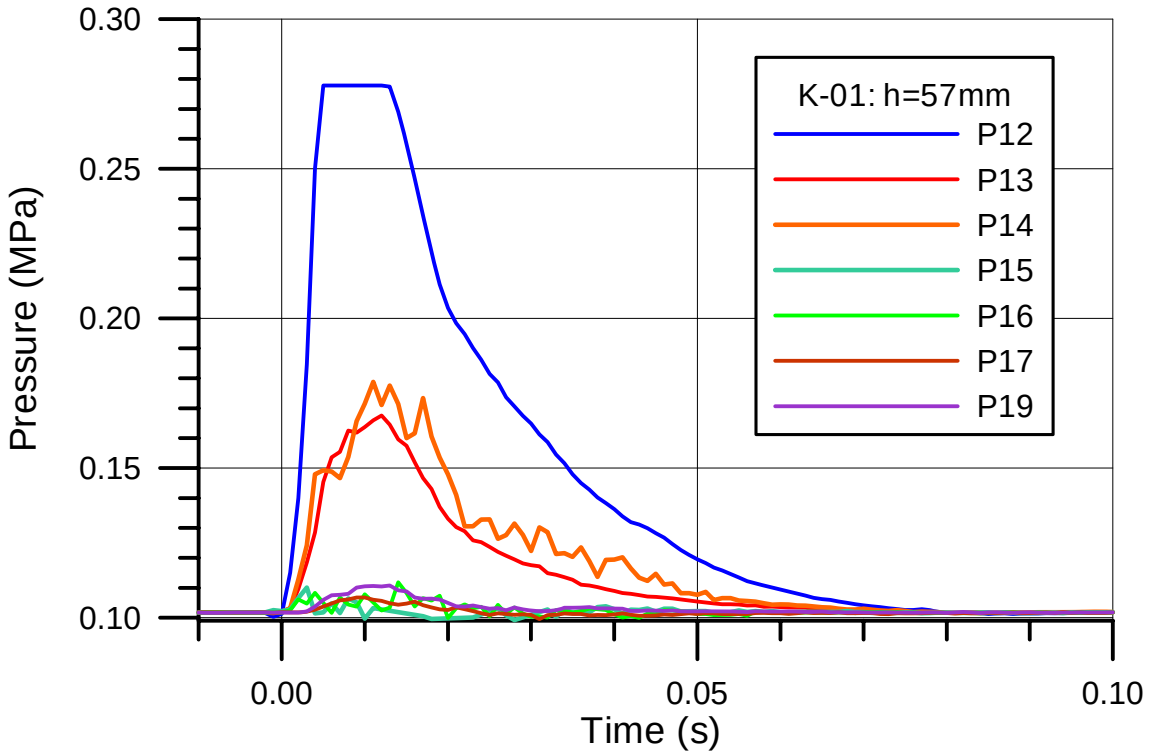

Fig. 5.126 K01 Pressure in the space at the RPV support and in the subcompartments

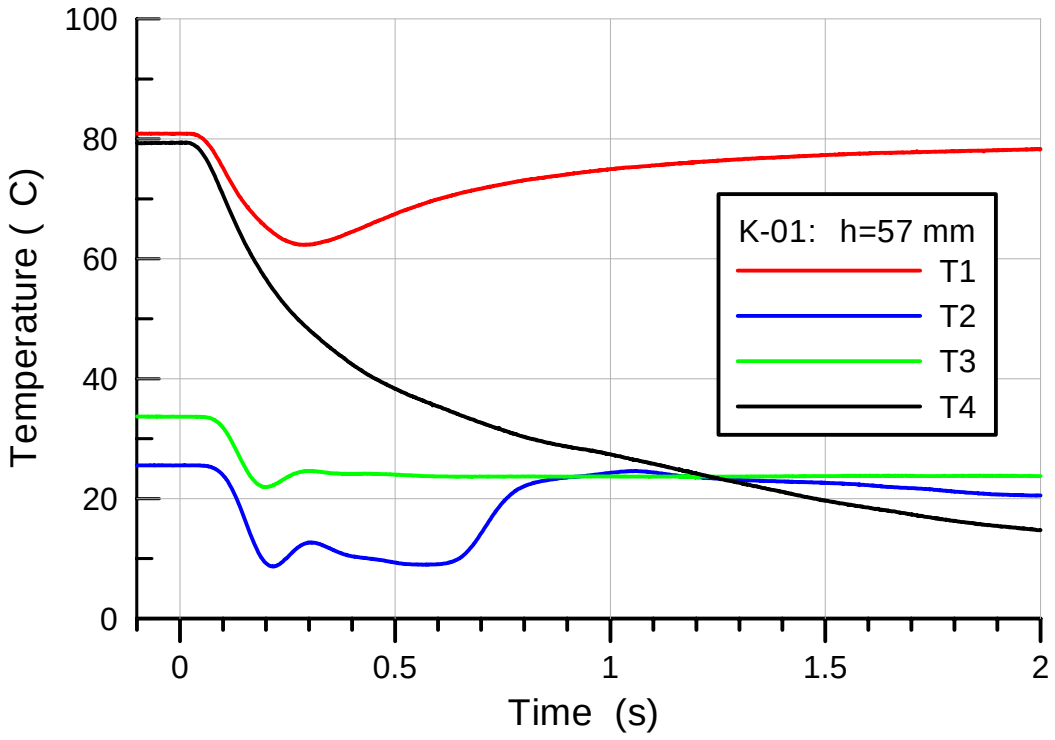

Fig. 5.127 K01 Gas temperatures in the RPV and the cavity

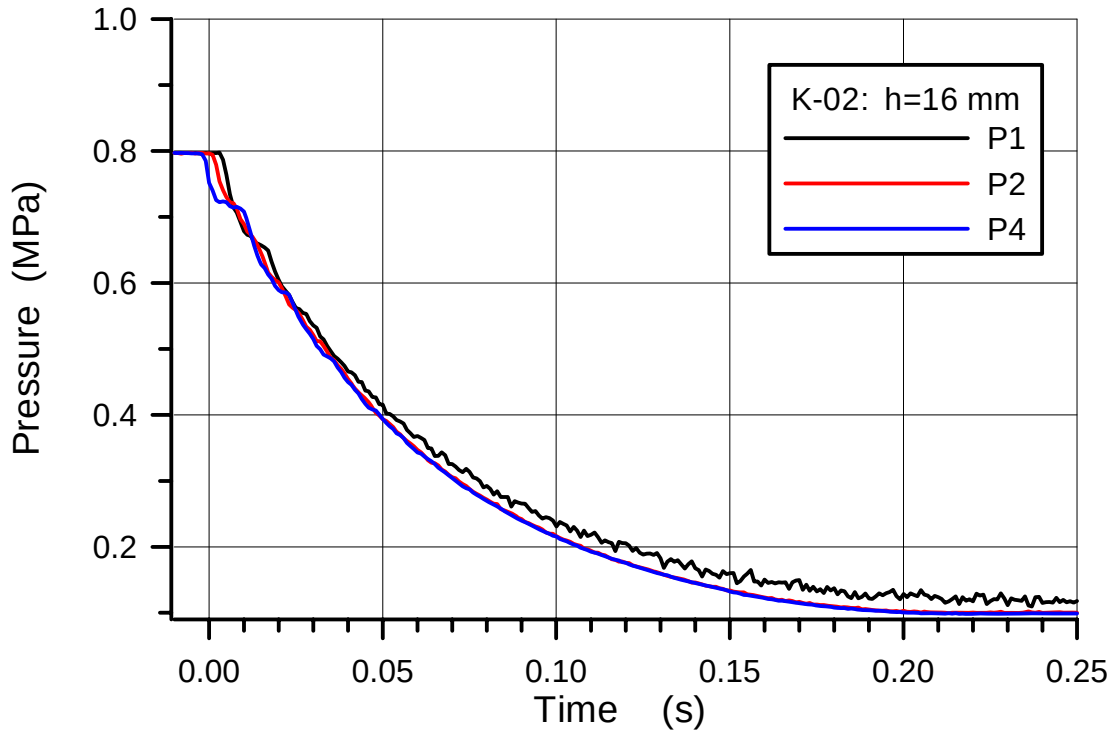

Fig. 5.128 K02 Blow down pressure at different positions in the RPV

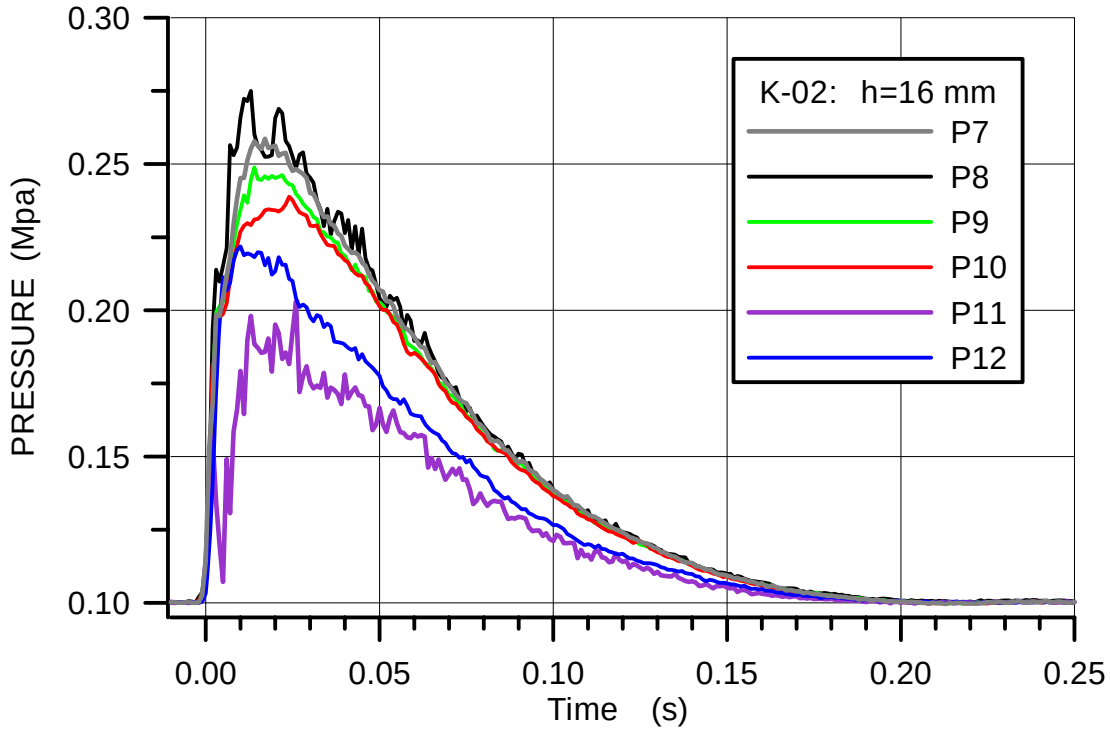

Fig. 5.129 K02 Pressures in the cavity

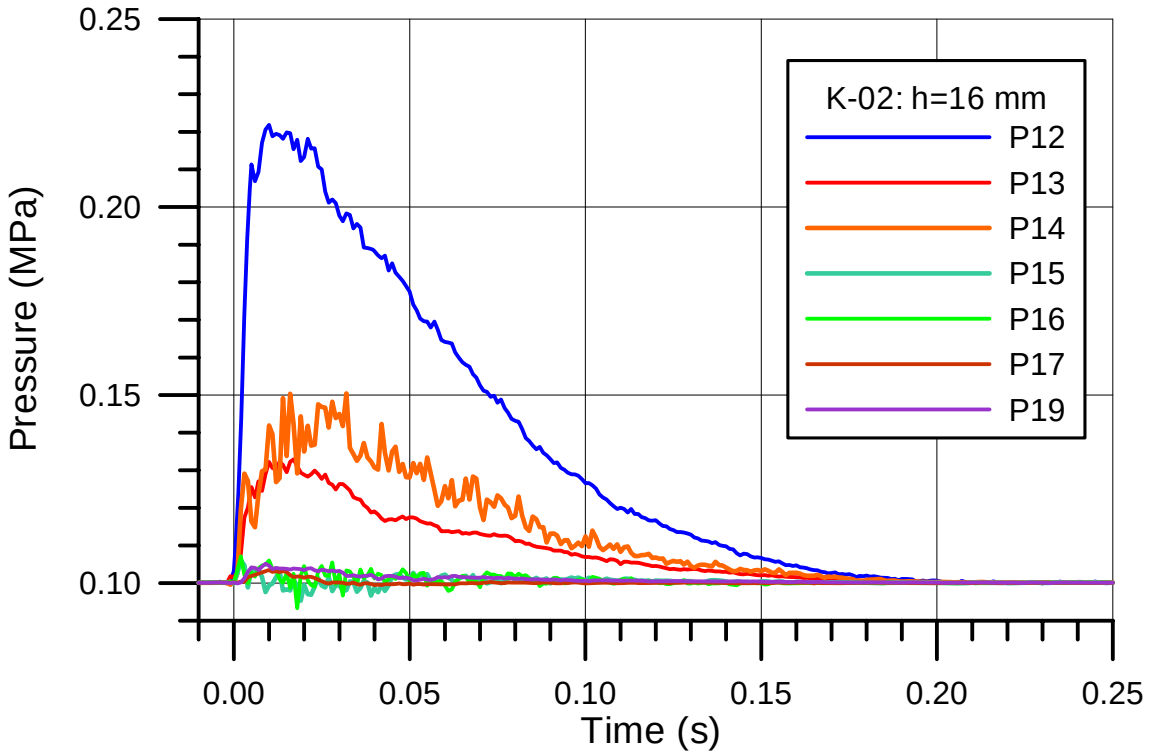

Fig. 5.130 K02 Pressure in the space at the RPV support and in the subcompartments

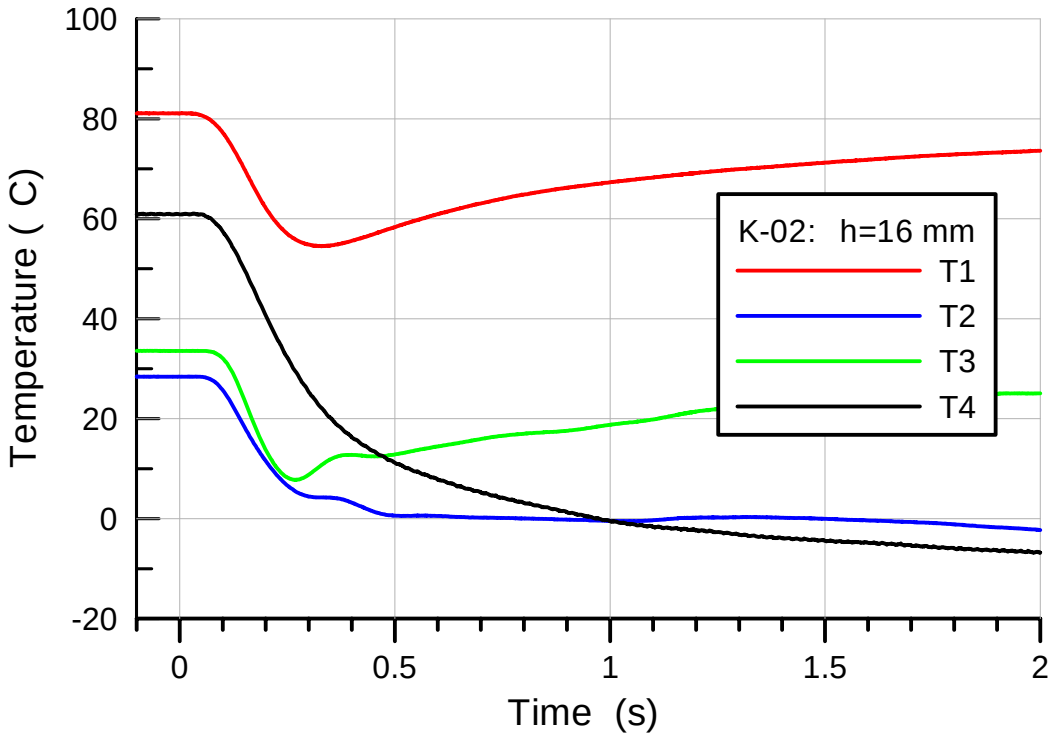

Fig. 5.131 K02 Gas temperatures in the RPV and the cavity

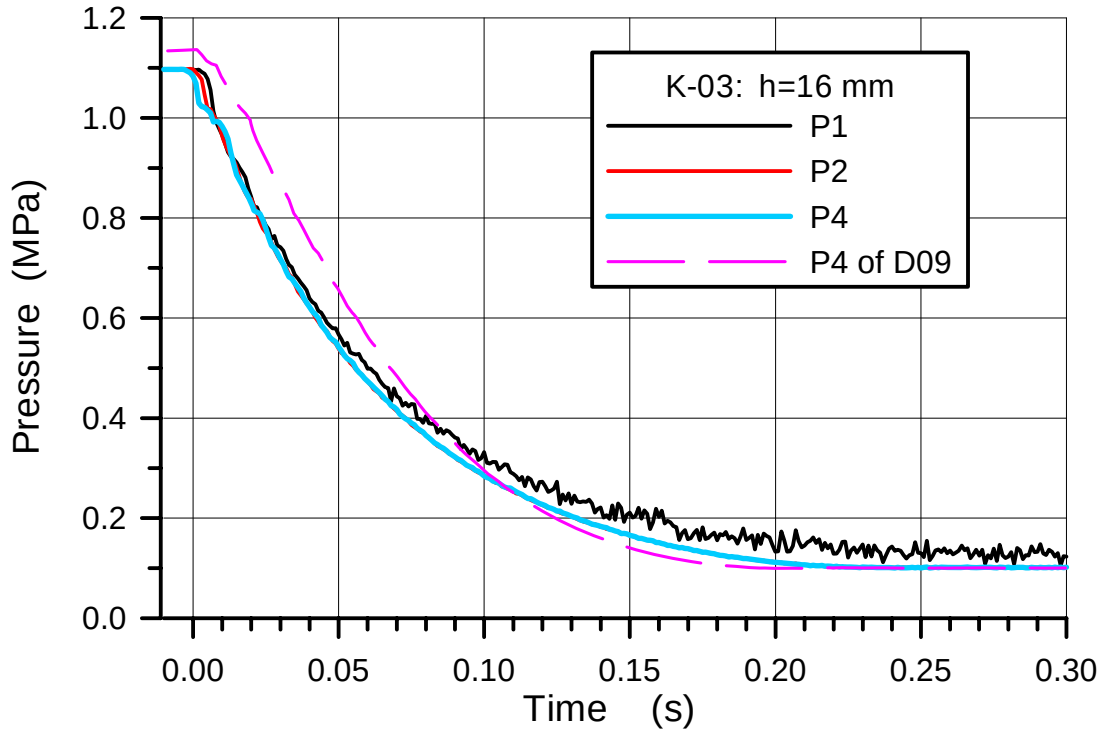

Fig. 5.132 K03 Blow down pressure at different positions in the RPV

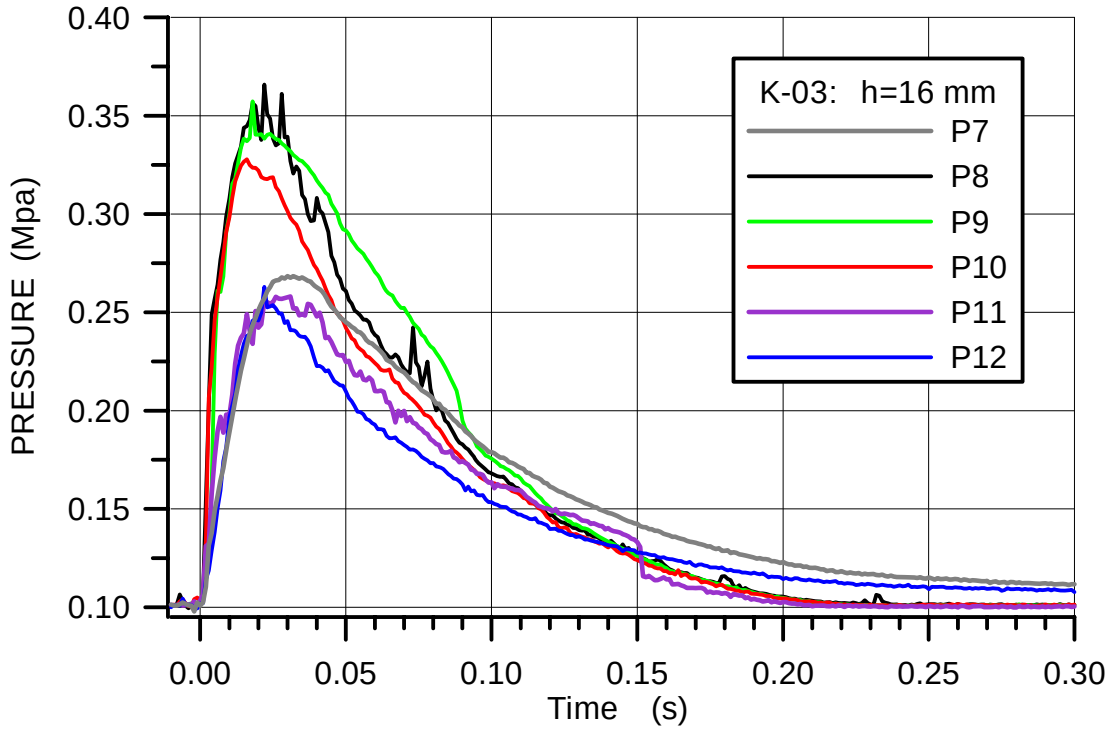

Fig. 5.133 K03 Pressures in the cavity

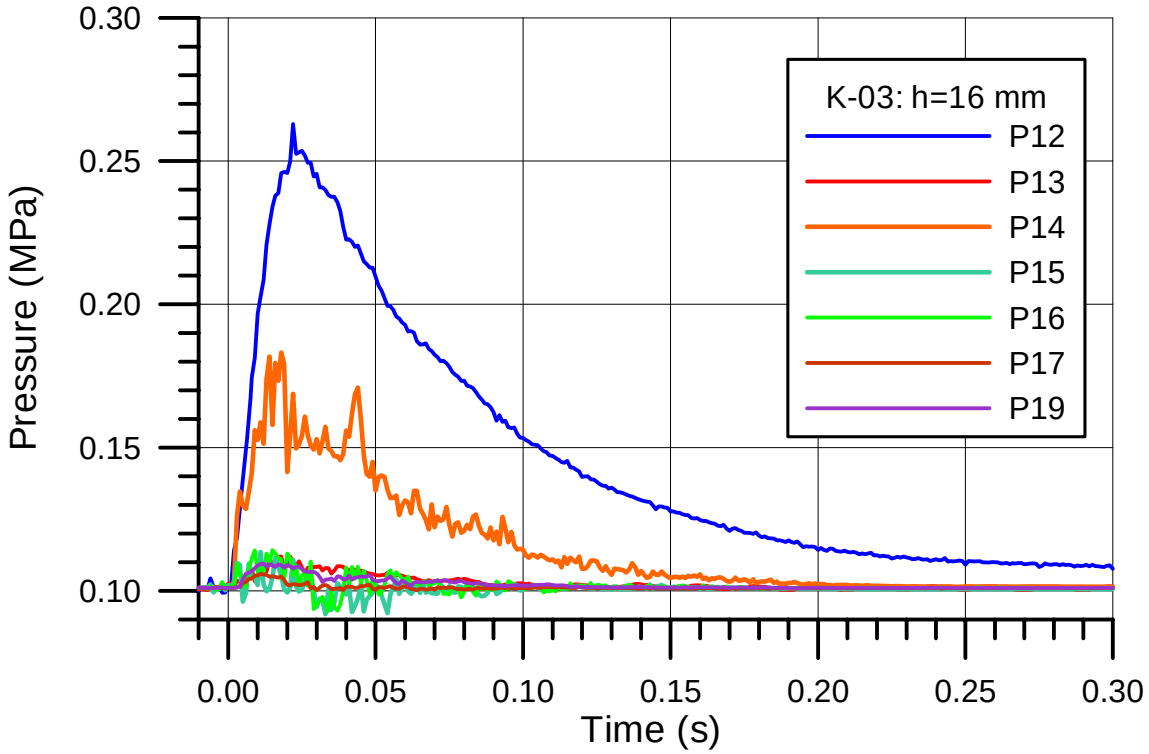

Fig. 5.134 K03 Pressure in the space at the RPV support and in the subcompartments

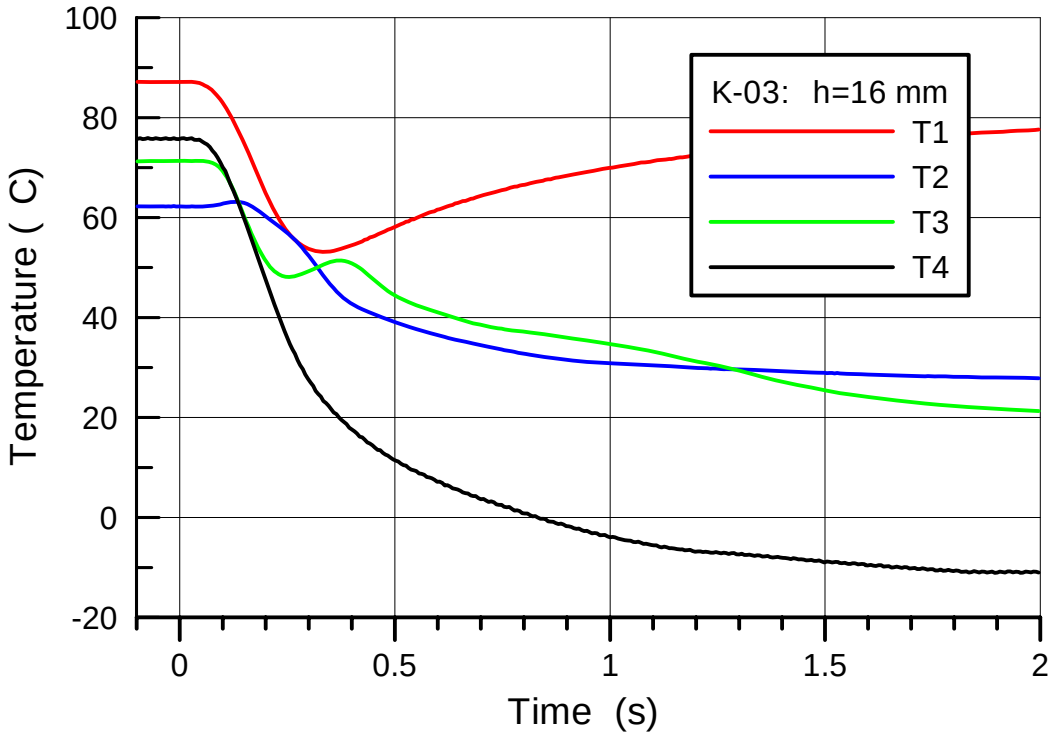

Fig. 5.135 K03 Gas temperatures in the RPV and the cavity

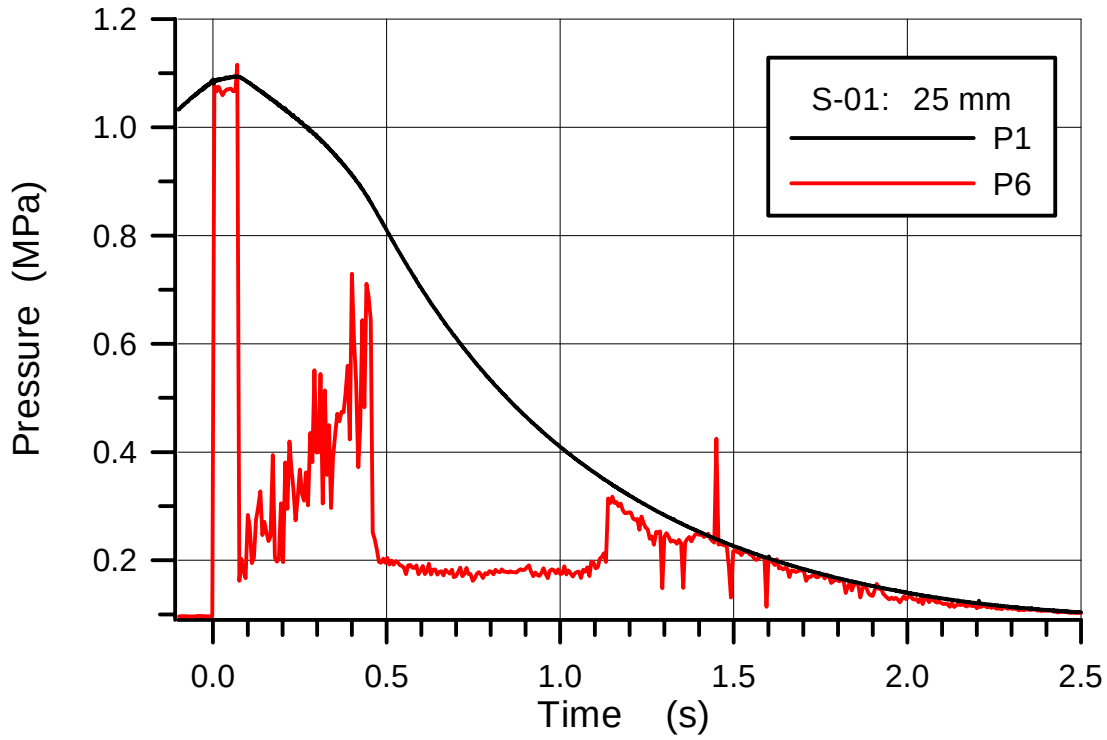

Fig. 5.136 S01 Blow down pressure in the RPV and total pressure on cavity floor below hole

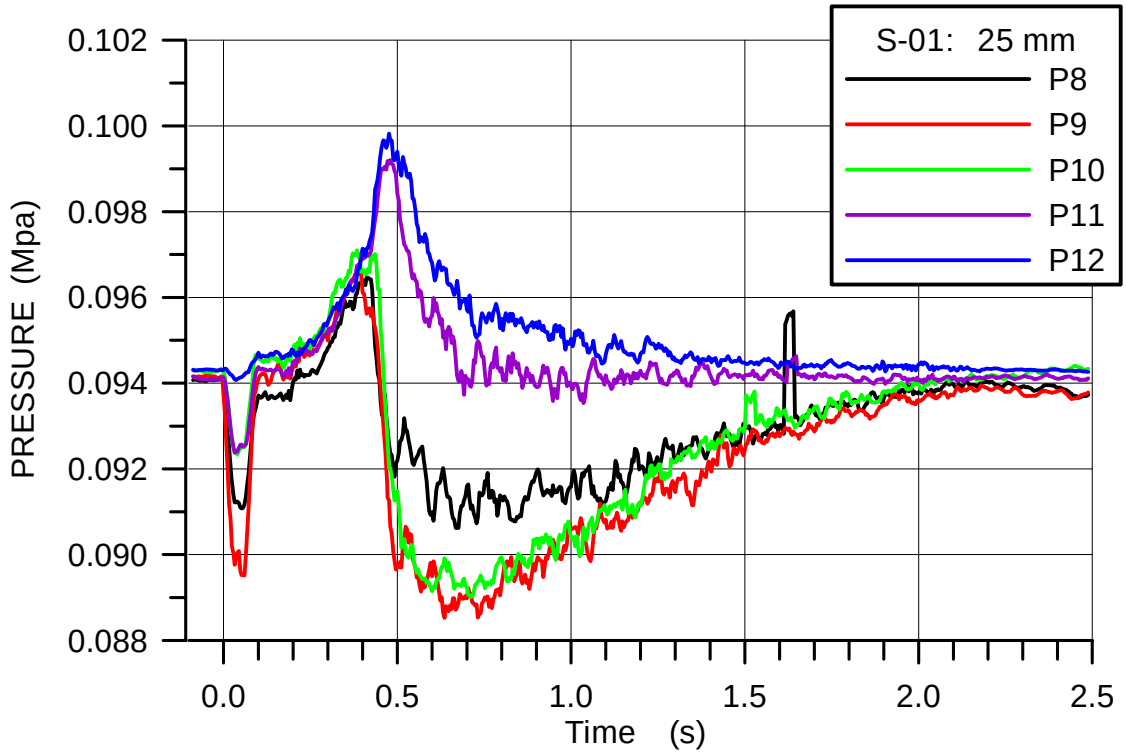

Fig. 5.137 S01 Pressures in the cavity

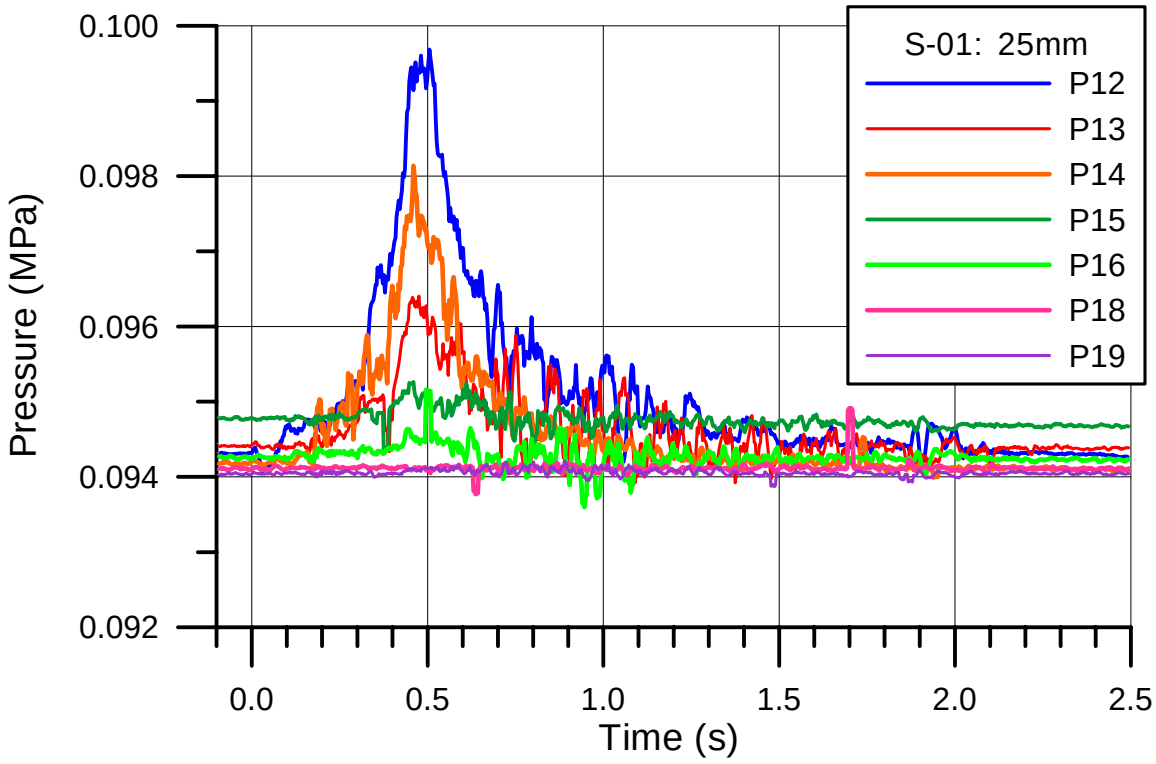

Fig. 5.138 S01 Pressure in the space at the RPV support and in the subcompartments

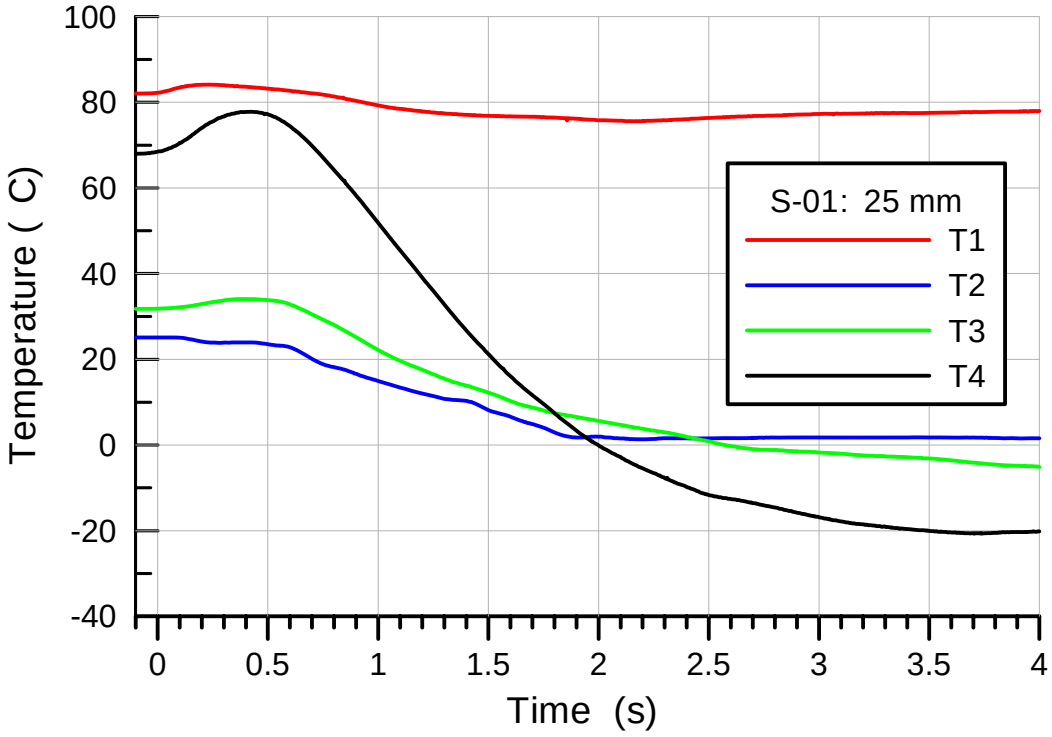

Fig. 5.139 S01 Gas temperatures in the RPV and the cavity

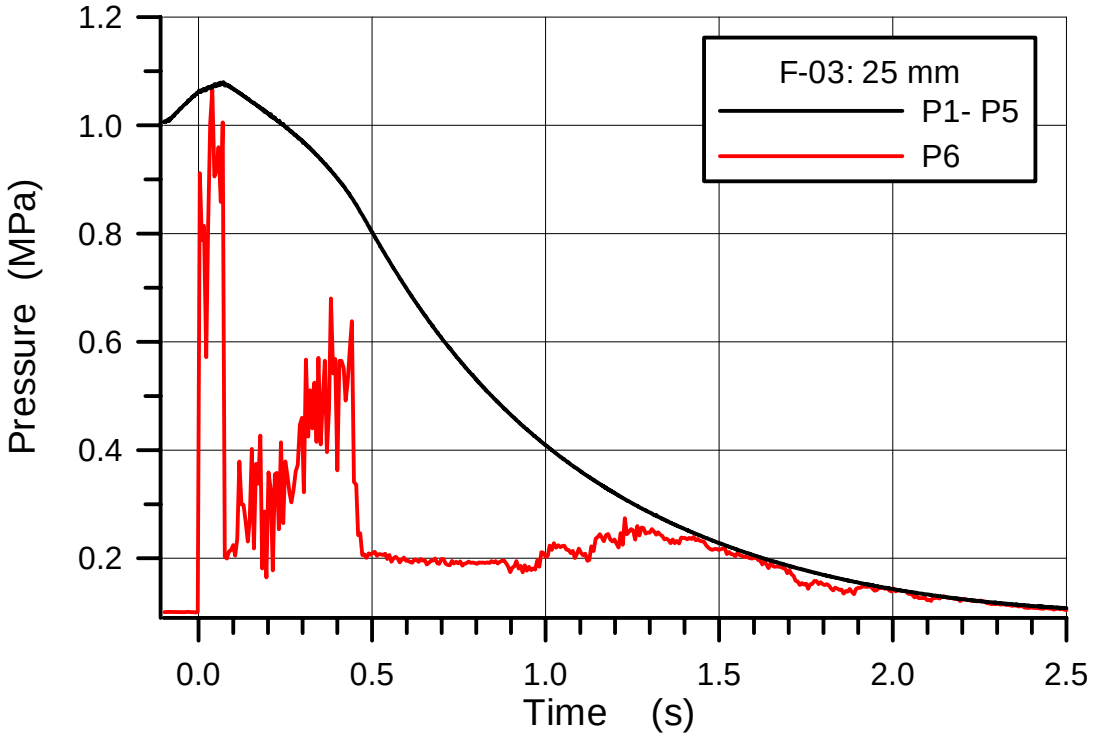

Fig. 5.140 F03 Blow down pressure in the RPV and total pressure on cavity floor below hole

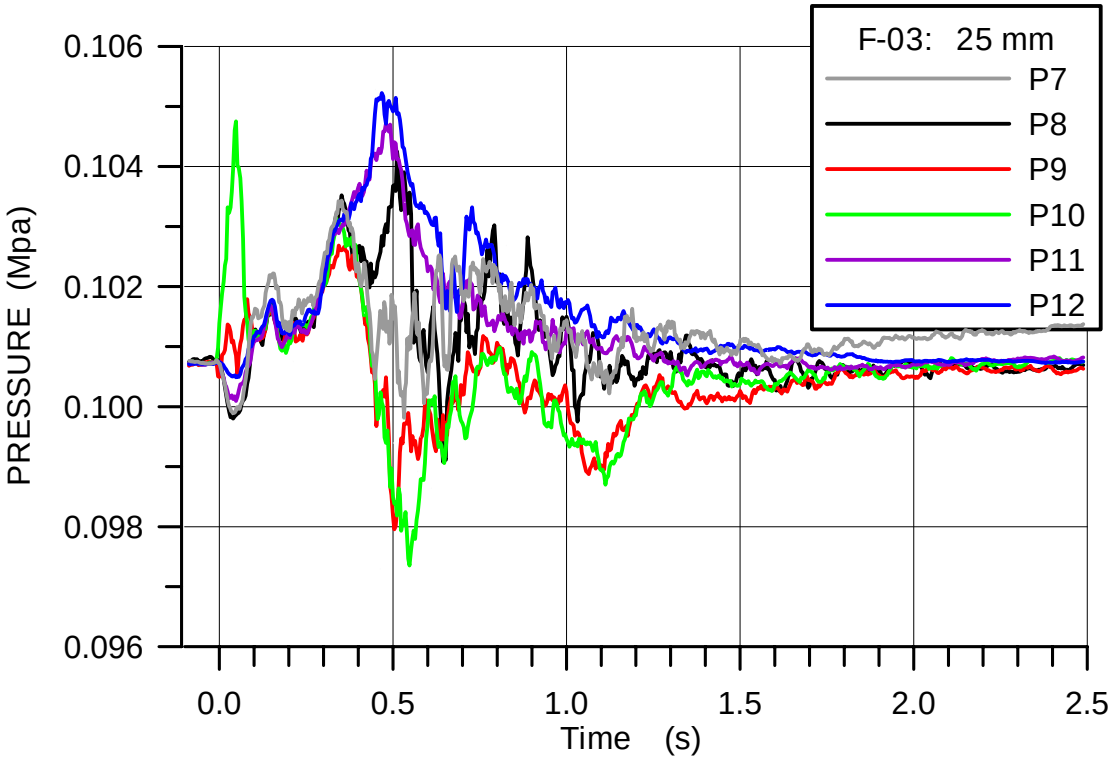

Fig. 5.141 F03 Pressures in the cavity

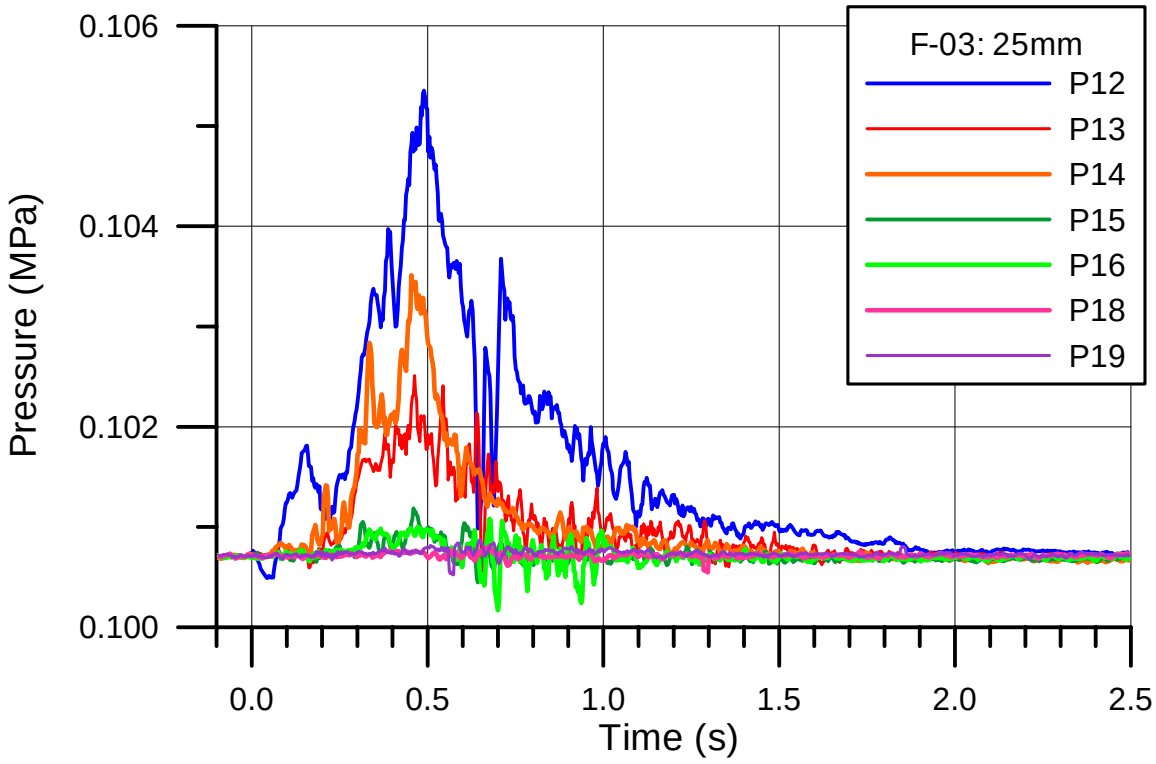

Fig. 5.142 F03 Pressure in the space at the RPV support and in the subcompartments

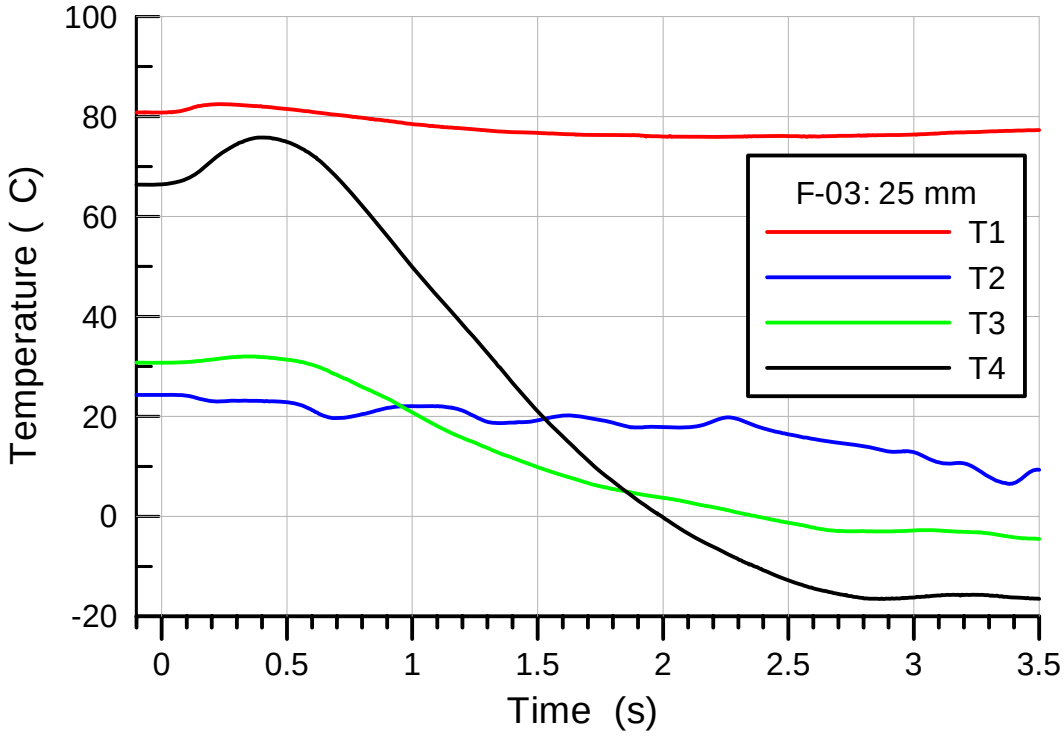

Fig. 5.143 F03 Gas temperatures in the RPV and the cavity

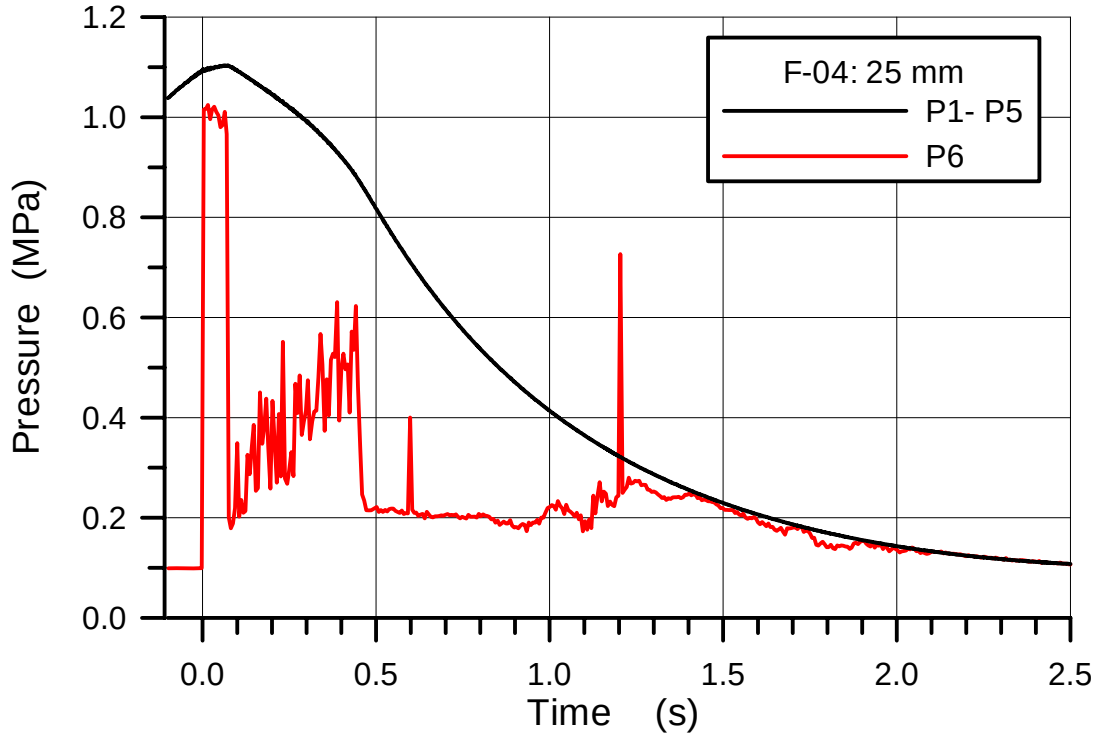

Fig. 5.144 F04 Blow down pressure in the RPV and total pressure on cavity floor below hole

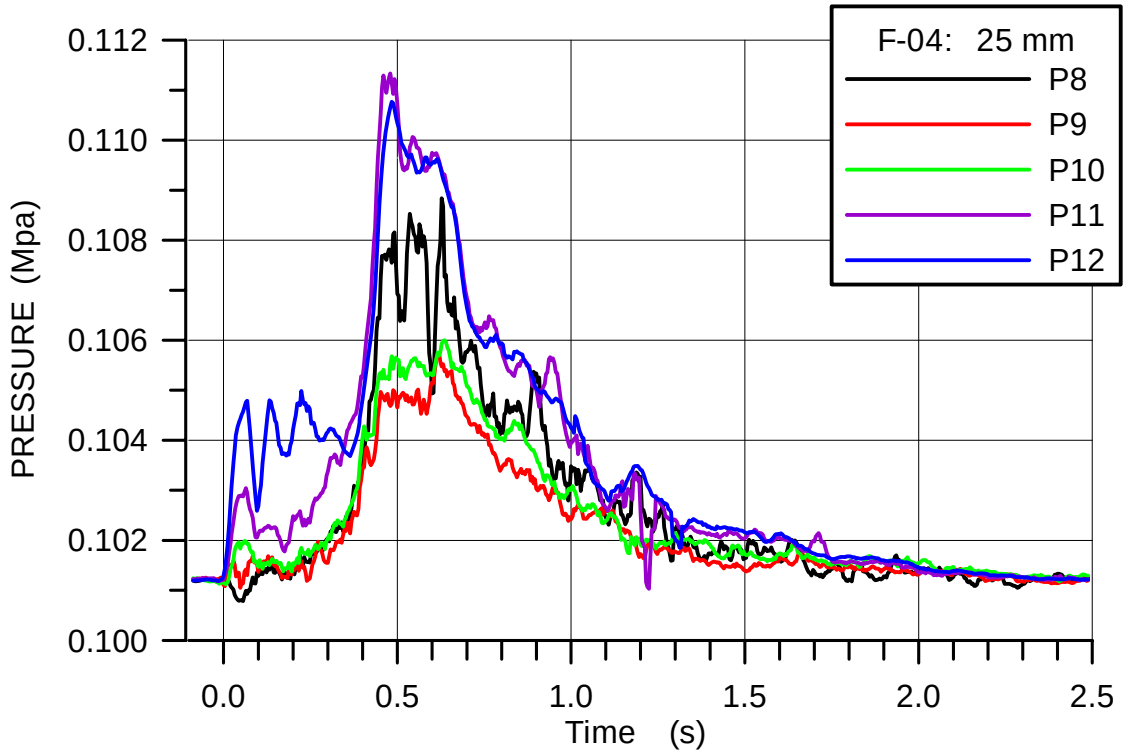

Fig. 5.145 F04 Pressures in the cavity

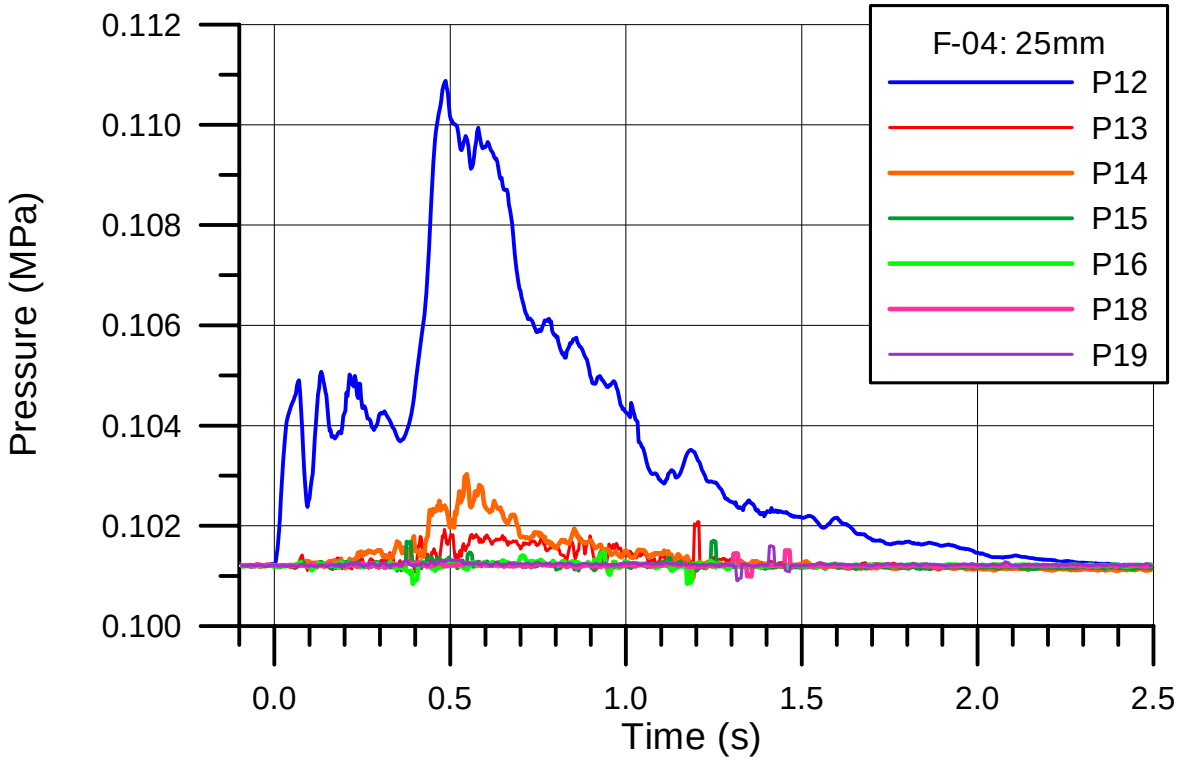

Fig. 5.146 F04 Pressure in the space at the RPV support and in the subcompartments

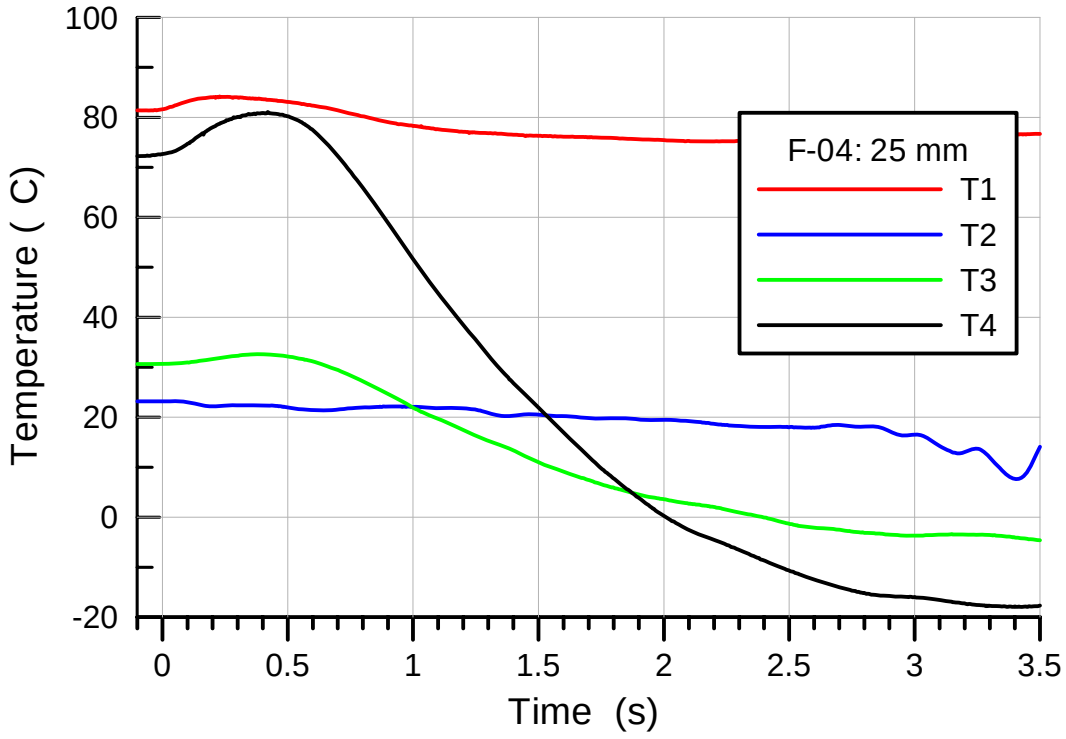

Fig. 5.147 F04 Gas temperatures in the RPV and the cavity

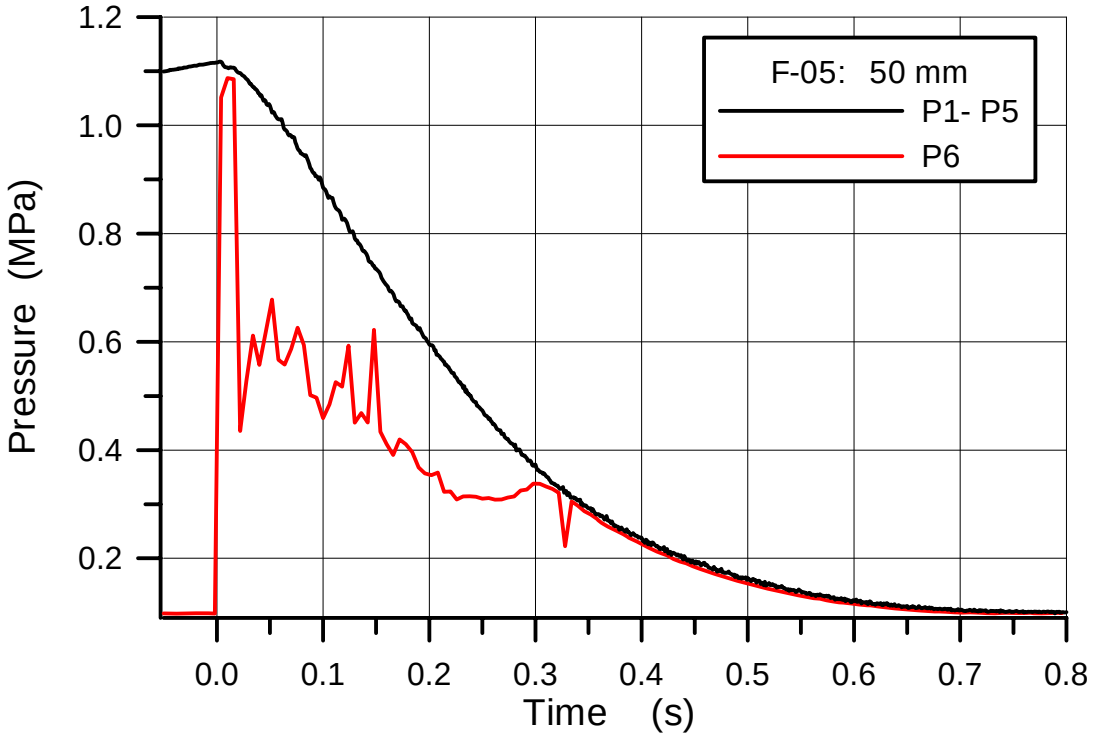

Fig. 5.148 F05 Blow down pressure in the RPV and total pressure on cavity floor below hole

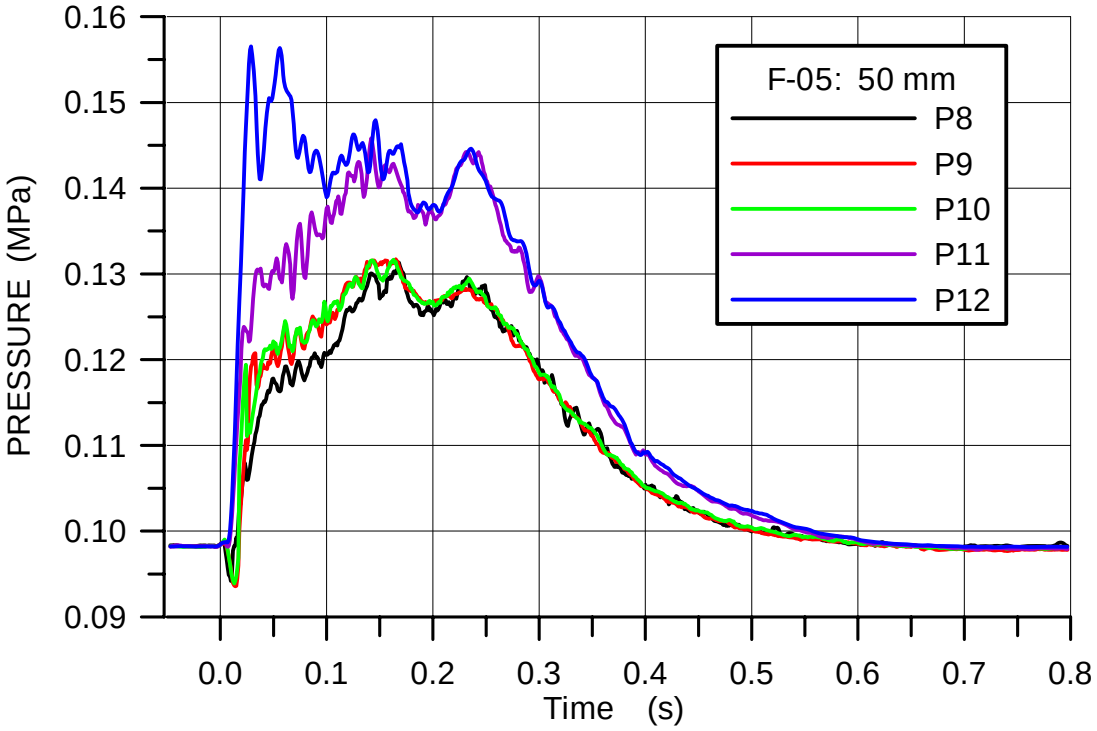

Fig. 5.149 F05 Pressures in the cavity

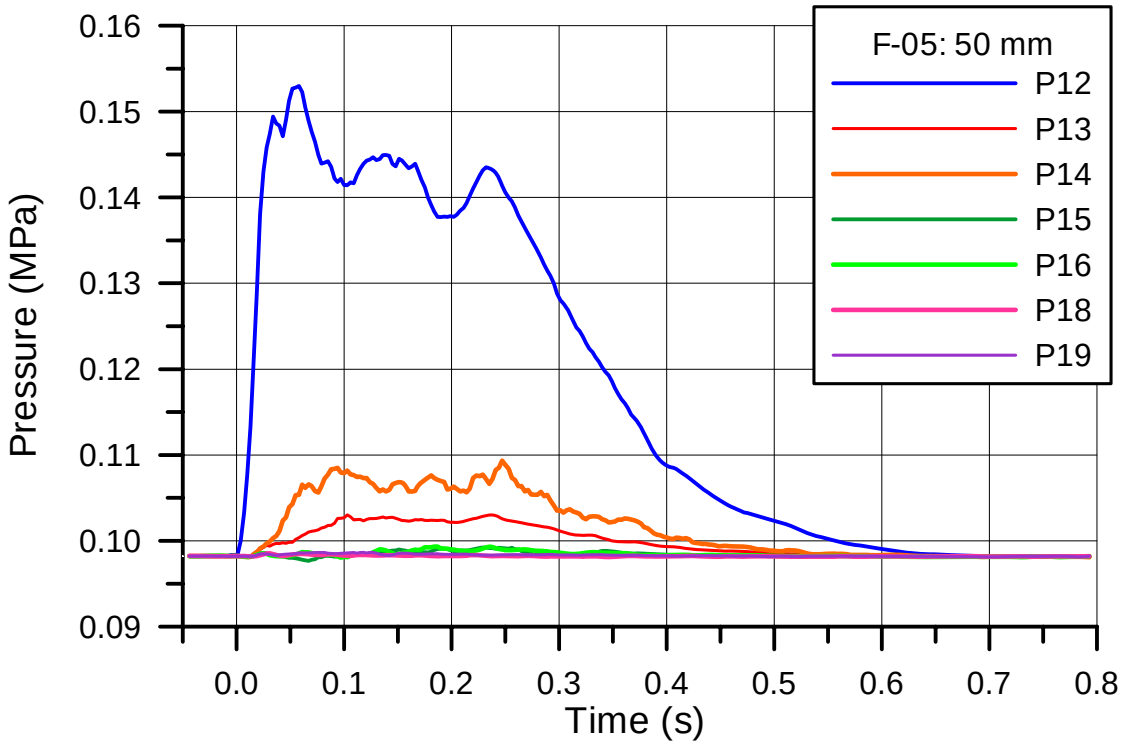

Fig. 5.150 F05 Pressure in the space at the RPV support and in the subcompartments

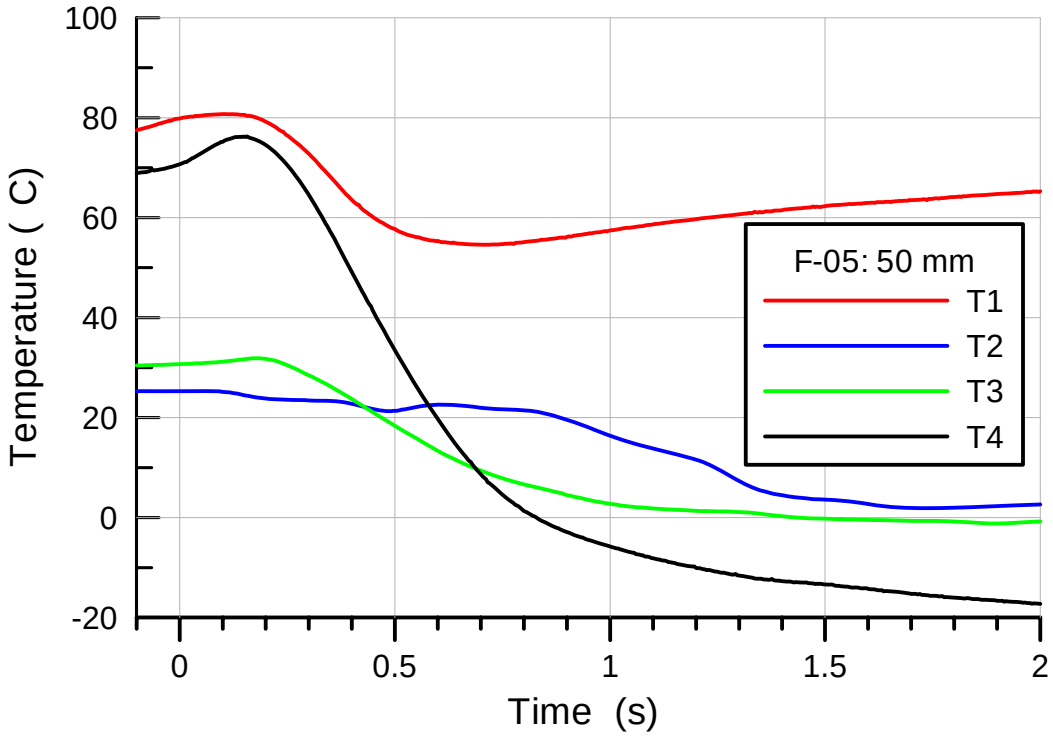

Fig. 5.151 F05 Gas temperatures in the RPV and the cavity

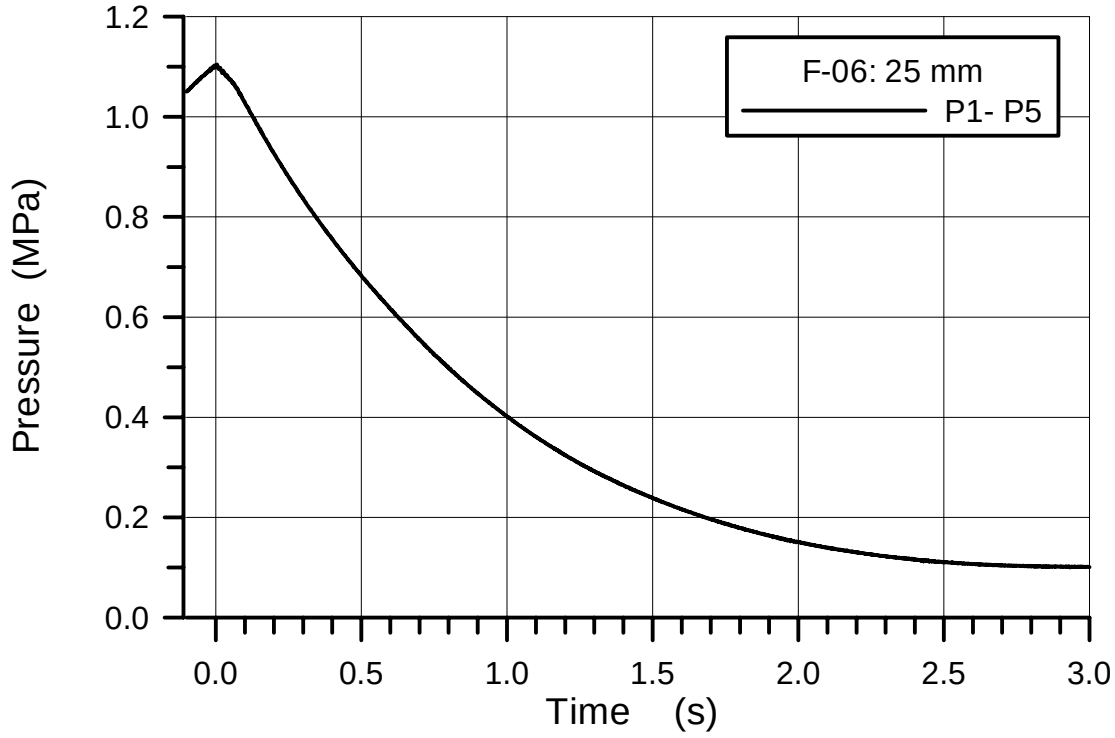

Fig. 5.152 F06 Blow down pressure in the RPV

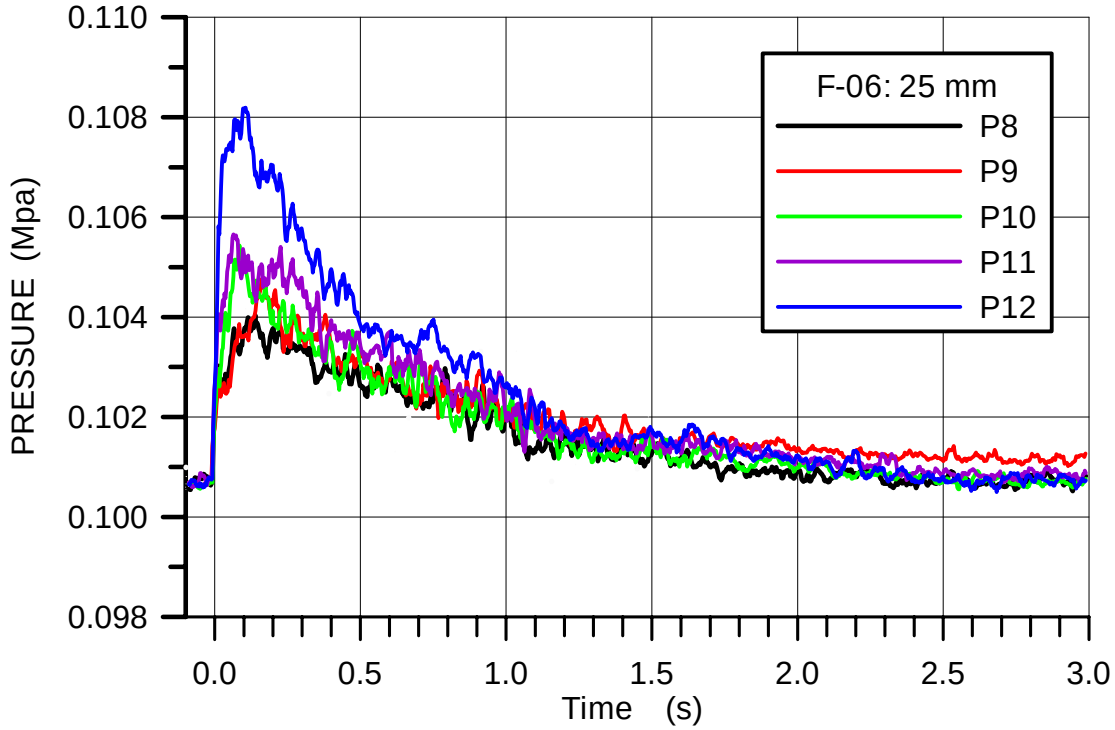

Fig. 5.153 F06 Pressures in the cavity

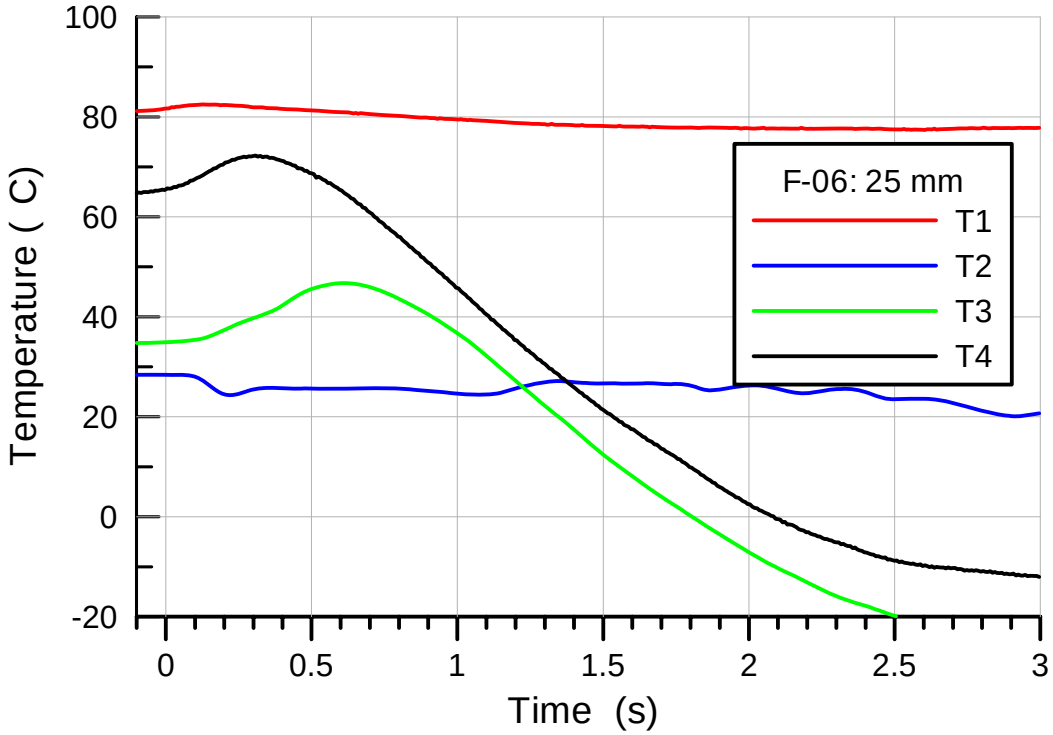

Fig. 5.154 F06 Gas temperatures in the RPV and the cavity

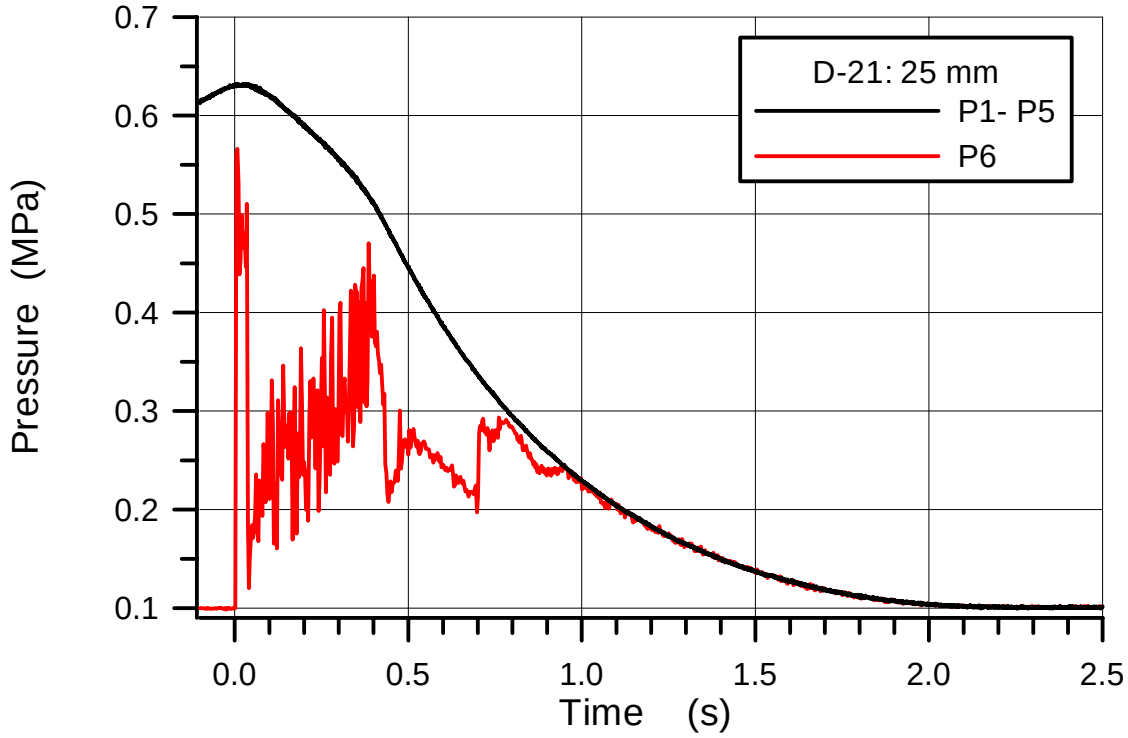

Fig. 5.155 D21 Blow down pressure in the RPV and total pressure on cavity floor below hole

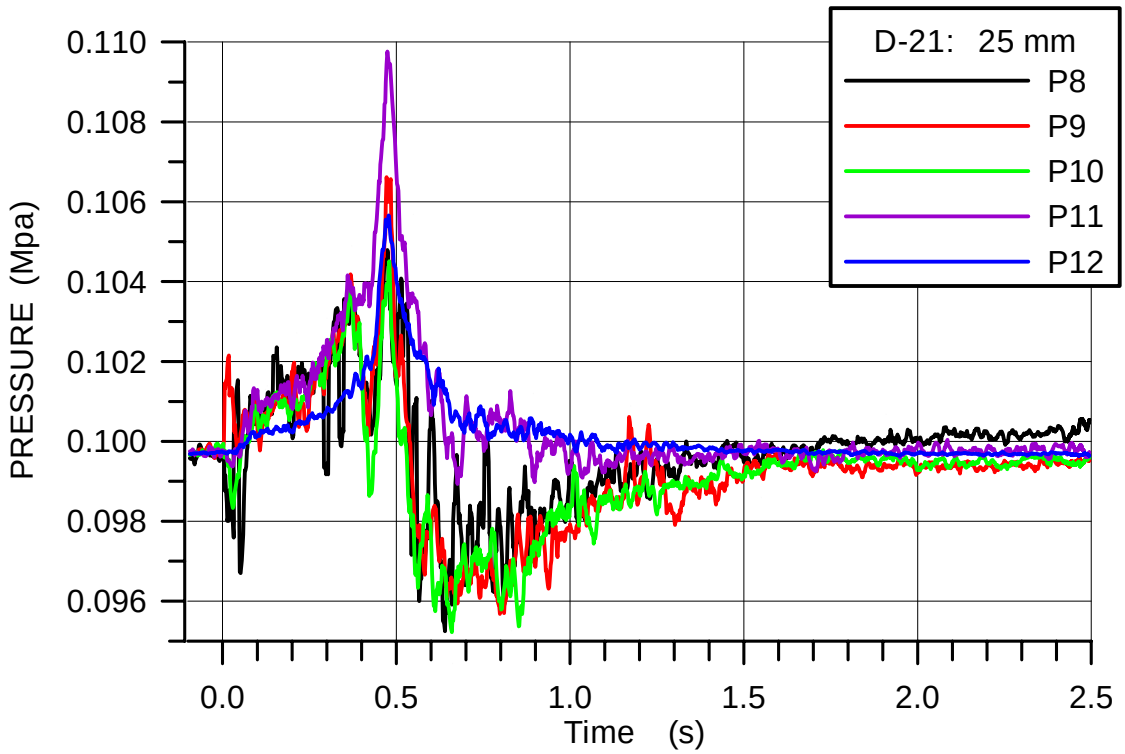

Fig. 5.156 D21 Pressures in the cavity

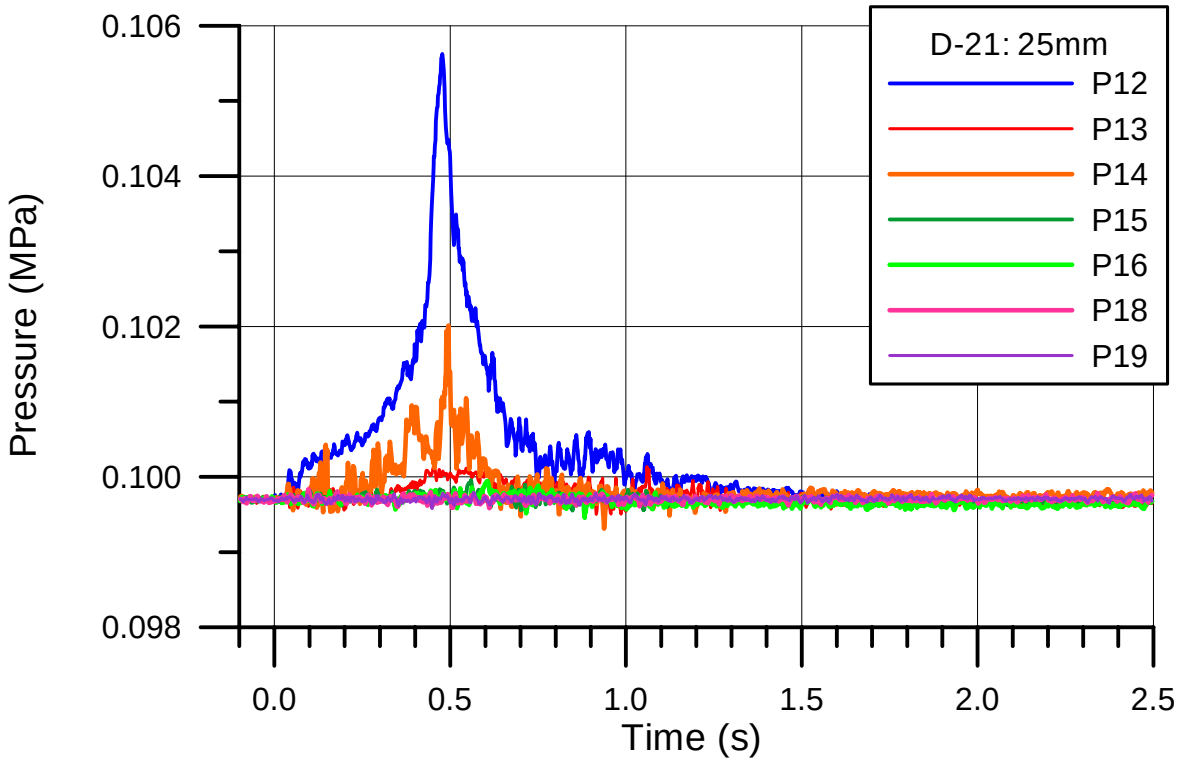

Fig. 5.157 D21 Pressure in the space at the RPV support and in the subcompartments

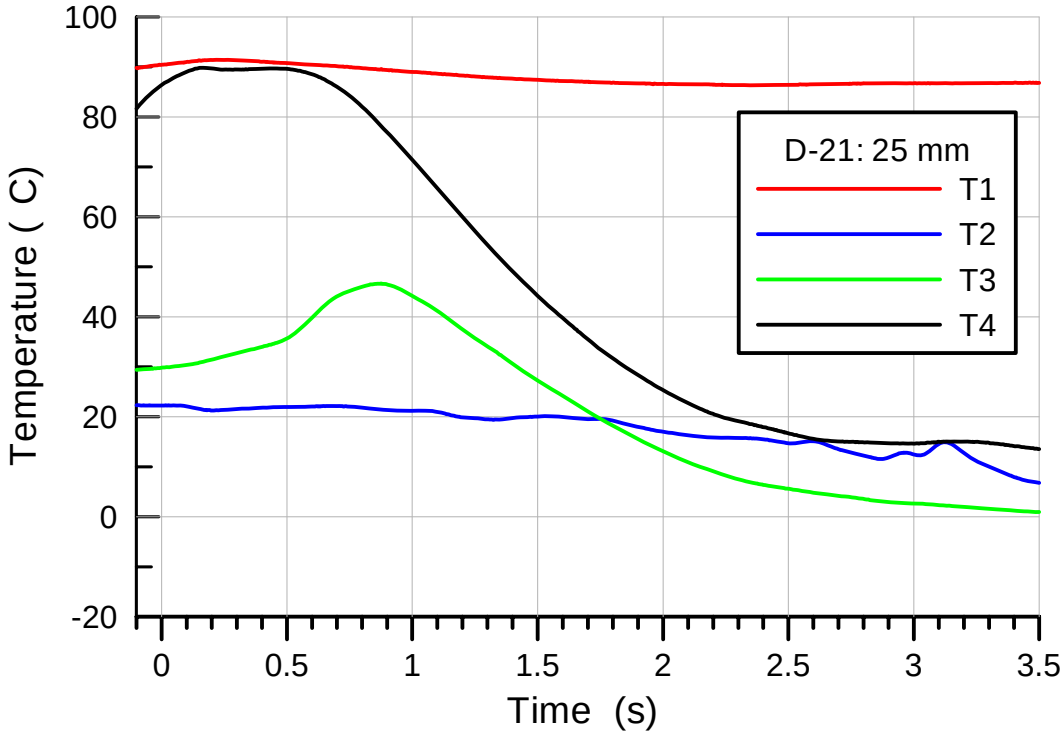

Fig. 5.158 D21 Gas temperatures in the RPV and the cavity

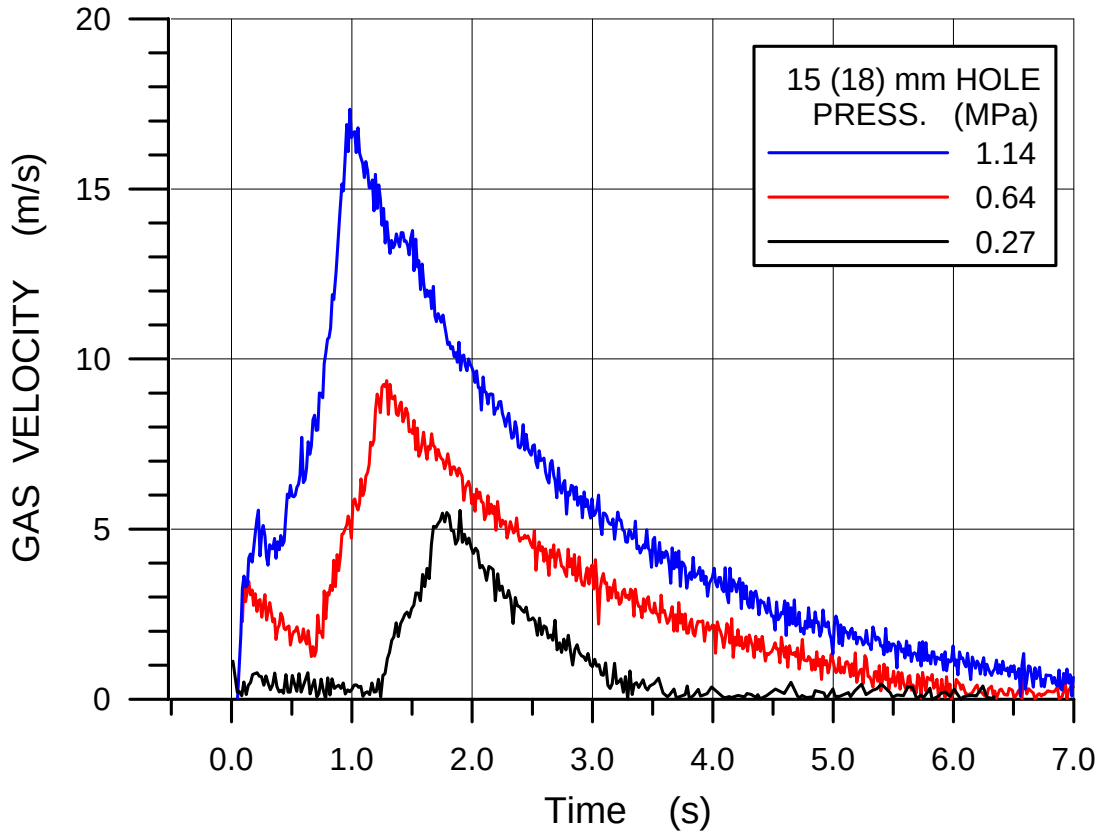

Fig. 5.159 Bulk gas velocities of nitrogen in the annular space in the cavity for 15 mm holes

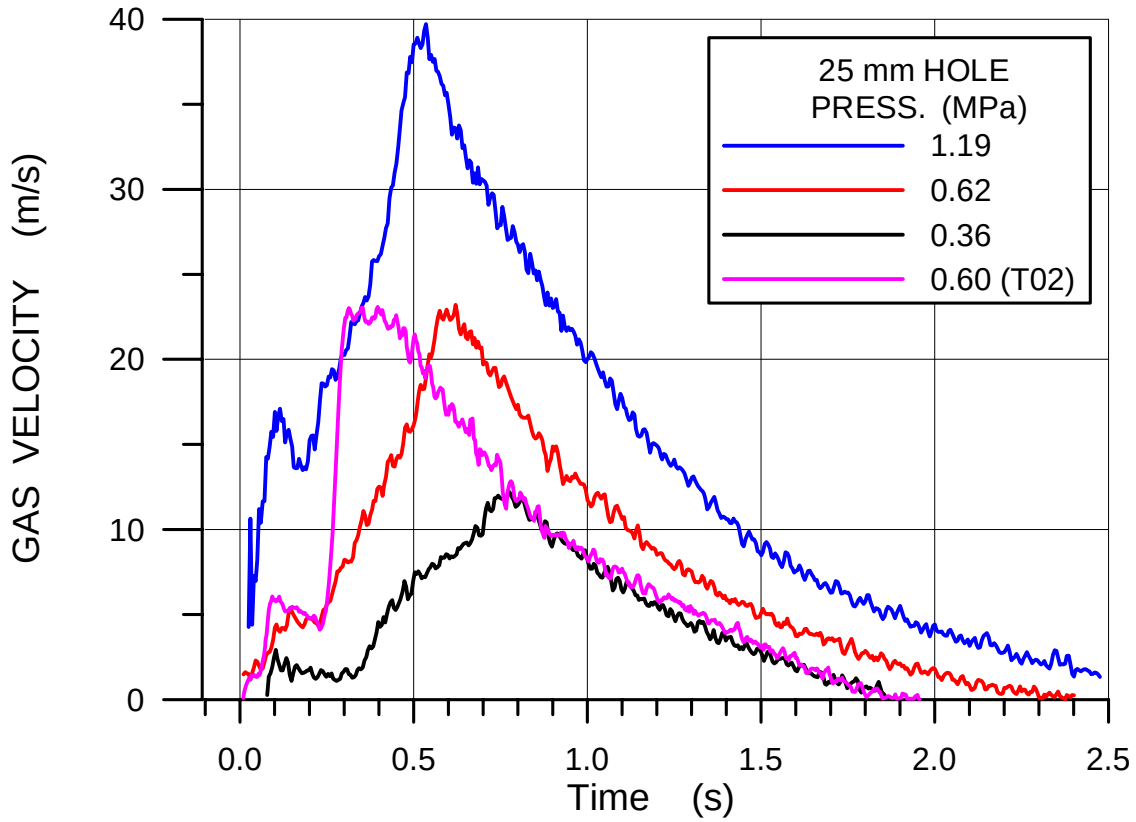

Fig. 5.160 Bulk gas velocities of nitrogen in the annular space in the cavity for 25 mm holes

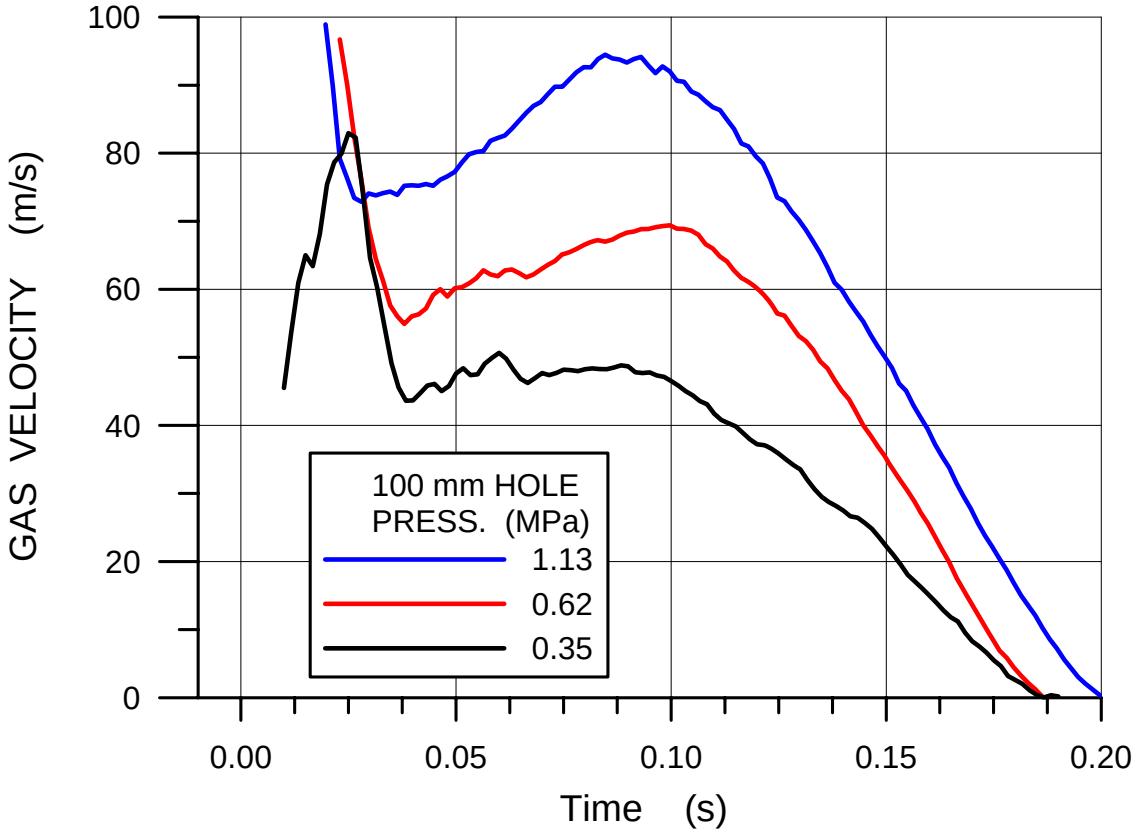

Fig. 5.161 Bulk gas velocities of nitrogen in the annular space in the cavity for 100 mm holes

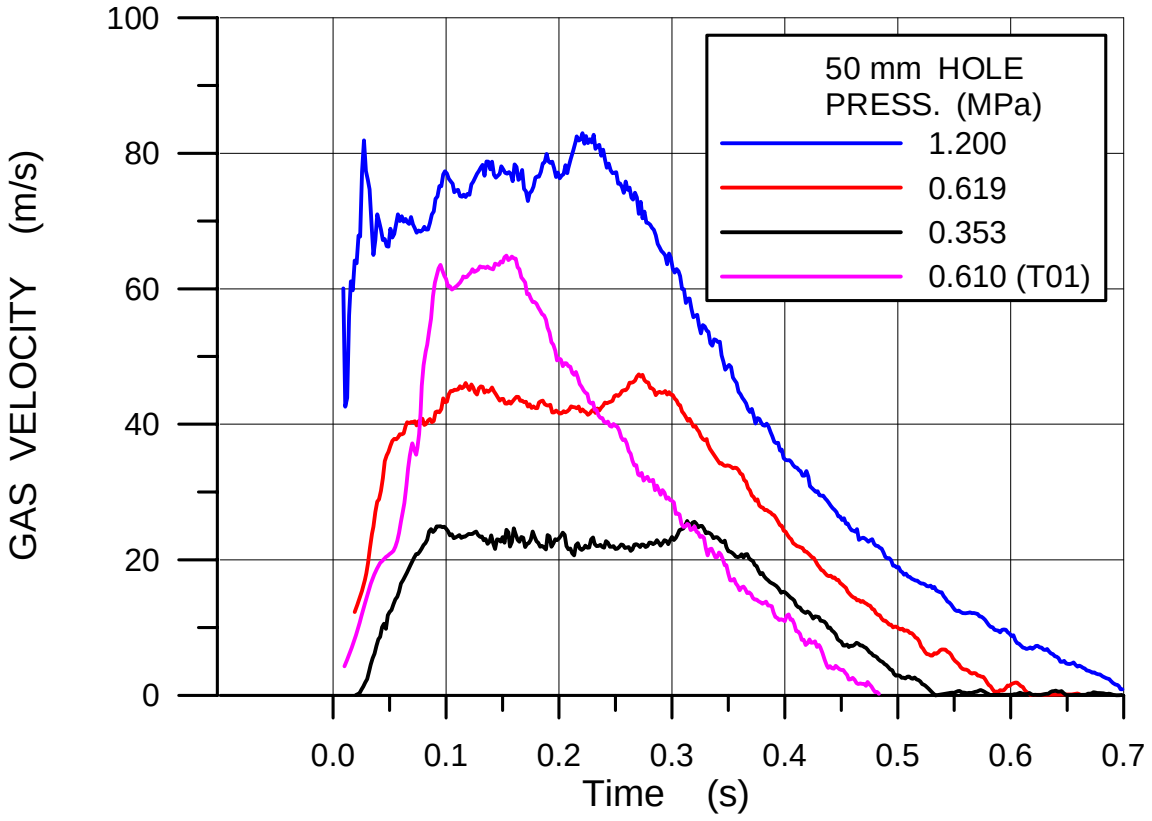

Fig. 5.162 Bulk gas velocities of nitrogen in the annular space in the cavity for 50 mm holes

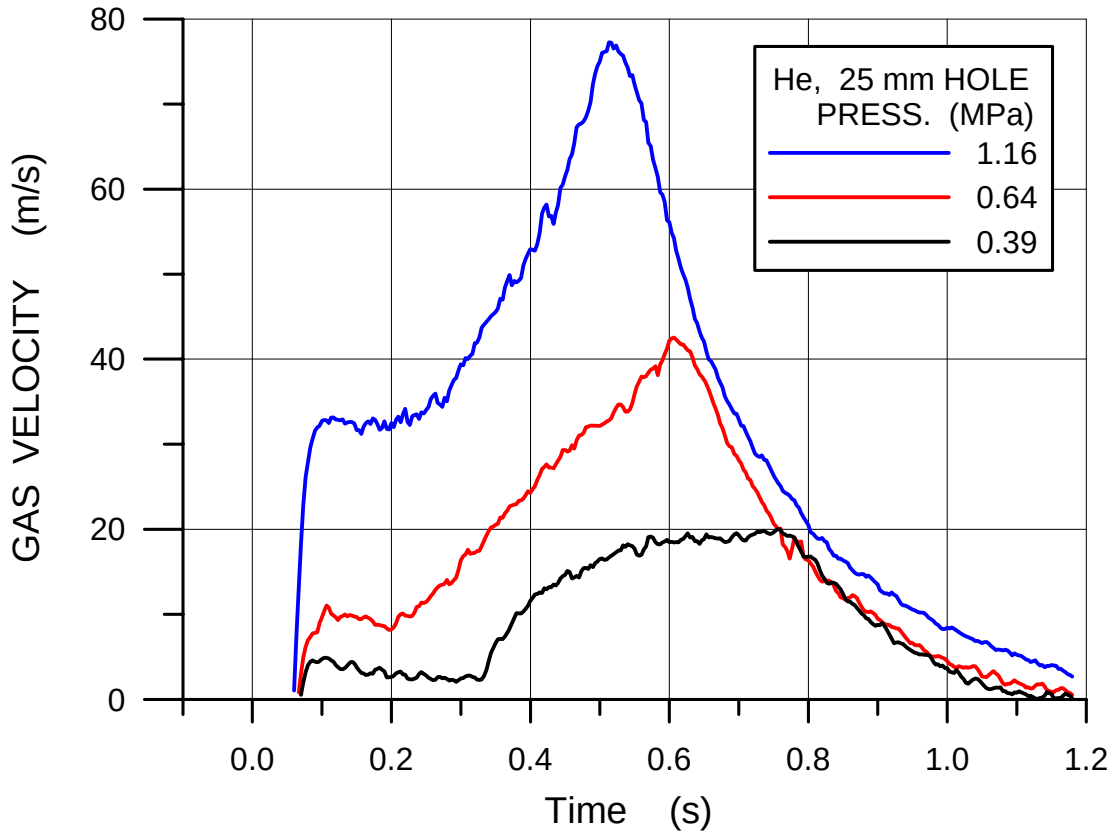

Fig. 5.163 Bulk gas velocities of helium in the annular space in the cavity for 25 mm holes

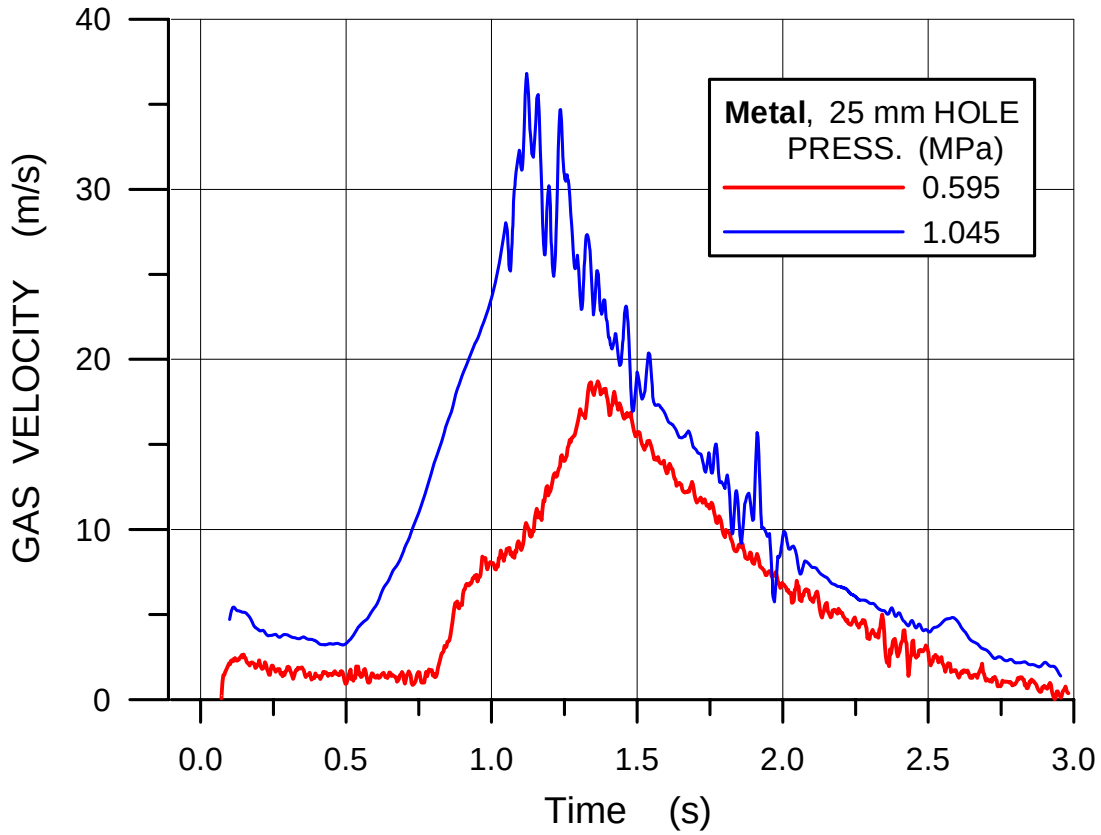

Fig. 5.164 Bulk gas velocities of nitrogen in the annular space in the cavity for 25 mm holes and liquid metal

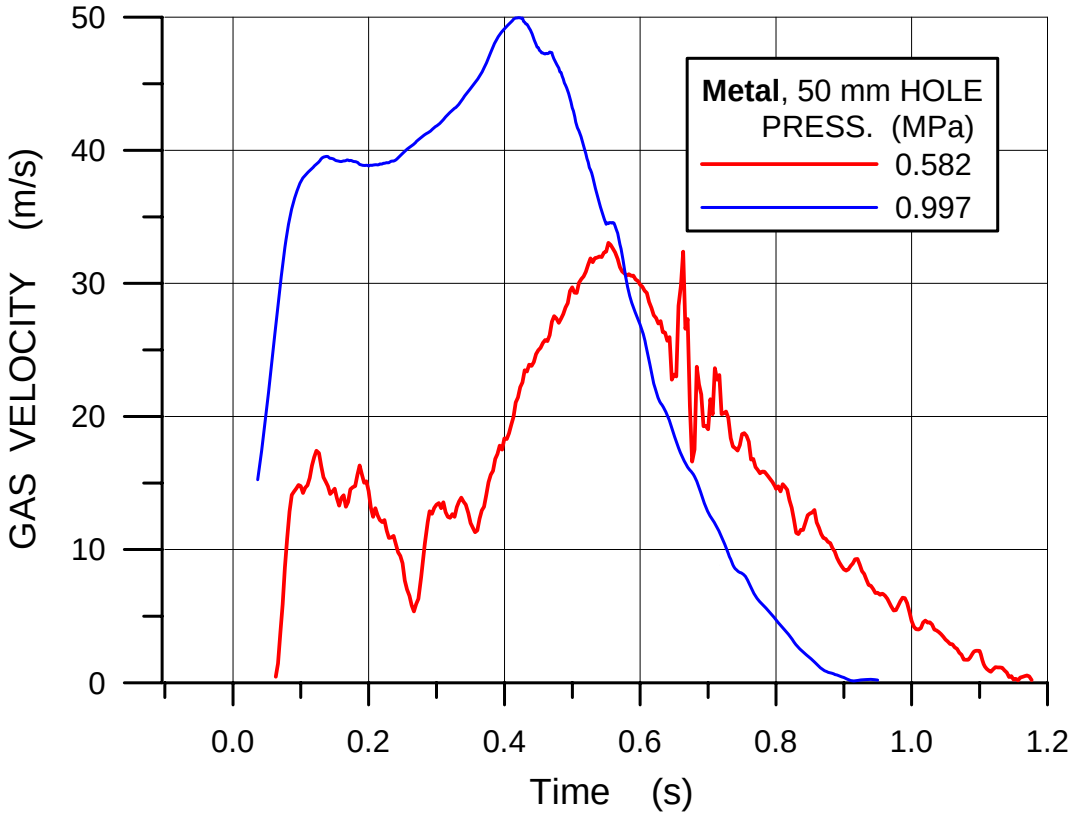

Fig. 5.165 Bulk gas velocities of nitrogen in the annular space in the cavity for 50 mm holes and liquid metal

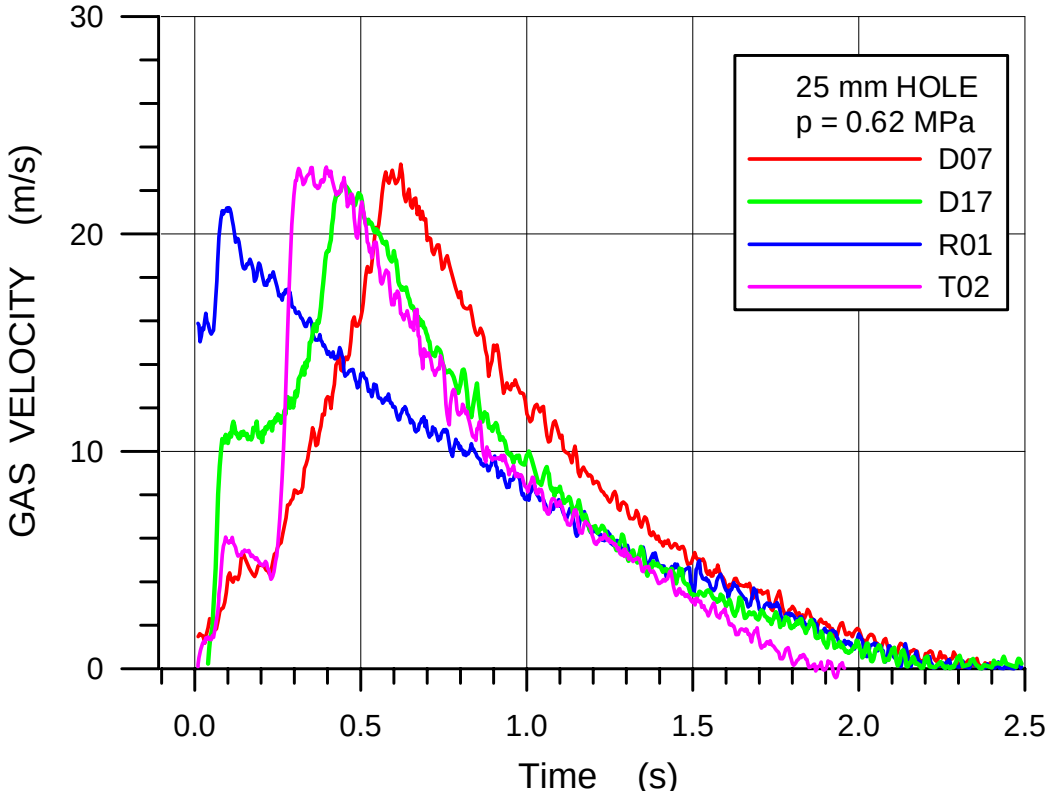

Fig. 5.166 Bulk gas velocities of nitrogen in the annular space in the cavity for 25 mm holes and liquid water, comparison of different liquid inventory (D07 and D17), different hole position and hole shape (D17 and R01), and different pool depth (D07 and T02)

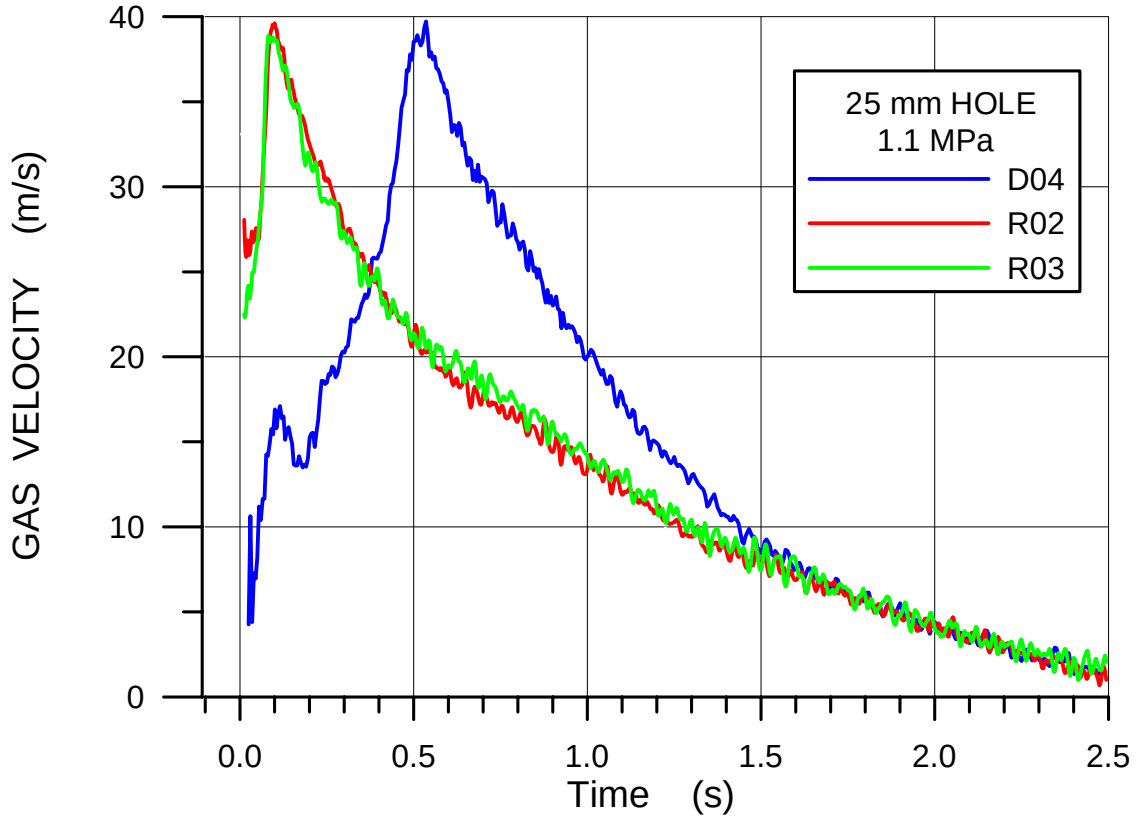

Fig. 5.167 Bulk gas velocities of nitrogen in the annular space in the cavity for 25 mm holes and liquid water, comparison of different hole position (D04 and R03), and different hole shape of lateral breaches (R03 and R02)

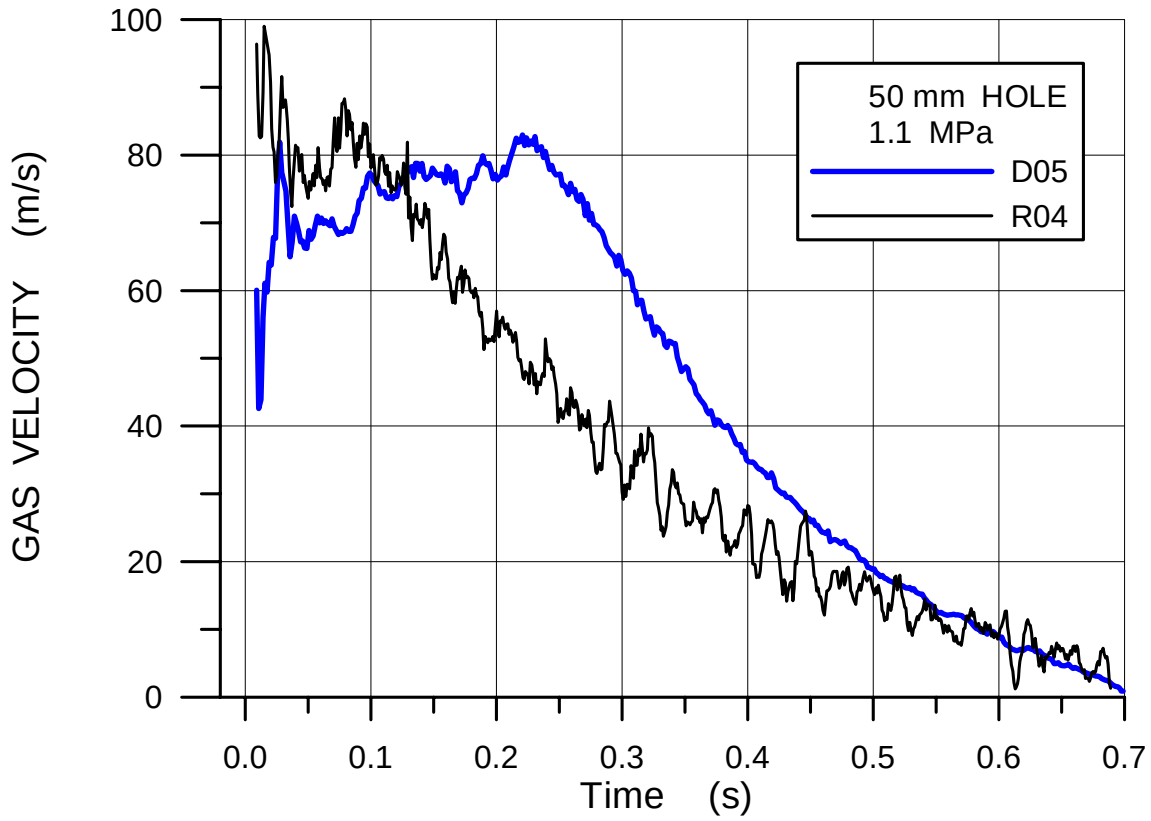

Fig. 5.168 Bulk gas velocities of nitrogen in the annular space in the cavity for 50 mm holes and liquid water, comparison of different hole position (D05 and R04)

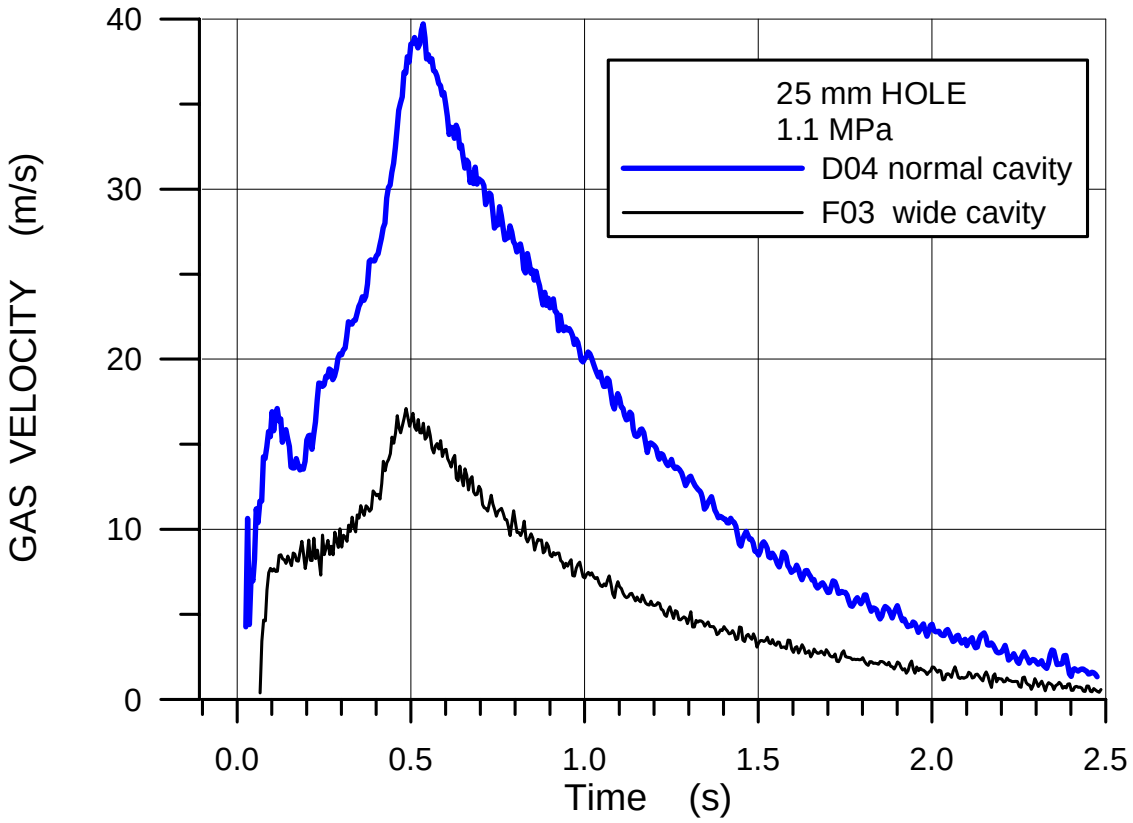

Fig. 5.169 Bulk gas velocities of nitrogen in the annular space in the cavity for 25 mm holes and liquid water, comparison of different cavity flow cross sections

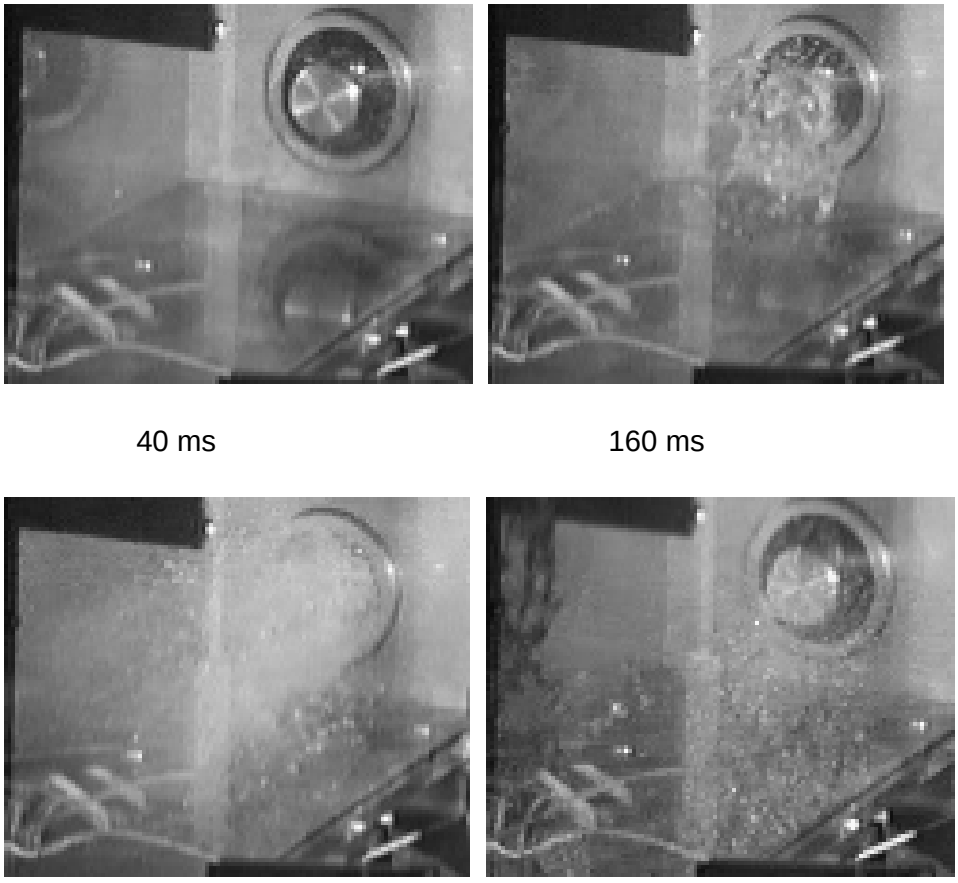

Fig. 5.170 D04 View of flow into subcompartments

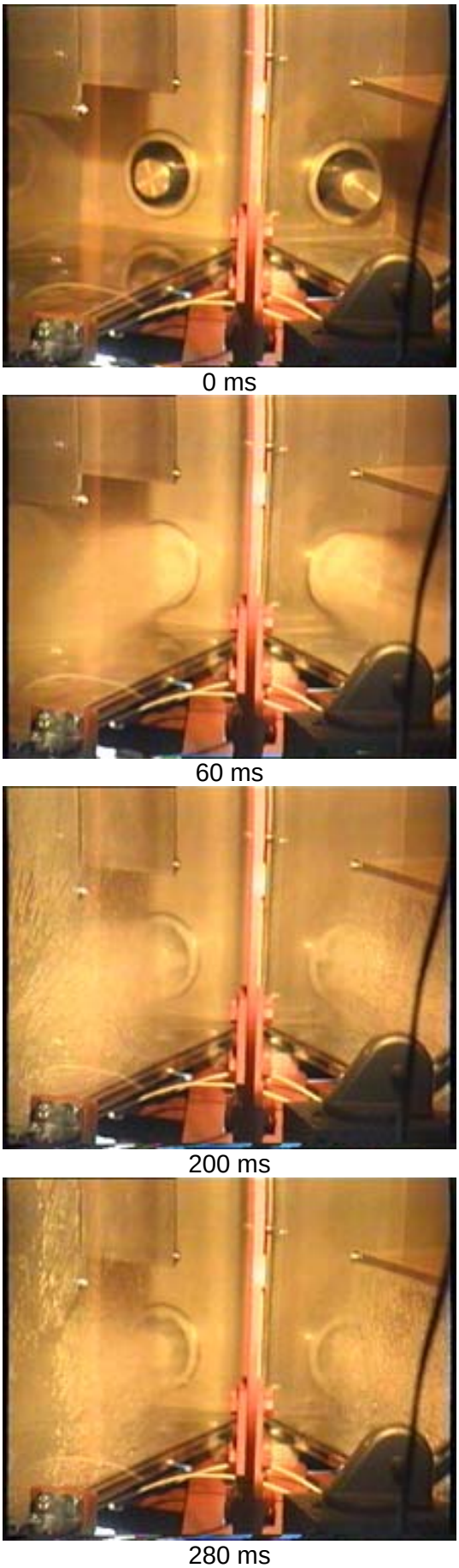

Fig. 5.171 D05 View of flow into subcompartments

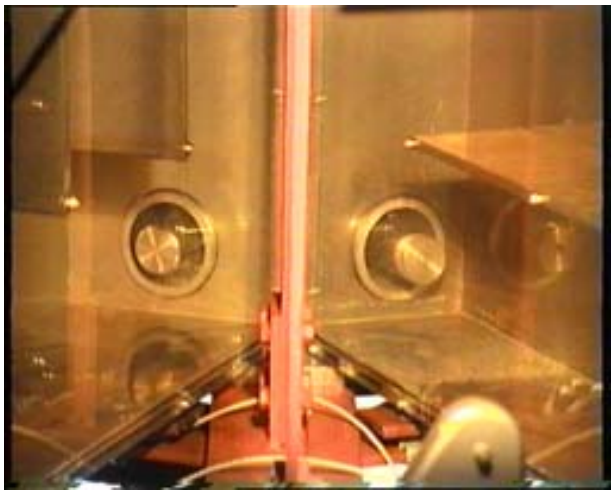

60 ms

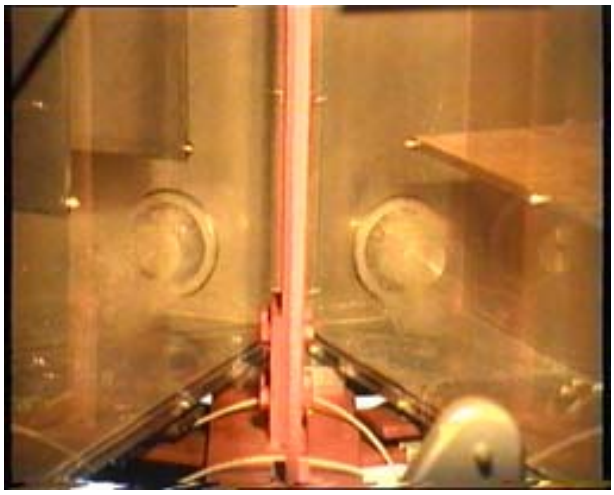

100 ms

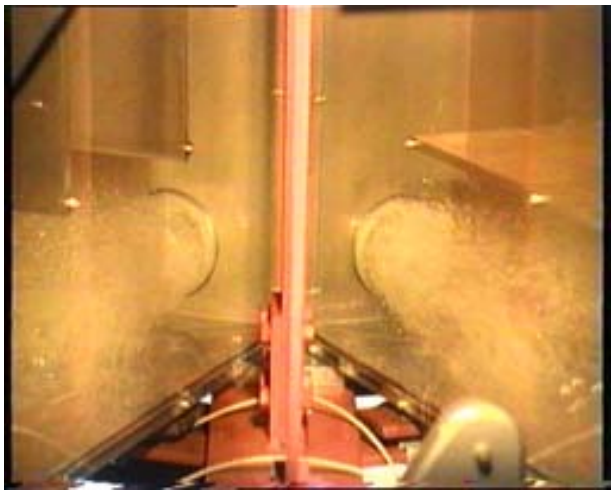

200 ms

Fig. 5.172 D06 View of flow into subcompartments

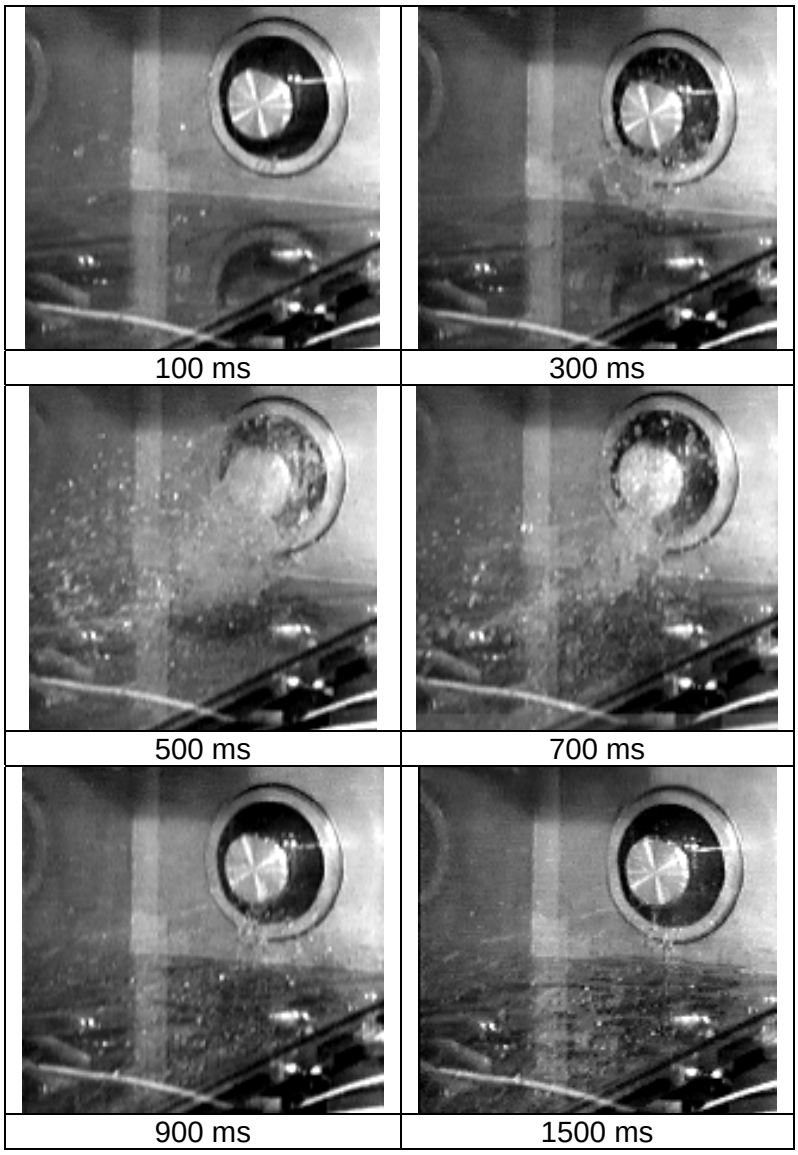

Fig. 5.173 D07 View of flow into subcompartment

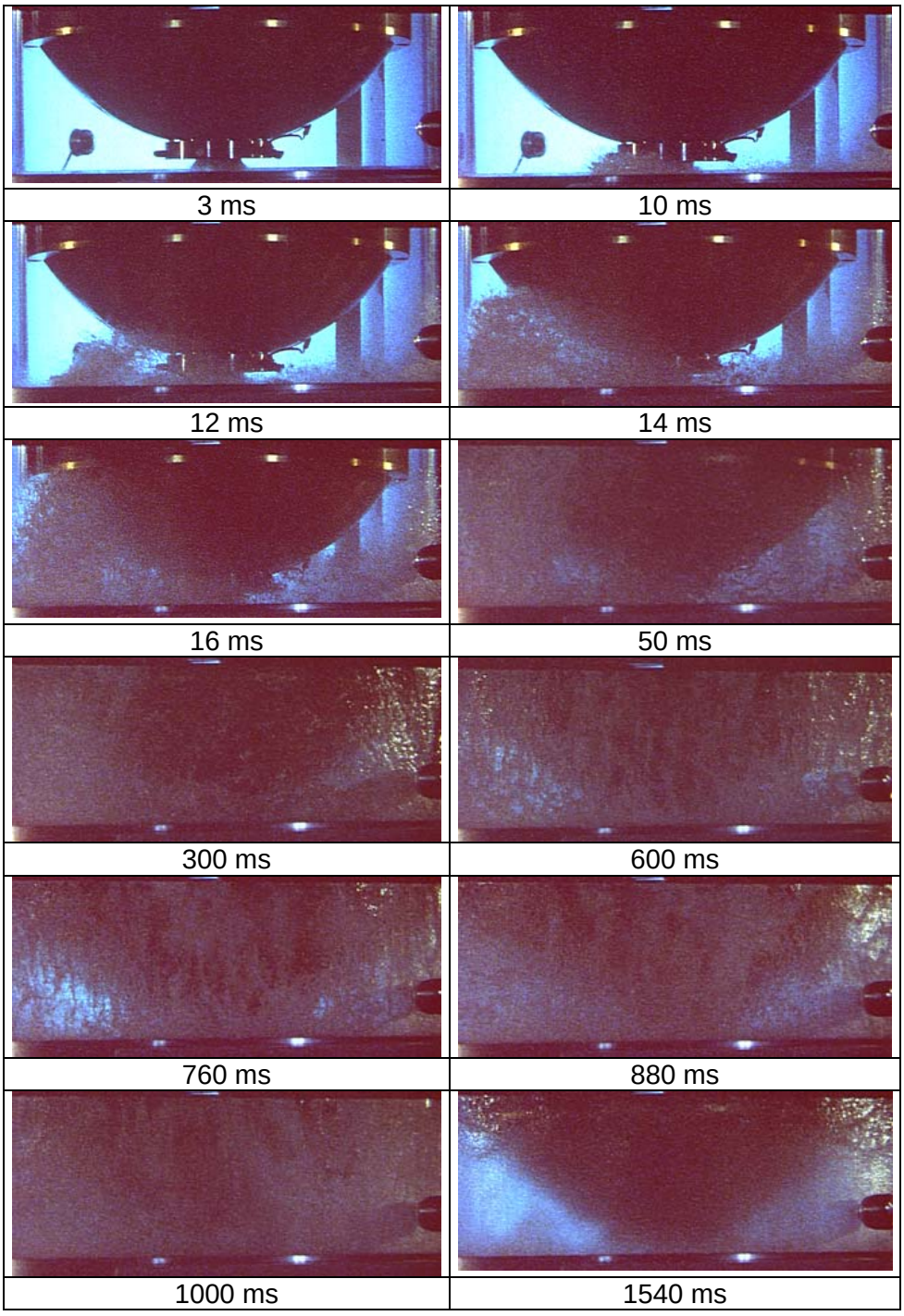

Fig. 5.174 D10 View of flow in the cavity

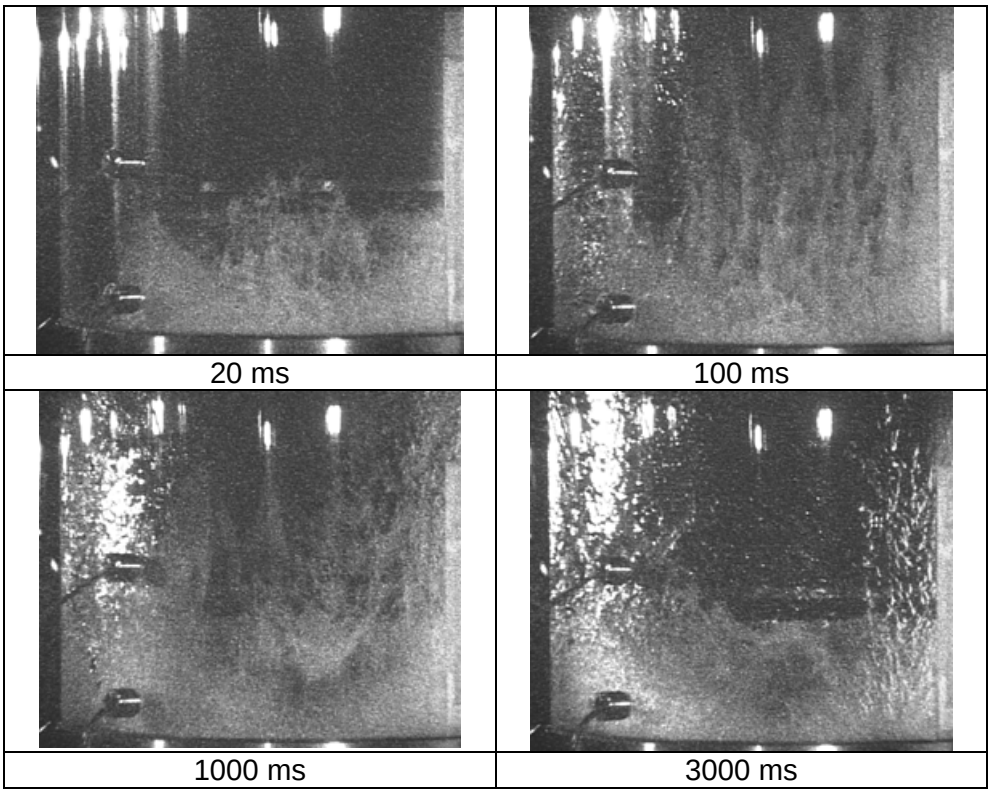

Fig. 5.175 D10 View of flow in the cavity

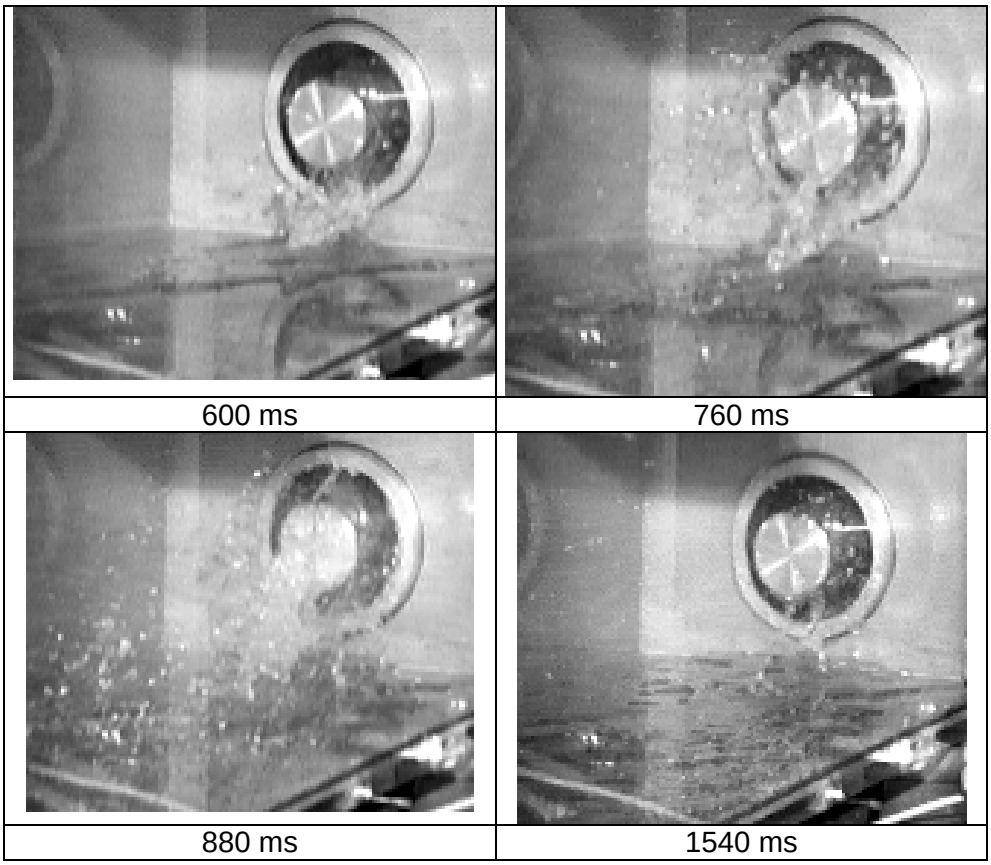

Fig. 5.176 D10 View of flow into subcompartment

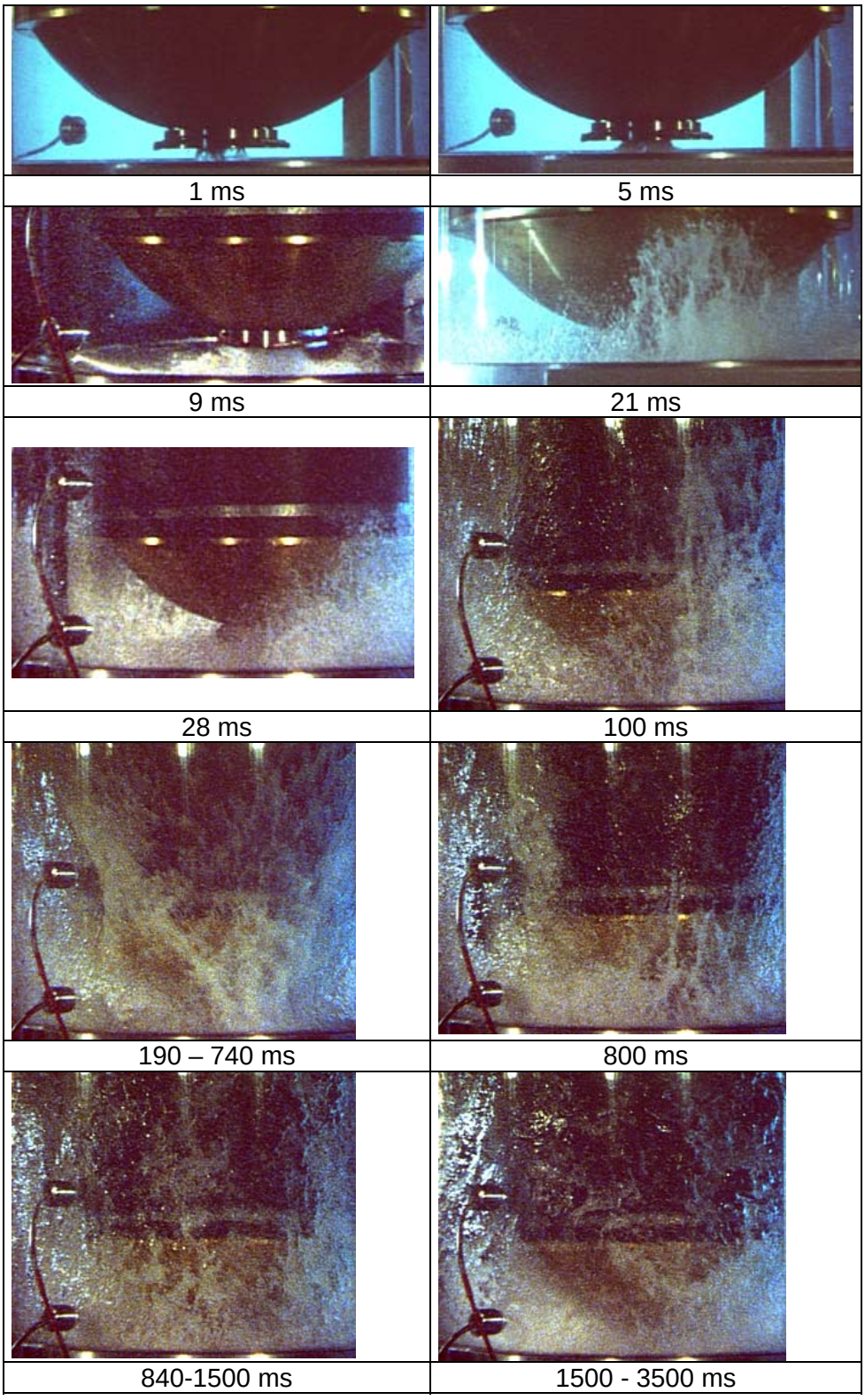

Fig. 5.177 D11View of flow in cavity
(part of the left side of the picture is cut off for t ≥ 100 ms)

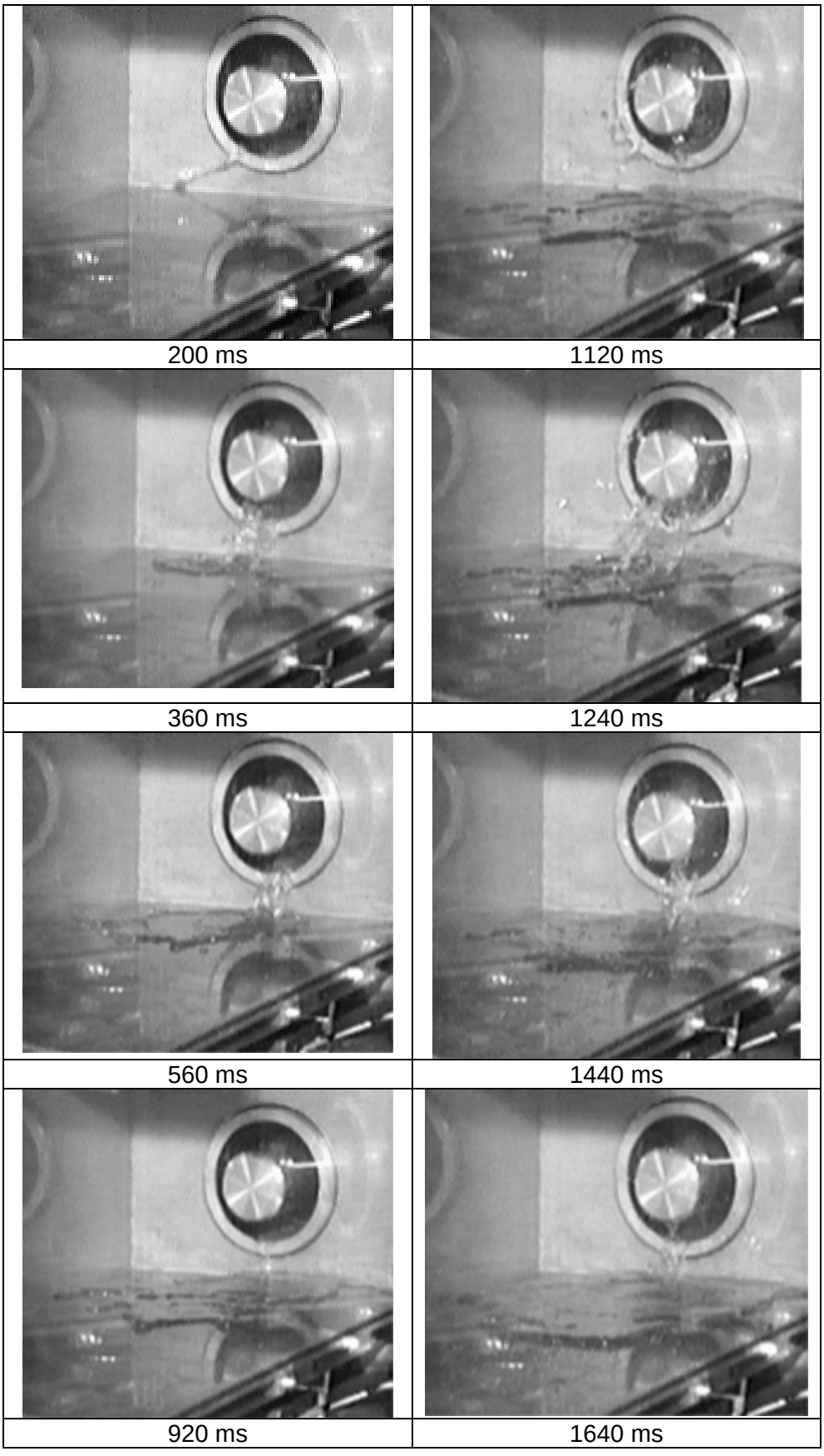

Fig. 5.178 D11 View of flow into subcompartment

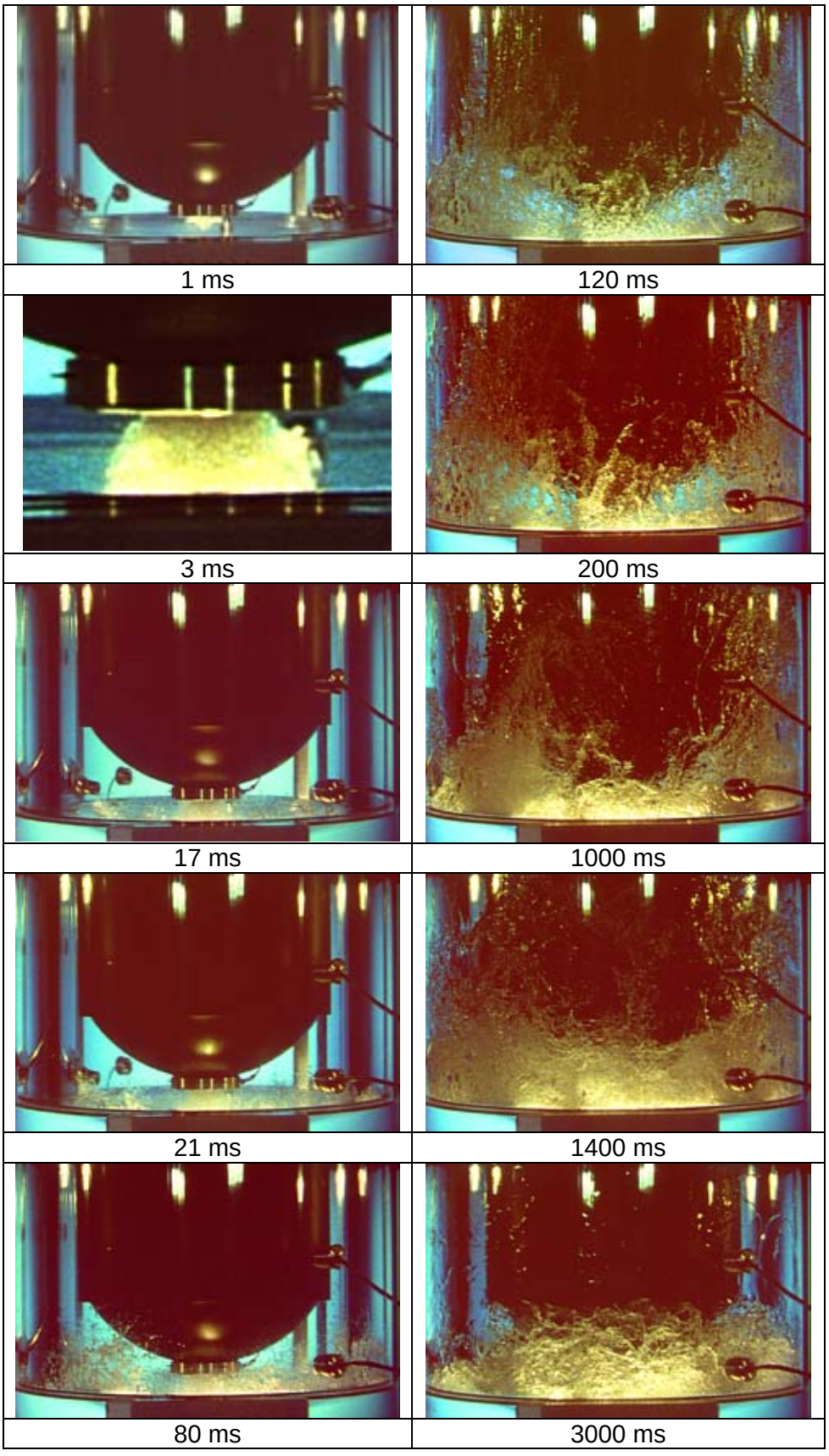

Fig. 5.179 D12 View of flow in cavity

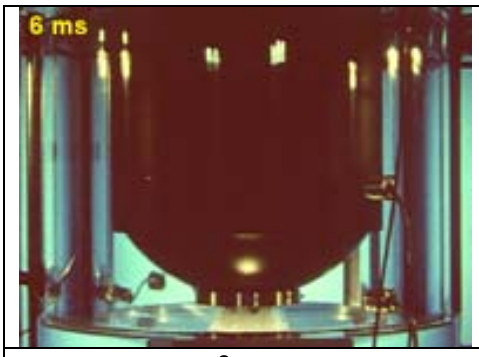

6 ms

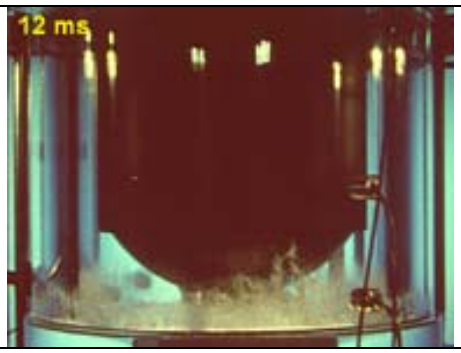

12 ms

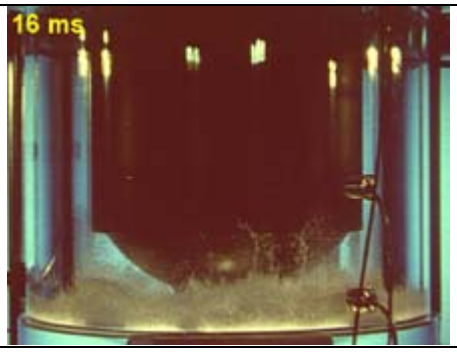

16 ms

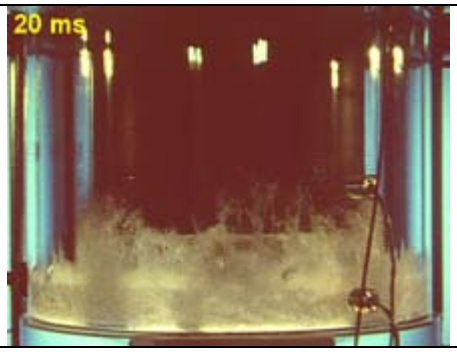

20 ms

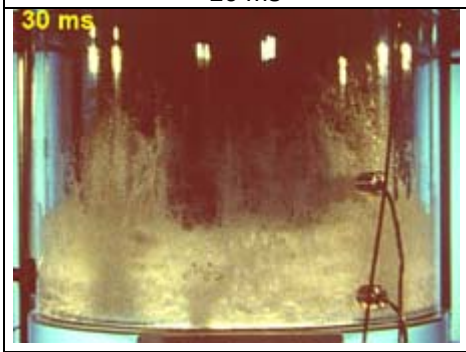

30 ms

40 ms

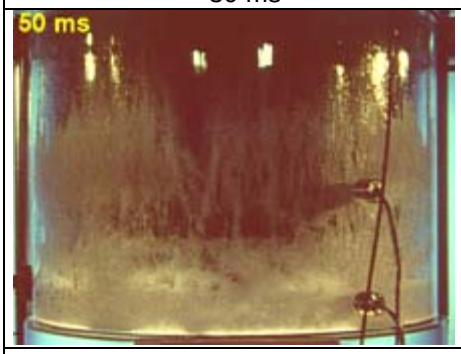

50 ms

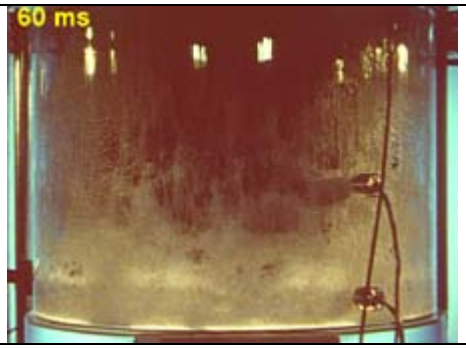

60 ms

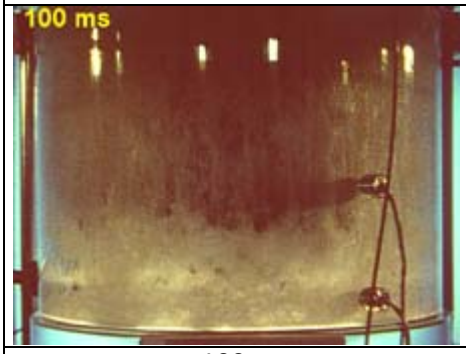

100 ms

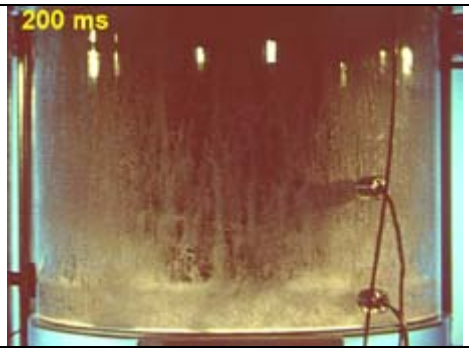

200 ms

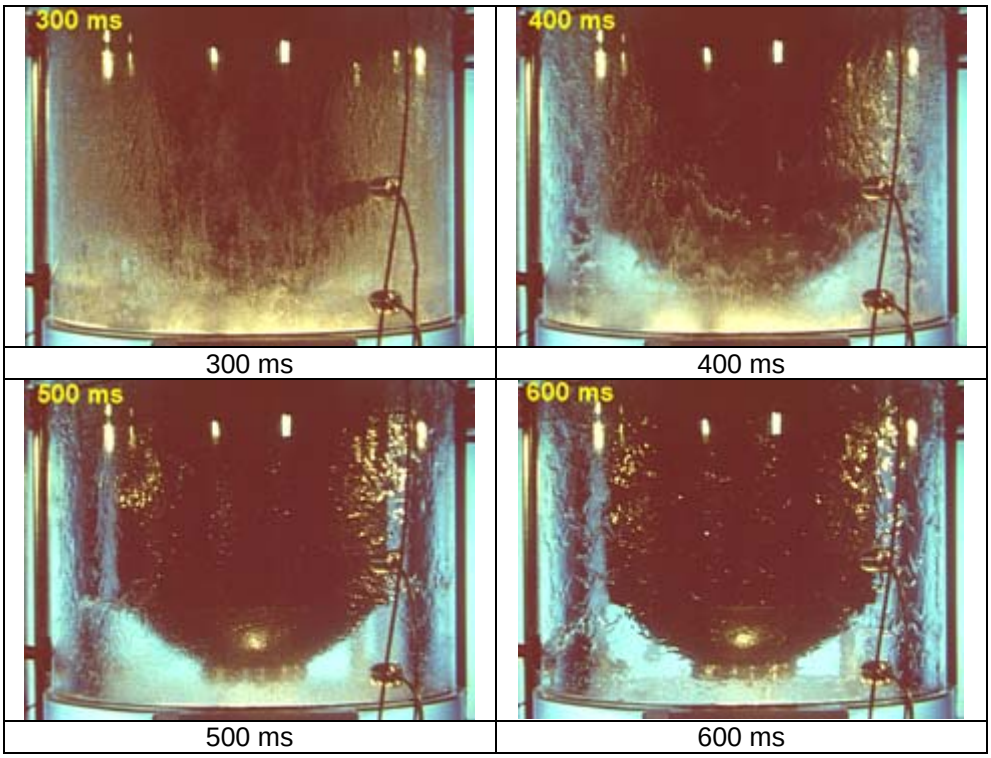

Fig. 5.180 D13 View of flow in the cavity

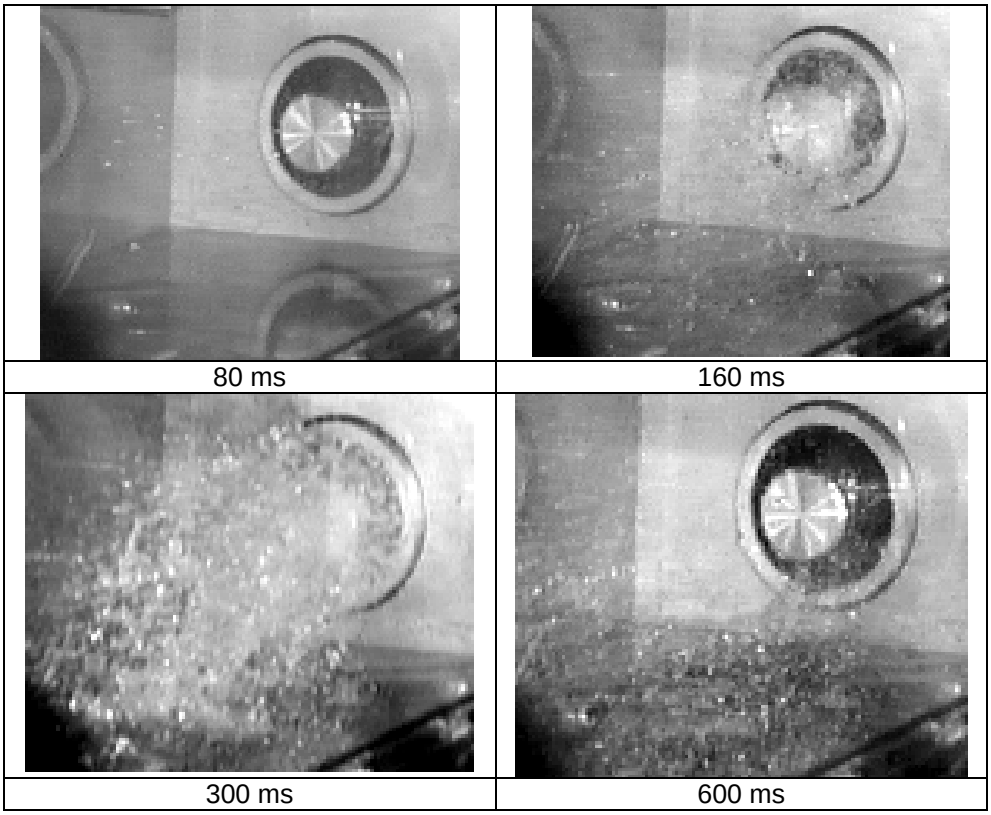

Fig. 5.181 D13 View of flow into subcompartment

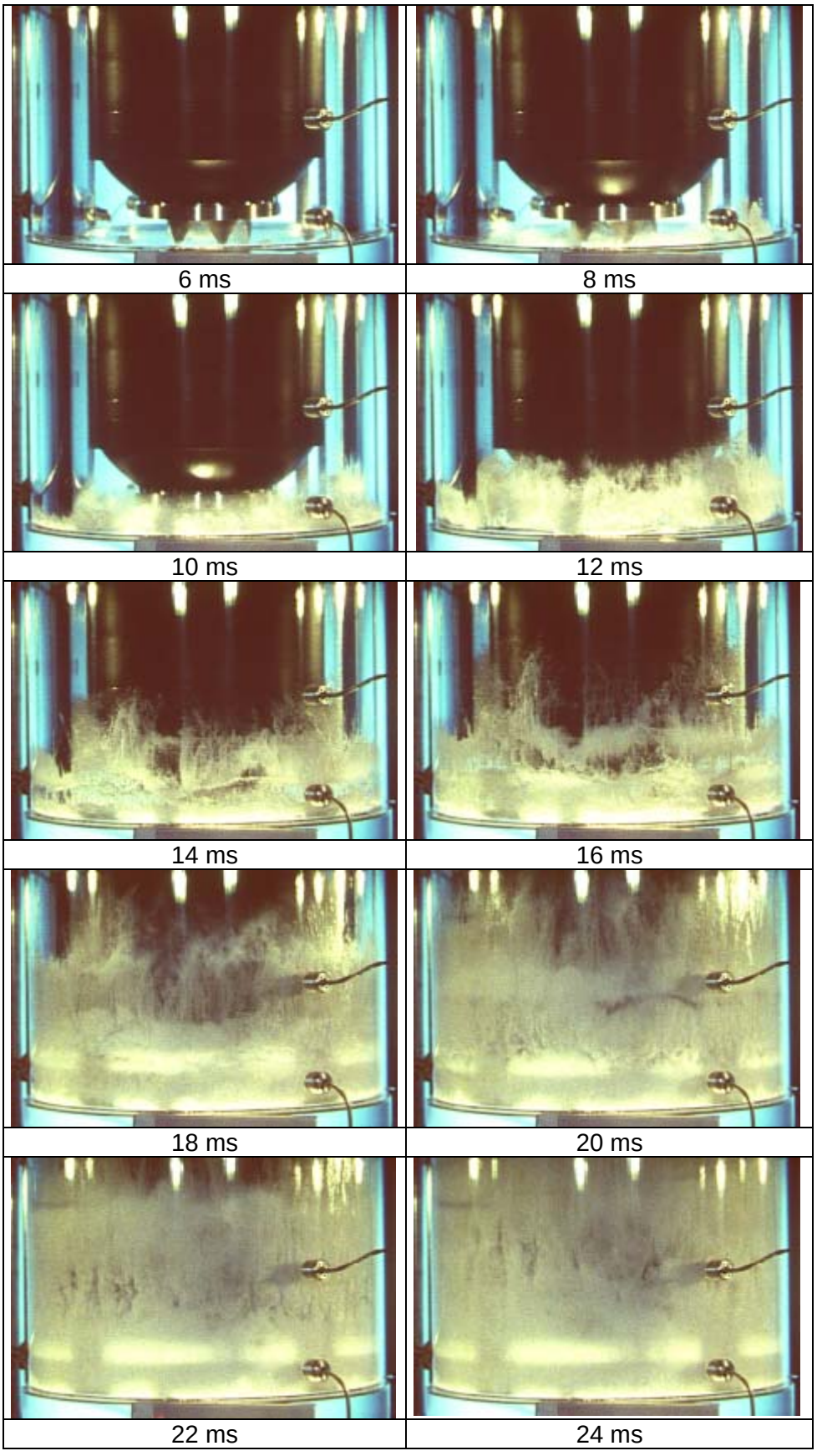

Fig. 5.182 D14 View of flow in the cavity

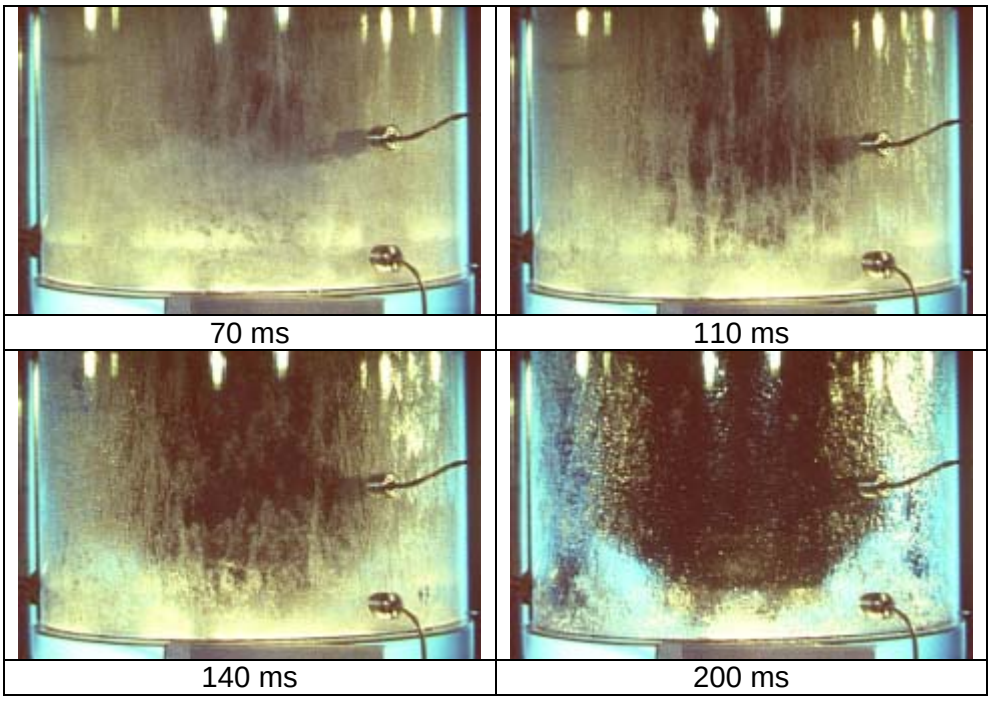

Fig. 5.183 D14 View of flow in the cavity

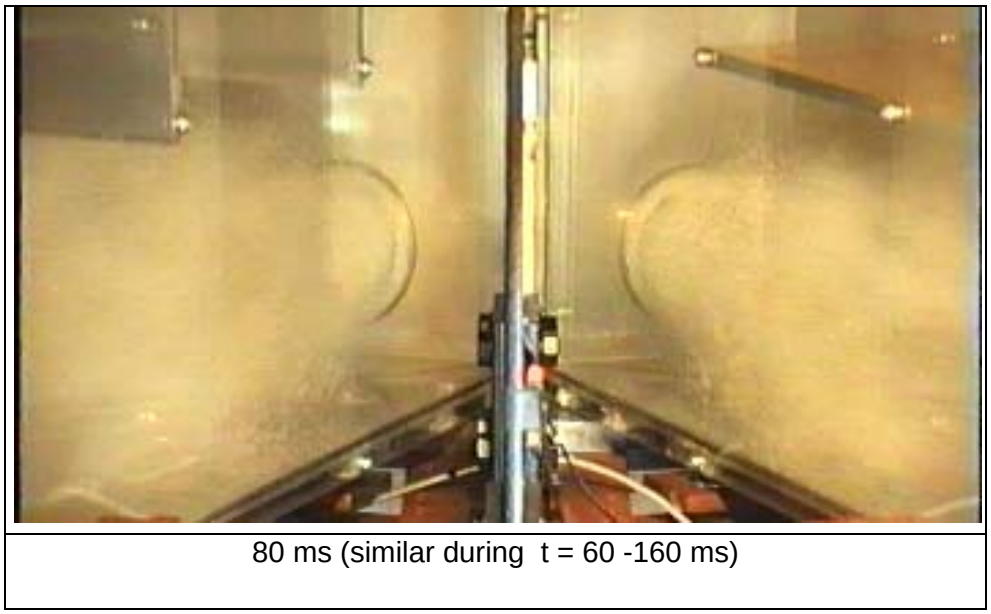

Fig. 5.184 D14 View of flow into subcompartments

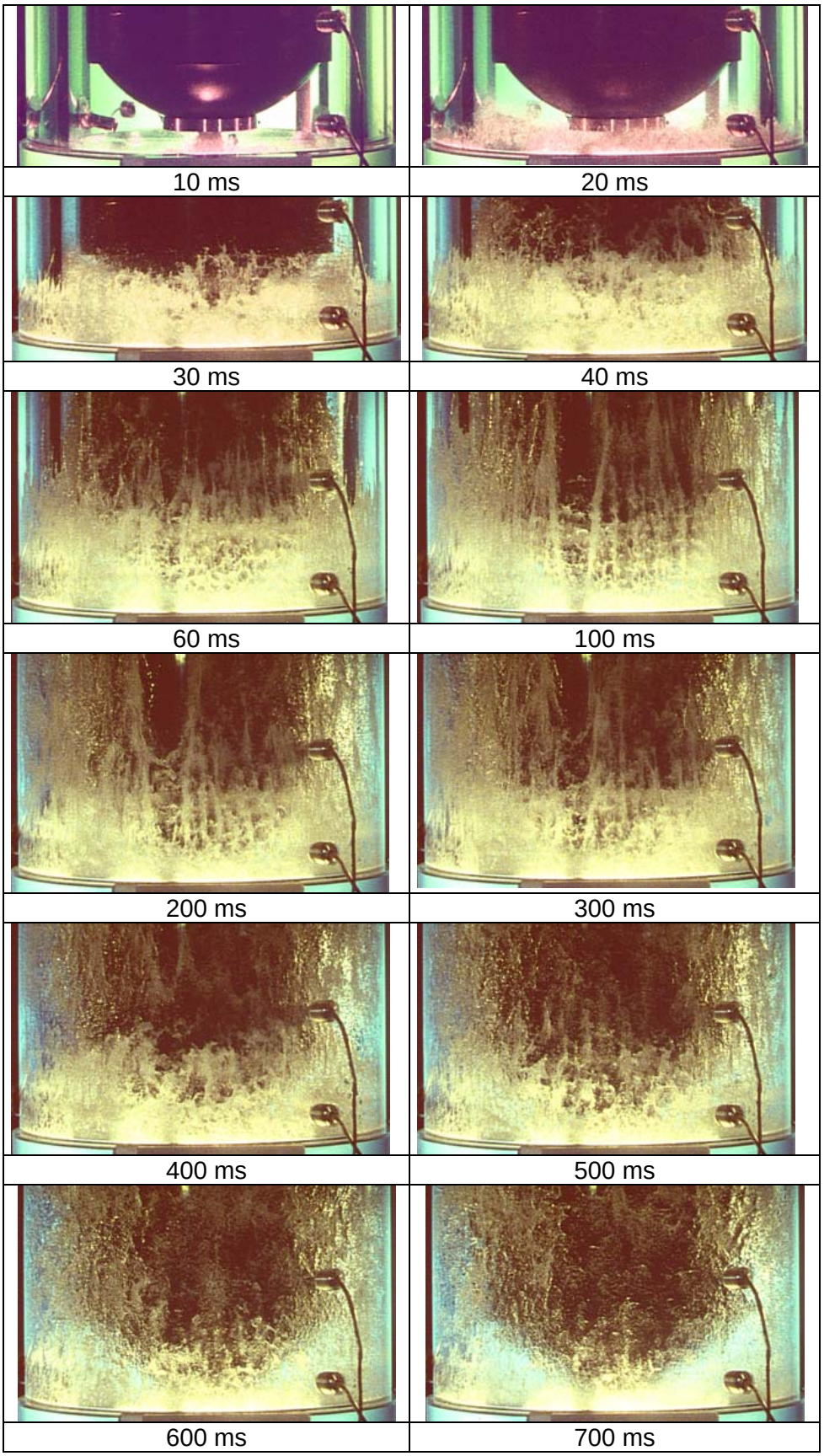

Fig. 5.185 D15 View of flow in the cavity

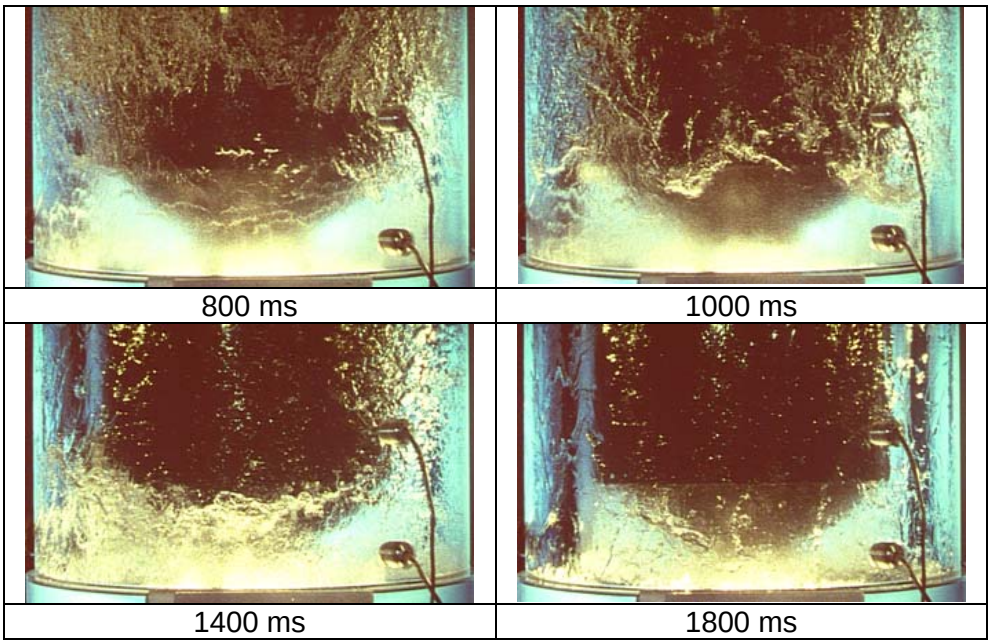

Fig. 5.186 D15 View of flow in the cavity

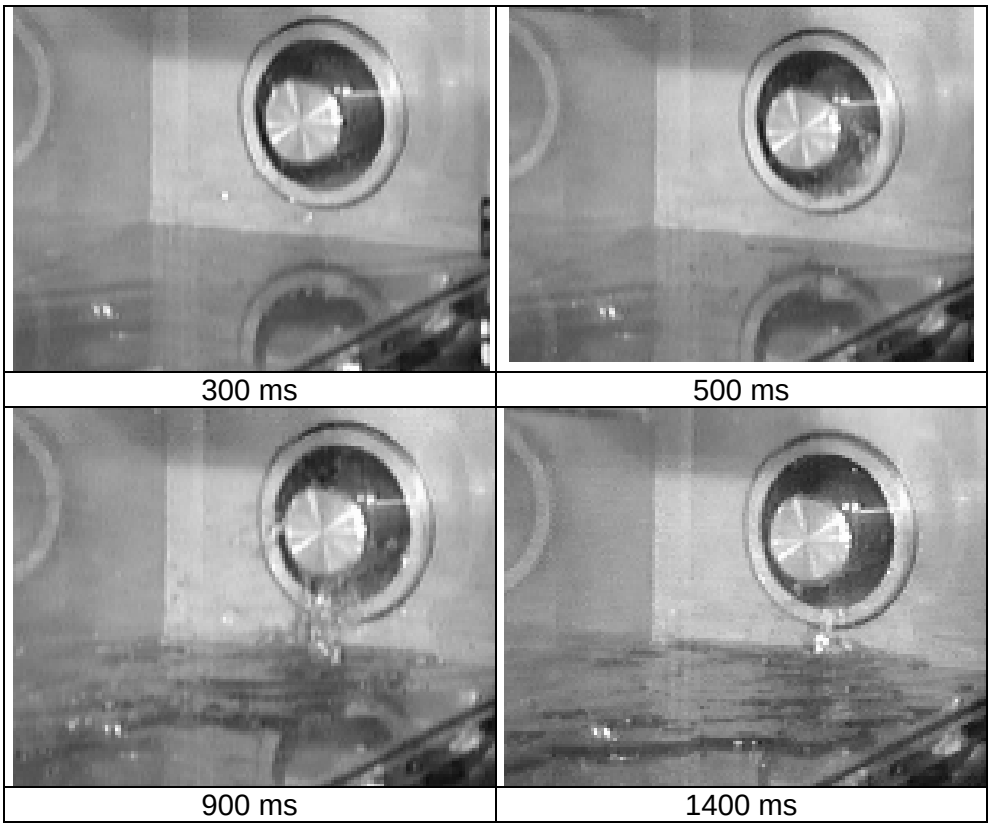

Fig. 5.187 D15 View of flow into subcompartment

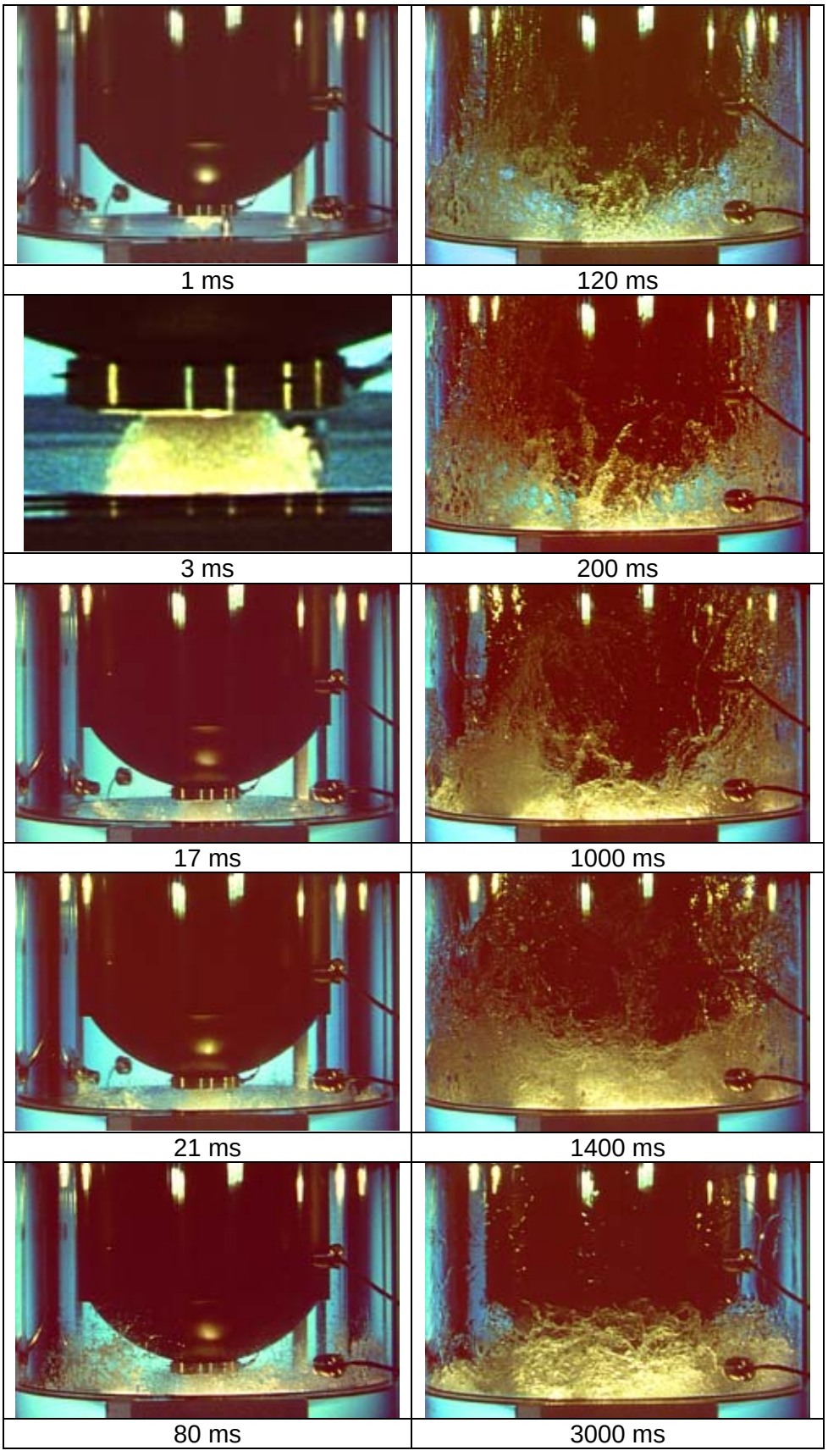

Fig. 5.188 D12 View of flow in cavity

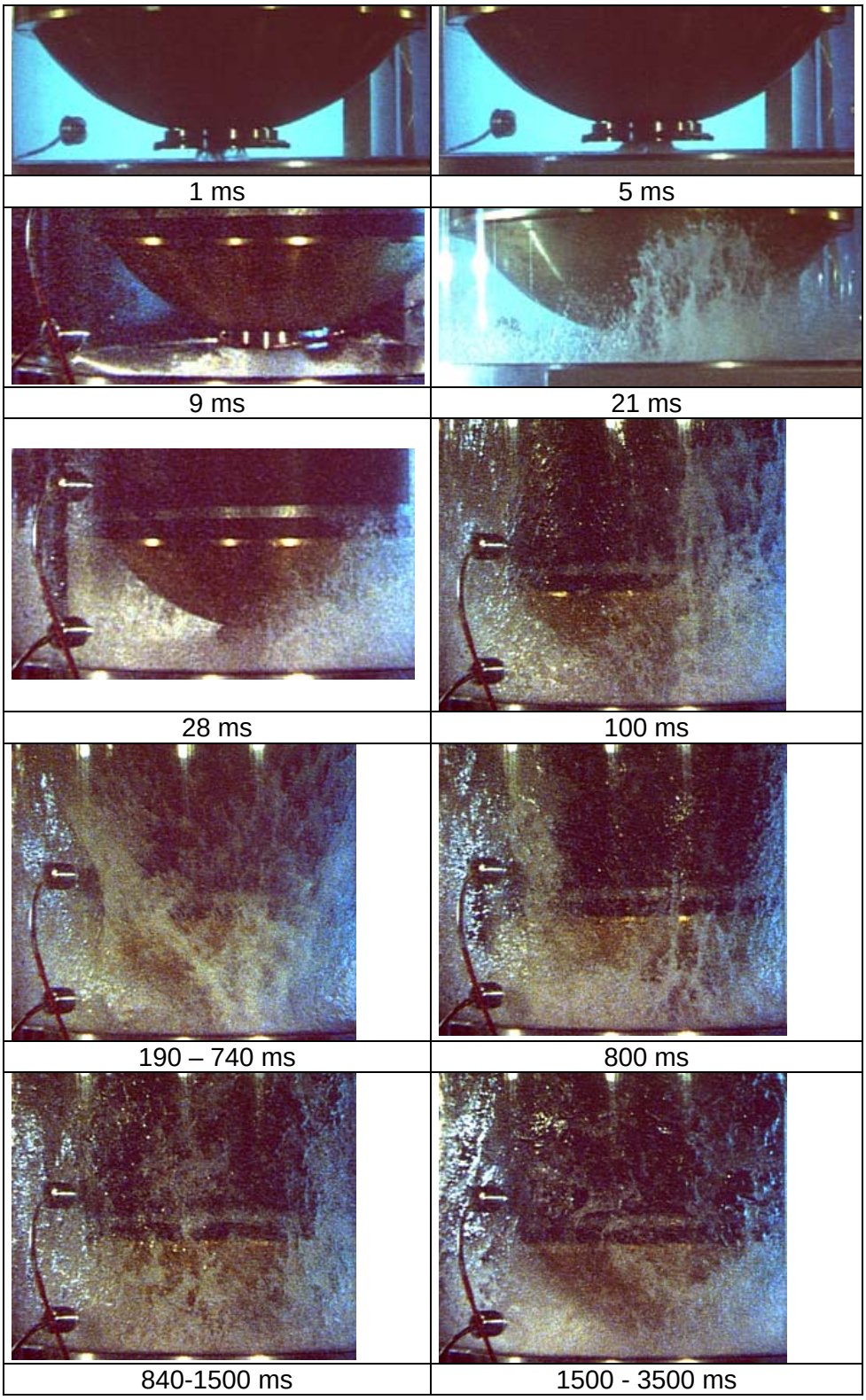

Fig. 5.189 D11 View of flow in cavity
(part of the left side of the picture is cut off for t ≥ 100 ms)

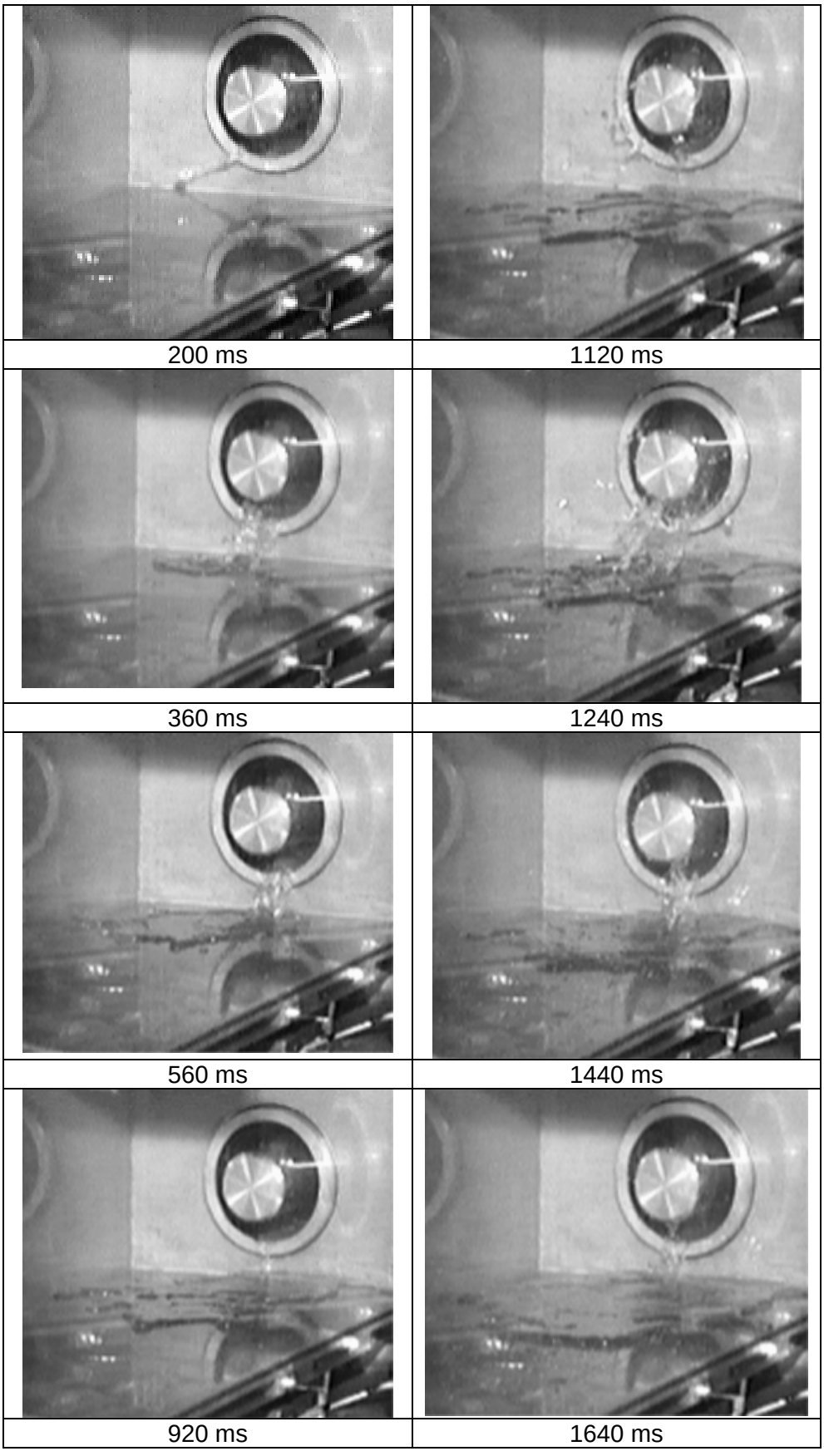

Fig. 5.190 D11 View of flow into subcompartment

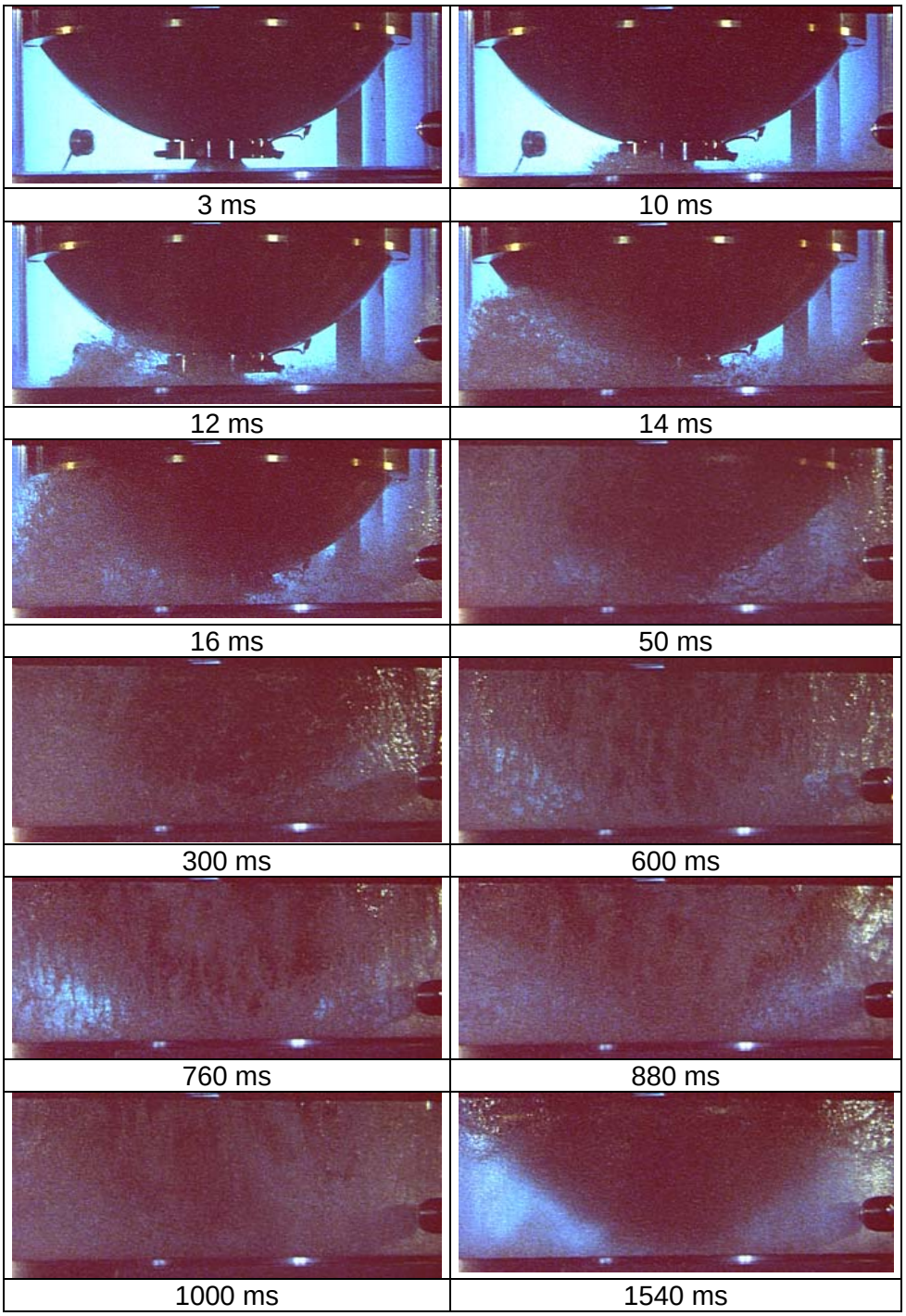

Fig. 5.191 D10 View of flow in the cavity

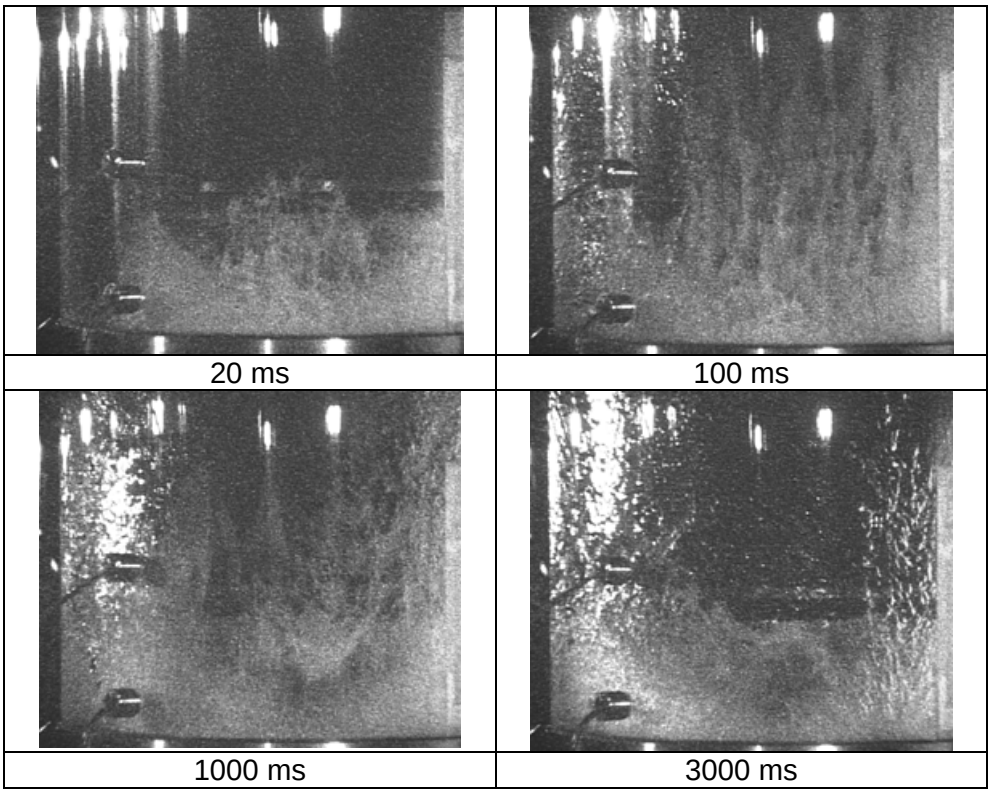

Fig. 5.192 D10 View of flow in the cavity

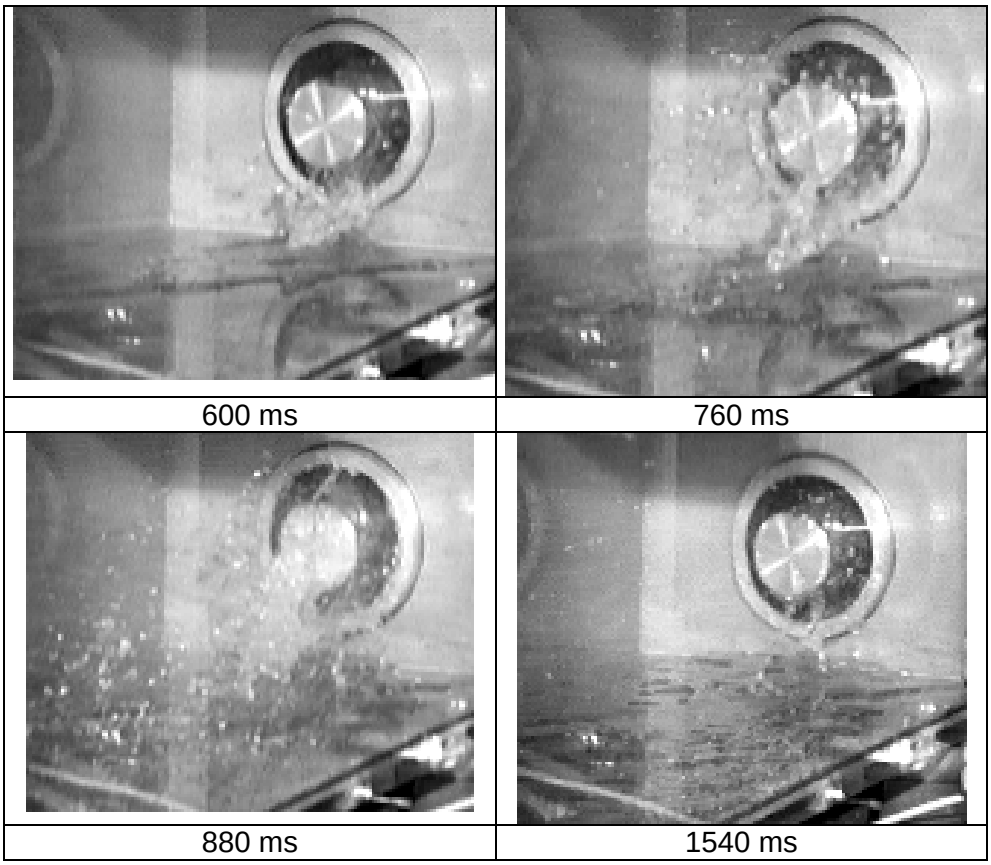

Fig. 5.193 D10 View of flow into subcompartment

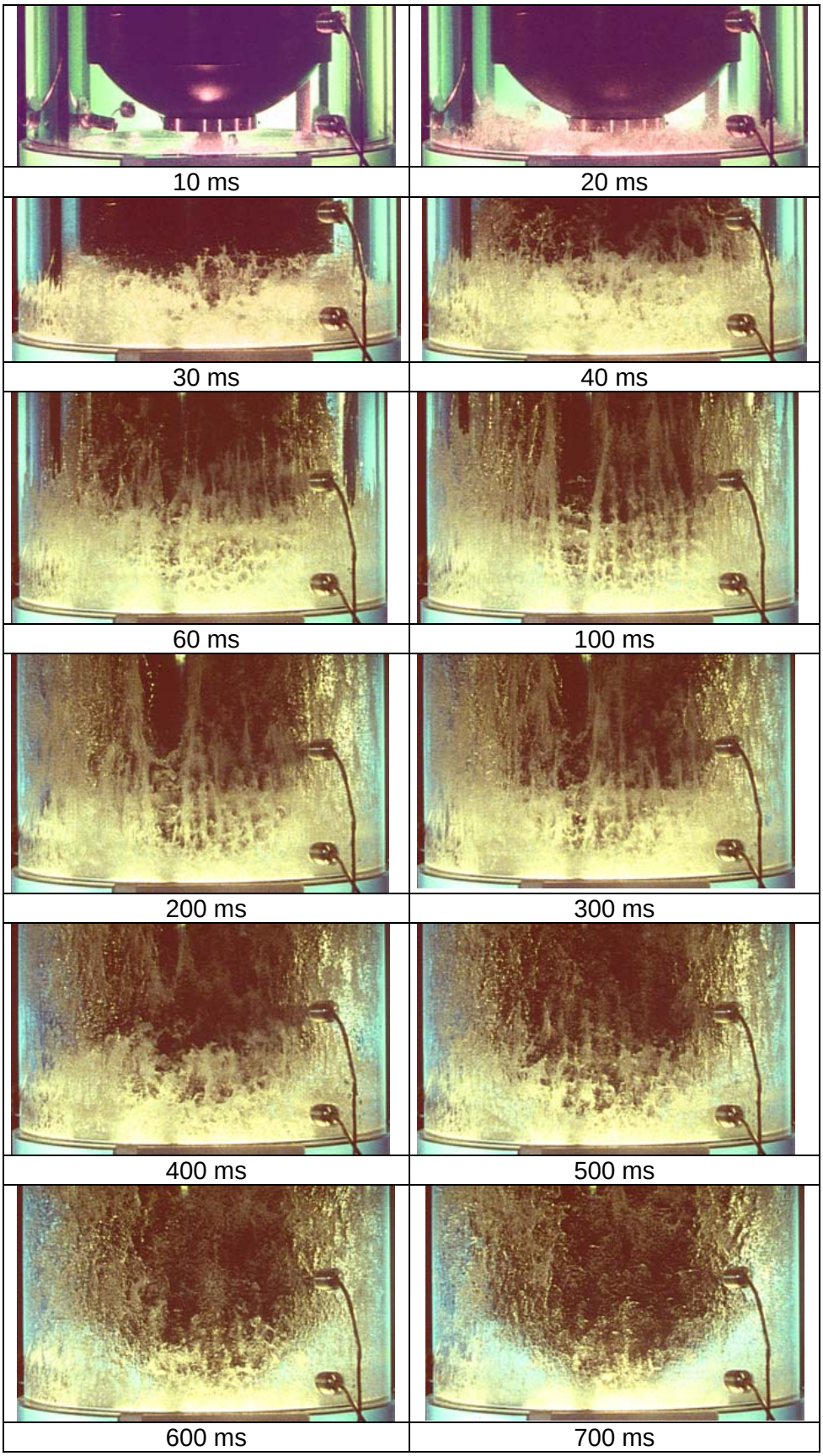

Fig. 5.194 D15 View of flow in the cavity

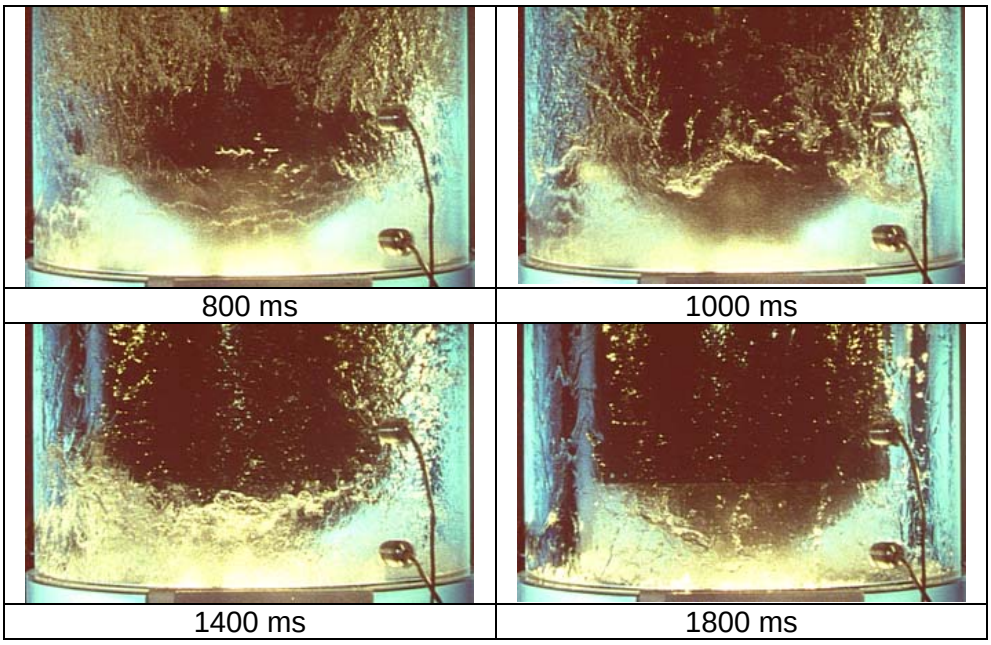

Fig. 5.195 D15 View of flow in the cavity

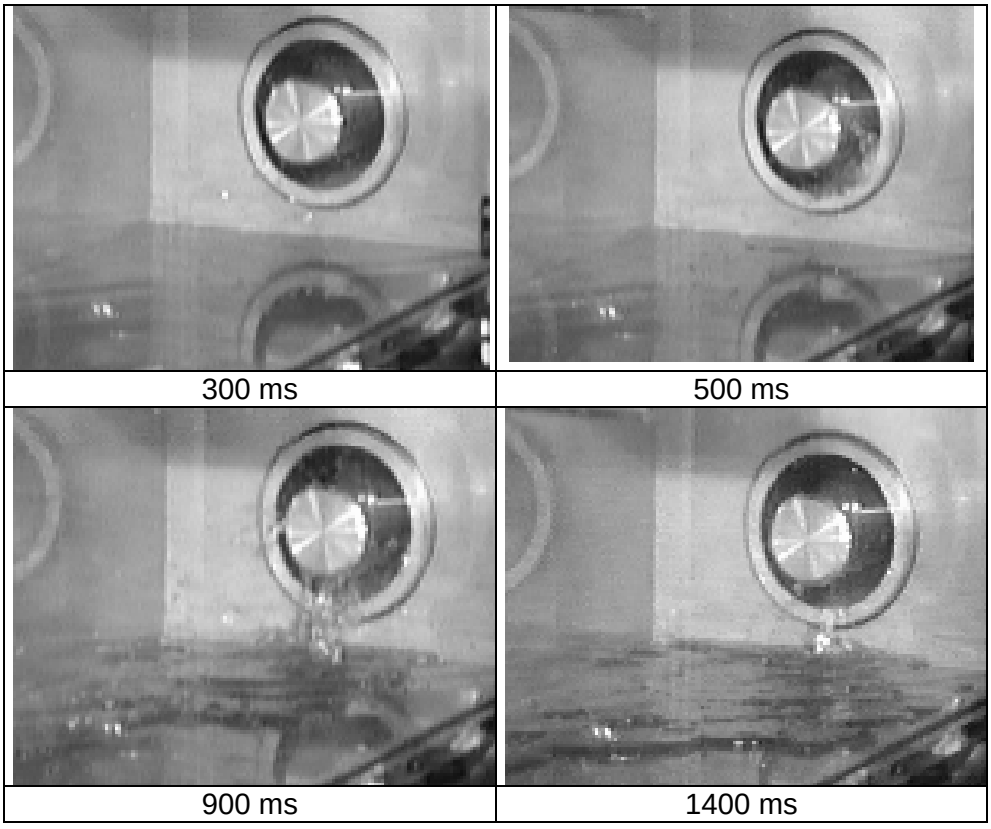

Fig. 5.196 D15 View of flow into subcompartment

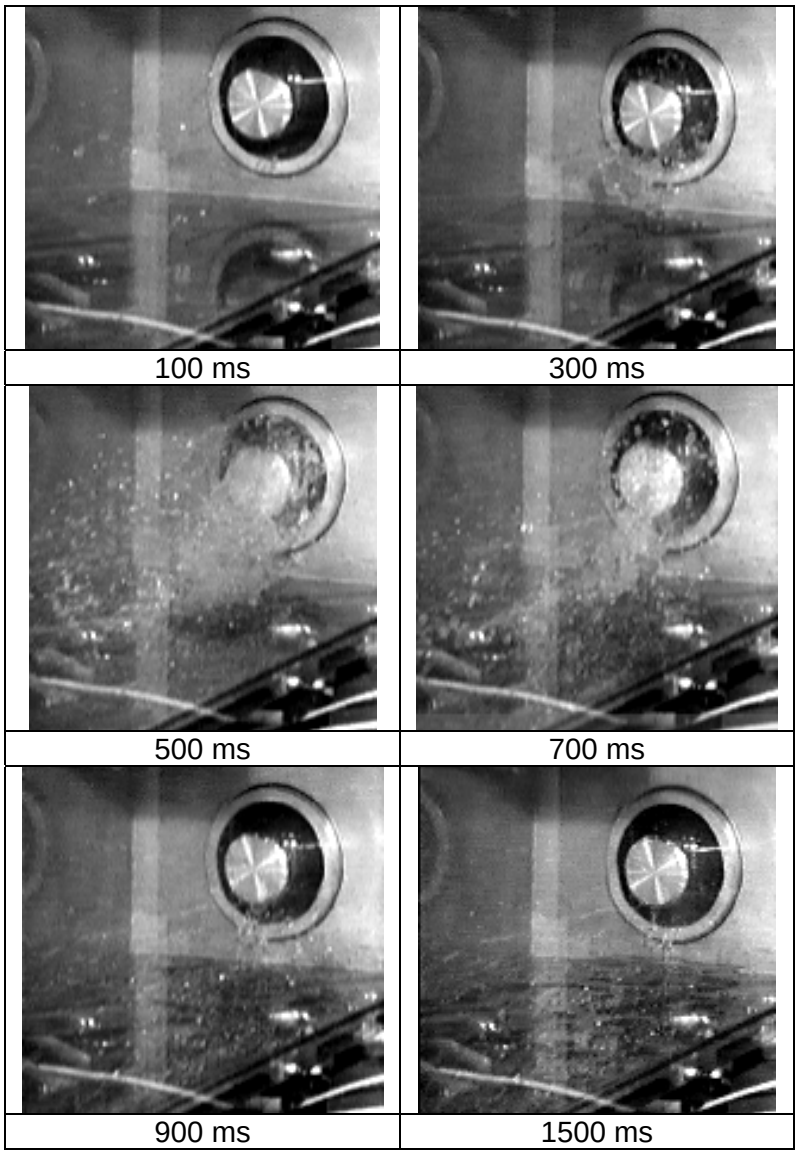

Fig. 5.197 D07 View of flow into subcompartment

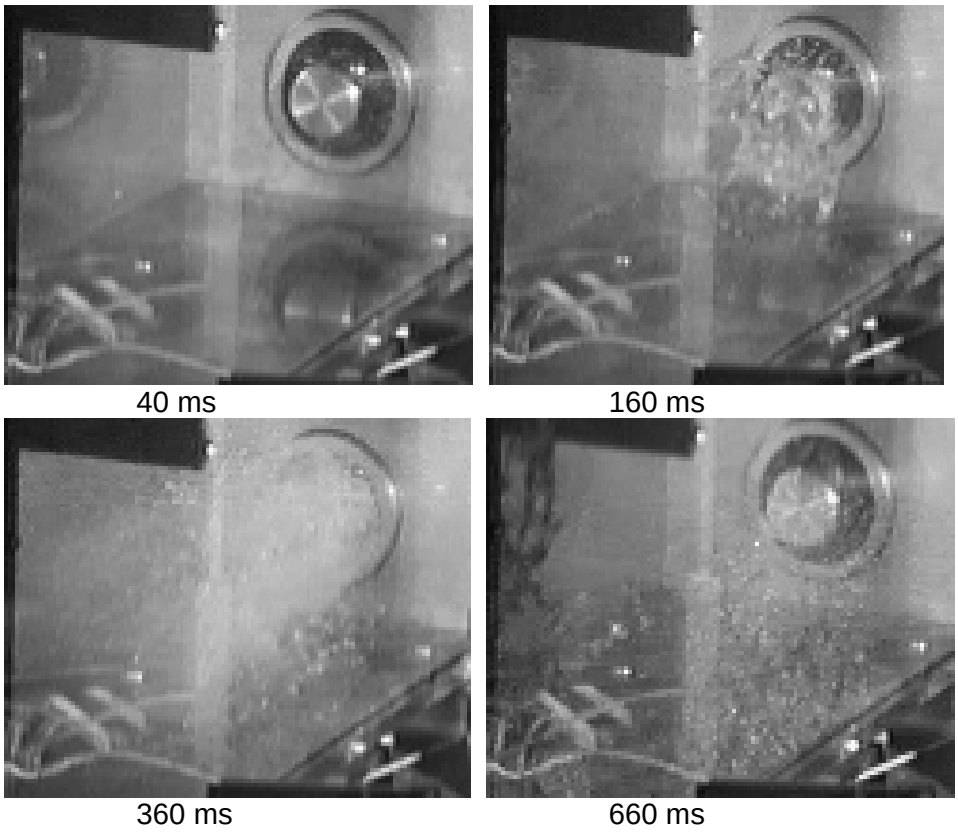

Fig. 5.198 D04 View of flow into subcompartments

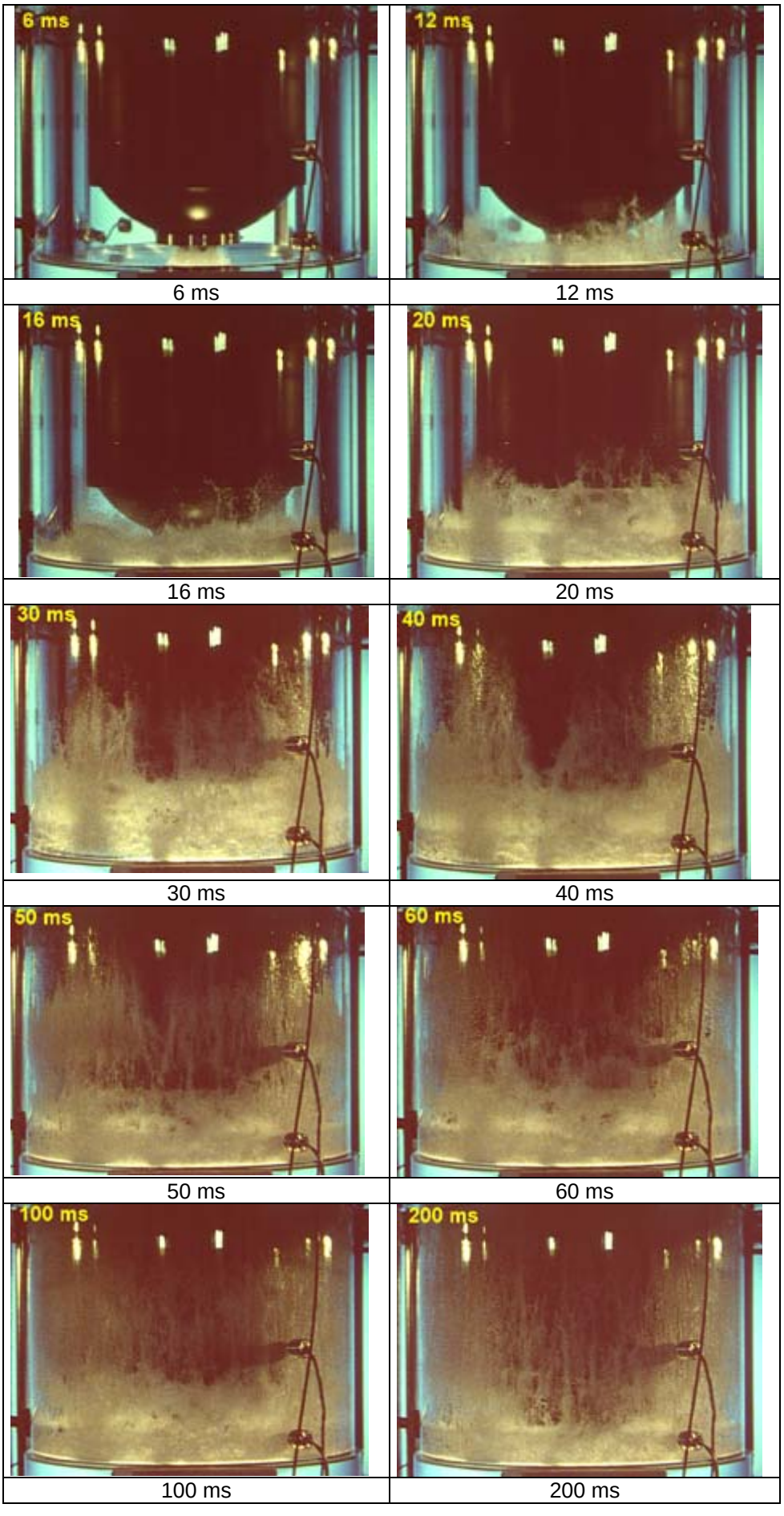
6 ms
12 ms
16 ms
20 ms
30 ms
40 ms
50 ms
60 ms
100 ms
200 ms

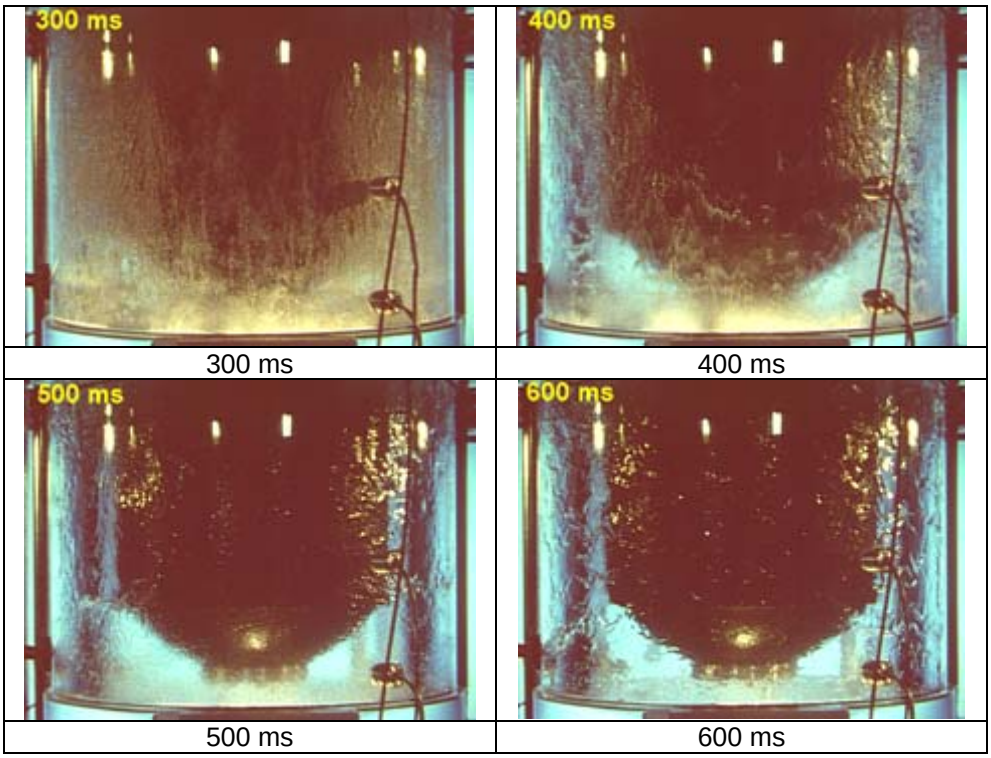

Fig. 5.199 D13 View of flow in the cavity

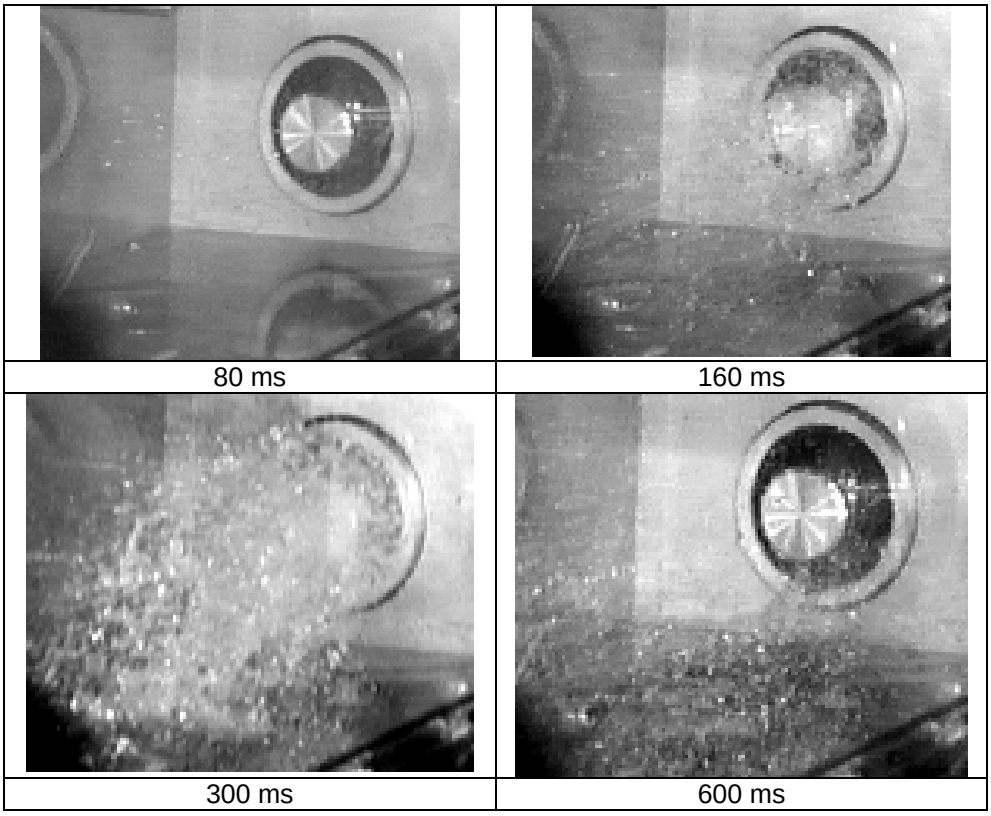

Fig. 5.200 D13 View of flow into subcompartment

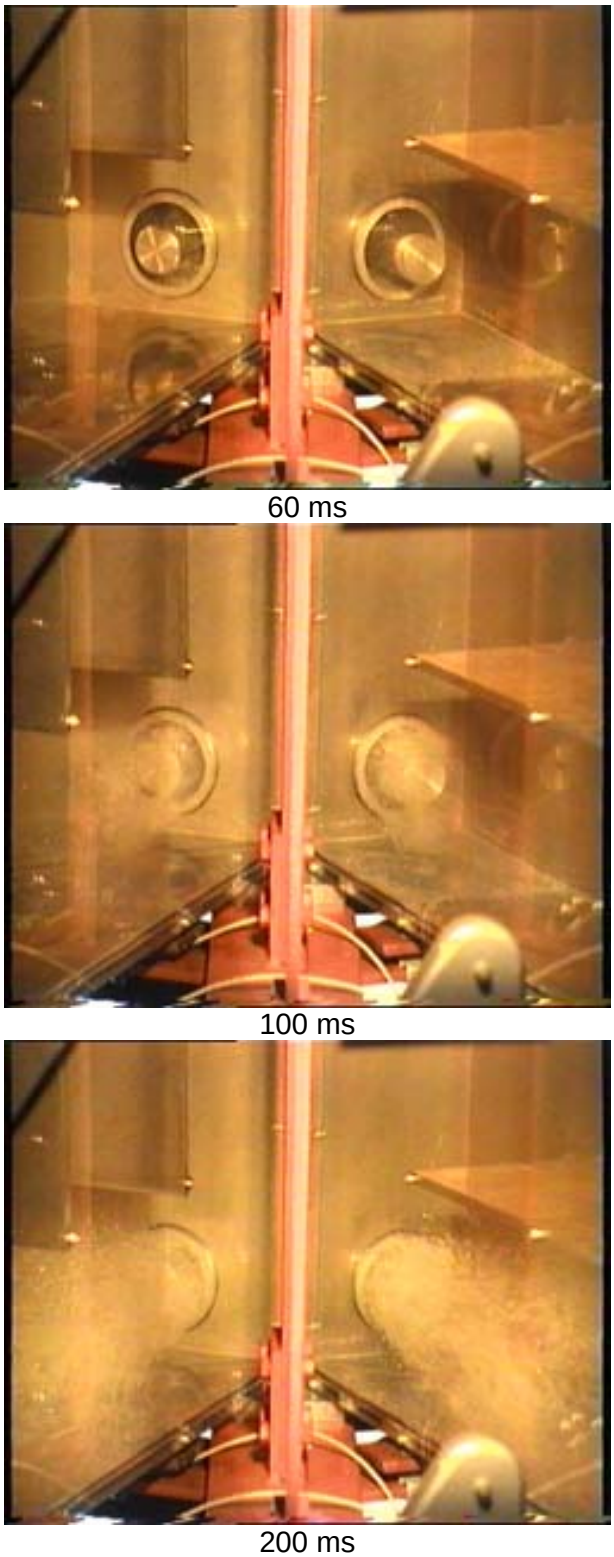

Fig. 5.201 D06 View of flow into subcompartments

0 ms

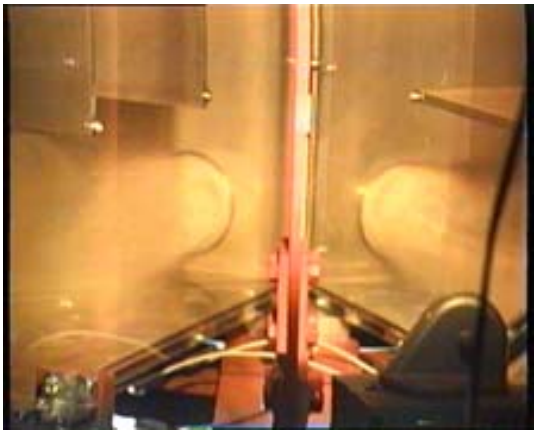

60 ms

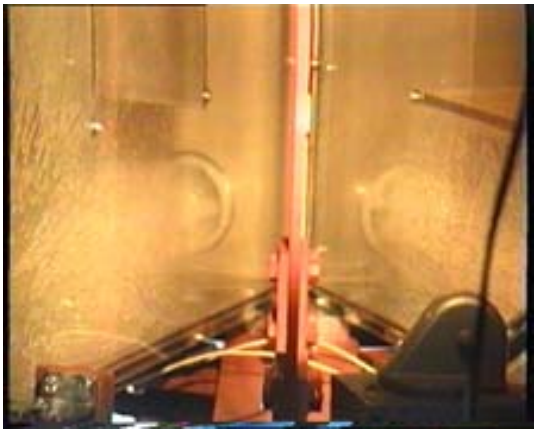

200 ms

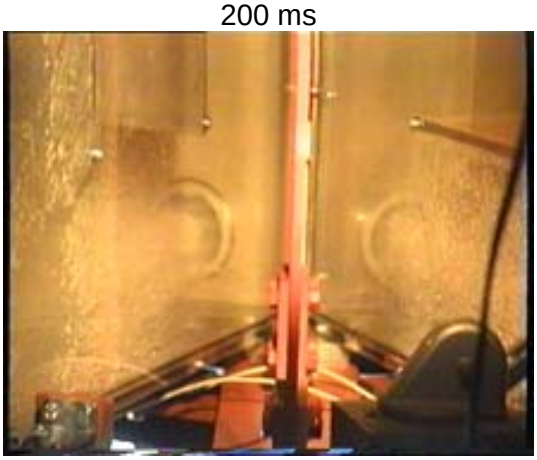

280 ms

Fig. 5.202 D05 View of flow into subcompartments

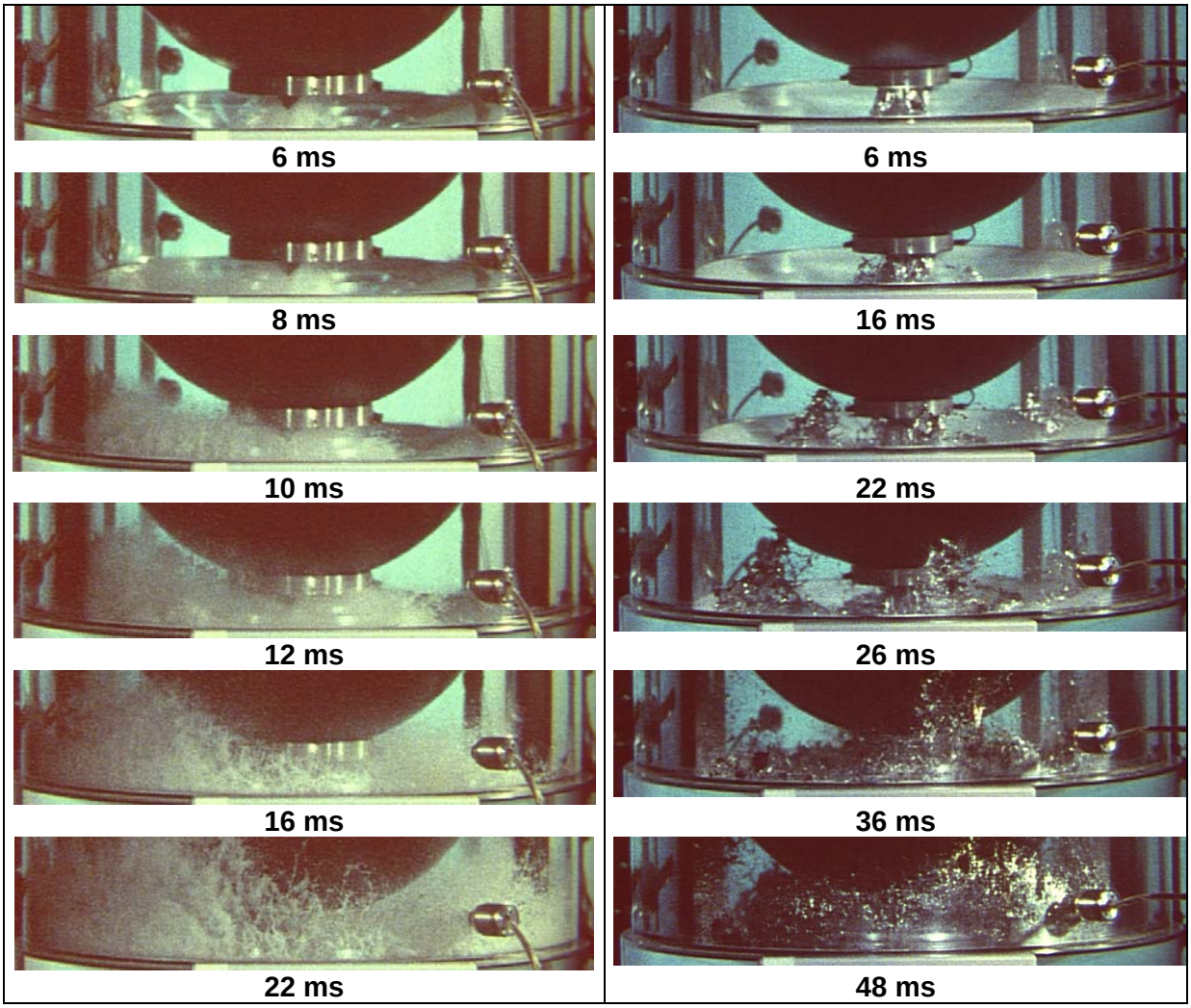

Fig. 5.203 M01: Discharge of jet (p = 0.6 MPa, hole diameter 25 mm, water: D07, metal M01)

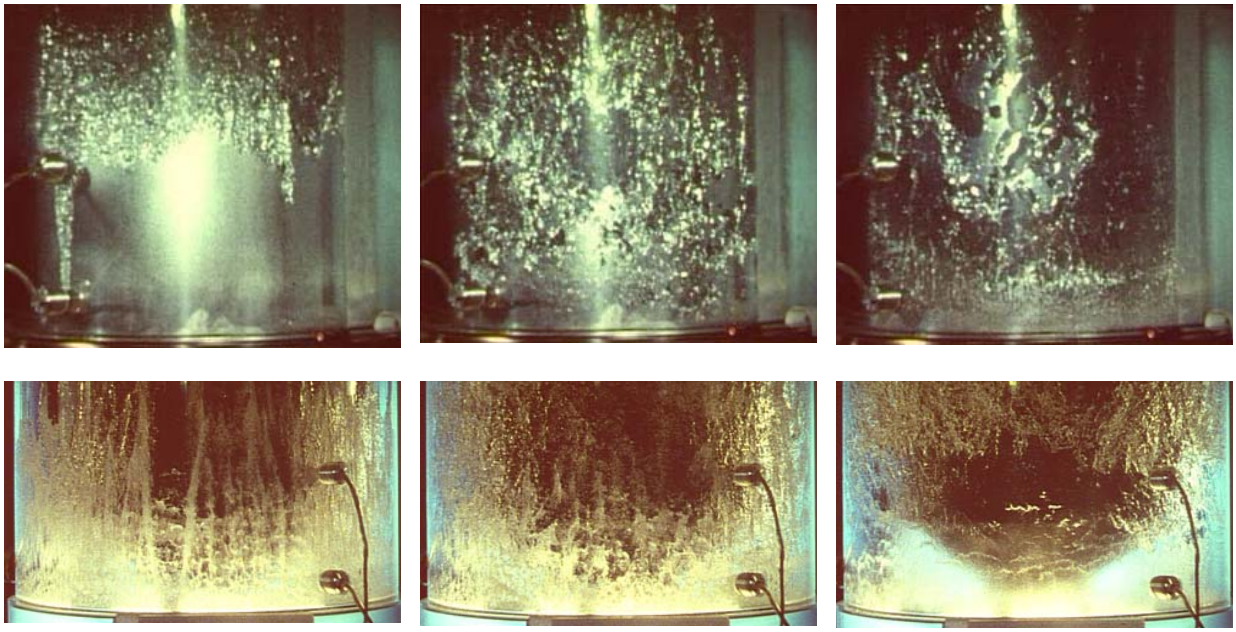

JET: Single-phase liquid flow | Two-phase flow | Single-phase gas flow

Fig. 5.204 Flow patterns in the cavity with metal (top row, M03) and water (bottom row) during different stages of the jet flow out of the RPV

metal
Liquid stream

metal
Large droplet flow

water
Small droplet flow

Fig. 5.205 Flow into subcompartment

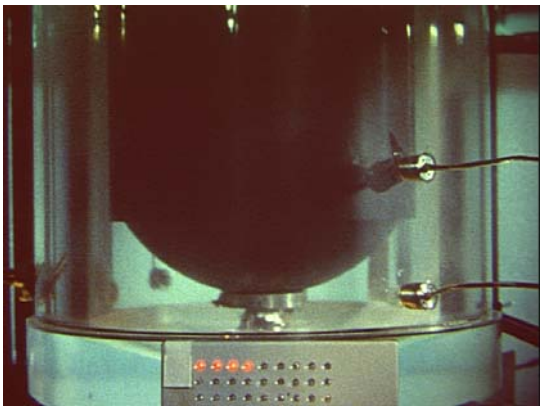

t = 4 ms: Exit of jet, single phase liquid flow

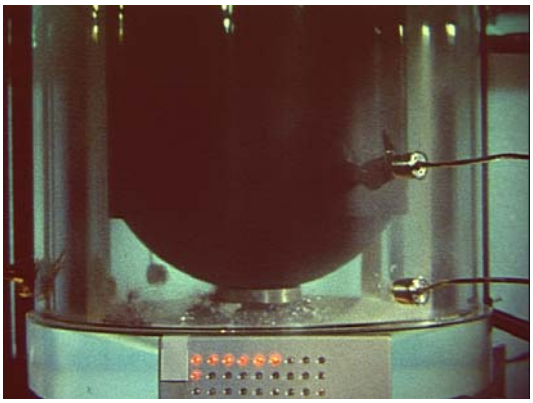

t = 16 ms: Splashing of the liquid front, droplets are generated.

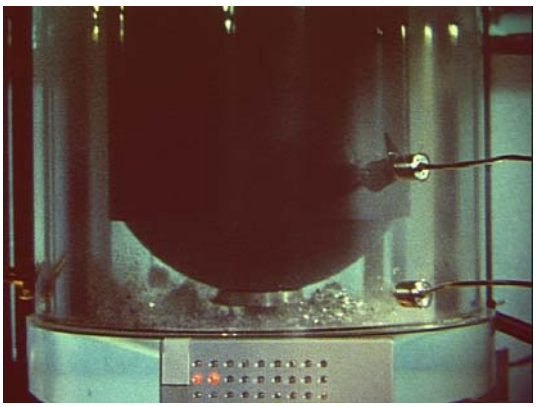

t =20 ms: Splashing on the cavity wall

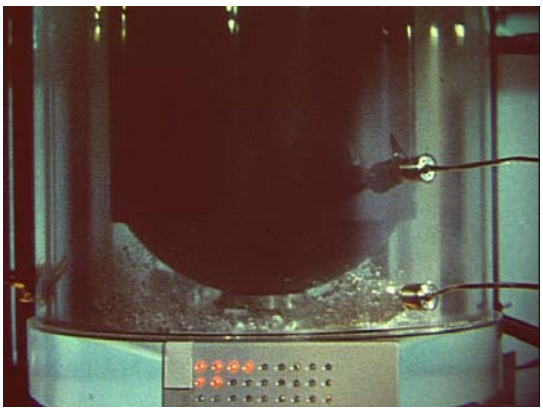

t =24 ms: Liquid moves up the wall.

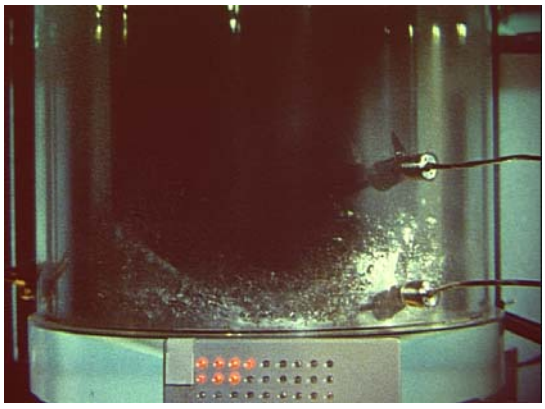

t =34 ms: A liquid film is formed at the cavity wall

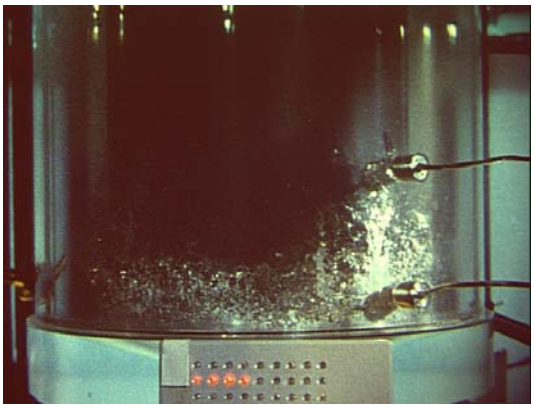

t =40 ms: The liquid film is fragmented at its front

Fig. 5.206 M02 Flow phenomena in the cavity in metal test (1 MPa , 25 mm hole)

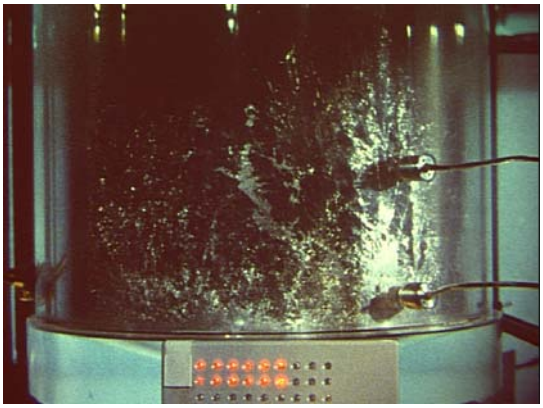

t =66 ms: Filaments and droplets are formed, still moving upwards

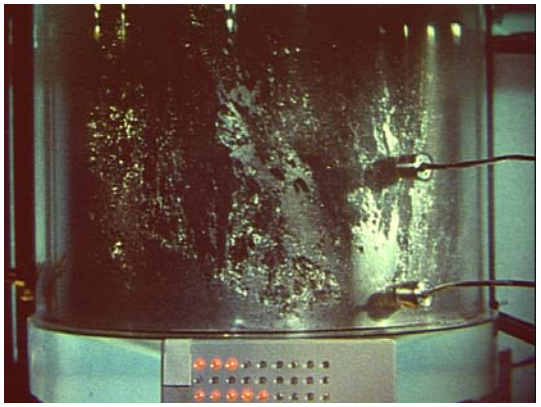

t =500 ms: Gas blow through at the RPV hole at that time

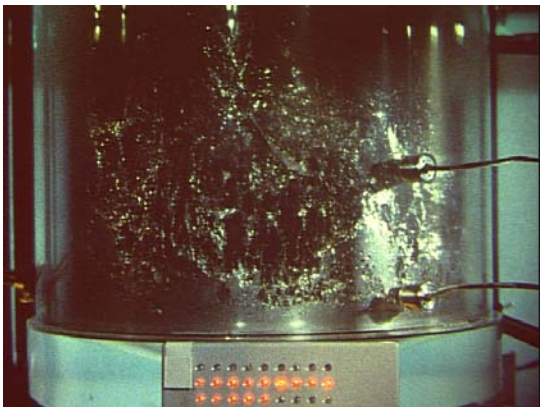

t =586 ms: More fragmentation of the liquid film due to two-phase flow at the hole

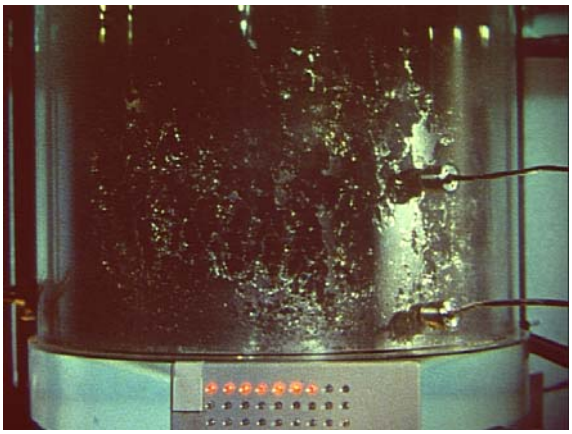

t =1000 ms: End of two-phase flow at the breach

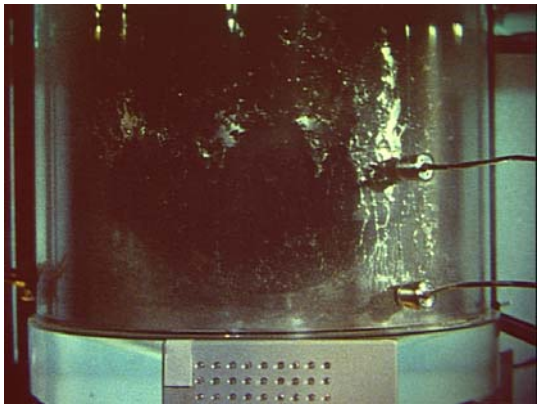

t =1110 ms: the liquid film becomes thinner and fades away

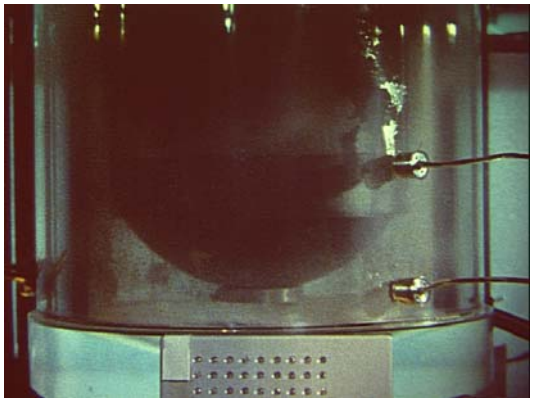

t =1200 ms: Pure gas flow in the cavity.

Fig. 5.206 continued

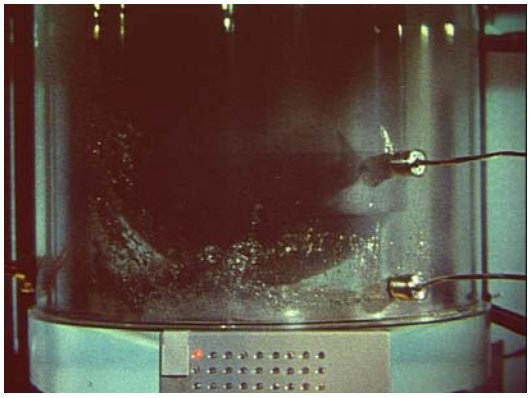

t =1500 ms: Liquid metal flowing downward in one part is driven up by the gas flow.

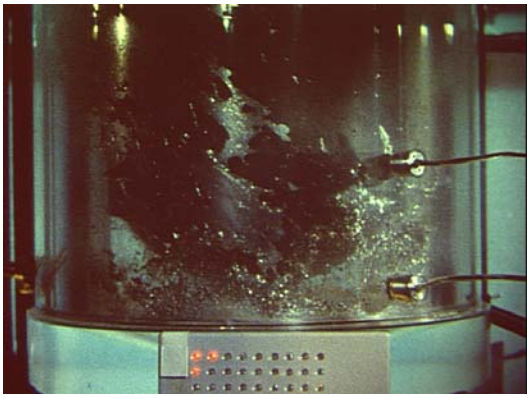

t =1670 ms: The metal flows from right to left; on the right side it falls down, on the left side it is blown upwards.

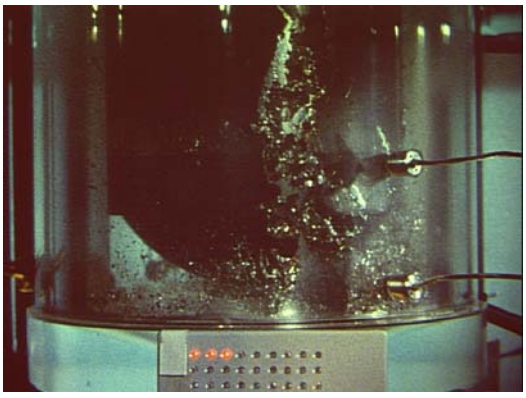

t =2000 ms: Most of the liquid moves downwards, gas entrains some droplets upwards.

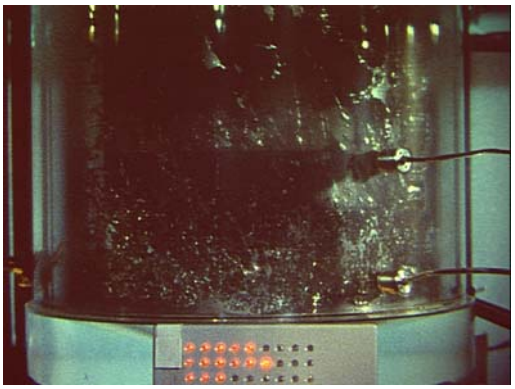

t =2420 ms: All liquid moves downwards

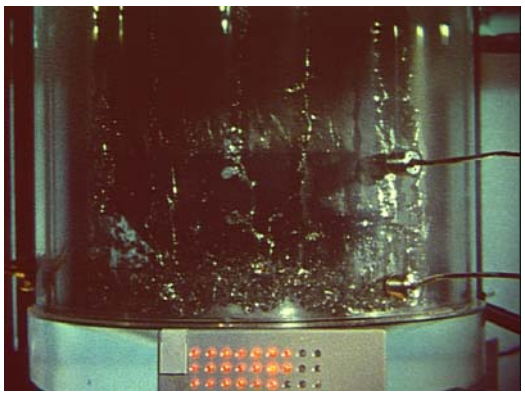

t =2730 ms: Filaments form and flow down in several rows.

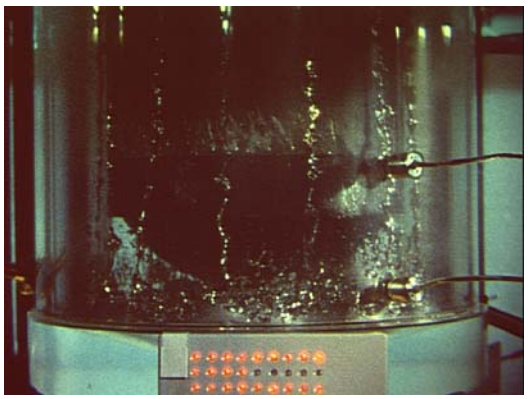

t =3000 ms: End of blow down, liquid continues to flow down in filaments.

Fig. 5.206 continued

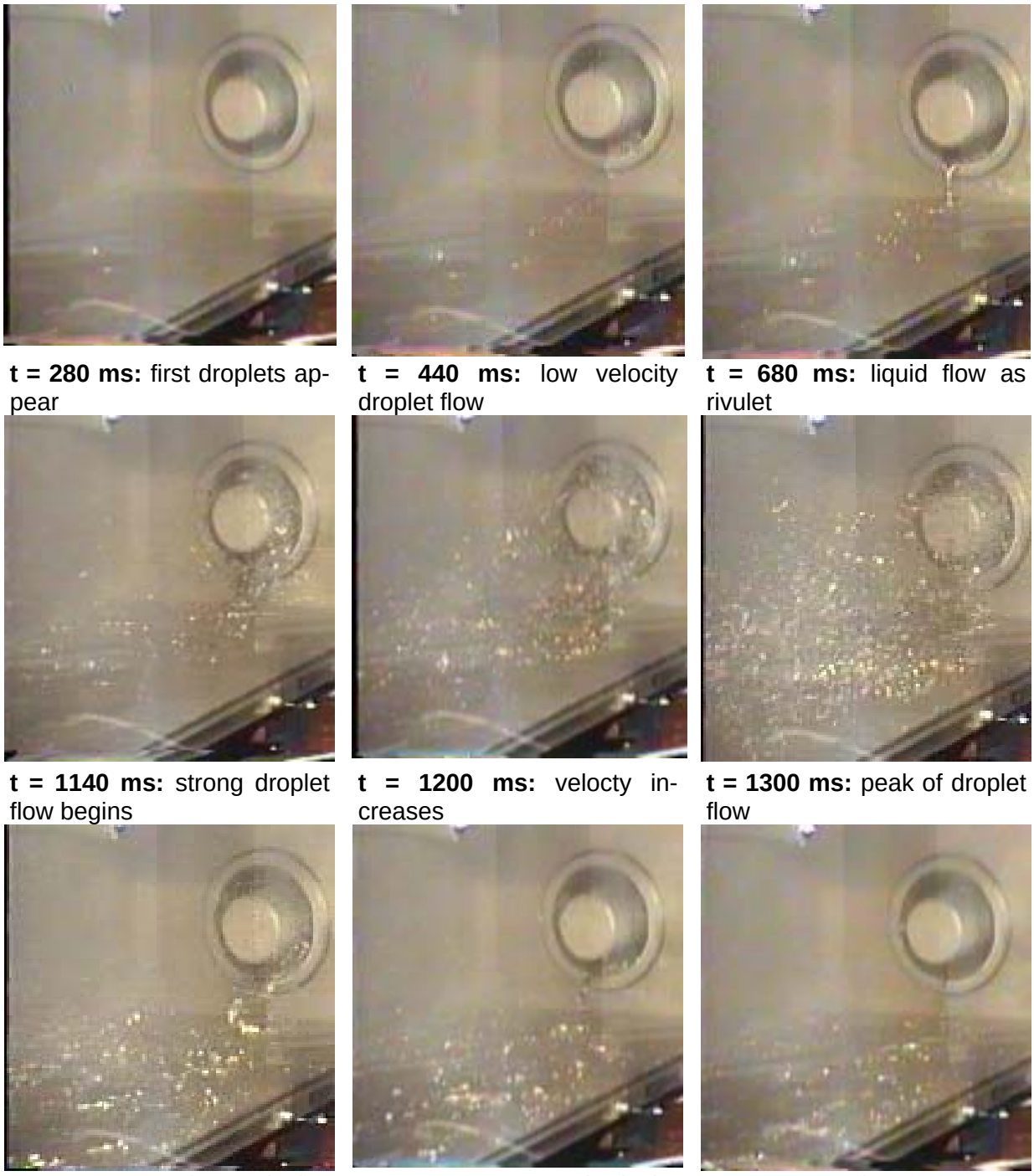

t = 280 ms: first droplets appear

t = 440 ms: low velocity droplet flow

t = 680 ms: liquid flow as rivulet

t = 1140 ms: strong droplet flow begins

t = 1200 ms: velocty increases

t = 1300 ms: peak of droplet flow

t = 1500 ms: low velocity, rivulet flow

t = 1600 ms: weak rivulet flow

t = 2200 ms: flow ceases

Fig. 5.207 M02 Flow at the nozzle, entrance into the subcompartment, in metal test (1 MPa , 25 mm hole)

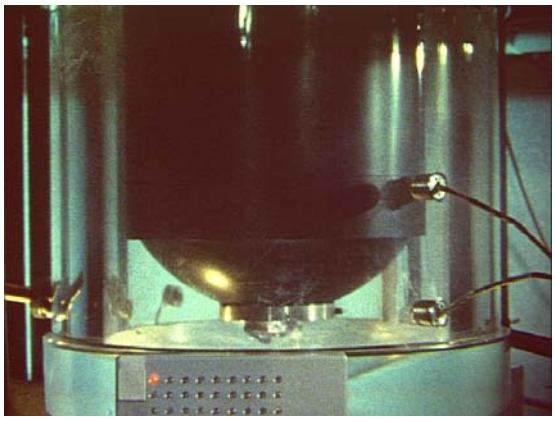

t = 2 ms: jet appears

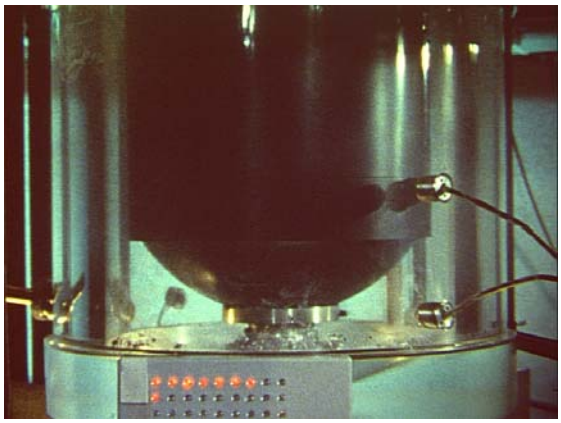

t = 18 ms: liquid spreads on cavity floor

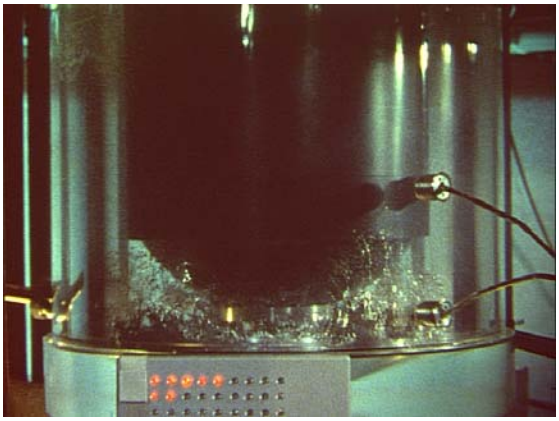

t = 26 ms: liquid front moves up the cavity wall

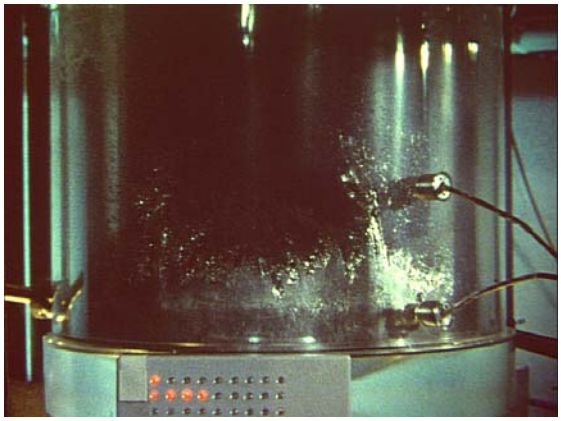

t = 42 ms: a continuous liquid film forms at the wall

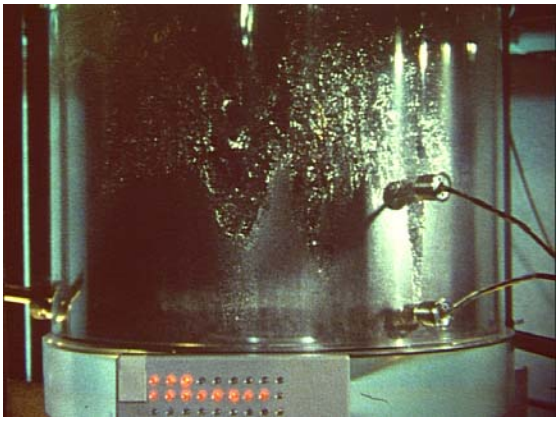

t = 84 ms: the liquid film is fragmented at its front

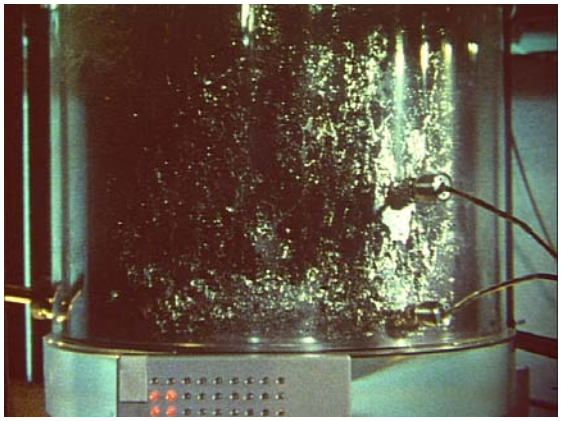

t = 220 ms: the liquid film is fragmented in whole (gas blow through at the breach started at 90 ms)

Fig. 5.208 M03 Flow phenomena in the cavity in metal test (0.58 MPa , 50 mm hole)

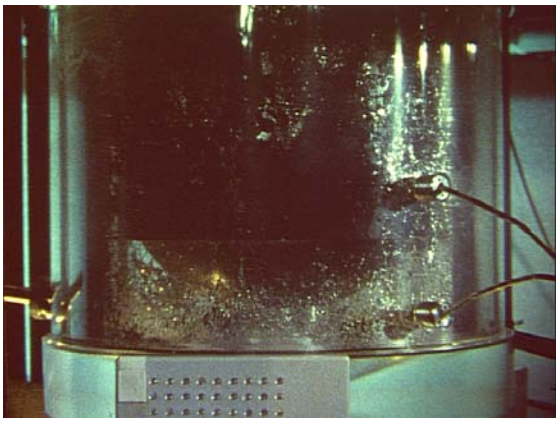

t = 670 ms: only droplets move up the cavity wall (single phase gas flow at the breach)

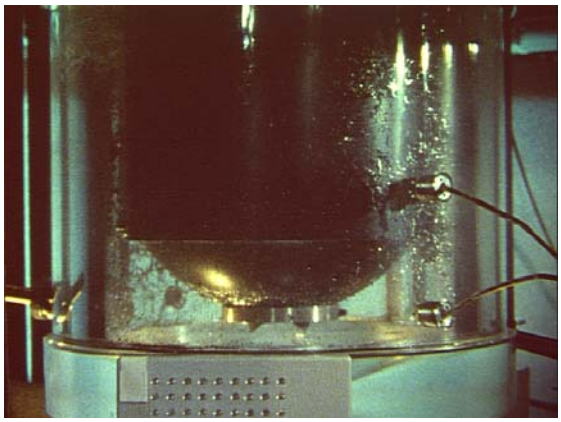

t = 800 ms: few droplets move upwards, some larger droplets start to fall down

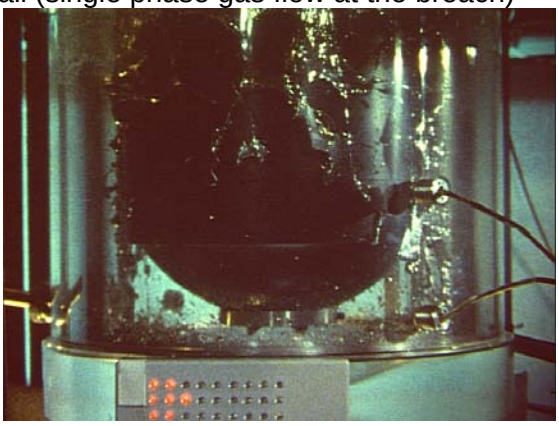

t = 1180: large liquid masses fall down

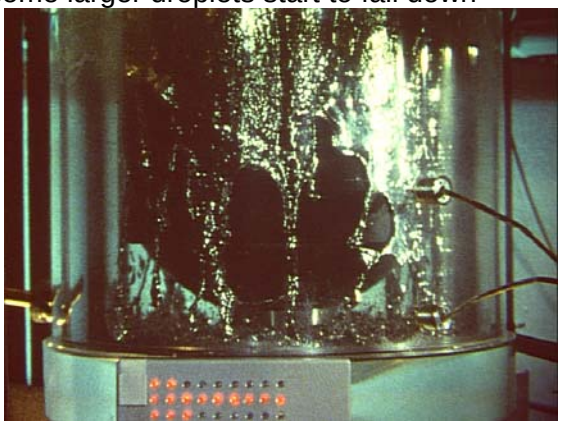

t = 1340 ms: a falling film is formed

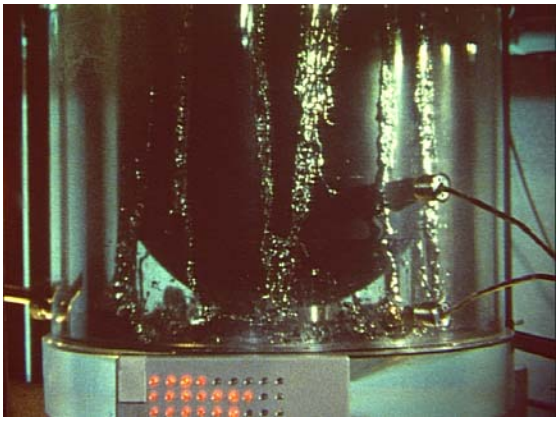

t = 1620 ms: the film is fragmented into streams

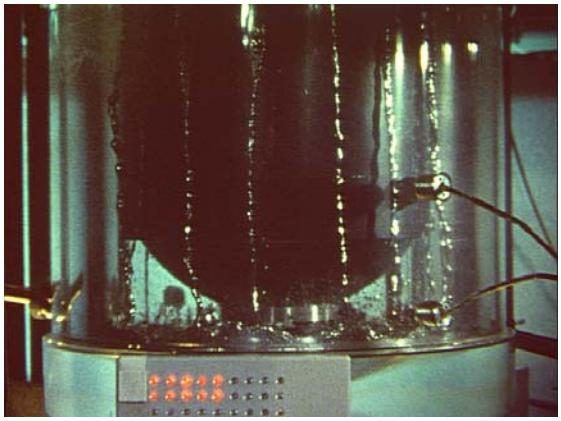

t = 2000 ms: some rivulets slowly die out.

Fig. 5.208 continued

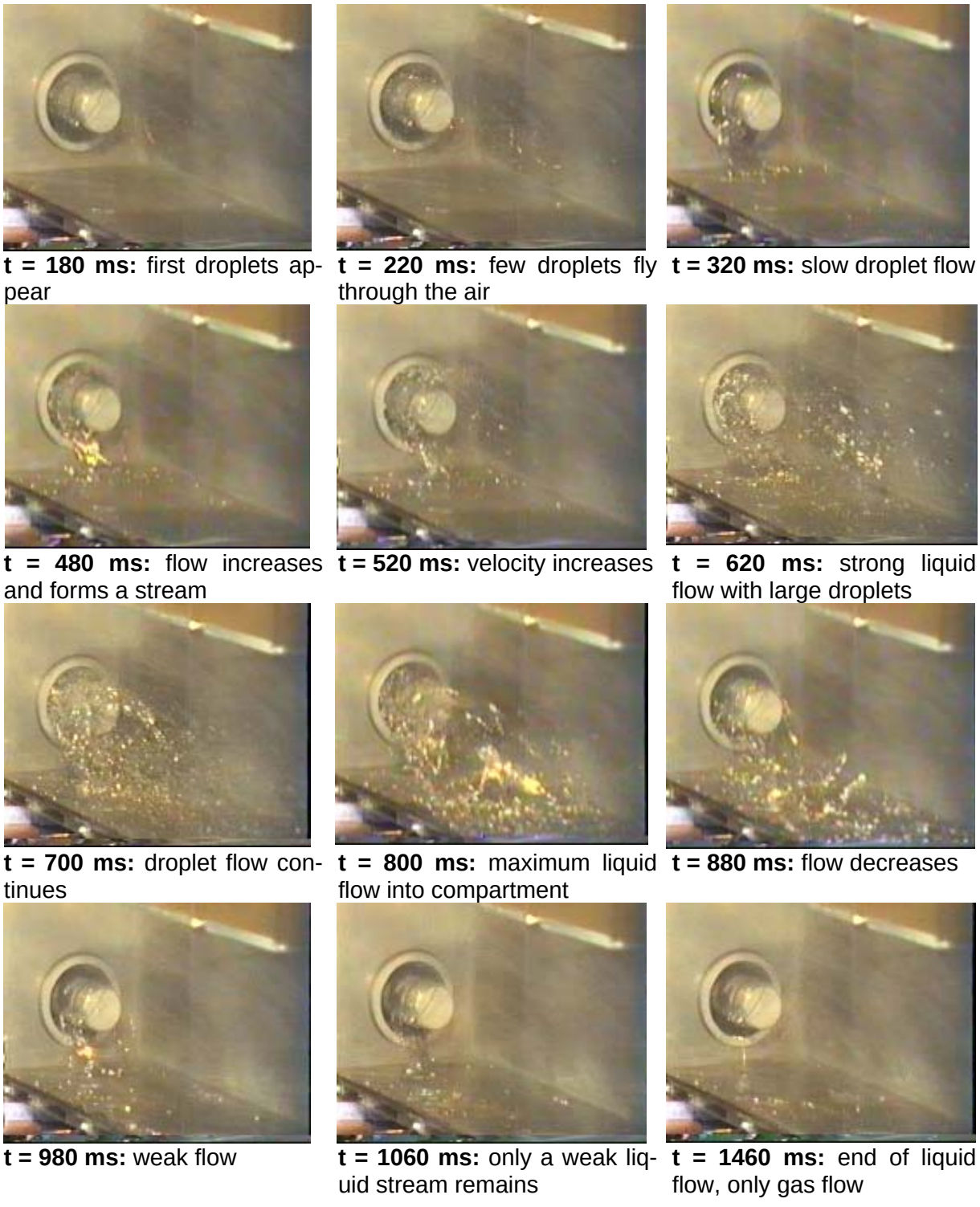

t = 180 ms: first droplets appear

t = 220 ms: few droplets fly through the air

t = 320 ms: slow droplet flow

t = 480 ms: flow increases and forms a stream

t = 520 ms: velocity increases

t = 620 ms: strong liquid flow with large droplets

t = 700 ms: droplet flow continues

t = 800 ms: maximum liquid flow into compartment

t = 880 ms: flow decreases

t = 980 ms: weak flow

t = 1060 ms: only a weak liquid stream remains

t = 1460 ms: end of liquid flow, only gas flow

Fig. 5.209 M03 Flow at the nozzle, entrance into the subcompartment, in metal test (0.58 MPa , 50 mm hole)

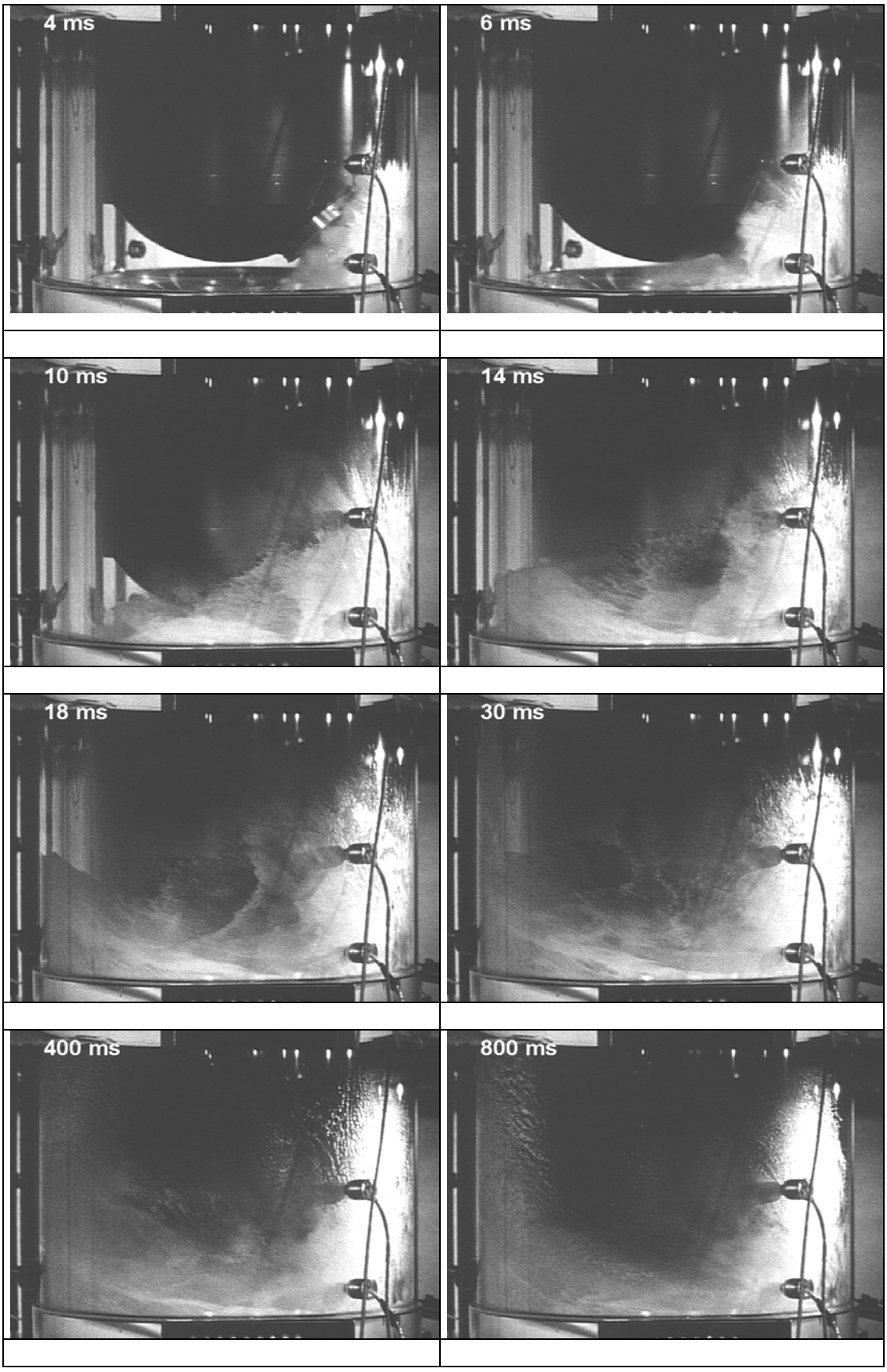

Fig. 5.210 R03 View of flow in the cavity

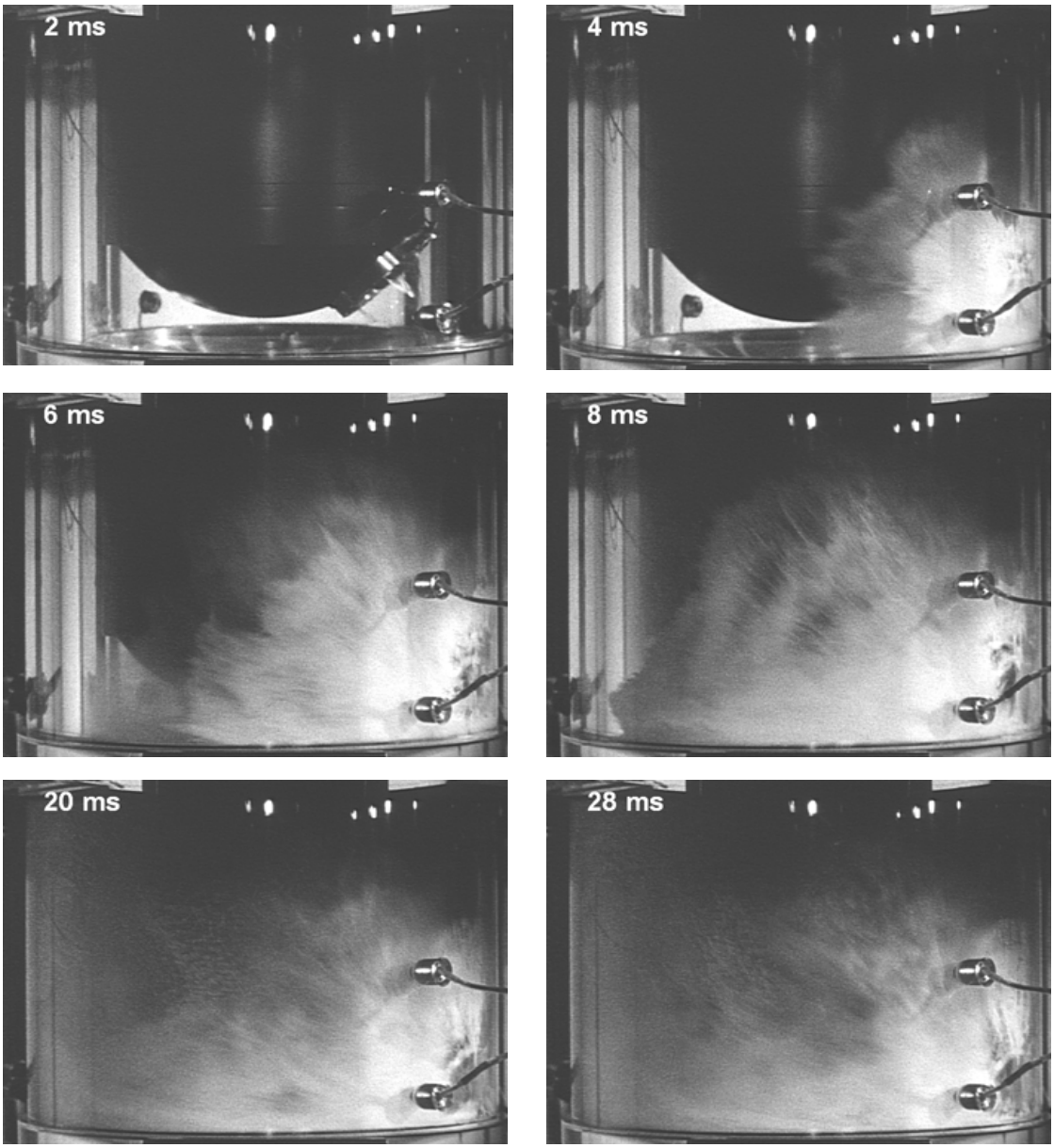

Fig. 5.211 R04 View of flow in the cavity

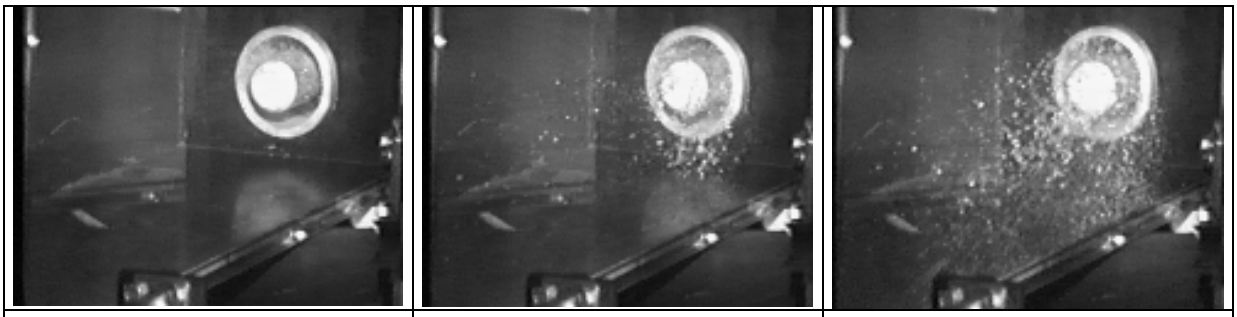

120 ms	200 ms	400 ms

Fig. 5.212 R03 View of flow into subcompartment

60 ms	100 ms	220 ms

Fig. 5.213 R04 View of flow into subcompartment

6 References

1. Nucl. Eng. Des., **164,** 1996 (Topical Issue on DCH)

2. Blanchat, T.K., M. Pilch, and M.D. Allen, Experiments to Investigate Direct Containment Heating Phenomena with Scaled Models of the Calvert Cliffs Nuclear Power Plant, NUREG/CR-6469, SAND96-2289, Sandia National Laboratories, Albuquerque, N.M., Feb. 1997.

3. Bertodano, M. L. de, A. Becker, A. Sharon, R. Schnider, DCH Dispersal and entrainment experiment in a scaled annular cavity, Nucl. Eng. Des.,**164,** 271-285, 1996

4. Blanchat, T.K., M.M. Pilch, R.Y. Lee, L. Meyer, and M. Petit, Direct Containment Heating Experiments at Lower Reactor Coolant System Pressure in the Surtsey Test Facility, NUREG/CR-5746, SAND99-1634, Sandia National Laboratories, Albuquerque, N.M., 1999.

5. Tutu, N.K., Ginsberg, C., A letter report on the results of melt dispersal experiments with the Surry and Zion cavity models, Brookhaven National Laboratory, Upton, New York, transmitted to the USNRC, Oct. 1990.

6. Pilch, M.M. R.O.Griffith, Gas Blowthrough and flow quality correlations for use in the analysis of high pressure melt ejection (HPME) events, SANDIA Report, SAND91-2322, UC-523, Sandia National Laboratories, June 1992.

7. Pilch, M.M., A Two-Cell Equilibrium Model for Predicting DCH, Appendix E of M.M.Pilch, H.Yan, T.G.Theofanous, The Probability of Containment Failure in ZION, Sandia National Laboratory report NUREG/CR-6075, SAND93-1535, July 1994

8. Jacobs, G., L. Meyer, Planned melt dispersal experiments in a scaled annular cavity, SMiRT 14 Post-Conference Seminar on Containment of Nuclear Reactors, CEA Saclay, France, August 25-26, 1997, p. 63 - 91.

9. Allen, M.D., M. Pilch, T.K. Blanchat, R.O. Griffith, and R.T. Nichols, May 1994, Experiments to Investigate Direct Containment Heating Phenomena with Scaled Models of the Zion Nuclear Power Plant in the Surtsey Test Facility, NUREG/CR-6044, SAND93-1049, Sandia National Laboratories, Albuquerque, NM.

10. Blanchat, T.K., M.D. Allen, M. Pilch, and R.T. Nichols, June 1994, Experiments to Investigate Direct Containment Heating Phenomena with Scaled Models of the Surry Nuclear Power Plant, NUREG/CR-6152, SAND93-2519, Sandia National Laboratories, Albuquerque, NM.

11. Tutu, N.K., Ginsberg, et.al., Debris Dispersal from Reactor Cavities during High-Pressure Melt Ejection Accident Scenarios, BNL, NUREG/CR-5146, 1988

12. Schmidt, E., Einführung in die Technische Thermodynamic, Springer Verlag, 1963, p. 273.

13. Yan, H., and T.G. Theofanous, The Prediction of Direct Containment Heating, Appendix D of M.M.Pilch, H.Yan, T.G.Theofanous, The Probability of Containment Failure in ZION, Sandia National Laboratory report NUREG/CR-6075, SAND93-1535, July 1994

14. Chu, T.Y., M. Pilch, J.H. Bentz and A.Behbahani, Experimental Investigation of Creep Behaviour of Reactor Vessel Lower Head, OECD/CSNI Workshop on In-Vessel Core Debris Retention and Coolability, Garching, Germany, 3-6 March, 1998, p. 297 - 306.

15. Kim, S.B, R.J. Park, H.D. Kim, Chevall and M.Petit, Reactor Cavity Debris Dispersal Experiment with Simulant at Intermediate System Pressure, Seminar Containment of Nuclear Reactors, Postconference to the 15th SmiRT, Seoul, Korea, August 23-24, 1999.

16. Gluck, D.F., J.P. Gille, D.J. Simkin and E.E. Zukoski, Distortion of the Liquid Surface During Tank Discharge Under Low g Conditions, Aerospace Chemical Engineering, No.61, Vol. 62, 1966.

17. Wilhelm, D., Transient Code Models for Low Pressure Corium Dispersion, OECD Workshop on Ex-Vessel Debris Coolability, Karlsruhe, Germany, 15-18 November 1999, Forschungszentrum Karlsruhe, wissenschaftliche Berichte, FZKA-6457 (Mai 2000), p. 45 - 53.

18. Zuber, N. et al., An integrated structure and scaling methodology for severe accident technical issue resolu-tion: Development of methodology, Nuclear Engineering Design, 186, 1-21, 1998; and NUREG/CR-5809 EGG-2659, 1991.

19. Ishii, M., H.G. No and G. Zhang, Stepwise integral scaling method and its application to severe accident phenomena, NUREG/GR-0009, 1993.

20. Pilch, M.M., A two-cell equilibrium model for predicting direct containment heating, Nuclear Engineering Design, 164, 61-94, 1996.